Toward erosion-free wind turbine operation: Physical insights into leading-edge erosion and their application to the erosion-safe mode

Barfknecht, N.

Important note

To cite this publication, please use the final published version (if applicable).
Please check the document version above.

Toward erosion-free wind turbine operation

Physical insights into leading-edge erosion and their application to the erosion-safe mode

Proefschrift

ter verkrijging van de graad van doctor

aan de Technische Universiteit Delft,

op gezag van de Rector Magnificus Prof. Dr. ir. T.H.J.J. van der Hagen,

voorzitter van het College voor Promoties,

in het openbaar te verdedigen op donderdag 5 december 2024 om 12:30 uur

door

Nils Barfknecht

Master of Science in Aerospace Engineering
Technische Universiteit Delft, Nederland,

geboren te Bad Pyrmont, Duitsland.

Dit proefschrift is goedgekeurd door de

promotor: Prof. Dr. D. von Terzi
promotor: Prof. Dr.-Ing. habil. S. Hickel

Samenstelling promotiecommissie:

Rector Magnificus	voorzitter
Prof. Dr. D. von Terzi	Technische Universiteit Delft
Prof. Dr.-Ing. habil. S. Hickel	Technische Universiteit Delft

Onafhankelijke leden:

Prof. Dr. S. J. Watson	Technische Universiteit Delft
Prof. Dr. M. Kühn	Carl von Ossietzky Universität Oldenburg, Duitsland
Dr. J. J. E. Teuwen	Technische Universiteit Delft
Dr. M. Caboni	Nederlandse Organisatie voor toegepast-natuurwetenschappelijk onderzoek (TNO)
Prof. Dr. ir. A. C. Viré	Technische Universiteit Delft, reservelid

TUDelft Delft University of Technology

An electronic version of this dissertation is available at
http://repository.tudelft.nl/.

Contents

Summary

Many wind turbines experience leading-edge erosion on their blades due to rain and hail impacting at speeds of up to 100 m/s. The impact speed is driven predominantly by the blade tip-speed, which is expected to grow in future turbine generations as they become larger. Erosion can remove substantial amounts of material from the blades. Eventually, the damage can reach deep into the structural layers of the blade, where it then starts to jeopardize its structural integrity. The associated roughening of the blade is accompanied by losses in the annual energy production (AEP). These are estimated to be up to several percent, depending on the severity of the erosion damage. While some leading-edge protection systems have been developed, no satisfying solution has been found, and the mechanisms that lead to erosion have yet to be fully understood. The aim of this thesis is to enhance the understanding of the physical mechanisms that promote erosion, understand which site conditions contribute to erosion and apply the gained insight in the erosion-safe mode.

This thesis starts in Chapter 2 by analyzing the impact of erosion on the AEP loss by using reduced-order modeling and subsequently compares it with the erosion-safe mode (ESM). The ESM is an alternative operational erosion mitigation strategy that aims to mitigate erosion by reducing the tip-speed of the turbine during precipitation events. It is shown that, depending on the mean wind speed and frequency of damaging rain at the site, the erosion-safe mode can lead to a lower AEP loss in comparison to a mildly eroded blade or a blade that was fitted with a leading-edge protection solution that leads to similar flow disturbance. However, it still needs to be sufficiently understood what rain is damaging and what other site conditions might promote erosion.

A step toward resolving this knowledge gap is taken in Chapter 3 by investigating the behavior of rain droplets before impact with the blade. Contrary to prior state-of-the-art, it is shown that droplets deform and break up near an incoming wind turbine blade. This finding contradicts the current approach in erosion research of modeling rain droplets as circular. It is shown that deformation reduces the impact velocity of rain droplets with the blade. This effect depends on the diameter of the rain droplets and can be in the order of 10 m/s. Small droplets experience significantly more slowdown than larger rain droplets. This reduction highly influences the formation of erosion damage since the main driver for erosion is the impact velocity. As droplet deformation and slowdown depend on the rain droplet diameter, the described effect can be termed *drop-size-dependent effect*.

Chapter 4 continues the investigation of drop-size-dependent effects in leading-edge erosion. An advanced erosion damage model is built that includes several drop-size-dependent effects. It is shown that the significant drop-size-effects all suggest that the erosiveness of rain droplets increases with increasing droplet diameter. This is found to be true on a per-drop basis but also when normalizing for droplet size. Therefore, selecting an appropriate droplet diameter for experiments and numerical studies is essential since not all droplet diameters contribute equally toward forming erosion damage. Drop-size effects have substantial implications for the ESM, as increasing rain intensities shift the composition of precipitation from primarily small droplets to a composition dominated by larger ones. For an equal rain column, high-intensity precipitation events are, hence, more erosive. It is found that, for a coastal site in the Netherlands, 50 % of the erosion damage is produced by the 10 % highest-rain intensity events. Thus, in ESM operation, it is advantageous to reduce the tip-speed mainly during high-intensity precipitation events to maximize lifetime and minimize AEP loss. However, a precise relation between precipitation intensity and tip-speed that optimizes this objective is not yet known in leading-edge erosion research. A novel semi-analytical approach is devised to bridge this gap, taking into account site conditions, turbine type, and drop-size effects. With this approach, it is possible to extend the erosion lifetime of a contemporary blade by a factor of 13 for a moderate AEP loss of 1 %.

A critical component for the successful utilization of the ESM is the accurate forecasting of precipitation events minutes to hours ahead. However, the best approach for obtaining this information is still debated. For the first time, Chapter 5 benchmarks a state-of-the-art weather-radar-based probabilistic rainfall nowcast product by the Royal Netherlands Meteorological Institute (KNMI). The performance of the nowcast is assessed for various lead times for three sample sites in the Netherlands and for two distinct ESM strategies. The results show that the quality of the nowcast degrades with increasing lead times. The 5- and 15-minute lead times exhibit sufficiently good accuracy and response time for the successful utilization of the ESM. Across the sites, for a large 15 MW turbine, a lifetime extension of factor five can be achieved for an AEP loss of about 1 %.

To summarize, this thesis introduced the highly significant effect of droplet slowdown and deformation occurring in the vicinity of wind turbine blades. It investigated drop-size-dependent effects and established their significance for ESM operation. It provided new theoretical insights into the ESM and used these to devise a method for finding optimal ESM strategies that exploit drop-size effects. Finally, it benchmarked the devised strategies using a state-of-the-art (operational) nowcasting product and showed that the ESM could already be a viable erosion-mitigation strategy.

Samenvatting

Veel windturbines ondervinden erosie aan de leading edge (voorzijde) van de bladen ten gevolge van regen en hagel met impactsnelheden tot 100 m/s. De impactsnelheid wordt voornamelijk gedreven door de snelheid van het uiteinde van de windturbinebladen. Deze zal naar verwachting bij de volgende windturbinegeneraties hoger worden door de toenemende afmetingen. Erosie kan aanzienlijke hoeveelheden aan materiaal van de bladen verwijderen. Op den duur kan de schade zo diep doordringen in de lagen van het blad, dat het uiteindelijk de structurele integriteit in gevaar brengt. De bijbehorende ruwheid van het blad gaat gepaard met een daling in de jaarlijkse energieproductie (AEP). Dit wordt geschat op enkele procenten, afhankelijk van de ernst van de schade. Hoewel er enkele systemen zijn ontwikkeld om de leading edge te beschermen, is er tot op heden geen bevredigende oplossing gevonden. De onderliggende erosiemechanismen zijn nog niet geheel duidelijk. Het doel van dit proefschrift is om deze mechanismen beter te begrijpen, uit te zoeken welke omstandigheden in het bijzonder bijdragen aan erosie en met de verkregen inzichten een strategie te ontwikkelen om erosie te voorkomen.

Dit proefschrift begint in Hoofdstuk 2 met het analyseren van de bijdrage van erosie aan het verlies van AEP door middel van reduced-order modeling. Vervolgens wordt dit vergeleken met de erosion-safe mode (ESM). De ESM is een alternatieve operationele mitigatiestrategie teneinde de erosie te verminderen door de tip-snelheid van de turbine ten tijde van neerslag te verlagen. Er wordt aangetoond dat, afhankelijk van de gemiddelde plaatselijke windsnelheid en regenfrequentie, de ESM kan leiden tot minder AEP-verlies in vergelijking tot een licht geërodeerd blad of een blad dat is uitgerust met een leading edge beschermingssysteem met vergelijkbare stromingsverstoringen. Het is echter nog onvoldoende duidelijk wat als schadelijke regen wordt beschouwd en welke plaatselijke omstandigheden erosie bevorderen.

Een stap in de richting tot het oplossen van dit vraagstuk volgt in Hoofdstuk 3 door middel van onderzoek naar het gedrag van regendruppels voordat deze contact maken met het blad. In tegenstelling tot eerdere state-of-the-art wordt hier aangetoond dat druppels vervormen en uiteenvallen in de nabijheid van een naderend windturbineblad. Deze bevinding staat haaks op de huidige benadering in erosieonderzoek, waarbij regendruppels als cirkelvormig worden gemodelleerd. Er wordt aangetoond, dat door de vervorming en het uiteenvallen van regendruppels de impactsnelheid (van de regendruppels op het blad) verminderd wordt. Dit

effect is afhankelijk van de diameter van de regendruppels en kan in de orde van grootte van 10 m/s liggen. Kleine druppels ondervinden aanzienlijk meer vertraging dan grotere regendruppels. Hierdoor vertraagt eveneens het ontstaan van erosieschade, aangezien de de impactsnelheid de belangrijkste component van erosieschade is. Aangezien de vervorming en vertraging afhankelijk zijn van de diameter van de regendruppels, kan dit effect worden aangeduid als het *druppelgrootte-afhankelijke effect*.

Hoofdstuk 4 zet het onderzoek naar druppelgrootte-afhankelijke effecten in leading-edge erosie voort. Er is een geavanceerd erosieschademodel ontwikkeld, dat verschillende druppelgrootte-afhankelijke effecten omvat. Er wordt aangetoond, dat alle onderzochte significante druppelgrootte-afhankelijke effecten suggereren dat de erosiviteit toeneemt naarmate de diameter van de druppels toeneemt. Dit blijkt niet allen te gelden als er gekeken wordt naar individuele druppels, maar ook wanneer genormaliseerd wordt voor het verschil in watervolume. Derhalve is het selecteren van een geschikte druppeldiameter voor experimenten en numerieke studies essentieel. Druppelgrootte-afhankelijke effecten hebben diepgaande gevolgen voor de ESM, doordat hogere regenintensiteiten de samenstelling van neerslag van voornamelijk kleine druppels naar overwegend grotere druppels verandert. Zodoende is voor een gelijke hoeveelheid aan regenval neerslag met een hoge intensiteit meer erosief. Er wordt vastgesteld, dat voor een kustlocatie in Nederland 50 % van de erosieschade wordt veroorzaakt door de 10 % hevigste regenbuien. Daarom is het tijdens het gebruik van ESM gunstig om de snelheid van de bladtip vooral tijdens zware neerslag te reduceren teneinde de levensduur te maximaliseren en AEP-verlies te minimaliseren. Een precies verband tussen neerslagintensiteit en tip-snelheid om deze laatstgenoemde doelen te bereiken bestaat tot op heden nog niet in leading edge onderzoek. Een nieuwe semi-analytische aanpak is ontwikkeld om deze kloof te dichten, waarbij rekening wordt gehouden met de plaatselijke weersomstandigheden, turbinetype en druppelgrootte-afhankelijke effecten. Met deze aanpak is het mogelijk om de levensduur van een hedendaags rotorblad te verlengen met een factor 13 bij een matig AEP-verlies van 1 %.

Een cruciaal element voor de praktische toepasbaarheid van de ESM is een nauwkeurige voorspelling van neerslag op de korte termijn (enkele minuten tot uren van tevoren). Echter, de beste aanpak om deze informatie te verkrijgen blijft onderwerp van debat. In Hoofdstuk 5 wordt voor het eerst een state-of-the-art weerradar-gebaseerd probabilistisch neerslag-nowcast product van het Koninklijk Nederlands Meteorologisch Instituut (KNMI) toegepast. De prestaties van de nowcast worden beoordeeld voor verschillende voorspellingshorizons op drie voorbeeldlocaties in Nederland en voor twee verschillende ESM-strategieën. De resultaten tonen aan dat de kwaliteit van de nowcast afneemt naarmate de voorspellingshorizon toeneemt. De 5- en 15-minuten voorspellingshorizons vertonen een voldoende

nauwkeurigheid en reactietijd voor de toepasbaarheid van de ESM. Voor alle drie locaties geldt dat voor een grote windturbine van 15 MW de levensduur hiermee met een factor vijf kan worden verlengt bij een AEP-verlies van ongeveer 1 %.

Samenvattend heeft dit proefschrift het zeer significante effect geïntroduceerd van de vertraging en vervorming van regendruppels in de nabijheid van de leading edge van de windmolenbladen. Er is onderzoek gedaan naar druppelgrootte-afhankelijke effecten en hun belang voor de werking van de ESM. Het heeft nieuwe theoretische inzichten gegeven in de ESM. Deze inzichten zijn gebruikt om een methode te ontwikkelen voor het vinden van optimale ESM-strategieën door middel van druppelgrootte-afhankelijke effecten. Ten slotte is de ESM getest met behulp van een daadwerkelijk (operationeel) nowcasting-product en is aangetoond dat de ESM met de huidige state-of-the-art weersvoorspellingen al een bruikbare erosie-mitigatiestrategie zou kunnen zijn.

1

INTRODUCTION

1.1. WHAT IS LEADING-EDGE EROSION OF WIND TURBINE BLADES?
Wind turbines are exposed to adverse weather such as extreme heat, humidity, storm, and precipitation. During operation, wind turbine blades accumulate damage at the very front of the blade. This damage manifests itself in the form of pits, craters, and cracks that can reach several centimeters deep into the structural layers of the blade. This damage is also called leading-edge erosion (LEE). Figure 1.1 shows leading-edge erosion on a turbine blade.

Figure 1.1: Leading-edge erosion damage on a wind turbine blade; photography reproduced from Telene (2021).

Erosion is caused by the three environmental conditions: rain, hail, and sand (Herring et al., 2019). This stands contrary to other origins of blade damage such as

1

lightning and bird strikes. The importance of rain, hail, and sand varies per region. Hailstone-induced erosion is a major concern for wind parks in the Great Plains in the USA (Letson et al., 2020). Hail can cause significant damage to wind turbine blades, which is unsurprising given that hailstones can reach several centimeters in diameter. In Europe, in 2021, there were 29 reports of hail with a diameter larger than 10 cm (ESSL, 2021). For offshore wind turbines, leading-edge erosion is mostly attributed to rain events (López et al., 2023). Some sources report erosion damage due to rain in merely two years of operation (Keegan et al., 2013). Usually, erosion damage is found toward the tip of the blade along the last 10 to 20 meters (Verma et al., 2021).

Blade damage must be repaired periodically to prevent failure. The repair of wind turbine blades is costly. Depending on the site and size of the wind turbine, workers usually need to rope down from the nacelle to reach the damaged location at the wind turbine blade. The current push to develop offshore wind energy complicates maintenance. While access to the wind turbine at land is usually not a problem, offshore turbines can only be reached by either boat or air transport. Additionally, offshore wind turbines are usually significantly larger than their onshore counterparts. During the writing of this thesis, the largest onshore turbine had a rotor diameter of 216 m while the largest offshore turbine had a rotor diameter of 260 m (CSSC Haizhuang, 2023; Mingyang Smart Energy, 2023).

Erosion also affects the aerodynamics of the blade. The roughening of the blades due to erosion damage disturbs the airflow and changes the transition of the boundary layer (Castorrini et al., 2020). This can lead to a significant performance loss in the order of up to a few percent of the annual energy production (AEP) (Herring et al., 2019). Hence, erosion also induces costs due to a reduction in electricity generation.

1.1.1. Costs associated with performance loss due to erosion

The extra capital expenditure (CapEx) costs due to erosion are significant. In the year 2022, there was a worldwide installed wind energy capacity of 902 GW, see Figure 1.2. Around 9 GW of capacity is lost when assuming that erosion reduces the power by about 1 %. IEA (2023) projects that the worldwide capacity will triple to 2742 GW by the year 2030 and will have grown by a factor of 8.5 (7616 GW) until the year 2050. Hence, the projected loss in capacity due to erosion will be in the range of 27.4 to 76.2 GW. At a conservative estimate of 1000 euros/kWh, erosion will nullify 76.2 billion euros worth of wind turbines by 2050.

Erosion also leads to costs due to lost revenue. For an IEA 15MW turbine with a capacity factor of 0.5, an electricity price of 100 euros/MWh and a power loss of 1 % due to erosion, the lost revenue in electricity per year equates to 65,700 euros. In a wind farm of 1 GW rated power, and 67 turbines, the total cost, just due to

AEP loss, is then around 4.4 million euros per year. Over a projected lifetime of 30 years this cost becomes 132 million euros. This number does not include any maintenance and opportunity costs. The Netherlands plans to reach an installed offshore capacity of 21 GW by 2032 (RVO, 2024). Hence, a conservative prediction is that the erosion-induced cost due to lost revenue for the (near-term) Dutch offshore fleet will be 2.7 billion euros over its lifetime.
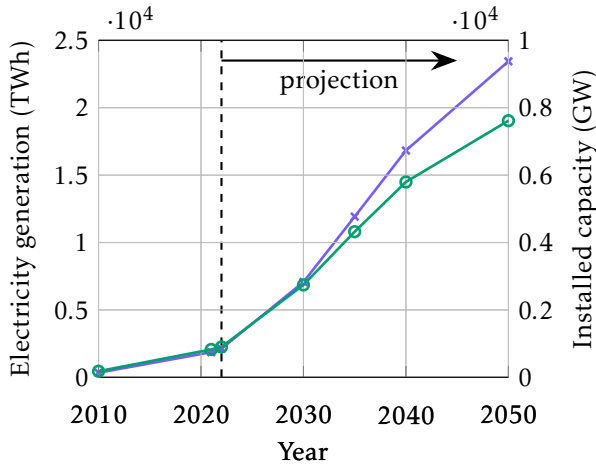
Figure 1.2: World wide electricity generation and installed capacity of wind energy; future projections according to the *Net Zero Emissions by 2050 Scenario* by IEA (2023); electricity generation: ──✳──, installed capacity: ──⊙──.

1.1.2. Current approaches to managing erosion

The industry-standard procedure to managing erosion is blade repair and the optional application of a leading-edge protection (LEP) system. Blade repair typically starts with surface preparation, such as sanding, degreasing and priming, to ensure good adhesion. Putty (filler) is applied and smoothed to restore the leading-edge profile. A topcoat can be applied as a finishing layer. All-in-one products exist as well (TEKNOS, 2020). The repair of a blade by rope technicians is shown in Figure 1.3a. Optional after the repair, is the application of LEP systems. They are either applied as a retrofit or straight from the factory. These protection systems come in different form and shapes. The market offers tapes or rubber-like sheets that can be bonded to blades (Hoksbergen, 2023; Kraiburg). More advanced approaches use pre-molded blade sections (Polytech, 2023). An application of such a solution is shown in Figure 1.3b. LEP systems can also come in the form of liquid coatings (Bergolin GmbH & Co. KG, 2023). Often LEP solutions are based on polyurethane. Sometimes liquid coatings are based on polyurea for accelerated hardening (Hoksbergen, 2023). Some research has been performed on metal

1

shields (Herring et al., 2019). Their cost effectiveness, bonding problems due to the stiffness mismatch between shield and blade, and influence on lightning protection still need to be better understood to make them a viable option. In general, all LEP systems promise to have properties that can better resist the impact of rain droplets compared to the default leading edge material.

(a) Rope technicians applying a leading-edge repair product; photograph reproduced from Belzona (2022).

(b) Application of a premolded leading-edge protection shield; photograph reproduced from Polytech (2023).

(c) A robot performing maintenance on a blade; photograph from AERONES.

Figure 1.3: Industry-standard repair and maintenance approaches for managing leading-edge erosion.

Blade repairs and LEP systems are not trouble-free. A blade repair only provides temporary relief from erosion and needs to be repeated as soon as erosion occurs again. LEP systems provide longer-term relief but cannot be regarded as maintenance-free either. An LEP also needs to be inspected and repaired, albeit

at a lower rate than an unprotected blade. A key issue of blade maintenance is the reliability of the process outside of a factory environment. The author of this dissertation has heard an anecdotal story that a large wind turbine operator only considers 50 % of its blade repairs to be successful. This indicates a significant mismatch between expectations and reality in the field.

Repaired blades and LEP systems can also experience an AEP loss. It is challenging to restore a damaged leading edge to its original shape. Likewise, LEP systems modify the shape of the leading edge as well. Usually, technicians try to smoothen out any (backward-facing) steps by filling the transition between LEP and blade. Hence, suppliers from the industry are often convinced that the LEP-induced AEP loss is negligible. For example, Polytech (2022a,b) claims that LEPs can lead to a (theoretical) performance loss in a wind tunnel but argue that in the field, no AEP loss can be observed. Their conclusion is based on the analysis of SCADA data from a turbine pair, with one being equipped with an LEP solution. However, Maniaci et al. (2023) argues that turbine pair comparisons based on SCADA data have considerable uncertainty, and, therefore, a relatively high number of turbine pairs is required to draw a statistically significant conclusion. Research by Forsting et al. (2023) has shown that a 0.1 mm imperfection already influences the aerodynamics of an airfoil. The results were obtained in a wind tunnel.

The logistical challenges of servicing a blade should also be considered. As explained, offshore locations are difficult to reach, and the size of turbines is ever-growing. The weather limits repair teams. At high wind speeds, repair jobs become too dangerous. Repair and LEP products are restricted by environmental conditions as well. They cannot be applied if the temperature is too low or the humidity is too high. Additionally, technicians and operators must respect the hardening and curing times of the products they use. Mishnaevsky (2019) reports one to three days of downtime for a repair job.

The industry is moving toward automating the inspection and maintenance of wind turbine blades using robots and drones. By now, it is standard practice to inspect wind turbine blades using drone photography (Shihavuddin et al., 2019). Robots can be used for blade repair. A rope-suspended robot performing blade repair is shown in Figure 1.3c. Multiple manufacturers have developed these robotic systems. They promise to make repairs more economical by reducing the required human labor (AERONES; BladeRobots A/S) and improve the accuracy and repeatability of the repair job. For example, Hamamura (2023) offers a robot that is equipped with a 3D scanner and a high-precision milling tool head. This robot scans the damaged leading edge, applies a filler material to the damaged sections, and subsequently machines it to the shape of the reference leading-edge profile, something that would be impossible to do using manual labor.

To conclude, the advantages and disadvantages of current industry-standard solutions should be viewed as case-dependent. Some solutions might be adequate for

1

particular scenarios, while in other circumstances, their success could be considered inadequate.

1.1.3. Physical aspects of erosion damage formation

The formation of leading-edge erosion is a complex interplay of different fields as visualized in Figure 1.4. The climate determines the expected precipitation at a site. Once released from the clouds, droplets fall through the air and impact with the blade. Impacts cause stress waves inside the leading-edge material, eventually yielding erosion damage. Leading-edge erosion encompasses, among others, the study of meteorology, fluid dynamics, and material sciences. This multidisciplinary nature makes prediction and mitigation of leading-edge erosion challenging.
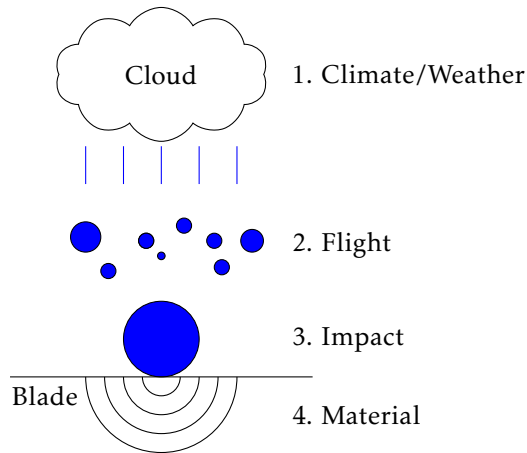
Figure 1.4: Aspects of the leading-edge erosion.

Meteorology is of major importance for leading-edge erosion. The conditions a turbine encounters are highly site-specific. In Figure 1.5, the mean annual precipitation in the North Sea region is shown. Precipitation varies from as low as 400 mm/year to as much as 2200 mm/year. Other vital metrics of interest are the rain frequency and the rain intensity distribution. This information is the starting point for an erosion damage prediction or erosion mitigation strategy. Weather forecasting is of interest as well, especially in the context of operational mitigation strategies, as will be discussed later.

The morphology of rain determines a significant part of the parameter space of the erosion problem. It is critical to have a good understanding of what (rain) hits the blade. Falling droplets can coalesce or break up during flight. The composition of rain can be described with a drop-size distribution. It associates the liquid water

content with a particular droplet size. Rain droplets eventually assume a terminal falling velocity and shape. They are also affected by the wind and interact at some point aerodynamically with the wind turbine.
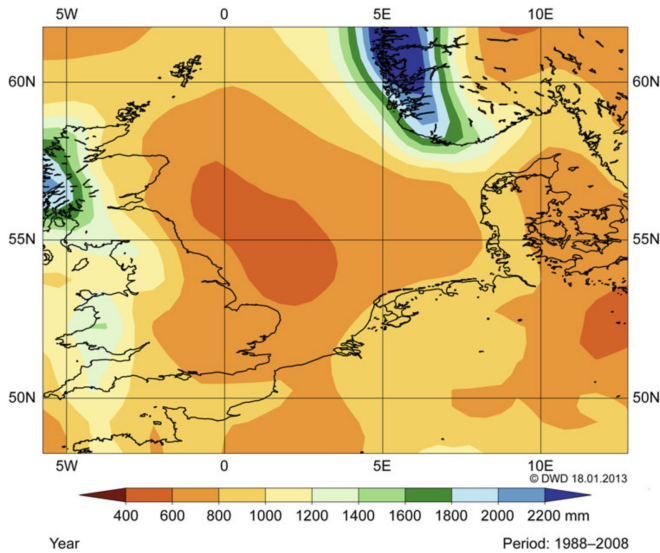
Figure 1.5: Mean annual precipitation in the North Sea region; reproduced from Quante et al. (2016); Hasager et al. (2021).

Figure 1.6a and 1.6b show the complex interaction between an impacting rain droplet and the leading-edge material. Waves are induced inside the material and the drop. Rayleigh waves move along the surface of the material. Inside the material, compression waves act along the longitudinal direction, whereas shear waves act in the transverse direction. The different layers of a leading edge, such as the top-coat and the substrate, have different material properties and thus also different acoustic impedances. Therefore, the waves are reflected at the interface of the different layers.

The manufacturing of leading edges and its process reliability are other important aspects. Mishnaevsky Jr et al. (2020) showed that manufacturing defects can lead to voids inside the leading-edge material (see Figure 1.6c). These voids create stress concentrations, promoting the formation of erosion. Surface defects can also lead to stress concentrations. Predicting erosion is, therefore, not only dependent on the properties of the leading edge material but also its shape.

The driver for erosion is the high impact speed of the rain droplets. Since erosion is observed mainly outboard of a wind turbine blade, the impact speed is approximately equal to the tip-speed of the turbine. For example, the IEA 15MW reference

turbine has a rated tip speed of 95 m/s (Gaertner et al., 2020). This is comparable to the jet velocity of a pressure washer (Guha et al., 2011), providing an intuitive reason why these velocities lead to erosive conditions.

The contact pressure at the instant of the first impact can be estimated by using the water hammer pressure.

$$p_{wh} = V_{impact}\, \rho_{water}\, c_{water}, \tag{1.1}$$

where V_{impact} is the impact speed, $\rho_{water} = 999.1$ kg/m^3 is the density of water and $c_{water} = 1466$ m/s is the speed of sound in water, both given for 15 °C. For an impact speed of 95 m/s, a contact pressure of about 139 MPa is obtained. Failure of the leading edge after numerous repeated impacts is, therefore, not surprising.
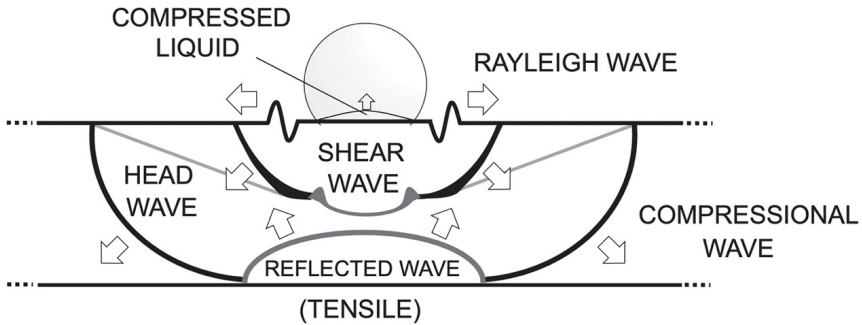
(a) Stress waves in the material due to rain droplet impact; reproduced from (Gohardani, 2011).
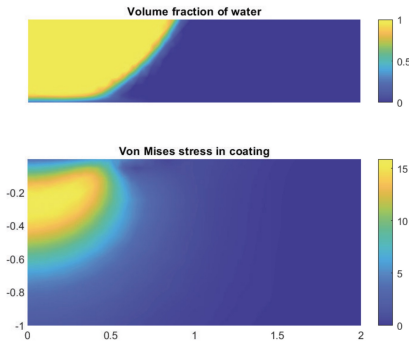
(b) Simulated stress field in a leading-edge substrate due to impact with a water droplet; reproduced from Hoksbergen (2023).
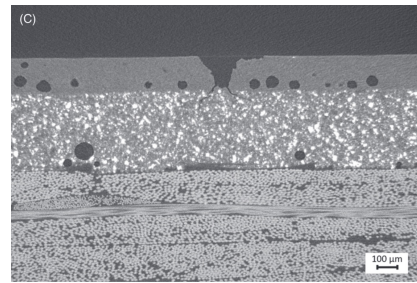
(c) Section of a leading edge with surface defects and voids; reproduced from Mishnaevsky Jr et al. (2020).

Figure 1.6: Interaction of impacting rain droplet and leading-edge.

The progression of erosion is not linear. Usually, it is described with a diagram such as shown in Figure 1.7 (Bartolomé and Teuwen, 2019). Initially, no mass loss occurs due to impacting droplets. Subsurface damage, however, occurs already (Hoksbergen, 2023). The incubation time measures the point when the first material is removed. After the incubation stage, the material removal rate is approximately constant. As the severity of erosion progresses, the rate starts to change and becomes increasingly undefined.
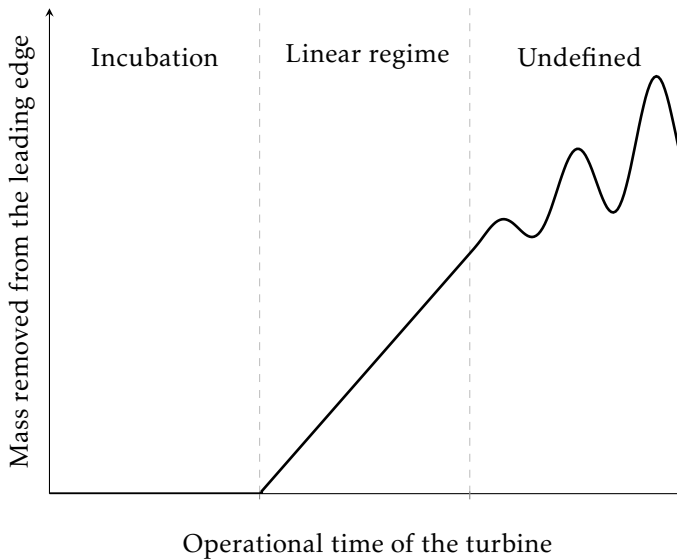
Figure 1.7: Sketch of the leading-edge mass loss experienced by a turbine over time; the figure is adapted from Bartolomé and Teuwen (2019).

1.1.4. The erosion-safe mode as an operational mitigation strategy

The crucial role of the impact speed can be exploited to mitigate erosion by making operational adjustments. To this end, the erosion-safe mode (ESM) was recently proposed. In this mode, the turbine is shut off, or the tip-speed of the turbine is limited when damaging precipitation events occur. This is illustrated in Figure 1.8, where the tip-speed is (arbitrarily) limited to 75 m/s during precipitation. Operating in the ESM has the potential to reduce or altogether avoid erosion (Bech et al., 2018; Picard and Canal Vila, 2019).

The ESM appears attractive due to the relation between erosion lifetime, i.e., end of incubation, and the impact speed. Usually, this relation is modeled using a power law.

$$N \propto \frac{1}{V_{\text{impact}}^{\beta}}, \tag{1.2}$$

1
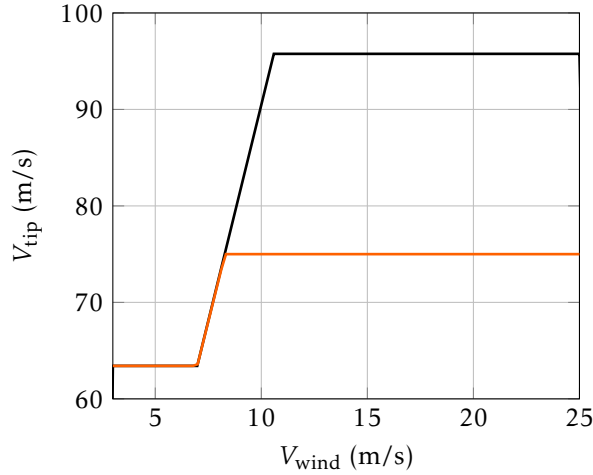
Figure 1.8: Tip-speed of the IEA 15MW turbine as a function of the wind speed; nominal tip-speed: ——, possible ESM strategy with 75 m/s limit: ——.

where V_{impact} is the droplet impact speed, and N is a metric for incubation, such as accumulated water column or the number of impacts. Of special interest is β, which is a material-specific constant. Values for β reported in literature vary from 5.7, 7.2-10.5, and 16.02 (Hoksbergen et al., 2022; Bech et al., 2022; Shankar Verma et al., 2021). Hence, irrespective of the exact value, already a small reduction in tip-speed has the potential to drastically increase the erosion lifetime.

The ESM is based on the concept of addressing the root cause of erosion, namely operation during precipitation events, rather than just treating its symptoms. However, shutting down (or limiting the tip-speed) of a turbine will also lead to a loss in AEP. As an illustration, the weather station in De Kooy, the Netherlands, indicates that it rains roughly 6.7 % of the time (KNMI, 2020). Limiting the tip-speed of a turbine so often will lead to a power loss that is higher than that of erosion, making this idea unfeasible. Therefore, the aim should be to employ the ESM only during precipitation events that really matter for erosion.

With the steady up-scaling of wind turbines and the resulting larger and larger rotor diameters, it is favorable from a systems perspective to increase the tip-speed. This, for example, allows for a reduction in the size of the drivetrain. Higher tip-speeds, however, will make turbines more susceptible to erosion. Erosion, therefore, not only causes structural and aerodynamic problems but could even be a potential roadblock for future wind turbine up-scaling. Erosion could become so severe that further tip-speed and, thus, rotor diameter increases are not favorable.

1.1.5. Recommended introductory literature for further reading
For further insights into the topic of erosion, the reader is recommended to study the (introductions of the) following dissertations. Keegan (2014) and Herring (2022) provide a good general overview about erosion. More in-depth information about erosion-test rigs is provided by Johansen (2020). For insights into materials and impact dynamics, the reader is recommended to read Hoksbergen (2023). Lastly, Tilg (2020) focuses on the meteorological aspects relevant to this field.

1.2. Objective
A qualitative and quantitative understanding of the physical mechanisms and precipitation conditions promoting erosion is critical. This knowledge is essential for determining the parameter space of the erosion problem, which is an important input for experiments and numerical studies. It also feeds directly into forecasting models, which are, for example, used to evaluate the erosion potential of wind turbine sites.

The successful utilization of the ESM depends on this knowledge as well. With an incomplete understanding, the ESM will be utilized sub-optimally, leading to reduced performance and potentially rendering the ESM unfeasible. So far, it is not clear which physics the ESM is sensitive to and which site conditions favor the utilization of the ESM.

With this discussion in mind, the aim of this thesis is:

> *Understand which precipitation conditions and physics promote erosion and how this gained understanding can be used in the erosion-safe mode.*

This thesis only concerns erosion due to rain. Erosion due to sand and hail is not part of this thesis.

1.3. Outline
This thesis comprises four main content chapters (excluding the conclusions). Each chapter is based on a paper published during the research that led to this thesis. Additionally, two appendices develop concepts that are used throughout this work. The structure of the thesis and the respective research question of each chapter are shown in Figure 1.9.

Chapter 2 - AEP loss of leading-edge erosion and erosion-safe mode operation: The erosion-safe mode represents an interesting and novel approach to tackle leading-edge erosion. However, it still needs to be determined whether it is a viable alternative. Especially, its inherent AEP loss is a point of concern. Therefore, this chapter presents an entitlement study aimed at establishing an initial ballpark estimate for the viability of the erosion-safe mode, to motivate future research. The

1

Ch. 3: How do rain droplets be-		**Ch. 4:** How do drop-size-
have in the vicinity of the blade		dependent effects influence
and how does this behavior influ-		leading-edge erosion and
ence leading-edge erosion?		erosion-safe mode operation?
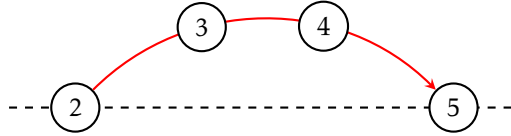
Ch. 2: Does the erosion-		**Ch. 5:** Can state-of-the-art
safe mode have the poten-		precipitation nowcasting be
tial to be a viable erosion		used to effectively drive the
mitigation strategy?		enhanced erosion-safe mode?

Figure 1.9: Thesis arc and key research questions.

AEP loss associated with operating in the erosion-safe mode is compared with the loss stemming from mild erosion or LEP systems. This entitlement study also aims to reveal sensitivities for the utilization of the ESM. To summarize, the chapter and its conclusions set the foundation for future research conducted in this thesis.

Chapter 3 - Rain droplet slowdown, deformation and breakup in the blade's vicinity: A thorough understanding of the physical mechanisms driving erosion damage formation is required to utilize the ESM efficiently. However, this understanding has yet to be fully obtained. This chapter aims to enhance this understanding by delving into the fundamental physics of erosion. In particular, this chapter studies the possible aerodynamic interaction of rain droplets and wind turbines. Up to now, this aspect has received almost no attention. This chapter collects measurements from literature and develops a model to study the droplet slowdown and deformation effect in leading-edge erosion. The significance is established by performing an elaborate sensitivity study.

Chapter 4 - Drop-size-dependent effects and erosion-safe mode operation: This chapter applies the newly acquired knowledge about the droplet slowdown and deformation effect and its dependence on the droplet diameter to the ESM. To this end, a cutting-edge erosion damage model is developed that incorporates the latest findings from erosion research. Particular focus is put on so-called drop-size effects, i.e., physical mechanisms, such as the droplet slowdown, that make the formation of erosion damage dependent on the diameter of rain droplets. Subsequently, this model is used to investigate how the ESM should be utilized and how the theoretical performance is altered compared to the previous state-of-the-art that neglected these effects.

Chapter 5 - Nowcast-driven erosion-safe mode control: The research of Chapter 3 and Chapter 4 led to a significant increase in the theoretical effectiveness of the ESM. However, it is not clear how the ESM's practical viability is influenced. This chapter aims to answer this question by performing a final entitlement study. In particular, a novel precipitation nowcast is used to drive the erosion-safe mode. The results of this chapter establish whether the knowledge acquired in this thesis makes the ESM practically viable. This chapter sets a new state-of-the-art and acts as the basis for future research.

Chapter 6 - Conclusions: Finally, the findings of the thesis are summarized by answering the four key research questions of Figure 1.9. Subsequently, the implications of these findings are discussed and an outlook is given.

Appendix A - The impingement collected by a wind turbine blade: A formal derivation for the impingement damage metric is given. This metric has become popular in recent research. However, a formal derivation has not yet been provided in the literature.

Appendix B - The ESM regime and a method for finding optimal ESM strategies: The ESM is formalized by defining its operational regime and its Pareto front. Additionally, a method is given for designing optimal ESM strategies. The designed optimal ESM strategies are used Chapter 4 and 5.

1

Bibliography

AERONES: Leading Edge Repair - Robotic Wind Turbine Care Systems, https://aerones.com/services/repair/, Website accessed: May 22, 2023.

Bartolomé, L. and Teuwen, J.: Prospective challenges in the experimentation of the rain erosion on the leading edge of wind turbine blades, Wind Energy, 22, 140–151, https://doi.org/10.1002/we.2272, 2019.

Bech, J. I., Hasager, C. B., and Bak, C.: Extending the life of wind turbine blade leading edges by reducing the tip speed during extreme precipitation events, Wind Energy Science, 3, 729–748, https://doi.org/10.5194/wes-3-729-2018, 2018.

Bech, J. I., Johansen, N. F.-J., Madsen, M. B., Hannesdóttir, Á., and Hasager, C. B.: Experimental study on the effect of drop size in rain erosion test and on lifetime prediction of wind turbine blades, Renewable Energy, 197, 776–789, https://doi.org/10.1016/j.renene.2022.06.127, 2022.

Belzona: New Leading Edge Repair And Protection Solution (With Video), 2022, https://blog.belzona.com/new-leading-edge-repair-an-protection-solution/, Website accessed: July 1, 2024.

Bergolin GmbH & Co. KG: Rotor blade repair, 2023, https://en.bergolin.de/rotorblatt-reparatur, Website accessed: May 22, 2023.

BladeRobots A/S: A Vestas Company, https://bladerobots.com/, Website accessed: May 22, 2023.

Castorrini, A., Cappugi, L., Bonfiglioli, A., and Campobasso, M.: Assessing wind turbine energy losses due to blade leading edge erosion cavities with parametric CAD and 3D CFD, Journal of Physics: Conference Series, 1618, 052 015, https://doi.org/10.1088/1742-6596/1618/5/052015, 2020.

CSSC Haizhuang: CSSC Haizhuang H260-18MW offshore wind turbine giant emerges, 2023, http://cssc-hz.com/?en/enNews/NewsReleases/148.html, Website accessed: May 22, 2023.

ESSL: Hailstorms of 2021, 2021, https://www.essl.org/cms/hailstorms-of-2021/, Website accessed: May 22, 2023.

Forsting, A., Olsen, A., Sørensen, N., and Bak, C.: The impact of leading edge damage and repair on sectional aerodynamic performance, in: 2023 AIAA SciTech Forum, 2023.

Gaertner, E., Rinker, J., Sethuraman, L., Zahle, F., Anderson, B., Barter, G. E., Abbas, N. J., Meng, F., Bortolotti, P., Skrzypinski, W., et al.: Definition of the IEA

15-Megawatt Offshore Reference Wind Turbine, Tech. rep., National Renewable Energy Lab.(NREL), Golden, CO (United States), 2020.

Gohardani, O.: Impact of erosion testing aspects on current and future flight conditions, Progress in Aerospace Sciences, 47, 280–303, https://doi.org/10.1016/j.paerosci.2011.04.001, 2011.

Guha, A., Barron, R. M., and Balachandar, R.: An experimental and numerical study of water jet cleaning process, Journal of Materials Processing Technology, 211, 610–618, https://doi.org/10.1016/j.jmatprotec.2010.11.017, 2011.

Hamamura, K.: Blade Repair Robot and smart solution of blade maintenance, 4th International Symposium on Leading Edge Erosion and Protection of Wind Turbine Blades, Technical University of Denmark, 2023, Lebo Robotics Inc., JP.

Hasager, C. B., Vejen, F., Skrzypiński, W. R., and Tilg, A.-M.: Rain Erosion Load and Its Effect on Leading-Edge Lifetime and Potential of Erosion-Safe Mode at Wind Turbines in the North Sea and Baltic Sea, Energies, 14, https://doi.org/10.3390/en14071959, 2021.

Herring, R.: Leading Edge Erosion of Wind Turbine Blades: An Assessment and Improvement of the Translation Between Test Results and In-situ Performance, Doctoral thesis, University of Bristol, 2022.

Herring, R., Dyer, K., Martin, F., and Ward, C.: The increasing importance of leading edge erosion and a review of existing protection solutions, Renewable and Sustainable Energy Reviews, 115, 109 382, https://doi.org/10.1016/j.rser.2019.109382, 2019.

Hoksbergen, N.: Predicting Rain Erosion Damage in Wind Turbine Blade Coating Materials, Ph.D. thesis, University of Twente, Netherlands, ISBN 978-90-365-5725-2, https://doi.org/10.3990/1.9789036557269, 2023.

Hoksbergen, N., Akkerman, R., and Baran, I.: The Springer model for lifetime prediction of wind turbine blade leading edge protection systems: A review and sensitivity study, Materials, 15, 1170, https://doi.org/10.3390/ma15031170, 2022.

IEA: Net Zero Roadmap A Global Pathway to Keep the 1.5 °C Goal in Reach - 2023 Update, 2023, https://iea.blob.core.windows.net/assets/9a698da4-4002-4e53-8ef3-631d8971bf84/NetZeroRoadmap_AGlobalPathwaytoKeepthe1.5CGoalinReach-2023Update.pdf, Website accessed: July 1, 2024.

Johansen, N.: Test Methods for Evaluating Rain Erosion Performance of Wind Turbine Blade Leading Edge Protection Systems, Ph.D. thesis, Technical University of Denmark, 2020.

1

Keegan, M.: Wind Turbine Blade Leading Edge Erosion: An Investigation of Rain Droplet and Hailstone Impact Induced Damage Mechanisms, Ph.D. thesis, University Of Strathclyde, 2014.

Keegan, M. H., Nash, D. H., and Stack, M. M.: On erosion issues associated with the leading edge of wind turbine blades, Journal of Physics D: Applied Physics, 46, 383 001, https://doi.org/10.1088/0022-3727/46/38/383001, 2013.

KNMI: Uurgegevens van het weer in Nederland - 235 - De Kooy, Website accessed 01.02.2022, 2020, https://cdn.knmi.nl/knmi/map/page/klimatologie/gegevens/uurgegevens/uurgeg_235_2021-2030.zip.

Kraiburg: KRAIBURG LEP – Leading Edge Protection, https://www.kraiburg-rubber-compounds.com/produkte/lep/, Website accessed: July 2, 2024.

Letson, F., Shepherd, T. J., Barthelmie, R. J., and Pryor, S. C.: WRF Modeling of Deep Convection and Hail for Wind Power Applications, Journal of Applied Meteorology and Climatology, 59, 1717 – 1733, https://doi.org/10.1175/JAMC-D-20-0033.1, 2020.

López, J. C., Kolios, A., Wang, L., and Chiachio, M.: A wind turbine blade leading edge rain erosion computational framework, Renewable Energy, 203, 131–141, https://doi.org/10.1016/j.renene.2022.12.050, 2023.

Maniaci, D., Reyna, A., Davies, R., and Paquette, J.: Validating Impacts of Leading Edge Erosion Repairs on Wind Turbine Power Performance, 4th International Symposium on Leading Edge Erosion of Wind Turbine Blades, 2023.

Mingyang Smart Energy: MySE 8.5-216, 2023, https://www.linkedin.com/posts/mingyangsmartenergy_hybriddrivestheworld-onshorewind-activity-7016245147449405440-lOBh/, Website accessed: May 22, 2023.

Mishnaevsky, L.: Repair of wind turbine blades: Review of methods and related computational mechanics problems, Renewable Energy, 140, 828–839, https://doi.org/10.1016/j.renene.2019.03.113, 2019.

Mishnaevsky Jr, L., Fæster, S., Mikkelsen, L. P., Kusano, Y., and Bech, J. I.: Micromechanisms of leading edge erosion of wind turbine blades: X-ray tomography analysis and computational studies, Wind Energy, 23, 547–562, https://doi.org/10.1002/we.2441, 2020.

Picard, T. and Canal Vila, M.: Wind turbine operation, U.S. Patent No. US10927813B2, 2019, issued: 2021.

Polytech: Disproving myths around leading edge protection (LEP), 2022a, https://web.archive.org/web/20231004040844/https://www.polytech.com/

blog/disproving-myths-around-leading-edge-protection-lep/, Website accessed: July 4, 2024.

Polytech: DNV report on turbine performance with ELLE, 2022b, https://web.archive.org/web/20231004040327/https://www.polytech.com/blog/dnv-report-on-turbine-performance-with-elle/, Website accessed: July 4, 2024.

Polytech: ELLE Product Brochure, 2023, https://www.polytech.com/media/fswfipob/elle-product-brochure-eng.pdf, Website accessed: July 1, 2024.

Quante, M., Colijn, F., Bakker, J. P., Härdtle, W., Heinrich, H., Lefebvre, C., Nöhren, I., Olesen, J. E., Pohlmann, T., Sterr, H., et al.: Introduction to the Assessment—Characteristics of the Region, in: North Sea region climate change assessment, pp. 1–52, Springer, 2016.

RVO: New planning for offshore wind energy: 21 gigawatts in 2032, 2024, https://english.rvo.nl/news/new-planning-offshore-wind-energy, Website accessed: July 1, 2024.

Shankar Verma, A., Jiang, Z., Ren, Z., Caboni, M., Verhoef, H., van der Mijle-Meijer, H., Castro, S. G., and Teuwen, J. J.: A probabilistic long-term framework for site-specific erosion analysis of wind turbine blades: A case study of 31 Dutch sites, Wind Energy, 24, 1315–1336, https://doi.org/10.1002/we.2634, 2021.

Shihavuddin, A., Chen, X., Fedorov, V., Nymark Christensen, A., Andre Brogaard Riis, N., Branner, K., Bjorholm Dahl, A., and Reinhold Paulsen, R.: Wind Turbine Surface Damage Detection by Deep Learning Aided Drone Inspection Analysis, Energies, 12, https://doi.org/10.3390/en12040676, 2019.

TEKNOS: Further improved new white version of the revolutionary TEKNOBLADE REPAIR 9000-20, 2020, https://www.teknos.com/product-news/teknoblade-repair-9000-20/, Website accessed: July 2, 2024.

Telene: Leading edge protection, 2021, https://www.telene.com/leading-edge-protection/, Website accessed: May 22, 2023.

Tilg, A.-M.: Precipitation in the context of wind turbine blade erosion, Ph.D. thesis, Technical University of Denmark, https://doi.org/10.11581/dtu:00000096, 2020.

Verma, A. S., Noi, S. D., Ren, Z., Jiang, Z., and Teuwen, J. J. E.: Minimum Leading Edge Protection Application Length to Combat Rain-Induced Erosion of Wind Turbine Blades, Energies, 14, https://doi.org/10.3390/en14061629, 2021.

2

AEP LOSS OF LEADING-EDGE EROSION AND EROSION-SAFE MODE OPERATION

Leading-edge erosion leads to a loss in a wind turbine's annual energy production (AEP). Leading-edge protection systems, such as tapes or soft shells, can be used to protect the blade. However, these can also negatively affect the AEP. A novel erosion-mitigation option is the so-called erosion-safe mode (ESM). In this mode, the blade speed of the wind turbine is limited or even reduced to zero when precipitation events occur. This, however, leads to a loss in AEP. This chapter aims to investigate, from an AEP perspective, the conditions under which the ESM might be advantageous and the knowledge required to successfully utilize the ESM.

Local table of contents

2.1. Introduction

Leading-edge erosion is associated with a performance loss of up to a few percent in AEP (Herring et al., 2019). The cause for this loss is an earlier transition from a laminar to a turbulent boundary layer over the airfoil, initiated by increased surface roughness. Typical mitigation techniques include coatings, tapes, or shields to protect the blade from erosion. Most of these techniques are also likely to incur a performance loss in the variable speed region of the power curve of the order of, but commonly lower than, an eroded blade. An alternative method proposed in the literature is to operate in the erosion-safe mode. Here, the tip speed of the turbine is limited during certain weather conditions to avoid erosion (Bech et al., 2018). However, the ESM may also lead to performance reductions, but more likely at rated power. In general, the trade-off between design and operation of turbines to minimize performance losses due to erosion or its mitigation is not well understood. This is, in particular, true for the next generation of giant turbines.

This work aims to compute and compare the AEP loss caused by leading-edge erosion or by operating in the ESM[1]. Two offshore reference turbines, the IEA 15MW, and the NREL 5MW turbine, will be analyzed using lower-fidelity methods (Gaertner et al., 2020; Jonkman et al., 2009). The IEA 15MW has a rotor diameter of 240 m and a maximum tip-speed of 95 m/s. The NREL 5MW is slightly smaller with a rotor diameter of 126 m and a tip-speed of 80 m/s. The main focus is to identify the major trends and trade-offs between operating with LEE or operating in an ESM. This way, the research directions for the remainder of this thesis will be explored. The precise quantification of the performance loss is not the aim of this chapter.

2.2. Methodology

The main tool pipeline used throughout this chapter is built using XFoil and CACTUS (Drela, 2013; Murray and Barone, 2011). The latter is a simulation tool developed by Sandia National Laboratories that allows for the simulation of various turbine configurations. It is based on a combination of the blade element and free

---

[1]A detailed introduction to the ESM is given in Section 1.1.4. More advanced topics are discussed in Appendix B.

vortex line method. The flowchart of the entire procedure is given in Figure 2.1 and explained block-wise below.
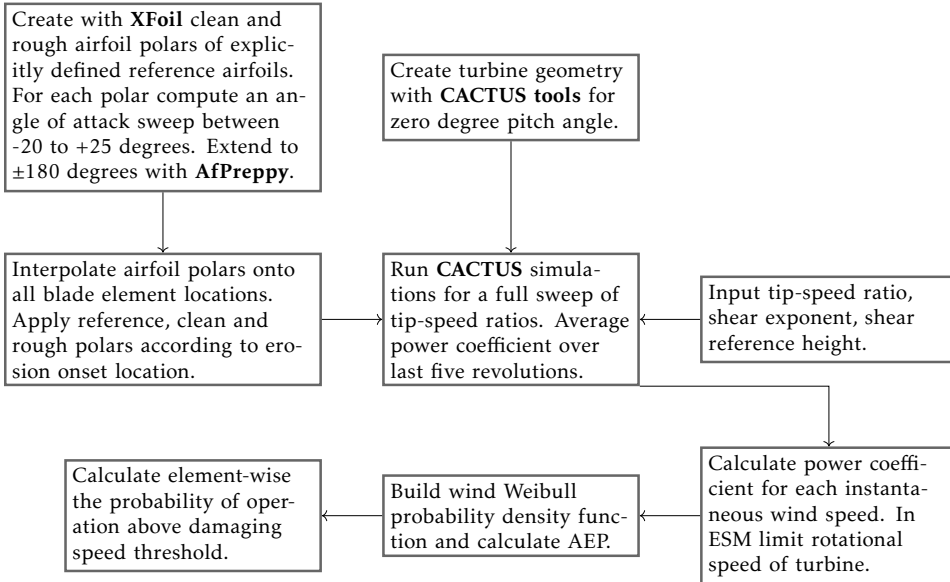
Figure 2.1: Flowchart of the methodology used throughout this chapter to compute data.

XFoil: For clean conditions, polars are provided with the definition of the reference turbines. This is not the case for rough, eroded blades. As such, we have redefined both the clean and rough polars for consistency. For this purpose, XFoil is used.

Eroded damage is modeled in XFoil by inducing boundary layer transition at fixed locations close to the leading edge (1 % top and 10 % bottom for positive angle of attack (AoA), flipped for negative AoA). Note that this approach only considers the airfoil's performance reduction due to the early transition but not due to the thickening of the boundary-layer from the airfoil roughness itself. Therefore, this study only considers erosion damage typical for moderately eroded blades. Modeling heavily eroded blades with deep surface imperfections requires high-order modeling techniques that are out of the scope of this work. For the simulations, a fixed Reynolds number of 8.5 million was chosen for the NREL 5MW turbine and 11.5 million for the IEA 15MW turbine. The Reynolds numbers were determined by weighing the local Reynolds number of every blade element by its contribution to the total power coefficient. The Reynolds number was kept constant for both turbines throughout the entire study. Thus independency of the polars with respect to the Reynolds number for different wind speeds, rotational speeds of the

turbine, and blade location was assumed. The same assumption has been made for the Mach number, which was set to zero. Since the integral boundary-layer method is questionable at high Reynolds numbers, a set of polars is generated with varying N-factors in the e^N-method. The N-factor represents the airfoil's sensitivity to promote turbulent transition and thus, to some extent, may capture the uncertainty in predicting the free transition location at high Reynolds numbers. The standard value chosen for this study in clean blade conditions is $N = 9$, while other values equal to 7, 8 and 10 are considered as well.

The airfoils are discretized with about 150 to 250 panels in XFoil. For each computed polar, the number of panels has been tuned carefully by trial and error to ensure complete convergence over the range from -20 to +25 degrees angle of attack. The polars were extended to the full ±180 range by using AirfoilPreppy's Viterna's method (Jonkman and Buhl Jr., 2020; Viterna and Janetzke, 1982).

CACTUS: The blade reference discretization according to the reference turbines' ontology files was preserved (60 points for IEA 15MW, 48 points for NREL 5MW). Two strategies have been used to apply the individual airfoil polars to their respective location along the blade. Consistent with the NREL 5MW's turbine definition, the airfoils, and thus also the polars, have been kept constant along the stations. Consistent with the IEA 15MW's definition, the polars were linearly interpolated between the stations. The reference polars were used for the cylindrical inboard sections of both turbines' blades. Additionally, for the most inboard airfoil of the IEA 15MW turbine (SNL-FFA-W3-500), the reference polar has been used as well due to its high thickness which led to convergence problems in XFoil. For every eroded simulation, a specific erosion onset location along the blade was assumed. The blade was assembled in CACTUS by using the reference polars inboard and by applying clean polars before the erosion onset location and the eroded polars outboard of the erosion onset location.
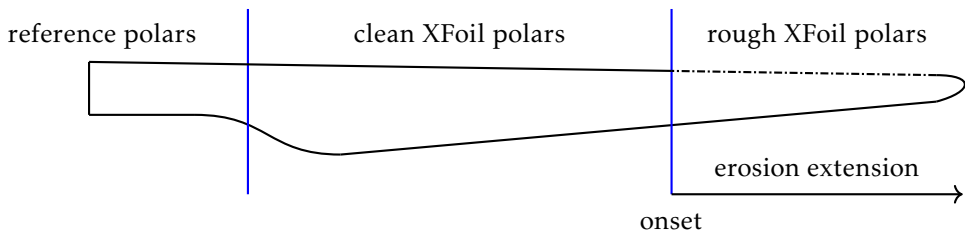

Figure 2.2: Use of reference and XFoil airfoil polars along the blade in the CACTUS simulations.

The CACTUS turbine geometries were created by using the horizontal-axis wind turbine (HAWT) tool from CACTUS-tools (Chiu et al., 2020). A convergence study

on the time steps and number of rotations was performed to ensure good numerical quality of the CACTUS simulations. Absolute errors in the power coefficient are in the range of $< 10^{-4}$ for $\lambda < 10$ and $< 10^{-3}$ for $\lambda > 10$, where λ is the tip-speed ratio (TSR). A discretization of 40 time steps per revolution is used, vortex elements are cut off after they have reached five rotor radii. The simulations were run for 50 rotations at design TSR and up to 90 rotations at maximum TSR.

Simulation with turbine controller: The power coefficients obtained from the CACTUS simulations were averaged over the last five revolutions. For the blade element data, the data were averaged over all blades over the last simulated revolutions. Subsequently, the power coefficients were fed to the steady-state turbine controller. The IEA 15MW controller was modified so that it only operates at zero pitch angle in order to limit the number of CACTUS simulations that were needed to be carried out. In ESM operation, the controller was adjusted according to two rules: *rotational* (ROT) and *relative* (REL). In the rotational mode, the assumption was made that the rain impact velocity is equal to the blade section speed V_{sec} of the blade, whereas for the relative mode also the free-stream hub-height inflow component was taken into account according to $V_{\mathrm{impact}} = \mathrm{norm}(V_{\mathrm{wind}}, V_{\mathrm{sec}})$. Here, induction is ignored. ROT and REL represent the limiting cases of droplet behavior. ROT corresponds to a droplet that does not get advected with the wind velocity, while REL corresponds to a droplet that gets perfectly advected with the wind velocity. To limit the number of free variables and complexity, the droplet terminal velocity has been neglected. In the case of ESM operation, the tip-speed of the turbine is limited so that the droplet impact speed, according to the ROT or REL mode, stays below a defined damage threshold.

Calculation of AEP (loss): The calculation of AEP is carried out for sites with different mean wind speeds at hub height, assuming a representative Weibull wind distribution with a shape parameter $k = 2$. A combined power curve is composed by weighting the clean and ESM power curves according to the assumed damaging rain frequency[2]. The AEP loss was calculated as the relative error between rough and clean cases, with the clean case being the baseline. A possible correlation between site mean wind speed and rain frequency was not considered. While important for the exact quantification of AEP losses, it is deemed not to have a significant impact on the trade-offs between operation with LEE and operating in an ESM.

---

[2]Here the concept of the *damaging rain frequency* is introduced. Not all rain is equally damaging, some events might contribute to erosion damage formation, while other events might have only a negligible impact. Hence, the *damaging rain frequency* is the frequency of rain that has a significant impact on the formation of leading-edge erosion.

2.3. Results

Figure 2.3 shows the lift coefficient as a function of the angle of attack for the most outboard airfoils of the IEA 15MW and NREL 5MW turbine in clean and rough conditions. The differences between the clean and rough lift polars are relatively small. This could be expected since the airfoils are operating at high Reynolds numbers, meaning the flow over the airfoil suction side is mostly turbulent even at small angles of attack. Forcing the flow to be turbulent close to the leading edge will only marginally affect the airfoil's performance. This easily follows from Figure 2.4, which indicates the location of the transition point from laminar to turbulent flow on the suction side of the airfoils, both for the clean and rough cases.

At low angles of attack, the largest differences may be identified between the clean and rough case. Here, free transition on the upper surface occurs downstream of the forced transition location set at 1 % of chord (as explained in Section 2.2). With increasing angle of attack, the location of free transition moves upstream. The NREL curve is concave, meaning that the transition point moves gradually forward with increasing angles of attack. In contrast, the IEA curve is convex. The transition point stays fairly constant until it abruptly shifts all the way to the leading edge. The IEA turbine shows convergence of the free and forced transition locations at an angle of attack of about four degrees, while the NREL gradually converges between zero and four degrees. At higher angles of attack, where the free and forced transition locations overlap, a small difference between both curves can still be identified in Figure 2.3. This may no longer be attributed to the forced transition on the suction side, but it can be related back to the forced transition on the pressure side. However, this contribution is significantly smaller. Although not shown is this chapter, similar observations can be made on the drag polar. Here, the effect on drag and thus also the lift-to-drag ratio is more pronounced. Nevertheless, small deviations in lift and drag may have significant effects on the turbine performance.

Figure 2.4 also presents the sensitivity of the transition location as a function of the N-factor. Note that high N-factors result in a free-transition location farther downstream. This implies that the effects of early transition on the airfoil's performance will be more pronounced at higher N-factors.

With the clean and rough airfoil polars, power curves for various erosion-specific operating conditions can be created. Figure 2.5 shows the mechanical power generated by the IEA 15MW turbine as a function of wind speed. In comparison to the clean power curve, rough turbine operation sheds performance in the variable load region. Rated power production is, therefore, delayed to higher wind speeds. Additionally, two ESM power curves are given for the ROT and REL ESM at one particular ESM speed. When operating in the ESM the turbine loses substantially
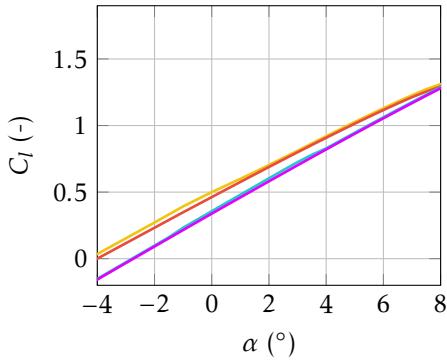
Figure 2.3: $C_l - \alpha$ for most outboard airfoils. FFA-W3-211 for IEA. NACA 64-618 for NREL; $N = 9$; IEA: clean: ——, rough: ——; NREL: clean: ——, rough: ——.
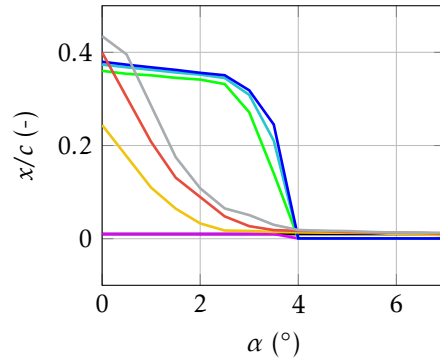
Figure 2.4: Transition point location on suction side for most outboard airfoils. FFA-W3-211 for IEA. NACA 64-618 for NREL; IEA: N7: ——; N9: ——, N10: ——, rough: ——; NREL: N7: ——, N9: ——, N10: ——, rough: ——.
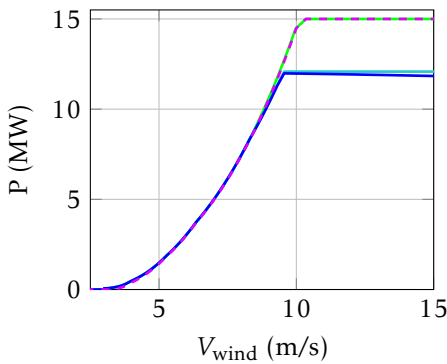
Figure 2.5: Power curve of IEA 15MW turbine; clean: ——, rough: - - -, ESM ROT 75 m/s: ——, ESM REL 75 m/s: ——.
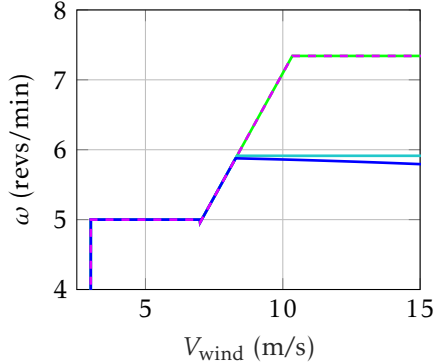
Figure 2.6: Rotational speed curve of IEA 15MW turbine; clean: ——, rough: - - -, ESM ROT 75 m/s: ——, ESM REL 75 m/s: ——.

performance at rated power. Due to the maximum generator torque and reduced rotational speed, the maximum power of the turbine is significantly limited. There is also a power loss in the partial load region. It occurs when, as can be seen in Figure 2.6, the rotational speed is limited, but the torque can still continue to increase at the higher wind speeds. In the REL ESM the rated power of the turbine does not stay constant after the maximum generator torque has been reached. Due

to the increasing wind inflow speed, the rotational speed has to decrease so that $V_{\text{impact}} = \text{norm}(V_{\text{wind}}, V_{\text{sec}})$ stays constant. It should be noted that when the ESM is utilized, the resultant power curve of the turbine is a linear combination of the clean and the ESM power curve depending on the ESM frequency i.e. how often there is a *damaging rain event*. To conclude, LEE negatively affects the power production below rated capacity while operating in ESM sheds performance mainly at rated power of the turbine.
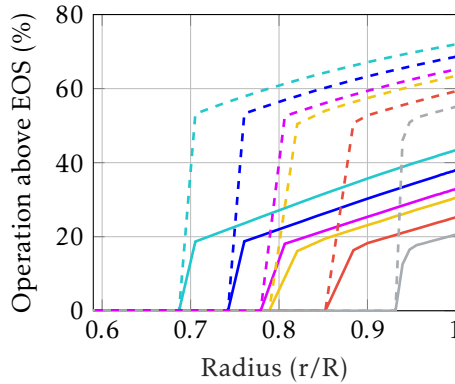
Figure 2.7: Percentage of operation above EOS; IEA 15MW: 5-65: ——, 5-70: ——, 5-75: ——, 10-65: - - -, 10-70: - - -, 10-75: - - -; NREL 5MW: 5-65: ——, 5-70: ——, 5-75: ——, 10-65: - - -, 10-70: - - -, 10-75: - - -; first number indicates mean wind speed, second number EOS, both in meter per second.

Figure 2.8: Strategy pairs of EOL in percentage span and ESM speeds for IEA 15MW and NREL 5MW turbine; results for the ROT and REL droplet impact speed models are given.

Speed	ROT	REL	ROT	REL
	IEA 15 MW		NREL5MW	
65 ms^{-1}	69 %	65 %	79 %	76 %
70 ms^{-1}	74 %	71 %	85 %	82 %
75 ms^{-1}	78 %	76 %	93 %	88 %

This study uses a simplified erosion model that depends on a so-called Erosion Onset Speed (EOS). The assumption is made that a blade element will experience erosion when a rain droplet impacts at or above the EOS. The impact speed of the droplet is evaluated according to the *ROT* and *REL* rules explained before. The term damaging rain event is used to highlight that not all rain events might cause damage to the blade. Erosion is treated as binary property, meaning a blade ele-

ment is either undamaged (clean) or eroded (rough). Different grades of erosion are not considered. By defining an EOS and a mean wind speed at a particular site, a graph can be created that shows for every blade element the probability of operation above the EOS (see Figure 2.7). It should be noted that the computed probabilities are independent of the turbines' polars and solely a function of the site conditions and the wind turbine control. Three EOS of 65, 70 and 75 m/s were chosen heuristically. In this study, it is assumed, for simplicity, that erosion starts where the probability becomes nonzero. This position is coined Erosion Onset Location (EOL). The graph shows that a specific EOS will yield a unique EOL. The wind turbine operator can choose between two strategies, do nothing and accept erosion from the EOL outwards or limit the tip-speed of the turbine to the EOS in the ESM to fully avoid erosion. Therefore strategy pairs of EOL and EOS can be found. They are tabulated in Table 2.8. It is important to compare these pairs when comparing erosion operating strategies to ensure fair results. While having interesting effects on the erosion onset and control of the turbine, an investigation into the REL mode showed that it did not have a meaningful impact on the conclusions of this chapter with respect to the ROT mode. Therefore, the REL mode was omitted in the further discussion. At the EOL in Figure 2.7, the probability increases linearly and subsequently starts to flatten out. When comparing the results of the two turbines one can see that, for a fixed EOS, the IEA turbine starts to erode about 10 to 15 percent of span further inboard. For a mean wind speed of 10 m/s, the probability (around 50 %) close to the EOL is similar for both turbines. In contrast, at the tip, the probability of the IEA turbine is about 10 % higher. Based on these observations one can infer that the rate of erosion at the EOL should be similar for both turbines, but increases for the IEA turbine when moving along the blade towards the tip. Figure 2.7 shows that a decrease in mean wind speed does not change the EOL. An explanation is straightforward, when reducing the mean wind speed the probabilities of high wind speeds in the Weibull distribution reduce, but never become zero. Thus, in this simplified erosion model, the EOL is invariant with mean wind speed. Mean wind speed has, however, a significant effect on the height of the curves. At 5 m/s mean wind speed and 65 m/s EOS, the IEA turbine operates at its tip around 40 % of the time above this threshold, with 10 m/s this probability increases to around 70 %.

Figure 2.9 and 2.10 show the AEP loss as a function of the Weibull mean wind speed for the NREL and IEA turbine. The AEP loss was normalized with respect to the clean configuration. Two general types of lines can be seen: falling and rising lines. A falling line corresponds to an AEP loss due to erosion, whereas a rising line belongs to an AEP loss due to operation in the ESM. Erosion is thus especially detrimental at low mean wind speeds, i.e. high probability of operation in the partial load region. On the contrary, operation in the ESM is very favourable at low wind speed, but leads to increased performance losses at high mean wind

2
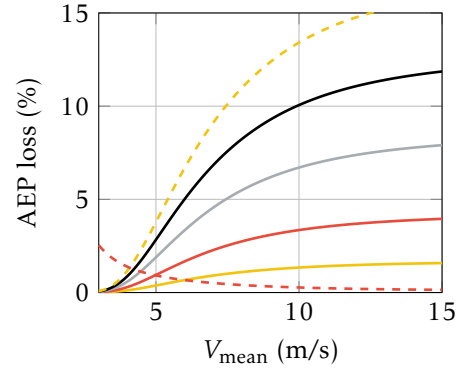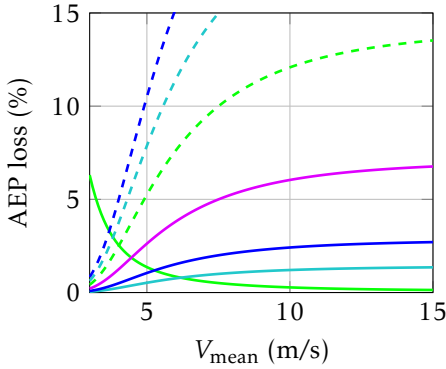
Figure 2.9: AEP loss due to LEE and ESM control for IEA 15MW turbine; LEE r/R 70 %: ——, ESM 65 m/s frequency 5 %: ——, 10 %: ——, 25 %: ——, 50 %: - - -, 75 %: - - -, 100 %: - - -.

Figure 2.10: AEP loss due to LEE and ESM control for NREL 5MW turbine; LEE r/R 70 %: - - -, ESM 65 m/s frequency 10 %: ——, 25 %: ——, 50 %: ——, 75 %: ——, 100 %: - - -.

speeds. An intersection point between the erosion and ESM curve exists. At this point, both strategies lead to equal AEP loss. By plotting ESM curves of different ESM frequencies different intersection points are generated that either move up or down on the erosion curve. Recording the combination of the Weibull mean wind speed and the ESM frequency at which an intersection occurs leads to Figure 2.11.

A comparison between Figure 2.9 and 2.10 reveals that the IEA turbine has a higher loss due to LEE than the NREL turbine at low mean wind speed sites. This difference vanishes with higher wind speeds. At about 8 m/s mean wind speed the losses due to LEE are equal for both turbines. The effect of operating in the ESM is for the IEA turbine more severe also. These findings assume a constant erosion onset location of 70 % and an ESM speed of 65 m/s. The IEA turbine shows more performance loss in the ESM due to its higher rated tip speed (95 m/s) than its NREL (80 m/s) counterpart. The higher susceptibility of the IEA turbine towards LEE can be explained by the aforementioned discussion of Figure 2.3 and 2.4. The NREL turbine has already at small angles of attack a transition point that is located at the very front of the leading edge. Thus, even in its clean configuration, it behaves already similar to an airfoil in rough condition. This is in contrast to the convex profile of the IEA turbine in Figure 2.4.

Figure 2.11 tracks the intersection point of ESM and LEE in the two-dimensional space spanned by the ESM frequency and the mean wind speed. When the operation point lies above the curve it is favorable to operate with LEE. In contrast,
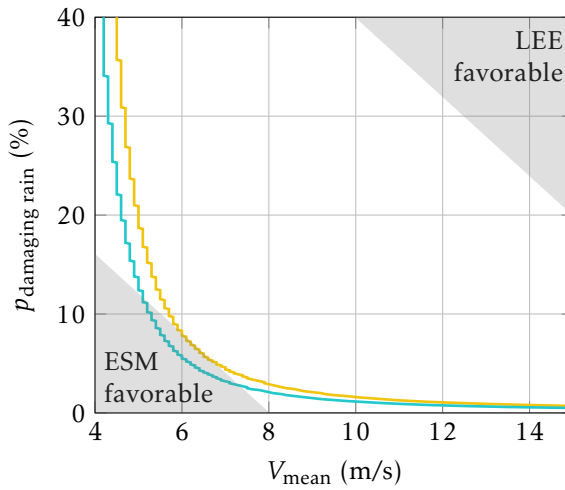
Figure 2.11: Intersection point of LEE and ESM for different rain frequencies and hub mean wind speeds; for reference, close to Den Helder in the Netherlands it rains about 6.7 % of the time, see Section 4.2.1; IEA 15MW: ——, NREL 5MW: ——.

when the operation point lies below the curve it is more advantageous to utilize ESM. The curves of both turbines rapidly rise at low mean wind speeds. There is a practical limit at which operation in the ESM is always better than operation with LEE. It is defined by the intersection of the LEE curve and the 100 % ESM curve as shown in Figure 2.9 and 2.10. The shape of the curve leads to a narrow band in its knee at which the most favourable mode of operation quickly changes. For example, the curve of the NREL turbine drops from about 7.5 % frequency at 6 m/s speed to about 2.5 % at 8 m/s. The allowable rain frequency for the ESM to be favorable is lower for the IEA turbine. This is interesting, since the IEA turbine shows a higher loss due to LEE. However, it is also more affected by the ESM, with the latter being dominant.

Figure 2.12 shows the effect of different ESM speeds on the optimum mode of operation. In this plot, it is assumed that the erosion onset location sits at 70 % span of the blade. As expected a higher ESM velocity shifts the entire graph up and to the right. When instead the pairs of Table 2.8 are considered, the curves move towards each other. This is shown in Figure 2.13. The curves only show a total shift of about 1 m/s of mean wind speed. Figure 2.14 gives an explanation for this. Two pairs of the NREL turbine are shown. With an increase in the EOS from 65 to 75 m/s both LEE and ESM loss curves move upward. However, their movement does not cause a shift in the intersection point itself. From the fact that the curves almost collapse onto each other, one can come to an interesting conclusion. Provided that the simplistic damage model of the EOS holds somewhat true, the optimum con-

2
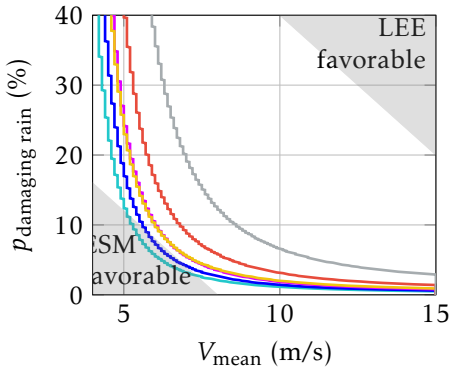
Figure 2.12: Intersection point of LEE and ESM for different ESM speeds at a fixed EOL of 70 %; IEA 15MW: ROT65: ——, ROT70: ——, ROT75: ——; NREL 5MW: ROT65: ——, ROT70: ——, ROT75: ——.
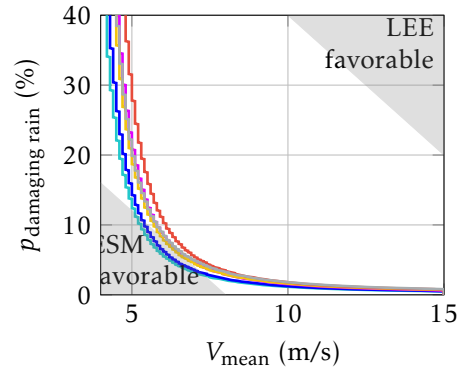
Figure 2.13: Intersection point of LEE and ESM for different ESM speeds; simulation pairs according to Table 2.8 are used; IEA 15MW: ROT65: ——, ROT70: ——, ROT75: ——; NREL 5MW: ROT65: ——, ROT70: ——, ROT75: ——.

trol strategy, i.e. whether to use LEE or ESM, is (almost) not influenced by the ESM speed, the erosion onset location and even the turbine type itself. The two parameters that matter (most) are the frequency of damaging rain and the mean wind speed of the site.

2.4. Conclusions

In this chapter, the performance loss of operating with LEE and in the ESM was investigated for the IEA 15MW and NREL 5MW reference wind turbines. The performance loss was evaluated with simulations employing the free-vortex method CACTUS by comparing calculations with erosion against reference calculations with clean polars. Erosion was assumed to lead to rough polars. The polars were obtained using XFoil. For the computations, both site-specific and turbine-specific parameters were varied. The first set includes mean wind speed and damaging rain frequency, whereas the second set includes erosion extent along the blades, critical speed for the onset of erosion and the transition location along the airfoil. The key takeaways of this study are:

- A break-even point for applying the ESM exists depending on the mean wind speed of the site. The reason is that LEE negatively affects the power production below rated capacity, while operating in ESM predominantly sheds performance at rated power of the turbine.
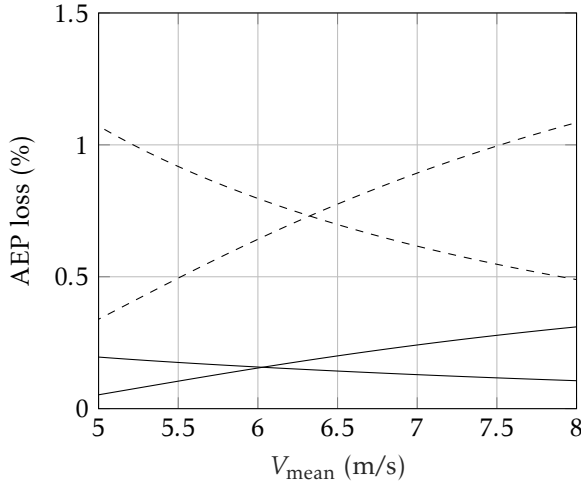
Figure 2.14: Shift in intersection point using simulation pairs of the NREL turbine with 10 % ESM utilization; 65 m/s ROT pair: - - - , 75 m/s ROT pair: ——.

- The break-even point strongly depends on the assumed frequency of damaging rain events. This is the most influential lever to make the ESM more attractive, e.g. by understanding better which rain events actually cause erosion and by better forecasting of these events. The effect of a possible correlation between rain frequency and site mean wind speed should be considered as well.

- The IEA 15MW reference turbine exhibits, in particular at lower wind speeds, a higher performance loss due to erosion than the NREL 5MW turbine. However, the break-even point for the ESM shows little sensitivity to the turbine design.

In conclusion, an erosion-optimal operation is strongly governed by the site characteristics and apparently much less by turbine design. The viability of an ESM strategy can be significantly expanded by a better understanding of blade damage mechanisms and improved forecasting of the related weather events.

Bibliography

Bech, J. I., Hasager, C. B., and Bak, C.: Extending the life of wind turbine blade leading edges by reducing the tip speed during extreme precipitation events, Wind Energy Science, 3, 729–748, https://doi.org/10.5194/wes-3-729-2018, 2018.

Chiu, P., Barone, M., and Murray, J. C.: CACTUS-tools, Sandia National Laboratories Water Power Technologies, 2020, https://github.com/SNL-WaterPower/CACTUS-tools.

Drela, M.: XFOIL 6.99, 2013, https://web.mit.edu/drela/Public/web/xfoil/.

Gaertner, E., Rinker, J., Sethuraman, L., Zahle, F., Anderson, B., Barter, G. E., Abbas, N. J., Meng, F., Bortolotti, P., Skrzypinski, W., et al.: Definition of the IEA 15-Megawatt Offshore Reference Wind Turbine, Tech. rep., National Renewable Energy Lab.(NREL), Golden, CO (United States), 2020.

Herring, R., Dyer, K., Martin, F., and Ward, C.: The increasing importance of leading edge erosion and a review of existing protection solutions, Renewable and Sustainable Energy Reviews, 115, 109 382, https://doi.org/10.1016/j.rser.2019.109382, 2019.

Jonkman, J. and Buhl Jr., M.: WISDEM - AirfoilPreppy, National Renewable Energy Lab.(NREL), Golden, CO (United States), 2020, https://github.com/WISDEM/AirfoilPreppy.

Jonkman, J., Butterfield, S., Musial, W., and Scott, G.: Definition of a 5-MW reference wind turbine for offshore system development, Tech. rep., National Renewable Energy Lab.(NREL), Golden, CO (United States), 2009.

Murray, J. and Barone, M.: The Development of CACTUS, a Wind and Marine Turbine Performance Simulation Code, https://doi.org/10.2514/6.2011-147, 2011, 49th AIAA Aerospace Sciences Meeting including the New Horizons Forum and Aerospace Exposition.

Viterna, L. A. and Janetzke, D. C.: Theoretical and experimental power from large horizontal-axis wind turbines, Tech. Rep. NASA-TM-82944, National Aeronautics and Space Administration, Cleveland, OH (USA). Lewis Research Center, 1982.

3

Rain droplet slowdown, deformation and breakup in the blade's vicinity

The previous chapter showed that the ESM can offer performance advantages compared to LEP systems. However, its successful application is dependent on the site conditions. In particular, the frequency of precipitation events that contribute significantly to erosion damage. An erosion damage model can be used to identify these events. A crucial input for such a model is the impact velocity of rain droplets, as the model's results are highly sensitive to this parameter. This chapter aims to investigate how rain droplets interact aerodynamically with a wind turbine blade prior to impact. It will be investigated whether this interaction leads to a change in the impact velocity and whether this change has a meaningful effect on the prediction of leading-edge erosion.

The content of this chapter was published in:

Local table of contents

3.1. Introduction

Forecasting and understanding the mechanisms that lead to erosion is important for solving the erosion problem. To this end, damage models play an important role. For example, they are used to assess the erosion potential of a particular site. This way, it is possible to decide a priori about the application of a particular LEP solution (Shankar Verma et al., 2021). Damage models are also required for the ESM to predict which meteorological conditions represent a hazard for the blade.

A key parameter to these models is the impact speed of the rain droplets. A common approach is to relate the droplet impact speed V_{impact} via a power law to an incubation metric N. N is a measure for the incubation time, which is the operational time until visible erosion damage occurs:

$$N \propto \frac{1}{V_{\text{impact}}^{\beta}}, \tag{3.1}$$

where β is a constant. The variable N can have various meanings depending on the damage model, such as the number of impacts or the impingement. Common to all models is that the magnitude of the parameter β is significant. Parameters for β reported in the literature are 5.7 in Hoksbergen et al. (2022), 16.92 in Shankar Verma et al. (2021) and 7.2-10.5 in Bech et al. (2022). While the reported values in the literature differ significantly based on the test apparatus used and exact definition of N, they all preserve the character of the equation, namely that small changes

in V_{impact} will yield vastly different erosion lifetimes. It is, therefore, important to accurately determine the impact speed. The impact speed is the surface normal component of the impact vector, which is calculated as the difference between the blade section and rain droplet velocity vector, i.e.,

$$V_{\text{impact}} = (\vec{V}_{\text{sec}} - \vec{V}_{\text{rain}}) \cdot \vec{n}_{\text{LE}}, \tag{3.2}$$

where n_{LE} is the surface normal component of the leading edge. The droplet's velocity vector is usually considered to be comprised of the droplet's terminal velocity and its advection velocity with the wind (Barfknecht et al., 2022; Verma et al., 2020). However, in aeronautics, it has been known already for a long time that rain droplets and wings can interact aerodynamically (Nicholson, 1968). This leads to rain droplet deformation and slowdown when observed from the wing (Vargas and Feo, 2011). Thus adding an extra velocity component to the problem. The potential slowdown of rain droplets has so far received no attention in the wind energy community. One exception is Prieto and Karlsson (2021), where, however, only limited results for spherical droplets were obtained. No droplet deformation was included in their analysis.

#4981 #5121 #5151   #5161   #5171   #5176   #5181   #5186   #5191
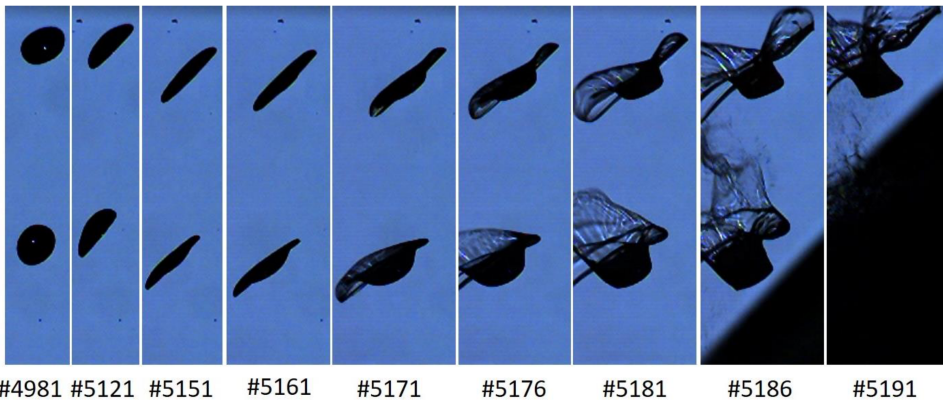
Figure 3.1: High-speed photography of falling water droplets of 1.75 mm diameter approaching an airfoil in a rotating-arm test-rig. The different frames show the temporal progression; the shadow that can be observed in the last two frames is the approaching airfoil; the droplets are first round, then become oblate and, before impact, break up with smaller droplets being emitted from the rim; free-stream velocity of 60 m/s, airfoil chord of 1.05 m; the photographs are reproduced with permission from Sor et al. (2019).

Sor et al. (2019) performed measurements in which water droplets were seeded in a rotating-arm test-rig. A blunt airfoil was mounted on the arm. High-speed photographs were taken that show the droplets close to impact with the wing. Fig-

ure 3.1 shows an excerpt of their results. As the airfoil approaches the droplets, they start to deform from a spherical to an oblate shape. Shortly before impact, the droplets undergo breakup. While the experiments were performed for aircraft icing research, the parameter space fits the one encountered in leading-edge erosion of wind turbines very well. These findings stand contrary to current practice in leading-edge erosion research, where it is assumed that the droplets are spherical at impact (Hoksbergen et al., 2023; Fæster et al., 2021; Keegan et al., 2012; Verma et al., 2020). The measurements of Sor et al. (2019) imply that rain droplets can undergo breakup, and, therefore, the rain droplets' appearance at impact can be considered complex in shape.
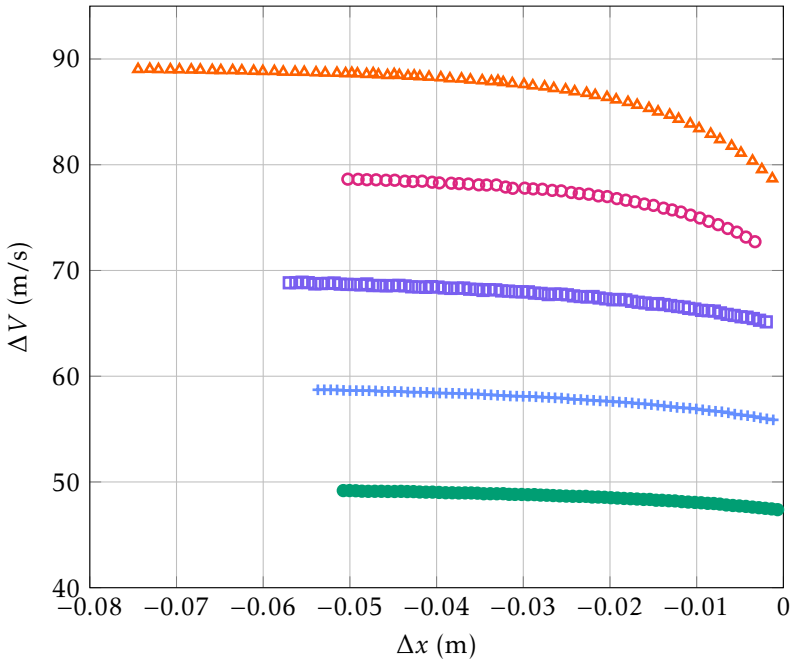
Figure 3.2: Relative velocity between a 0.49 mm diameter water droplet and an airfoil; relative velocity is given as a function of the distance to the leading edge; blunt airfoil with a chord length of 0.47 m; five different free-stream velocities of: 50 m/s: ●, 60 m/s: +, 70 m/s: □, 80 m/s: ○ and 90 m/s: △; data were collected in a rotating-arm test-rig and are reproduced from Vargas and Feo (2011).

Figure 3.2 shows the results of a similar experiment performed by Vargas and Feo (2011). It can be observed how the rain droplets' relative speed changes in front of the airfoil. The water droplets slow down as they approach the leading edge of the rotating airfoil. Droplets with a free-stream velocity of 90 m/s experience a velocity reduction of almost 12 m/s. Considering the exponent of the damage

law in Equation 3.1, this effect is highly relevant. It appears, therefore, that the effect of droplet slowdown and deformation cannot be neglected when studying leading-edge rain erosion and needs to be further understood.

The research presented here investigates the impact of rain droplet slowdown and deformation on the erosion lifetime prediction of wind turbine blades. It is important to note that this study assumes that the problem is observed in the reference frame of the airfoil. From an airfoil's perspective, the incoming droplet's speed reduces; hence the term *slowdown* is used. An observer located on the ground will see the droplets gain speed. Since the effect reduces the impact speed, the term slowdown seems appropriate. The chapter is organized as follows: Section 3.2 gives a brief introduction to droplet deformation and breakup. Additionally, the parameter space of the problem is investigated. In Section 3.3, an existing droplet model, developed for research in aircraft icing, is adapted, extended, calibrated, and validated to study the slowdown and deformation process. Subsequently, Computational Fluid Dynamics (CFD) simulations are performed on airfoils of reference turbines to obtain their background velocity field to determine parameters needed in the model. Finally, the used precipitation data and the damage model are discussed in further detail. In Section 3.4, the proposed slowdown and deformation model is employed to analyze the sensitivity of the droplet model with respect to the droplet diameter and the airfoil's aerodynamic nose radius. This is followed by combining the model with the precipitation data and then computing the impact of the droplet slowdown and deformation on the lifetime of two reference turbines. Finally, in Section 3.5 a summary is provided, conclusions are drawn and recommendations are given.

3.2. Discussion of the underlying physics

An understanding of the physics encountered by droplets along their trajectory is necessary before a suitable approach can be chosen to model droplet slowdown and deformation. A complete review of the known processes encountered during aerodynamic droplet deformation and breakup is out of the scope of this work. However, since droplet deformation and breakup is a rather new phenomenon for the leading-edge erosion community, a brief summary with a discussion of the parameter space seems appropriate.

For aerodynamic droplet deformation and breakup, the important non-dimensional numbers are the Weber number (We) and the Ohnesorge (Oh) number (Jackiw and Ashgriz, 2021). They read

$$
\text{We} = \frac{\rho_{\text{air}} V_{\text{slip}}^2 \phi_0}{\sigma_{\text{water}}}, \qquad\qquad \text{Oh} = \frac{\mu_{\text{water}}}{\sqrt{\rho_{\text{water}} \sigma_{\text{water}} \phi_0}}, \qquad (3.3)
$$

with density ρ, surface tension σ and dynamic viscosity μ, where the subscripts $_\text{air}$ and $_\text{water}$ indicate the corresponding medium. ϕ_0 represents the droplet diameter and V_slip is the slip velocity, i.e., the difference between the velocity of the air (V_air, see Section 3.3.2) and the droplet (V_x, see Section 3.3.1). The Weber number relates the inertial forces to the surface tension forces, whereas the Ohnesorge number relates the viscous to the inertial and surface tension forces. Depending on the Weber number, droplets subject to aerodynamic forces can first undergo deformation and subsequently also break up. Figure 3.3 shows an often-cited graph taken from Hsiang and Faeth (1995). It depicts how droplets are expected to behave depending on the Weber and Ohnesorge number. From the figure, it is evident that for Oh < 0.1, the expected behavior is a function of the Weber number only.
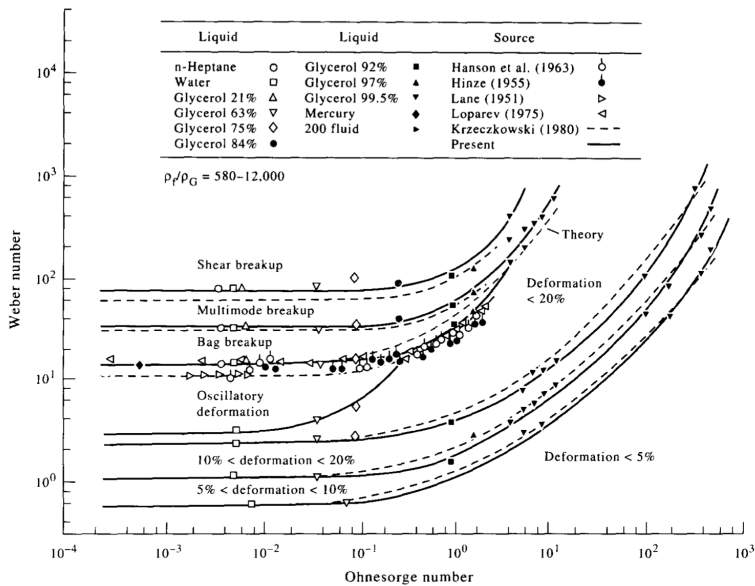
Figure 3.3: Droplet deformation and breakup modes as a function of the Weber and the Ohnesorge number; the figure is reproduced with permission from Hsiang and Faeth (1995).

Aerodynamic droplet breakup consists of two phases, the initiation, also called the deformation phase, and the breakup phase (Jackiw and Ashgriz, 2021). During the deformation phase, the droplet's shape flattens. At some point the droplet breaks up into smaller droplets. This process is also called secondary breakup. Different breakup modes exist such as bag, bag and stamen, multimode and shear breakup. Some of these modes are shown in Table 3.1. After the breakup stage is complete, the original droplet will have decayed into a series of small drops that can be characterized by a drop-size distribution. Subsequently, the resultant

droplets might deform and break up again, forming a decay cascade. For more information about the fundamental mechanics of droplet dynamics, the reader is recommended to read (Jackiw and Ashgriz, 2021, 2022).
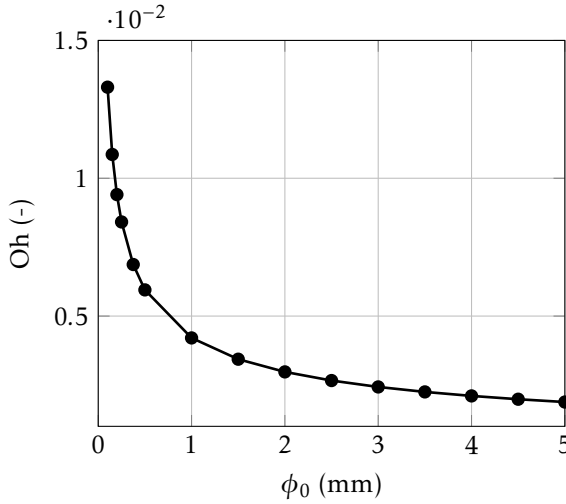
Figure 3.4: Ohnesorge number plotted against the rain droplet diameter; the values of the Ohnesorge stay below 0.1.
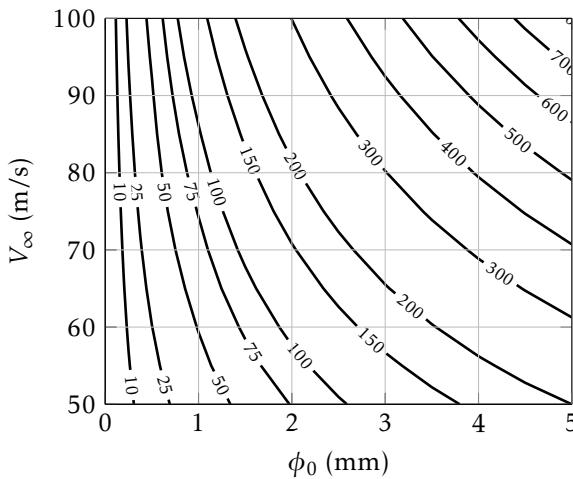
Figure 3.5: Contour plot of Weber numbers at impact time as a function of droplet diameter and free-stream velocity; the slip velocity required for the Weber number computation was calculated with the model from Section 3.3.1; the model parameters are $R_c = 0.07$ m and $n = 1.1$.

3

Two figures were created to analyze the parameter space for the leading-edge erosion problem in more detail. Figure 3.4 and 3.5 show the Ohnesorge and the Weber numbers, respectively, for droplets of varying sizes and free-stream velocities.[1] This set of simulations spans the parameter space in terms of non-dimensional numbers for the erosion problem. The Ohnesorge number is not dependent on the flow velocity and is, apart from the physical constants, a function of the droplet diameter only. Figure 3.4 shows that the Ohnesorge numbers stay below 0.1, indicating that the droplet breakup is governed by the Weber number only. The Weber numbers lie in a very broad range of 1 to 800.
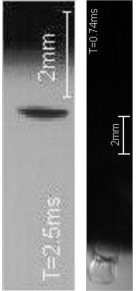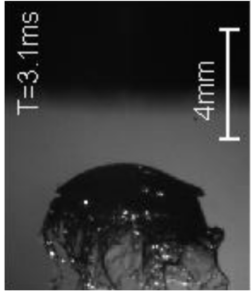
The wide range of Weber numbers encountered in this problem leads to very different droplet behaviors. The droplet behavior is expected to range from simple deformation for small and slow droplets to shear breakup for larger and faster droplets. In Table 3.1, example images of the different breakup modes in a rotating-arm test-rig are given, together with an approximate Weber number close to impact.

Most fundamental research in the literature about droplets is based on experiments in shock tubes and steady disturbances (Hsiang and Faeth, 1995). However, in the present problem, the droplets traverse through a velocity field that changes depending on the distance to the airfoil. Figure 3.6 gives an example velocity field. Therefore, it is not possible to directly translate the graph of Figure 3.3 to, e.g., the outcomes in Table 3.1. For this problem, the shape and extent of the background velocity field must also be considered. It is intuitive to assume that a larger airfoil will have more influence on the behavior of the droplet than a small airfoil, even though the Weber number of the droplet is similar for both airfoils close to impact. Therefore, one needs to conclude that, while the general body of droplet breakup and deformation is extensive, only very limited knowledge exists that is applicable to the wind turbine rain erosion problem.

Since current erosion research treats droplets as spherical and thus as a coherent structure when impacting with a blade, it is also assumed that the entire water mass of a single droplet possesses the same impact velocity. The question is whether droplet breakup invalidates this assumption. If the velocity that describes the droplet deformation is in the same order as the droplet slowdown itself, then, with Equation 3.1 in mind, the damage potential of a droplet might be significantly influenced. To understand this aspect further, additional frames of the 0.191 mm droplet from Table 3.1 are shown in Figure 3.7. In six distinct frames, a purple and an orange arrow indicate the maximum extent of the bag that forms during the breakup. With the timestamp and indicated length scale, the growth velocity of this bag can be obtained by using a simple Backward Euler Finite Difference scheme.

---

[1] As will be shown later in Figure 3.20 rainfall is almost exclusively composed of droplets in the range from 0 to 4 mm size. Some instances of larger droplets have been recorded in the literature (Jones et al., 2010).

Table 3.1: Examples of droplet deformation and breakup in the measurement campaigns of García-Magariño (2016); estimated Weber numbers at impact calculated with the model from Section 3.3.1.

Image	Estimated We	Mode	ϕ_0 (mm)	V_∞ (m/s)	Reference in García-Magariño (2016)
	≈ 29	Deformation	0.788	50	Figure 3.8
	≈ 17	Bag	0.191	90	Figure 5.6
	≈ 72	Bag and stamen	0.782	90	Figure 3.7
	≈ 388	Shear	3.2	90	Figure 5.9
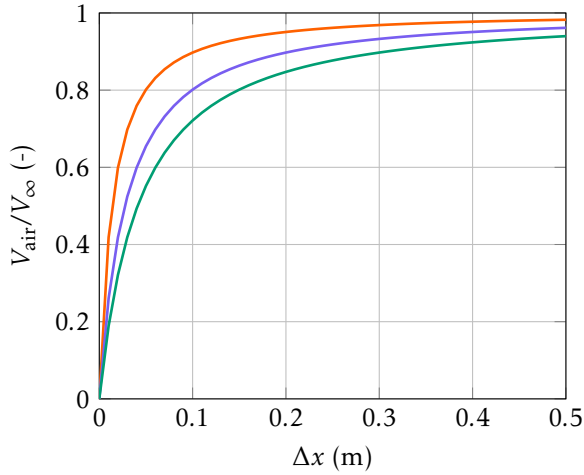
Figure 3.6: Non-dimensional velocity field along stagnation streamline vs. the dimensional distance to the leading edge; the FFA-W3-211 airfoil of the IEA 15MW turbine at 0-degree angle of attack was chosen; calculated with the methodology from Section 3.3.2; 0.5 m chord: ——, 1.0 m chord: ——, 1.5 m chord: ——.
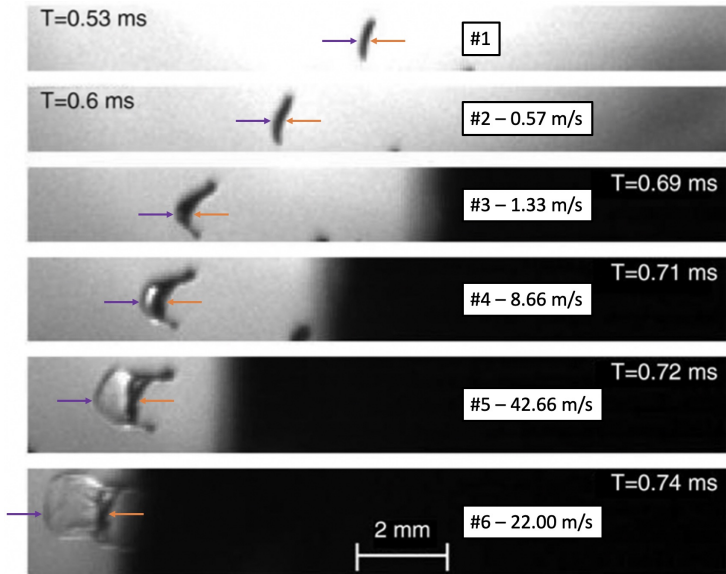
Figure 3.7: 0.191 mm diameter droplet approaching an airfoil and showing a bag breakup mode; the scale, time, frame identifier, and bag expansion speed are also indicated; the photographs are reproduced with permission from Figure 5.6 of García-Magariño (2016).

The obtained velocities are indicated next to the frame number in the figure. It can be seen that the velocity is fairly low in Frame 2 and 3 when the bag is just beginning to form. However, as soon as the bag starts rapidly growing, the velocity quickly increases to a peak of 42.66 m/s. Close to impact, this velocity reduces to a still significant value of 22 m/s. This example shows that the water's velocity inside a droplet that undergoes breakup (close to impact) is not constant in space and time. The exact velocity distribution inside the droplet is probably breakup-mode-dependent, and droplets that only undergo gradual deformation will preserve a reasonably constant velocity throughout the droplet. To further elaborate on this argument, if droplets fracture into sub-droplets during a breakup, each resulting droplet will have a distinct impact velocity. To conclude the findings, experiments suggest that droplets approaching wind turbine-sized airfoils are either deformed or will show breakup shortly before impact. Additionally, droplets that undergo breakup will show a non-homogeneous impact velocity distribution across their water mass.

3.3. Methodology

3.3.1. One-way coupled Lagrangian particle model

The influence of droplet deformation and breakup on the blade lifetime under erosion is investigated with a model that adequately describes the relevant physical processes. Various Lagrangian droplet deformation models exist in the literature, such as the TAB, NLTAB3, DDB, and DRD models (Sor and García-Magariño, 2015; Schmehl, 2004). However, to the author's knowledge, to date, no single Lagrangian model can describe the full range of complex phenomena of droplet slowdown and breakup in sufficient detail. Some advanced models attempt to model particular regimes, such as in Sichani and Emami (2015) for a droplet under deformation and up to the onset of bag rupture. Direct numerical simulation (DNS) of the air and water phase could capture all relevant physics and phenomena, especially when higher-order numerical schemes are applied. However, its computational expense makes it prohibitive when a large parameter space is supposed to be studied. Thus a gap exists with computationally affordable but low-accuracy Lagrangian particle models on one side and highly accurate but extremely costly DNS codes on the other.

This dilemma is resolved by simplifying the problem based on educated assumptions. In particular, it is argued that the model's foremost aim must be the accurate prediction of the droplet slowdown velocity. As shown in Equation 3.1, a small error in the impact velocity leads to a large error in the computed erosion lifetime. The second central simplification is that, for the conclusions of this study, the exact droplet's shape *at impact* does not need to be predicted very accurately. This simplification is based on the assumption that an error in the droplet's shape during

impact has a smaller influence on the erosion lifetime than an error in the impact velocity. However, at the same time, the prediction of the droplet's shape *prior to impact* needs to be accurate enough to minimize the error in the impact velocity. It is noteworthy that the droplet's shape at impact can be an input for a damage metric that is required to calculate an erosion lifetime. This aspect is discussed in Section 3.3.4.

Additional simplifying assumptions are made to model the problem in a Lagrangian one-particle setting. It is assumed that droplets will preserve a coherent shape during the entire approach toward the airfoil, i.e., not fracture, and thus can be represented as a single particle. This assumption neglects the potential effect of the non-homogeneous impact velocity of rain droplets during and after breakup. Based on the reference measurements from the literature that were presented before, it is also assumed that the cascade breakup does not occur.

Considering these requirements, the Droplet Ratio Deformation (DRD) model from Sor and García-Magariño (2015); Sor et al. (2016) was chosen. It was specifically developed to compute the trajectory of water droplets in the vicinity of approaching airfoils and stems from the same research group that has also published the measurements on droplet breakup discussed before. It has shown superior performance compared to other droplet models and is based on a one-way coupled Lagrangian approach. The original method uses three equations. One equation models the rain droplet's deformation from a sphere to the shape of an oblate spheroid. The other two equations model the movement of the droplet in a two-dimensional space. For the present study, the model was modified in such a way that the movement of the droplet can be considered one-dimensional only. It is important to note that the DRD model neither accounts for droplet breakup nor imposes any limit on the maximum deformation of a droplet. As a remedy, a heuristic modification is proposed in the following.

Two fundamental Equations of Motion (EOM) are at the model's core. They read

$$m\frac{d^2x}{dt^2} = F_{\text{drag}}, \tag{3.4}$$

$$\frac{3}{16}m\frac{d^2a}{dt^2} = F_\sigma + F_p. \tag{3.5}$$

Equation 3.4 represents the EOM along the droplet trajectory, whereas Equation 3.5 is the EOM that represents the deformation of the droplet from a spheroid to an oblate spheroid. $m = 4/3\pi R_0^3 \rho_{\text{water}}$ is the mass of the droplet and x is the position of the droplet along its trajectory. The possible candidates for the droplet trajectory will later be discussed in Section 3.3.2 together with Figure 3.10. a is the semi-major axis of an oblate spheroid, as shown in Figure 3.8. b is the semi-minor axis and can be calculated as $b = R_0^3/a^2$, where R_0 is the starting radius of a spherical rain droplet.

(a) Spheroid   (b) Oblate spheroid
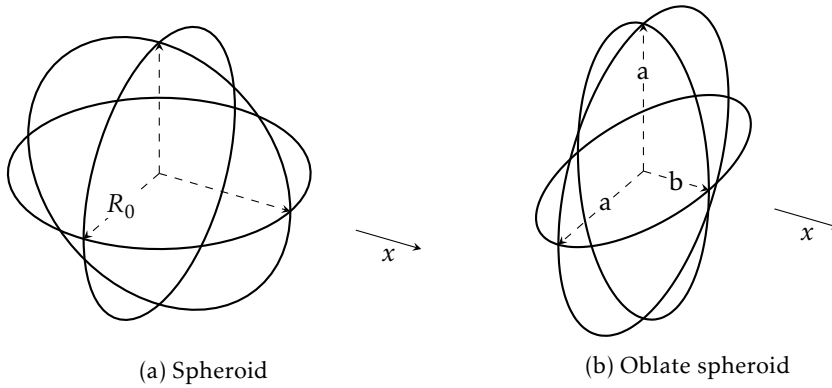
Figure 3.8: Representation of the droplet shapes used in the model with the relevant geometrical parameters.

The drag force acting on the droplet is computed by using

$$F_{\mathrm{drag}} = \frac{1}{2}\rho_{\mathrm{air}}V_{\mathrm{slip}}^2 C_D A_a. \tag{3.6}$$

V_{slip} is the velocity difference between the air and the droplet; it reads

$$V_{\mathrm{slip}} = V_{\mathrm{air}} - \frac{dx}{dt}. \tag{3.7}$$

The calculation of the background velocity V_{air} at a particular x is explained in Section 3.3.2. The droplet's instantaneous frontal area A_a is calculated by simply taking $A_a = \pi a^2$. The drag coefficient is composed of a static and a dynamic component,

$$C_D = C_{\mathrm{static}} + C_{\mathrm{dynamic}}. \tag{3.8}$$

They read

$$C_{\mathrm{static}} = C_{D_{\mathrm{sphere}}}^{b/a} C_{D_{\mathrm{disk}}}^{1-b/a}, \tag{3.9}$$

$$C_{\mathrm{dynamic}} = k\frac{b}{V_{\mathrm{slip}}^2}\frac{dV_{\mathrm{slip}}}{dt}, \tag{3.10}$$

where k is a calibration constant. The static component represents an interpolation between the drag coefficient of a sphere and a disk. In Equation 3.5, two forces are acting against each other. The surface pressure term drives deformation, whereas the surface tension term counteracts deformation. The pressure term is calculated as

$$F_p = \frac{1}{2}\rho_{\mathrm{air}}V_{\mathrm{slip}}^2 C_p A_0. \tag{3.11}$$

C_p is again a calibration constant. Also, note the constant frontal area that is calculated with the initial droplet radius R_0, that is $A_0 = \pi R_0^2$. This choice is motivated in more detail in the original paper of the model. The surface tension force is written as

$$F_\sigma = -\frac{4}{3}\sigma_{\text{water}}\frac{dA_s}{da},\tag{3.12}$$

where σ_{water} is the surface tension of water and $\frac{dA_s}{da}$ is the derivative of the surface area of an oblate spheroid with respect to a. Following the approach of Sor and García-Magariño (2015); Sor et al. (2016); Sor and García-Magariño (2021); Schmehl (2004), the surface area of an oblate spheroid A_s reads

$$\frac{A_s}{A_{s,0}} = \frac{1}{2}\left(\frac{a}{R_0}\right)^2 + \frac{1}{2}\left(\frac{R_0}{a}\right)^4\frac{\text{arctanh}\,\epsilon}{\epsilon},\tag{3.13}$$

where $A_{s,0} = 4\pi R_0^2$ is the surface area of a sphere. The derivative becomes

$$\frac{1}{A_{s,0}}\frac{dA_s}{d\bar{a}} = \bar{a} - \frac{2}{\bar{a}^5}\frac{\text{arctanh}\,\epsilon}{\epsilon} + \frac{3}{2\bar{a}^5(\bar{a}^6-1)}\left(\bar{a}^6 - \frac{\text{arctanh}\,\epsilon}{\epsilon}\right),\tag{3.14}$$

where

$$\epsilon = \sqrt{1-\left(\frac{b}{a}\right)^2} = \sqrt{1-\frac{1}{\bar{a}^6}},\tag{3.15}$$

and

$$\bar{a} = \frac{a}{R_0}.\tag{3.16}$$

Finally $\frac{dA_s}{da}$ is obtained by

$$\frac{dA_s}{da} = \frac{1}{R_0}\frac{dA_s}{d\bar{a}}.\tag{3.17}$$

$C_{D_{\text{sphere}}}$ has been calculated with the Schiller-Naumann relation as given in Sommerfeld et al. (2008),

$$C_{D_{\text{sphere}}} = \begin{cases} 27.6 & \text{Re} \leq 1, \\ \frac{24}{\text{Re}}\left(1 + 0.15\text{Re}^{0.687}\right) & 1 < \text{Re} < 1000, \\ 0.4383 & \text{Re} \geq 1000. \end{cases}\tag{3.18}$$

Note that the drag coefficient was clamped for $\text{Re} \leq 1$ and $\text{Re} \geq 1000$. The Reynolds number Re reads

$$\text{Re} = \frac{V_{\text{slip}}\rho_{air}2R_0}{\mu_{air}}.\tag{3.19}$$

In the original form, the model does not account for the influence of droplet breakup. The model permits the droplet to grow without restriction. From the

literature, such as Jackiw and Ashgriz (2021, 2022); Hsiang and Faeth (1995); Schmehl (2004), it is known that, depending on the Weber number, there exists a maximum diameter at which droplets start to break up. It usually lies in the range of 1.5 to 2 a/R_0. In this study, the assumption is made that when the droplets reach a specific maximum a, they will stop growing, and the value of a will be fixed for the remainder of the simulation. In particular, the following formula is used

$$\frac{a_{\max}}{R_0} = \min\left(2.2, 3.4966\text{We}_\infty^{-0.1391}\right). \tag{3.20}$$

The formula was obtained by fitting an exponential curve to a set of reference data shown in Figure 3.9. Further, the limit of 2.2 was chosen based on the data in Figure 3 of García-Magariño et al. (2021). It is important to note that

$$\text{We}_\infty = \frac{\rho_{\text{air}} V_\infty^2 \phi_0}{\sigma_{\text{water}}}, \tag{3.21}$$

which is different to Equation 3.3 since the free-stream velocity (Equation 3.26) is used instead of the slip velocity (Equation 3.7). The motivation for this is the fact that for the limited sets of published data on $a_{\max}/R_0$, the corresponding impact velocity is not always given. Additionally, $\text{We}_{\text{impact}}$ is not known a priori but rather a result of the simulation, therefore, necessitating an iterative approach for solving the set of equations. The assumption can be justified by realizing that $V_{\text{impact}} \approx V_\infty$ represents a conservative estimate. Since $a_{\max}/R_0$ should be decreasing with increasing $\text{We}_{\text{impact}}$, assuming $\text{We}_{\text{impact}} \approx \text{We}_\infty$ will lead to a higher estimated Weber number. Thus, droplet slowdown will be underpredicted due to an underprediction in $a_{\max}/R_0$. Section 3.3.3 shows that the limiter introduced here deals with the droplet breakup satisfactorily.

The resulting set of differential equations describing the droplet model is

$$\frac{dx}{dt} = V_x, \qquad\qquad \frac{dV_x}{dt} = \frac{F_{\text{drag}}}{m}, \tag{3.22}$$

$$\frac{da}{dt} = V_a, \qquad\qquad \frac{dV_a}{dt} = \frac{16}{3}\frac{F_\sigma + F_p}{m}. \tag{3.23}$$

The initial conditions for the droplet equations are set as

$$x_0 = 0, \qquad\qquad V_{x,0} = 0, \tag{3.24}$$

$$a_0 = R_0 + \text{eps}, \qquad\qquad V_{a,0} = 0, \tag{3.25}$$

eps is a very small number, e.g. 10^{-12}. This is necessary since Equation 3.14 is not defined for $a = R_0$. V_x is the velocity of the droplet and V_a is the expansion velocity of the semi-major axis. An additional differential equation is needed to describe
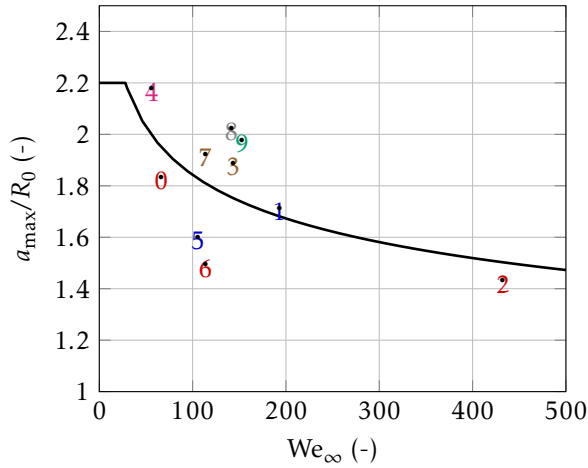
Figure 3.9: The limit of maximum droplet dimension $a_{\max}/R_0$ as a function of free-stream Weber number; the sources of data points are given in Table 3.2; —— corresponds to Equation 3.20.

Table 3.2: Sources of reference data for maximum droplet dimension limiter $a_{\max}/R_0$ that is shown in Figure 3.9.

Symbol	Reference
1	Figure 15 of Vargas et al. (2012)
2	Figure 5.9 of García-Magariño (2016)
3	Figures 8 and 9 of Vargas et al. (2012)
4	Table II of Feo et al. (2012)
5	Figure 3.4 of García-Magariño (2016)
6	Figure 3.9 of García-Magariño (2016)
7	Figure A.3.4 of Sor (2017)
8	Figure A.3.5 of Sor (2017)
9	Figure A.3.6 of Sor (2017)
0	Table I of Feo et al. (2012)

the movement of the blade. It reads

$$\frac{dx_{\text{blade}}}{dt} = V_{\text{blade}} = V_\infty = \text{const}, \qquad (3.26)$$

with the initial conditions sufficiently far away from the droplet:

$$x_{\text{blade},0} \gg R_c, \qquad (3.27)$$

where a sufficiently far distance can, for example, be $20R_c$. The definition of R_c is explained in Section 3.3.2. In this study, the differential equations were solved using a simple Runge-Kutta method. The simulation is stopped when the distance between the airfoil and the droplet falls below a certain threshold, i.e.,

$$\Delta x = |x - x_{\text{blade}}| < \text{eps}, \tag{3.28}$$

where 'eps' is once again a small number. The relative velocity between the droplet and the airfoil can be defined as

$$\Delta V = |V_x - V_{\text{blade}}|, \tag{3.29}$$

see Figures 3.2 and 3.17. Also the slowdown velocity can be defined as

$$V_{\text{slowdown}} = \left(\frac{dx}{dt}\right)_{\text{at impact}}, \tag{3.30}$$

which is just the velocity gained by the droplet, since $V_{\text{blade}} = \text{const}$. The slowdown velocity can be interpreted as the reduction in impact velocity.

Table 3.3 summarizes the physical and calibrations constants used in the model. In the original method of Sor et al. (2016) C_p was given as $C_p = 0.93$. However, in this study, it was found that setting $C_p = C_{D_{disk}}$ provided results that matched more closely the impact velocities of the validation cases in Figure 3.17.

Table 3.3: Constants used in the model; physical properties at ambient temperature 288.15 Kelvin and ambient pressure of 101325 Pa.

Constant	Value	Unit	Reference
k	9	(-)	(Sor et al., 2016)
C_p	1.17	(-)	-
$C_{D_{disk}}$	1.17	(-)	(Sor et al., 2016)
ρ_{air}	1.225	kg/m^3	-
μ_{air}	1.7965E-5	Pa s	-
ρ_{water}	999.1	kg/m^3	-
σ_{water}	0.07349	N/m	-

3.3.2. Calculation of the background velocity

A necessary input to the model is the background velocity field V_{air}. The droplet traverses through this field while approaching the airfoil (see Equation 3.7). It is dependent on the size and shape of the wind turbine's airfoil. This study treats the

problem as one-dimensional. From this assumption, a range of possibilities for the implied trajectory of the droplet emerge. Figure 3.10 illustrates these possibilities. In the limit, there are two possible trajectories for small and large droplets, respectively. Very small droplets are expected to follow the streamline of the flow, while large droplets are expected to follow a ballistic trajectory. In practice, the rain droplets will follow a trajectory that lies in the region between these two. To find a characteristic velocity field that can be used for further study, two popular reference turbine designs were chosen, the NREL 5MW and the IEA 15MW (Jonkman et al., 2009; Gaertner et al., 2020).
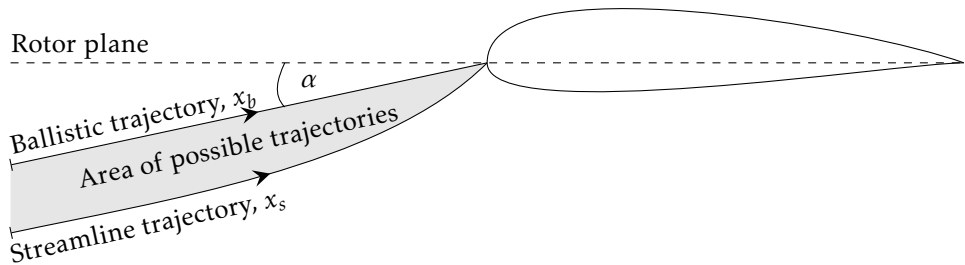
Figure 3.10: Ballistic and streamline trajectories of a droplet approaching an airfoil operated under an angle of attack α; blade twist angle and pitch are set to zero.

The first step, taken here, toward obtaining V_{air} is to perform CFD calculations of the flow field surrounding the reference turbines' airfoils using OpenFoam. The simulations were carried out by using the simpleFoam solver with the $k - \omega$ SST turbulence model. A free-stream velocity of 90 m/s was chosen. A 2D mesh of around 100,000 cells has been used for the computations. In this application, a rather coarse computational grid is satisfactory since the area of interest is located ahead of the leading edge. In this area, the solutions are well-behaved and problematic areas with flow separation are located far downstream. Subsequently, the one-dimensional velocity field was extracted from the solution by using ParaView. Two fields were extracted, one for the ballistic trajectory and one for the streamline trajectory. The latter was obtained by seeding an upstream streamline from the leading edge in ParaView and subsequently extracting the velocity vector along this line.

Instead of directly using the extracted fields as a model input, they were parameterized, which allows to better compare the different airfoils by looking at the model parameters. As in Lopez-Gavilan et al. (2020), the underlying parametrization model is the potential flow solution of a cylinder representing the nose of the airfoil. The horizontal velocity component for the potential flow in the stagnation streamline reads

$$\frac{V_{\text{air}}}{V_\infty} = 1 - \frac{1}{\left(1 - \frac{\Delta x}{R_c(\alpha)}\right)^n}. \tag{3.31}$$

$R_c(\alpha)$ is the radius of the cylinder and Δx is the distance (from the droplet) to the cylinder. However, here n and $R_c(\alpha)$ are free parameters that are fitted to the extracted field from the CFD simulation. Therefore, $R_c(\alpha)$ and n should not be regarded as geometric but rather as *aerodynamic* parameters, i.e., $R_c(\alpha)$ is the aerodynamic nose radius. It is also a function of the angle of attack. It is heuristically found that it is possible to collapse the one-dimensional velocity field for different angles of attack, i.e., the solution is self-similar to an (arbitrary) scaling value. In this case, the self-similar variable is taken to be the distance from the leading edge at which the velocity has dropped to the 95 % value of the free-stream velocity ($x_{95\%}$). This self-similar property is shown in Figure 3.11. The left plots shows the velocity field against the dimensional distance to the leading edge. In the right plot the velocity field is collapsed by scaling with $x_{95\%}$.
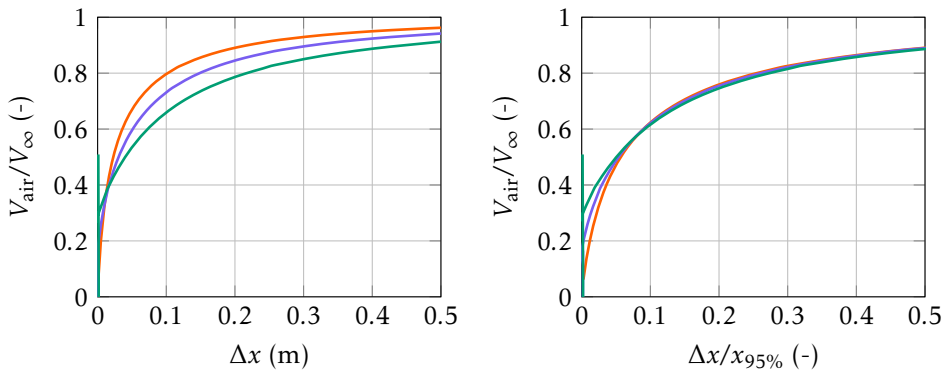
Figure 3.11: Non-dimensional velocity field along the stagnation streamline vs. the dimensional (left) and non-dimensional (right) distance to the leading edge; airfoil: FFA-W3-211; angle of attack: 0°: ——, 7.5°: ——, 15°: ——.

The self-similarity allows the velocity field to be represented at different angles of attack by scaling $R_c(\alpha)$. The influence of the angle of attack variation on the self-similar parameters can be sufficiently represented by considering a second-order polynomial. Therefore,

$$x_{95\%}(\alpha) = \left(C_1 \alpha^2 + C_2 \alpha + 1\right) x_{95\%,0}, \tag{3.32}$$

and thus also

$$R_c(\alpha) = \left(C_1 \alpha^2 + C_2 \alpha + 1\right) R_{c,0}, \tag{3.33}$$

where $R_{c,0}$ is the aerodynamic nose radius at zero angle of attack. In Figure 3.12 the FFA-W3-211 airfoil's variation of $x_{95\,\%}(\alpha)$ is shown in conjunction with the polynomial fit. The first step in the parametrization process is to find $x_{95\,\%}(\alpha)$ for every angle of attack. The zero-degree angle of attack field is then used to find the parameters n and $R_{c,0}$. Last but not least, the parameters C_1 and C_2 are found by fitting the polynomial to $x_{95\,\%}(\alpha)$. All best-fit parameters were found by using MATLAB's *fmincon* function and a least squares minimization function.
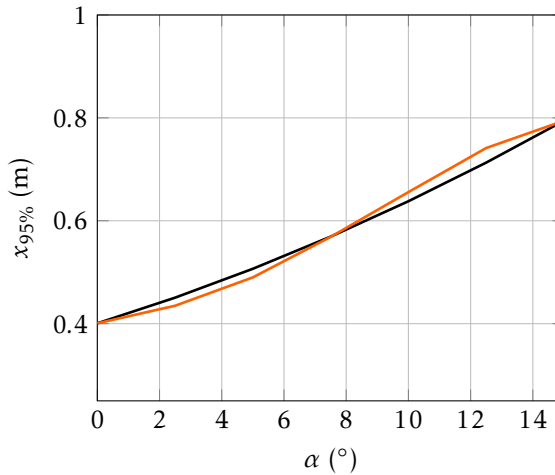
Figure 3.12: $x_{95\,\%}$ location of the FFA-W3-211 airfoil as a function of angle of attack; velocity field along the streamline trajectory; $x_{95\,\%}$ from CFD simulations: ——, quadratic fit of Equation 3.33: ——.

The final parameters are given in Table 3.4. The values of $R_c(\alpha)$ were made dimensionless with the airfoil chord c. The table shows a general trend when comparing thicker airfoils to thinner airfoils. Thicker airfoils have a higher aerodynamic nose radius and exponent. Therefore, the $x_{95\,\%}$ is also higher, meaning thicker airfoils influence droplets farther upstream. Two diverging behaviors can be noticed regarding the parameters for the angle of attack correction. For the flow that follows a ballistic trajectory, an increasing angle of attack leads to a decreasing $R_c(\alpha)$, whereas for the flow along the stagnation streamline an increasing $R_c(\alpha)$ can be noticed. Therefore, in comparison to the zero-degree angle of attack, small droplets are expected to be influenced more, whereas large droplets are expected to be influenced less when the angle of attack is increased.

Table 3.4: Best-fit parameters of V_{air} for the NREL 5MW and IEA 15MW turbine airfoils; subscript b and s stand for ballistic and streamline path, respectively; the coefficients C_1 and C_2 are dimensional; they are given for the angle of attack α in degrees, see Equation 3.33; their units are given in the brackets of the column header.

Airfoil	$R_{c,0}/c$	n	$C_{1,b}$ (deg^{-2})	$C_{2,b}$ (deg^{-1})	$C_{1,s}$ (deg^{-2})	$C_{2,s}$ (deg^{-1})
IEA 15MW Cylinder 2	0.3253	1.9542	3.17E-12	-3.86E-11	1.84E-04	-5.19E-04
DU-99-W-405	0.1444	1.6546	5.29E-04	-1.22E-02	6.94E-04	7.80E-03
DU-99-W-350	0.0934	1.4508	-1.25E-04	-9.20E-03	8.09E-04	1.52E-02
DU-97-W-300	0.0580	1.2708	-5.17E-04	-6.47E-03	1.16E-03	2.22E-02
DU-91-W2-250	0.0414	1.1889	-1.19E-03	2.22E-03	1.34E-03	3.20E-02
DU-93-W-210	0.0297	1.1154	-9.01E-04	-3.71E-03	1.40E-03	4.47E-02
NACA-64-618	0.0215	1.0494	-8.86E-04	-5.05E-03	1.34E-03	6.10E-02
SNL-FFA-W3-500	0.2275	1.8662	4.15E-12	-5.05E-11	5.10E-04	-1.26E-03
FFA-W3-360	0.1423	1.7035	6.13E-04	-1.41E-02	8.36E-04	8.53E-03
FFA-W3-330blend	0.1114	1.5777	2.16E-04	-1.37E-02	9.40E-04	1.90E-02
FFA-W3-301	0.0804	1.4260	-7.04E-04	2.85E-03	1.19E-03	2.16E-02
FFA-W3-270blend	0.0584	1.3084	-6.49E-04	-2.09E-03	1.58E-03	2.50E-02
FFA-W3-241	0.0438	1.2227	-1.19E-03	2.22E-03	1.85E-03	3.09E-02
FFA-W3-211	0.0282	1.0974	-9.01E-04	-3.71E-03	1.61E-03	4.42E-02

Figures 3.13 and 3.14 show the dimensional aerodynamic nose radius R_c and the exponent n along the blade of the NREL 5MW and the IEA 15MW wind turbines. For consistency with the official definitions of both reference turbines, the airfoils were kept constant between the officially defined stations of the NREL turbine but were linearly interpolated between the stations of the IEA turbine. This explains the saw-tooth pattern in the results of the NREL turbine in both plots. Figure 3.15 gives the angle of attack distributions along the blade that are used in Equation 3.33. The influence on the angle of attack on the aerodynamic nose radius is less than 5 % for the ballistic trajectory and around 30 % for the streamline trajectory. Both R_c and n are larger for the IEA reference turbine than for the NREL design. This has three main reasons. The IEA turbine has a higher dimensionless aerodynamic nose radius R_c/c for its airfoils. It also has a larger chord, and the angle of attacks are higher. Due to the similarity of the IEA 15MW turbine to current state-of-the-art off-shore turbines, it is argued that the values of $R_c = 0.07$ m and $n = 1.1$, as they can be found at around $r/R_{\text{blade}} = 0.9$, represent a good baseline for the remainder of this study. With these findings in mind, it is worth noting that with $R_c = 0.071$ m and $n = 1.2$, one obtains a very good fit of the reference velocity field of *Case F* and *Case G* (see Table 3.5). Hence, the parameter space of the reference data is close to the parameter space encountered in leading-edge erosion.
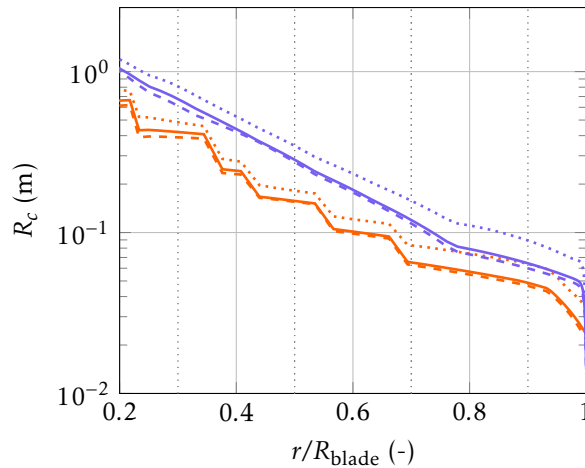
Figure 3.13: Dimensional aerodynamic nose radius R_c along the dimensionless blade distance; IEA 15MW: No correction: ——, ballistic: - - -, streamline: ·······; NREL 5MW: No correction: ——, ballistic: - - -, streamline ·······.
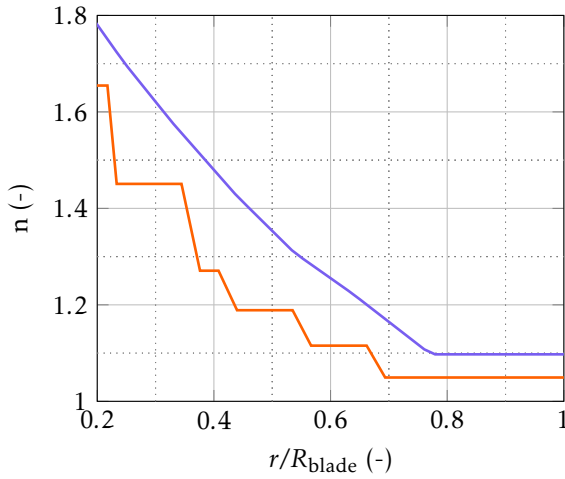
Figure 3.14: Aerodynamic exponent n along the dimensionless blade distance; IEA15 MW: ———; NREL5 MW: ———.
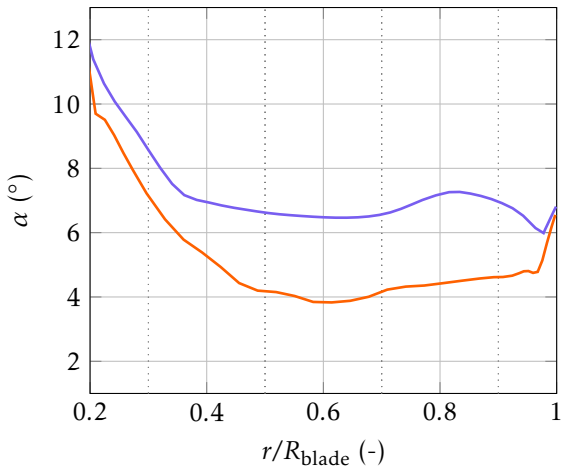
Figure 3.15: Element-wise angle of attack α along the dimensionless blade distance. The data were obtained from vortex method simulations in Barfknecht et al. (2022) with tip-speed ratio of 9 for the IEA 15MW and 7.55 for the NREL 5MW turbine; IEA 15MW: ———, NREL 5MW: ———.

3.3.3. Validation of the model

Two tests are performed to validate the model. First, the model is compared against well-known relations for the terminal falling conditions of water droplets. To this end, V_{air} was set to zero and a gravity term was added to Equation 3.4. Secondly, for comparison, a set of rotating-arm test-rig reference data is compiled from different sources.

Best (1950b) gives a relation for the terminal velocity of falling water droplets that reads

$$V_\phi = 9.32 e^{0.0405h} \left(1 - e^{-(0.565\phi_0)^{1.147}}\right), \tag{3.34}$$

where h is the altitude in kilometers that was set to zero for this study. In this equation, the droplet diameter ϕ_0 must be given in millimeters. A relation for the shape (a_ϕ/R_0) of droplets at terminal conditions is given by Brandes et al. (2002). It reads

$$\frac{a_\phi}{R_0} = \left(0.9951 + 0.02510\phi_0 - 0.03644\phi_0^2 + 0.005030\phi_0^3 - 0.0002492\phi_0^4\right)^{-1/3}. \tag{3.35}$$

Note, in the original formulation, Equation 3.35 was given as the ratio a/b. This has been converted here to a_ϕ/R_0 by assuming the shape of an oblate spheroid. Also, ϕ_0 must be given in millimeters for this equation. Figure 3.16a and 3.16b compare both formulas with the results from the model. An excellent agreement is achieved for the shape of the droplet. For up to 2.5 mm droplet diameter, the terminal velocity is almost identical to the reference value. Afterwards, a slight deviation can be noticed.
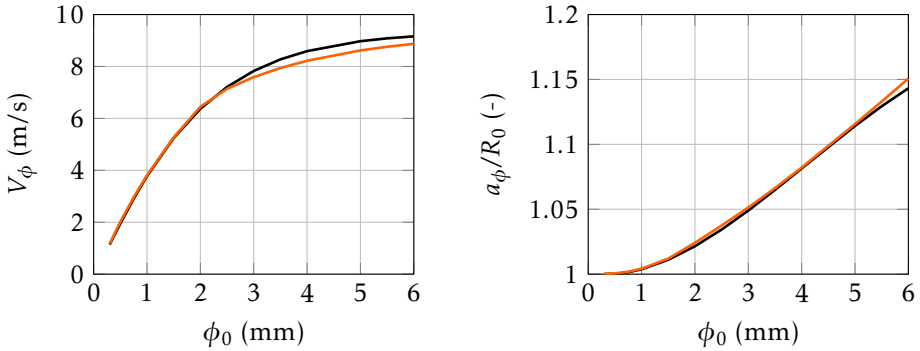
(a) Terminal velocity for falling droplets as a function of droplet diameter; simulation: ——; reference (Equation 3.34): ——.

(b) Terminal dimensionless semi-major axis for falling water droplets as a function of droplet diameter; simulation: ——; reference (Equation 3.35): ——.

Figure 3.16: Validation of the model with the terminal velocity and terminal semi-major axis of a falling droplet.

A set of reference data from the literature has been compiled for the second test. Unfortunately, the data quality differs based on whether they were directly available or had to be derived by, e.g., measuring distances on published images of high-speed photography. Table 3.5 summarizes the reference cases.

Table 3.5: Summary of rotating-arm test-rig reference data used in the validation of the proposed model.

Name	ϕ_0 (mm)	V_∞ (m/s)	c (m)	Data	Source
Case A	0.490	50	0.47	extracted from graph	Figure 25 from Vargas and Feo (2011)
Case B	0.490	60	0.47	extracted from graph	Figure 25 from Vargas and Feo (2011)
Case C	0.490	70	0.47	extracted from graph	Figure 25 from Vargas and Feo (2011)
Case D	0.490	80	0.47	extracted from graph	Figure 25 from Vargas and Feo (2011)
Case E	0.490	90	0.47	extracted from graph	Figure 25 from Vargas and Feo (2011)
Case F	1.062	90	0.71	extracted from graphs	Figures 5, 10 from Vargas et al. (2012)
Case G	1.431	90	0.71	derived from multiple graphs	Figures 10, 14, 15 from Vargas et al. (2012)
Case H	3.201	90	0.69	from measuring features in images	Figure 5.9 from García-Magariño (2016)

Figure 3.17 compares the model and measurements. It can be seen that there is a good agreement between the model and the measurements. The model overpredicts the slowdown for *Case F*. Interestingly, the slight discrepancy starts already at a distance of about 0.05 m from the leading edge, a region where the other cases show excellent agreement. *Cases D* and *E* suffer from a slight underprediction of the slowdown close to the leading edge. Arguably, *Case C* overpredicts the slowdown. Data extraction of *Case H* was challenging and had to be done manually from a small series of published photographs. Therefore, the data can only be considered fair. Nevertheless, the simulation and measurements still agree reasonably well.

To summarize, the model agrees well with reference data for both validation cases. Recall, even slight differences in the impact speed will lead to very different lifetime predictions due to the large exponent in Equation 3.1. Nevertheless, with the available data and the simple reduced-order Lagrangian model in mind, the validation results are considered adequate for lifetime predictions.
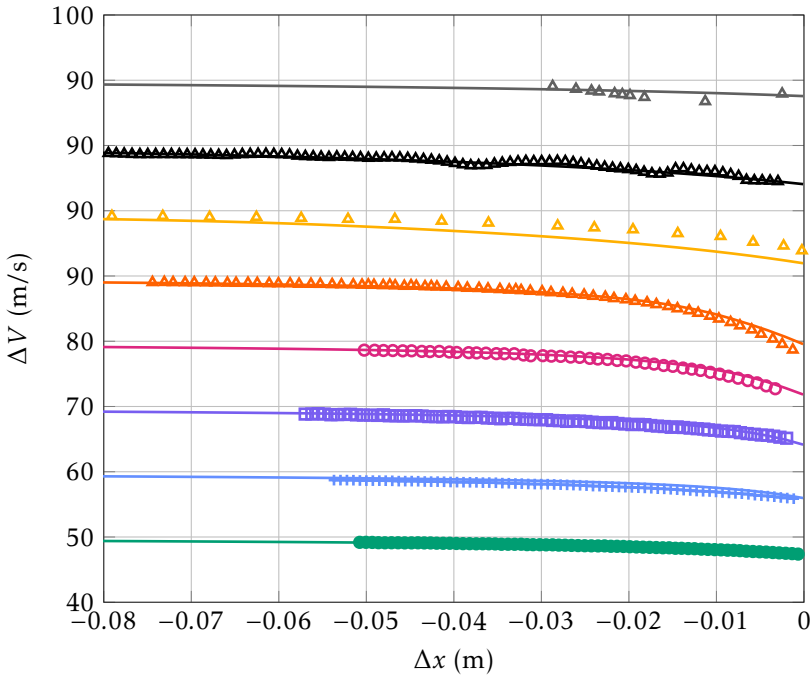
Figure 3.17: Validation of the trajectory model with reference data summarized in Table 3.5; markers indicate reference data and solid lines results of the model; note, the y-axis contains repeated ticks for better visualization of cases with equal free-stream velocity; Case A: ——, Case B: ——, Case C: ——, Case D: ——, Case E: ——, Case F: ——, Case G: ——, Case H: ——.

3.3.4. Damage model and relevant rain droplet diameters

A damage model is required to evaluate the magnitude of the slowdown effect on the lifetime of a blade. The damage model proposed in this chapter is described in the following. Additionally, the equations developed here are also used to compute the relevant rain droplet diameter range for the present study.

Several damage metrics have been proposed to calculate an erosion lifetime: the water hammer pressure metric, which is often used in conjunction with the Springer model (Hoksbergen et al., 2022), impingement (Bech et al., 2022), kinetic energy (Bech et al., 2018) or the material's strain (Verma et al., 2020). Arguably, the two most common models are currently the Springer model and the impingement metric. This study uses the impingement metric to calculate an erosion lifetime. The choice is motivated in the following.

The Springer model (as described in Hoksbergen et al. (2022)) gives an equation for the erosion lifetime by considering the number of allowable repeated impacts on one location N_i^*. The model is derived by computing the impact force $F = p_{\text{wh}} A_{\text{projected}}$, where p_{wh} is the (modified) water hammer pressure and $A_{\text{projected}}$ is the projected area of the droplet onto the impact target. In case of an oblate spheroid this would be $A_{\text{projected}} = A_a = \pi a^2$. The assumption is made that the water hammer pressure is constant for the entire projected area of the droplet. Subsequently, a stress field within the target is computed using an analytical equation of the form $\sigma(F, r, ...)$, where r is the distance to the impact location. Further, $\sigma \propto F$. After some steps, N_i^* is obtained. The entire derivation for the (uncoated) Springer model is given in Springer and Baxi (1972). A problematic assumption within the Springer model is the calculation of the impact force. If, for example, a single droplet is infinitely stretched, that is $A_{\text{projected}} \rightarrow \infty$, then $\sigma \rightarrow \infty$ and therefore $N_i^* \rightarrow 0$. Alternatively, a droplet that is significantly squeezed, i.e., $A_{\text{projected}} \rightarrow 0$, will have a lifetime of $N_i^* \rightarrow \infty$. Both results seem unphysical and thus question the validity of the Springer model. Since the rain droplets deform significantly and, therefore, grow in the projected area, the Springer model does not seem to be an adequate choice for the present study.

Impingement is a damage metric representing the total water column that the blade intercepts until coating failure. Since impingement only considers the amount of water, it is, at least conceptually, agnostic to the impacting droplet's shape; a property that seems advantageous considering the complex shape of droplets during impact. Due to this property and its recent gain in popularity, as shown in Bech et al. (2022); Visbech et al. (2023); Badger et al. (2022), it was chosen as the damage metric for this study.

The general formula for the accumulated impingement H during operation is

$$H(t) = W V_{\text{collection}} t. \tag{3.36}$$

3

W is the accumulated water column in meters per meter of swept air, t is the time, and $V_{\text{collection}}$ is the speed at which water is collected. Here it is assumed that $V_{\text{collection}} = V_\infty$.

The *impingement until end of incubation*, dubbed *allowed impingement*, is also required. H_{allowed} reads

$$H_{\text{allowed}} = \frac{\alpha}{V_{\text{impact}}^{\beta}}. \tag{3.37}$$

The equation has the form of Equation 3.1. The parameters α and β were found using the measurements of Bech et al. (2022). They performed measurements in a rotating-arm erosion test-rig, where they recorded H_{allowed} of a generic blade coating with respect to V_{impact}[2]. Tests with four distinct droplet sizes ranging from 0.76 to 3.5 mm were performed. The measurements are shown in Figure 3.18. Their raw data were used in this study to fit a function through the data points, leading to the best-fit parameters of $\alpha = 3.4860 \times 10^{20}$ and $\beta = 9.5774$. Figure 3.18 shows that the measurements collapse well. It should be noted that the authors of the study argue that the data show some drop-size dependency with $7.2 \leq \beta \leq 10.5$. This range is found when best-fit functions are created for every droplet size individually. Nevertheless, the assumption made here is that this dependency can be neglected for the conclusions drawn in this study.

Since, as indicated earlier, there is a wide spread of reported values for β in the literature, two other exponents were considered to ensure the robustness of the drawn conclusions with respect to β. The other two exponents that were chosen are 5.7 and 7. The exponent of 5.7 originates from the Springer model (Hoksbergen et al., 2022). Even though Springer does not measure impingement, but rather impacts (per surface area), it is still considered to be worth showing. The exponent 7 represents an arbitrary value between 5.7 and 9.5774.

Equations 3.36 and 3.37 can be used in a Palmgren-Miner damage rule, yielding the total damage that reads

$$D = T_{\text{rain}} \int_0^\infty \int_0^\infty \frac{\partial_t H_{I,\phi}}{H_{\text{allowed}}} d\phi dI. \tag{3.38}$$

T_{rain} is the time of operation during rain. $\partial_t H_{I,\phi}$ is the impingement collection rate as a function of the rain intensity I and droplet diameter ϕ_0. It is defined as

$$\partial_t H_{I,\phi} = W_\phi V_{\text{collection}} f_I, \tag{3.39}$$

---

[2]More information about the coating material that was used in the study of Bech et al. (2022) can be found in Section 4.2.1
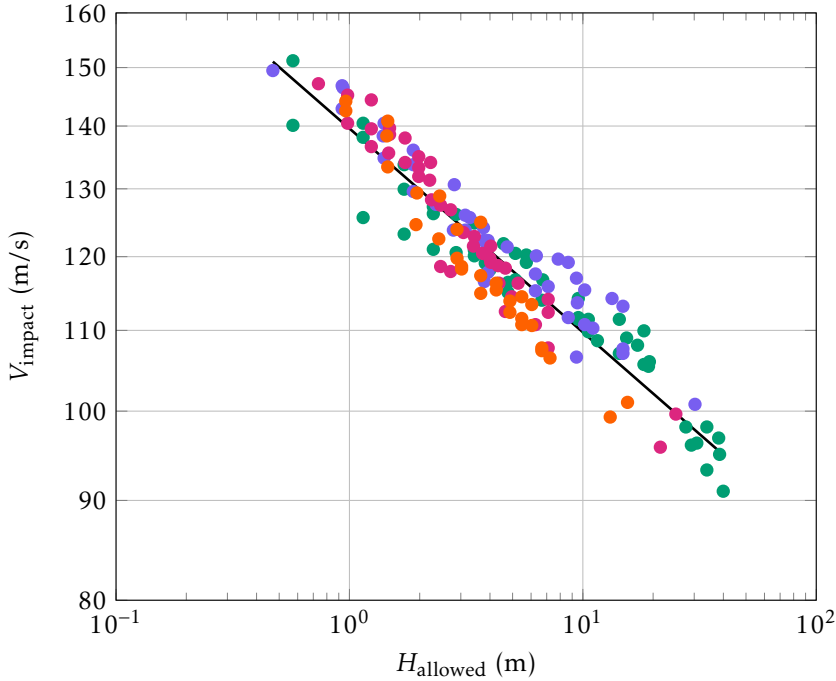
Figure 3.18: Rotating-arm erosion test-rig results by Bech et al. (2022) that relate impact velocity to impingement; droplet diameters are 0.76 mm: ●, 1.90 mm: ●, 2.38 mm: ●, 3.50 mm: ●; fit of all diameters: —.

and is analogous to Equation 3.36, but with W_ϕ, which depends on the droplet diameter ϕ_0, given by

$$W_\phi = \frac{f_{\phi,\text{plane}}I}{V_\phi},\tag{3.40}$$

where $f_{\phi,\text{plane}}$ is a distribution that describes the amount of water associated with every droplet diameter that passes through an imaginary plane in the air. One popular model that can be used to obtain $f_{\phi,\text{plane}}$ is the Best model (Best, 1950a). It gives a probability density function (pdf) of the water mass associated with every droplet diameter in a control volume in air and is given as

$$f_{\phi,\text{air}} = 2.25\left(\frac{1}{1.3I^{0.232}}\right)^{2.25}\phi_0^{2.25-1}e^{-\left(\frac{\phi_0}{1.3I^{0.232}}\right)^{2.25}},\tag{3.41}$$

where here, notice the units, I is the rain intensity in millimeters per hour and ϕ_0

is the droplet diameter in millimeters! $f_{\phi,\text{air}}$ can be converted into $f_{\phi,\text{plane}}$ by using

$$f_{\phi,\text{plane}} = \frac{f_{\phi,\text{air}} V_\phi}{\int_0^\infty f_{\phi,\text{air}} V_\phi d\phi}. \tag{3.42}$$

Note that if $f_{\phi,\text{plane}}$ is supposed to be obtained for droplet diameters in meters, then the integral in the denominator should be computed with ϕ in meters. $f_{\phi,\text{plane}}$ is plotted for five different rain intensities in Figure 3.19. One can see that the water volume of lighter rain events is mainly composed of droplets with smaller diameters in the order of 0.5 to 1 mm. With increasing rain intensity, the amount of water contained in larger droplets is increasing.
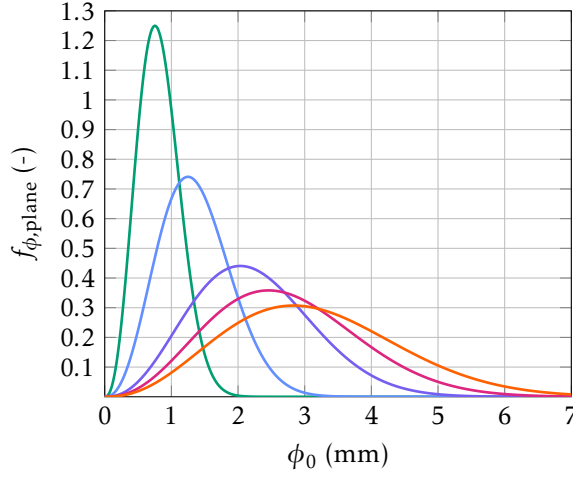
Figure 3.19: Best's distribution over a plane as a function of droplet diameter in millimeters for five different rain intensities; rain intensities 0.1 mm/hr: ——, 1 mm/hr: ——, 10 mm/hr: ——, 25 mm/hr: ——, 50 mm/hr: ——.

The time of operation during rain, i.e., the rain collection time, T_{rain} over one year of operation is given by

$$T_{\text{rain}} = p_{\text{rain}} \, T_{\text{year,spinning}}, \tag{3.43}$$

where $T_{\text{year, spinning}}$ is the number of seconds in a year that the turbine spins and p_{rain} is the probability of rain at a particular site. It should be noted that in the results section of this study the damage is presented in its non-dimensional form. p_{rain} and $T_{\text{year, spinning}}$ cancel during non-dimensionalization since they are both constant. f_I is the probability density function for the various rain intensities. To find f_I, in this study, we consider the coastal site De Kooy located in The Netherlands at coordinates (52.924, 4.780). Hourly precipitation data from a 10-year window from 2011 to 2020 were used (KNMI, 2020). The probability density function

was determined by using the same approach as in Shankar Verma et al. (2021) where a lognormal distribution that reads

$$f_I = \frac{1}{I\sigma\sqrt{2\pi}} e^{-\frac{(\ln I - \mu)^2}{2\sigma^2}} \tag{3.44}$$

was fitted using Matlab's *lognfit* function to the measured precipitation data of the site. μ is the mean and σ is the standard deviation. Note here the different meanings of the symbols in comparison to before. For a rain intensity given in mm/hr, the coefficients read $\mu = -0.1987$ and $\sigma = 0.9693$, whereas when I is given in m/s, the coefficients become $\mu = -15.29$ and $\sigma = 0.9693$.

By combining the previous equations one obtains the universal Palmgren-Miner damage for an element along the blade reading

$$D = p_{\text{rain}} \, T_{\text{year,spinning}} \, V_{\text{collection}} \int_0^\infty I f_I \int_0^\infty \frac{f_{\phi,\text{plane}}/V_\phi}{H_{\text{allowed}}(V_{\text{impact}}(\phi))} d\phi dI. \tag{3.45}$$

Here it is assumed that the turbine always spins at a constant velocity. The formula written in its cumulative form with respect to the rain intensity reads

$$D_{\text{cumulative}}(I) = p_{\text{rain}} \, T_{\text{year, spinning}} \, V_{\text{collection}} \int_0^I I' f_{I'} \int_0^\infty \frac{f_{\phi,\text{plane}}/V_\phi}{H_{\text{allowed}}(V_{\text{impact}}(\phi))} d\phi dI'. \tag{3.46}$$

A special version can be derived that gives the damage associated per meter of impingement at a particular rain intensity. It reads

$$\frac{D(I)}{H(I)} = \int_0^\infty \frac{f_{\phi,\text{air}}}{H_{\text{allowed}}} d\phi, \tag{3.47}$$

where $H(I)$ is the collected impingement as a function of rain intensity

$$H(I) = T_{\text{rain}} \int_0^\infty \partial_t H_{I,\phi} d\phi, \tag{3.48}$$

and $D(I)$ the accumulated damage as a function of rain intensity

$$D(I) = T_{\text{rain}} \int_0^\infty \frac{\partial_t H_{I,\phi}}{H_{\text{allowed}}} d\phi. \tag{3.49}$$

The derivation of Equation 3.47 uses the fact that

$$f_{\phi,\text{air}} = \frac{f_{\phi,\text{plane}}/V_\phi}{\int_0^\infty f_{\phi,\text{plane}}/V_\phi d\phi}. \tag{3.50}$$

The distribution of water mass that is associated with every droplet diameter at a particular site can be found by combining the functions of $f_{\phi,\text{plane}}$ and f_I. The result reads

$$f_{\phi,\text{site}} = \frac{\int_0^\infty I f_{\phi,\text{plane}} f_I \, dI}{\int_0^\infty \int_0^\infty I f_{\phi,\text{plane}} f_I \, dI \, d\phi}, \tag{3.51}$$

with the corresponding cumulative density function of

$$F_{\phi,\text{site}} = \int_0^\phi f_{\phi',\text{site}} \, d\phi'. \tag{3.52}$$

Both functions are plotted in Figure 3.20. It can be seen that the droplets in the range of 0 to 4 mm contain around 99 % of the total water content. This range needs to be studied for the slowdown effect. The droplets in the range of 0.5 to 3.0 mm account for about 92.5 % of water. $F_{\phi,\text{site},50\ \%}$ is found at a diameter of 1.54 mm.
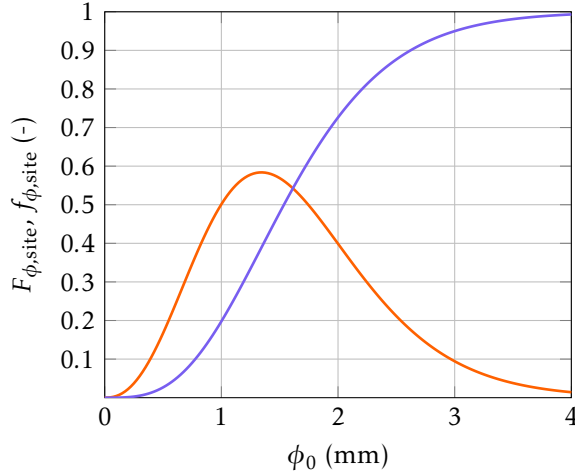
Figure 3.20: Distribution and cumulative function of the total rain column associated with every droplet diameter; distribution $f_{\phi,\text{site}}$: ——, cumulative $F_{\phi,\text{site}}$: ——.

3.4. Results

In this part, the slowdown and deformation model from the previous section is applied. First, in Sections 3.4.1 and 3.4.2, the sensitivities of the droplet diameter and the aerodynamic nose radius on the slowdown and deformation are investigated. Subsequently, in Section 3.4.3, the model's influence on the erosion damage associated with rain intensities is determined. In Section 3.4.4, the distribution of the slowdown velocity along the blades of the two reference turbines is discussed. Finally, these velocities are used to determine an updated damage distribution.

3.4.1. The influence of the droplet diameter and shape on the impact velocity

This section discusses the sensitivity of the droplet slowdown with respect to the diameter. Two types of droplets are considered, spherical and oblate droplets. The results of the spherical droplets serve as a conservative bound to the problem and represent the minimum slowdown. As per Figure 3.20, droplets in the range of 0.1 to 4 mm were considered for free-stream velocities ranging from 50 to 90 m/s.

Figure 3.21a shows the dimensional impact velocity of spherical droplets. A significant slowdown of the droplets can be observed for droplets under 0.5 mm diameter. Larger droplets show a more gradual slowdown. The origin of this behavior can be found in the ratio of surface area to mass, which is much larger for smaller droplets, thus making them more affected by the drag force. Non-dimensionalizing the impact velocity reveals that the impact velocity for spherical droplets is self-similar, i.e., the curves collapse onto each other, as shown in Figure 3.21b. The resulting curve describes the coefficient that relates the non-dimensional slowdown to the droplet diameter. For spherical droplets, this coefficient is not dependent on the free-stream velocity.

The results for the deformed droplets, as shown in Figure 3.21c, reveal additional effects. First, it can be observed that the impact velocities are noticeably lower. For example, droplets of 1 mm diameter and 90 m/s free-stream velocity are slowed down by around 2.5 m/s when kept spherical, whereas deformation leads to a slowdown of about 10 m/s. The reason for this is that the larger surface area due to the deformation leads to higher drag forces, increasing the slowdown for oblate droplets. The impact velocity graphs of the spherical droplets have a concave shape. In the graphs of the oblate droplets, a saddle point appears in the region of 0.5 mm diameter. The prominence of this saddle point increases with increasing free-stream velocities. From 70 m/s the impact velocity is not monotonically increasing but shows a slight dip at the saddle point. It is, therefore, possible that a larger droplet has a lower impact velocity. The location of the saddle point coincides approximately with the maximum deformation of the droplet, as shown in Figure 3.21e. In this figure, the deformation is shown to rise to a maximum, after which it begins to decline. The maximum corresponds to the diameter at which the limiter of Equation 3.20 starts to restrict the growth of the droplets. However, the limiter is not the reason for the occurrence of the saddle points. This can be shown by simulations without limiter where the prominence and extent of the saddle point grows. Therefore, the saddle point must be a consequence of the non-linear coupling of the momentum and deformation equation and cannot be attributed to the limiter. It would be interesting to know whether this saddle point can also be observed in experiments. The non-dimensional impact velocity of oblate droplets is self-similar outside the region of the saddle points. In the region of the saddle

3

(a) Spherical droplets; dim. velocity.

(b) Spherical droplets; non-dim. velocity.

(c) Oblate droplets; dim. velocity.

(d) Oblate droplets; non-dim. velocity.

(e) Oblate droplets; droplet semi major axis.
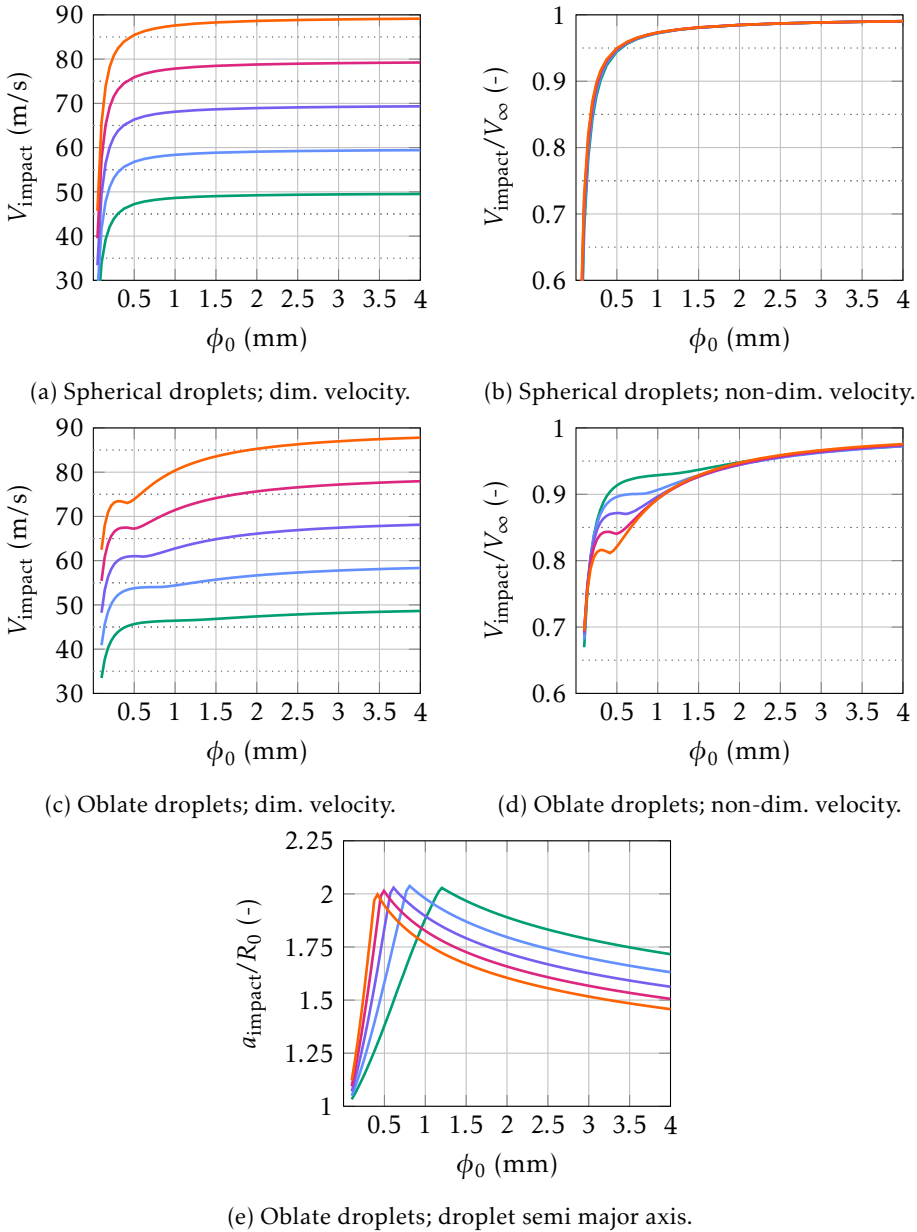
Figure 3.21: Impact velocity for different droplet diameters and free-stream velocities; aerodynamic nose radius $R_c = 0.07$ m, exponent $n = 1.1$; V_∞ of 50 m/s: ——, 60 m/s: ——, 70 m/s: ——, 80 m/s: ——, 90 m/s: ——.

point, the non-dimensional impact velocities are lower for higher free-stream velocities, indicating that an extra slowdown is obtained greater than the common scaling factors of the self-similar solution. It is also evident that with increasing free-stream velocities, the overlap of the curves becomes larger, meaning that, for example, the solutions of 80 m/s and 90 m/s are more self-similar than the ones of 50 m/s and 90 m/s. It can be summarized that oblate droplets slow down more than their spherical peers and that the slowdown effect is sensitive with respect to the droplet diameter.

3.4.2. The influence of the aerodynamic nose radius on the impact velocity

The influence of the aerodynamic nose radius on the impact speed is investigated in this section for a combination of spherical and oblate droplets of 0.5 and 2.0 mm diameter. Figure 3.22 shows that 0.5 mm droplets are much more sensitive to a change in R_c than the larger droplets of 2.0 mm. For example, spherical droplets of 0.5 mm diameter have their normalized impact velocity reduced by about 0.1 when R_c is increased from 0.1 to 0.2 m. The impact velocity of the 2.0 mm droplets decreases in the same range by only about 0.01. In general, the curves of the spherical droplet closely overlap, indicating a self-similarity. Oblate droplets show much greater sensitivity toward R_c, as seen when comparing Figures 3.22c and 3.22d. Over the entire range of the investigated nose radii, the velocities of the 2.0 mm spherical droplets decrease by about 0.05, whereas a decrease of approximately 0.25 to 0.3 can be observed for the oblate droplets, i.e., five times larger. No self-similarity can be observed for 0.5 mm oblate droplets as shown in Figure 3.22b. The curves of the different free-stream velocities spread out as R_c increases. Here, it is interesting to note that rotating-arm test rigs will not be able to capture this effect due to their small-scale airfoils and, hence, small R_c. Consequently, the non-dimensional slowdown in the test rigs will appear similar for all free-stream velocities, while on an actual turbine it is not. The dependency on the free-stream velocity originates from the non-linear coupling of the momentum and deformation equation as discussed in the previous section, see the result for the 0.5 mm droplets of Figure 3.21d. For oblate droplets of 2.0 mm, the curves again overlap closely, as was also the case in Figure 3.21d. To conclude, droplets in the saddle point region are especially sensitive to a change in the nose radius. This property is interesting since it means that, especially for faster tip-speeds, a higher R_c gives extra slowdown and thus reduces blade damage. Therefore, from a mitigation perspective, it appears to be attractive to utilize *aerodynamically thicker* airfoils; see Table 3.4. To summarize, the slowdown effect for oblate droplets is highly sensitive to the aerodynamic nose radius. This sensitivity provides an interesting opportunity as an erosion mitigation strategy.

3

(a) $\phi_0 = 0.5$ mm; spherical droplets.

(b) $\phi_0 = 0.5$ mm; oblate droplets.

(c) $\phi_0 = 2.0$ mm; spherical droplets.

(d) $\phi_0 = 2.0$ mm; oblate droplets.
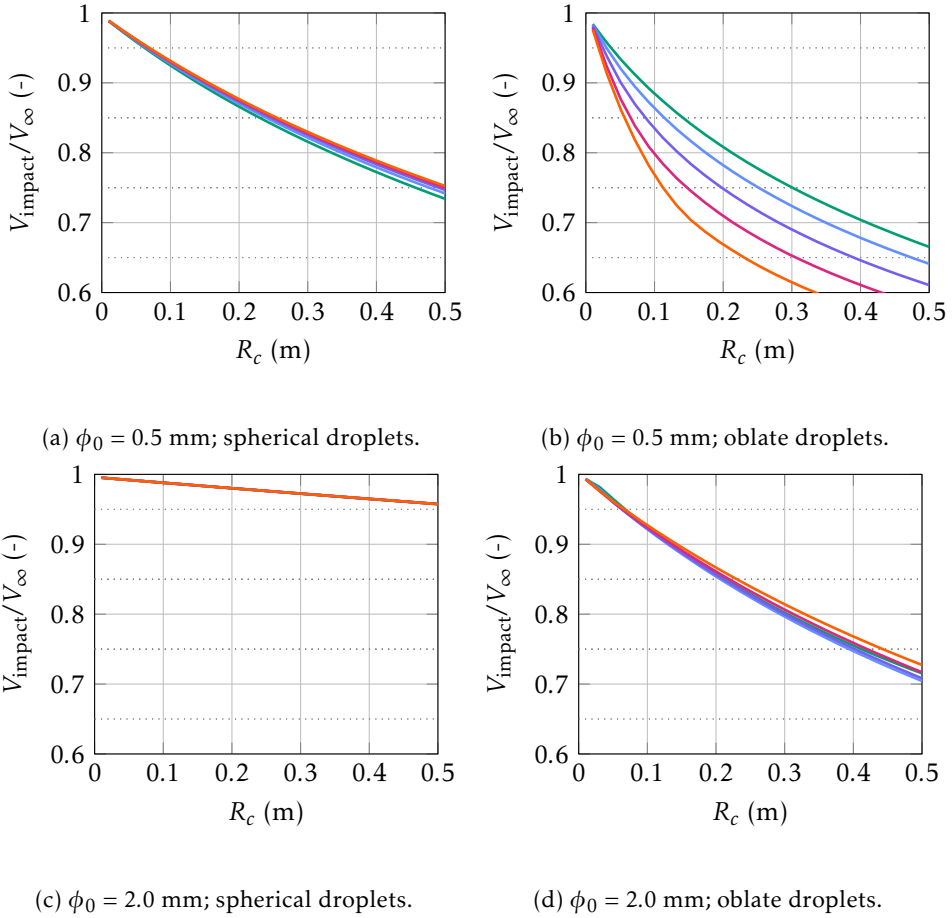
Figure 3.22: Non-dimensional droplet impact velocity for different aerodynamic nose radii R_c and free-stream velocities; exponent, $n = 1.1$; V_∞ of 50 m/s: ——, 60 m/s: ——, 70 m/s: ——, 80 m/s: ——, 90 m/s: ——.

3.4.3. Sensitivity of erosion damage with respect to rain intensity
This section investigates how the droplet slowdown influences the sensitivity of the erosion damage with respect to the rain intensity. First, Equation 3.47 is considered, which gives the damage associated with 1 m of impingement at a particular rain intensity. The average droplet impact speed must vary with rain intensity since every rain intensity has a distinct drop-size distribution. As a result, equal amounts of impingement originating from different rain intensities lead to varying degrees of damage. Without the slowdown effect, the impact speed of all droplets, irrespective of their diameter, is equal, and there will be no distinction in damage across the rain intensities. Note that the terminal velocity of a droplet and its

dependency on the diameter is neglected here. Equation 3.47 was brought into a non-dimensional form with

$$\overline{\left(\frac{D(I)}{H(I)}\right)} = \frac{D(I)/H(I)}{(D(I)/H(I))_{\text{no slowdown}}}. \tag{3.53}$$

The three distinct damage exponents β from Section 3.3.4 were considered to establish the robustness of the results with respect to the damage metric. The results are shown in Figure 3.23. Droplets without slowdown are non-dimensionalized with themselves and, thus, show a damage of unity in the entire plot. The damage for spherical and oblate droplets varies with rain intensity. At low rain intensity, most water mass is contained in the smaller droplets, which experience a significant slowdown, as shown before in Figures 3.21a and 3.21c. Therefore, low intensity rain shows a large reduction in its damage. As the rain intensity increases, so does the fraction of large droplets within the rain. The large droplets experience considerably less slowdown and, thus, are much more damaging.
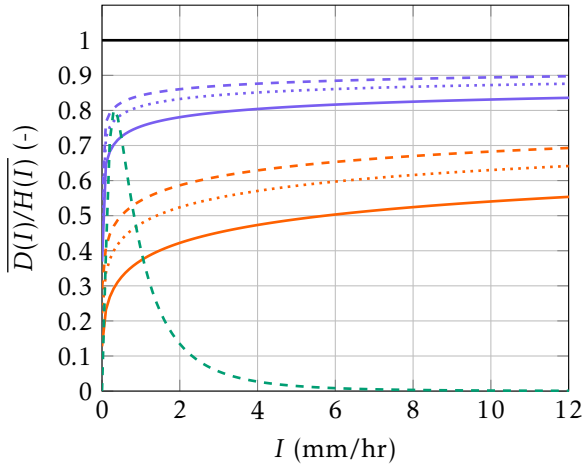
Figure 3.23: Normalized erosion damage for 1 m of rain impingement at different rain intensities; default parameters of $V_\infty = 90$ m/s, $R_c = 0.07$ m, $n = 1.1$; no slowdown: ——; spherical droplets: $\beta = 5.7$: ‐ ‐ ‐ , $\beta = 7$: ·······, $\beta = 9.58$: ——; oblate droplets: $\beta = 5.7$: ‐ ‐ ‐ , $\beta = 7$: ·······, $\beta = 9.58$: ——; normalization reference is with respect to no-slowdown droplets; f_I: ‐ ‐ ‐ .

Even though the exponents span a wide range, the spherical and oblate droplets' curves remain close together with respect to themselves. The difference in damage between the highest and the lowest exponent is fairly constant for both types of droplets across the entire range of rain intensities. This difference is approximately 0.1 and 0.175 for spherical and oblate droplets, respectively. Spherical

droplets, especially for smaller rain intensities, already show so much damage reduction that the slowdown effect cannot be neglected. The difference in damage between spherical and oblate droplets is even more significant than between spherical droplets with and without slowdown. Thus it is not sufficient to assume that droplets are spherical, but the deformation needs to be taken into account as well. Figure 3.23 also shows f_I, which is the pdf of the rain intensities. Around 80 % of all precipitation events are of the magnitude 2 mm/hr and lower. In this range, the slowdown also has the highest effect.

The non-dimensional cumulative site damage reads

$$(F_D(I))_{\text{no slowdown}} = \frac{D_{\text{cumulative}}}{D_{\text{no slowdown}}}. \tag{3.54}$$

It is plotted in Figure 3.24a as a function of I for all droplet types and damage exponents. Since the damage is written in its cumulative form, the damage of droplets without slowdown reaches unity for $I \to \infty$. The plot shows that for a turbine located at the De Kooy weather station, the inclusion of the droplet slowdown leads to predicted damage of 0.77 to 0.85 for spherical and 0.41 to 0.57 for oblate droplets. Or expressed in the reciprocal, the predicted lifetime is twice as long for oblate droplets. Figure 3.24a also shows which rain intensities contribute the most to erosion damage. E.g. for droplets without slowdown, all rain events between 0 and 2 mm/hr contribute to about 55 % of the total erosion damage. From this, the question arises whether the slowdown also influences which rain intensities contribute the most toward erosion damage. To study this, a different non-dimensionalization is used

$$F_D(I) = \frac{D_{\text{cumulative}}}{D}. \tag{3.55}$$

Here every case is non-dimensionalized with itself so that the erosion damage for $I \to \infty$ is always unity. Hence, Equation 3.55 can also be seen as the cumulative distribution function of the damage with respect to the rain intensity. The results are shown in Figure 3.24b. For oblate droplets, the 55 % mark of relative damage is shifted to around 2.3 mm/hr compared to 2 mm/hr for the case without slowdown. This shows that the slowdown effect not only significantly reduces the predicted erosion damage but also slightly shifts the *production* of erosion damage to higher rain intensities.

The shift in *production* of the erosion damage could also influence the viability of erosion mitigation strategies such as the erosion-safe mode. The erosion-safe mode aims at avoiding damage by either reducing the tip-speed or shutting down the turbine during precipitation events. To develop this point further, the damage
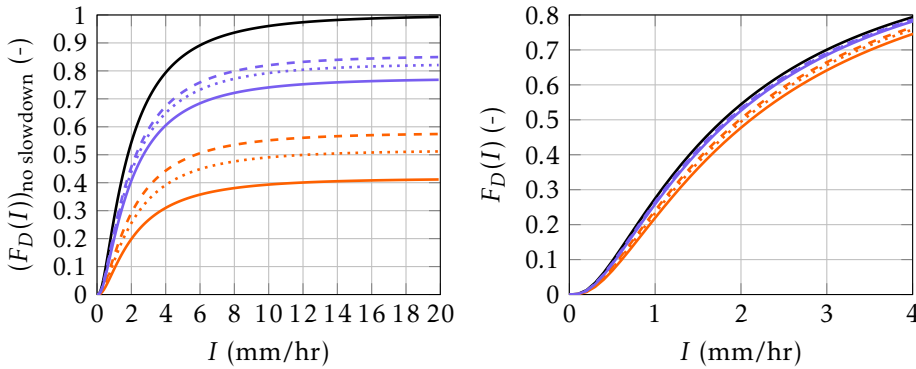
(a) Normalization with respect to no slow-down droplets. See Equation 3.54.

(b) Normalization with respect to itself. See Equation 3.55.

Figure 3.24: Normalized cumulative damage distribution for De Kooy weather station; $R_c = 0.07$ m, $n = 1.1$ and $V_\infty = 90$ m/s; no slowdown: ——; spherical droplets: $\beta = 5.7$: – – – , $\beta = 7$: ⋯⋯, $\beta = 9.58$: ——; oblate droplets: $\beta = 5.7$: – – – , $\beta = 7$: ⋯⋯, $\beta = 9.58$: ——.

of Equation 3.55 can be expressed as $(1 - F_D(I)) \cdot 100\%$ and be plotted against

$$(1 - F_I(I)) \cdot 100\% = \left(1 - \int_0^I f_{I'}(I')dI'\right) \cdot 100\%, \qquad (3.56)$$

resulting in Figure 3.25. The figure should be interpreted as how much damage will be saved if X % of the highest intensity precipitation events can be avoided. As an example, the figure shows that for droplets without slowdown (——), turning off a turbine during the 20 % highest intensity precipitation events will reduce the erosion damage by 49 %. Likewise, avoiding the 50 % highest intensity rain events will save 79 % of all damage. When droplet deformation and slowdown are taken into account, this curve shifts. Depending on the damage exponents avoiding the 20 % most intense rain events now avoids 53 % to 55 % of the erosion damage. Alternatively, when moving laterally, 49 % of erosion damage can be saved when 15.9 % to 17.5 % of the highest rain intensity events are avoided. From the figure, it is also visible that the assumption of purely spherical droplets also shifts the curve. However, this shift's magnitude is fairly low compared to oblate droplets. To conclude, the deformation and slowdown effect reduces erosion damage and impacts the viability of erosion-mitigation strategies. In case the erosion-safe mode is used, neglecting the slowdown effect will yield a sub-optimal utilization by reducing power production in conditions that are not contributing the most toward erosion damage.
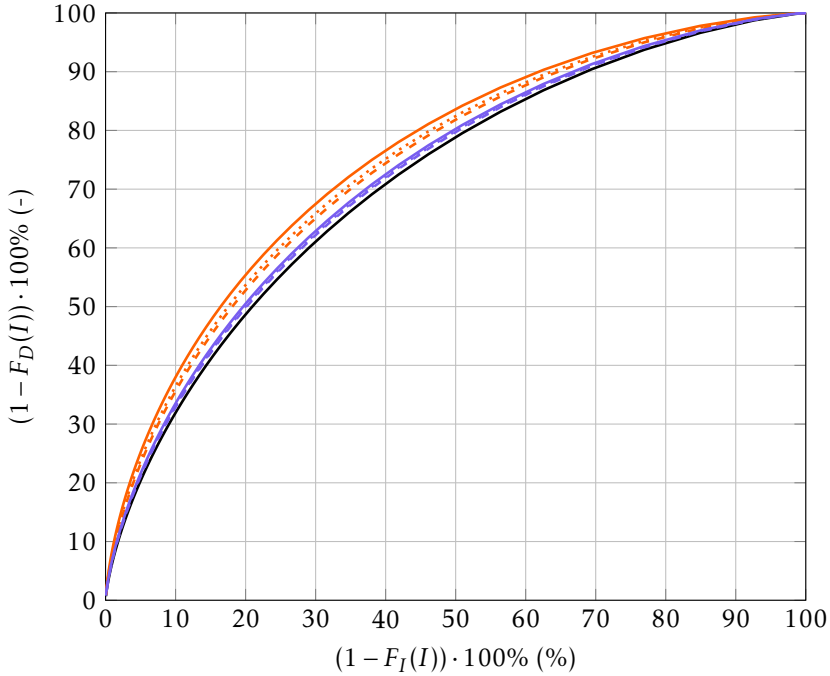
Figure 3.25: Savings in damage distribution against the X % of heaviest rain events; $R_c = 0.07$ m, $n = 1.1$ and $V_\infty = 90$ m/s; no slowdown: ———; spherical droplets: $\beta = 5.7$: – – –, $\beta = 7$: ·······, $\beta = 9.58$: ———; oblate droplets: $\beta = 5.7$: – – –, $\beta = 7$: ·······, $\beta = 9.58$: ———.

3.4.4. Droplet behavior for reference turbines

The impact of the droplet slowdown along the blades of two reference turbines is investigated. As previously discussed, the NREL 5MW and IEA 15MW turbines were chosen for this purpose. The turbines were assumed to be located at the De Kooy weather station. First, the slowdown velocities are analyzed, and the resulting normalized damage distribution is subsequently investigated. Nominal turbine operating conditions at design tip-speed ratio (TSR) were chosen as the control set point for the comparison (IEA TSR = 9, NREL TSR = 7.55). The parameters from Figure 3.13, 3.14, and 3.15 were used for the blade elements. The ballistic angle of attack correction coefficients of Table 3.4 were applied. As explained previously, the philosophies of the original reference turbines were used. This means that the airfoils of the NREL 5MW turbine stay constant between the officially defined stations, whereas, for the IEA 15MW turbine, airfoils are linearly interpolated between stations. Hence, a saw-tooth pattern is expected in the results of the NREL turbine.

Figure 3.26 shows the slowdown along the blades of the reference turbines. The calculations were performed for spherical and oblate droplets and for diameters of 0.5, 1.0, 2.0, and 3.0 mm. The slowdown velocities are approximately twice as high for the IEA turbine. The reasons can be found in the slightly higher tip-speed of the IEA turbine and the larger aerodynamic nose radius, as shown in Figure 3.13. The latter, as discussed in Figure 3.22, is a significant driver for the slowdown of droplets. The IEA's aerodynamic nose radius R_c is higher due to the larger chord, but also due to airfoils that have, in general, a higher $R_{c,0}/c$ as shown in Table 3.4.

(a) NREL 5MW; spherical droplets.

(b) NREL 5MW; oblate droplets.

(c) IEA 15MW; spherical droplets.

(d) IEA 15MW; oblate droplets.
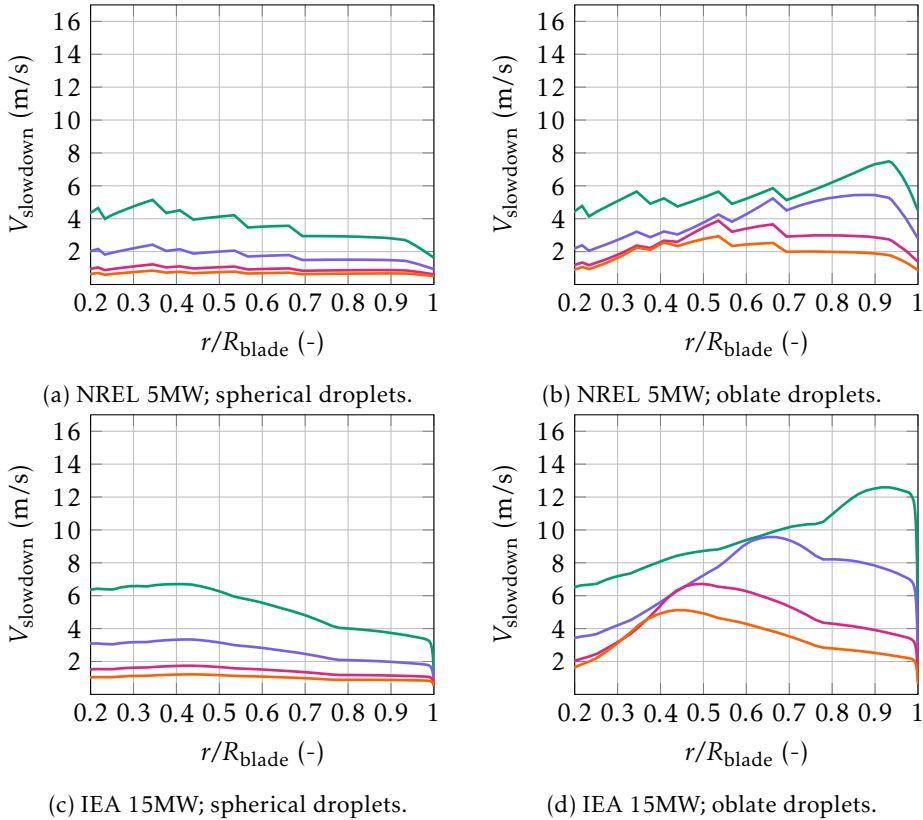
Figure 3.26: Droplet slowdown along the non-dimensional blade distance of the NREL 5MW and IEA 15MW turbine; spherical and oblate droplets are considered; slowdown is shown for droplets of 0.5 mm: ——, 1.0 mm: ——, 2.0 mm: ——, 3.0 mm: ——.

As expected, smaller droplets show a more significant slowdown along the blade. Spherical droplets experience a decrease in the slowdown velocity from inboard to outboard. This is, at first glance, counterintuitive since the blade element speed is higher toward the tip of the blade. However, the decrease of the aerodynamic nose

radius and the aerodynamic exponent, as shown in Figure 3.13, offsets the increase in blade element velocity. Oblate droplets show an inverted behavior where the slowdown velocities increase to a maximum when traveling outboard. There, the slowdown effect starts to diminish again. As with the spherical droplets, there is a sharp drop at the blade's tip. In general, in the tip region, the slowdown velocities for oblate droplets are about two to three times higher than for spherical droplets. Outboard, the higher free-stream velocities must promote the deformation of droplets, leading to a larger slowdown. The sharp drop in slowdown at the very tip of the blade can be explained by the rapidly decreasing chord[3]. To conclude, the deformation and resulting slowdown of the droplets are also critical when actual wind turbines are considered.

The point of maximum slowdown for oblate droplets shifts outboard with decreasing droplet diameters. Larger droplets see their maximum slowdown inboard, whereas the smaller droplets see their maximum outboard of the blade. This reveals another drop-size-dependent non-linearity of the slowdown effect. Larger droplets see a reduced slowdown compared to their smaller peers, and the slowdown is unevenly distributed along the blade. Large droplets see inboard a relatively large slowdown, whereas small droplets are slowed down significantly in the erosion-prone outboard region of the blade.

An interesting observation can be made in Figure 3.26d where the curves of the various droplet sizes are not only offset but also briefly overlap, e.g. at $r/R_{\text{blade}} = 0.65$ for the 0.5 and 1.0 mm diameter droplets. Even though the droplets have different sizes, they see the same absolute slowdown. This effect was found before in Figure 3.21c, where a saddle point was observed. The position of the saddle point with respect to the droplet diameter shifts for variations in R_c and n and thus leads to different overlapping points along the blade.

Figure 3.27 shows the non-dimensional damage along the blade. The damage was calculated using the Equation 3.45 with the non-dimensionalization of

$$\overline{D} = \frac{D}{D_{\text{no slowdown}}}. \tag{3.57}$$

The damage was calculated for every blade section with $V_{\text{collection}} = V_{\text{sec}}$. As before, to investigate the sensitivity of the results, the three damage exponents of 5.7, 7, and 9.58 were considered. A damage of unity represents the damage accumulated from a turbine without any droplet slowdown.

For both turbines, the damage decreases toward the blade root, which, at first glance, seems counterintuitive. However, the slowdown velocities stay reasonably constant along the entire blade. In contrast, the blade section speeds vary linearly

---

[3]The tip vortex might influence the results at the tip. The methodology does not account for this.

from close to zero to 82 and 95 m/s for the NREL 5MW and IEA 15MW turbines, respectively, when moving toward the blade's tip. Hence, the ratio between slowdown and blade element speed is much higher inboard of the blade, and, therefore, the slowdown leads inboard to a proportionally higher damage reduction. Still, at the blade's tip, the slowdown effect is non-negligible. Large damage reductions are observed at r/R_{blade} of 0.9. Under the assumption of spherical droplets, the normalized damage is in the range of 0.82 to 0.9 for the NREL turbine. The range for oblate droplets is 0.53 to 0.7. The IEA turbine shows slightly lower non-dimensional damage. As in Figure 3.23, the band formed by the damage exponents is fairly constant along the entire blade span, indicating that the results are robust with respect to the damage exponent.

To conclude, the slowdown effect significantly impacts the lifetime prediction of actual wind turbine blades. Adding droplet deformation changes the magnitude and the characteristics of the slowdown velocity along the blade. Even though the highest damage reduction can be found inboard, the slowdown effect remains significant at the blade tip. The results of Figures 3.26 and 3.27 show how a larger R_c can effectively increase the slowdown and thus mitigate erosion damage. This lever seems especially interesting by considering the properties of the airfoils shown in Table 3.4, i.e., $R_{c,0}/c$ and the angle of attack correction.

(a) NREL 5MW

(b) IEA 15MW
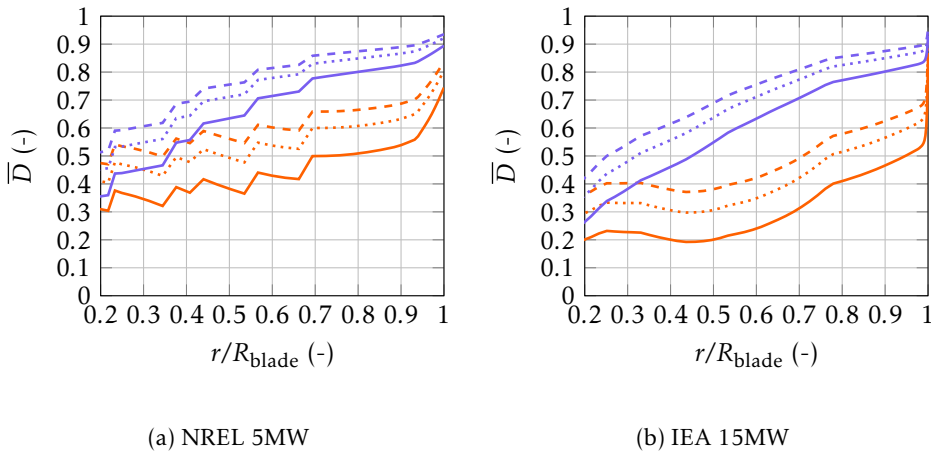
Figure 3.27: Damage distribution along the non-dimensional blade distance; spherical droplets: $\beta = 5.7$: - - - , $\beta = 7$: ······, $\beta = 9.58$: ——; oblate droplets: $\beta = 5.7$: - - - , $\beta = 7$: ······, $\beta = 9.58$: ——.

3.5. Conclusions

Based on previous findings in the literature, it can be said that experiments in a rotating-arm test-rig environment that used a parameter space relevant to current wind turbine designs have shown that droplets slow down and break up when they approach an airfoil. Hence, slowdown and deformation are also most likely occurring on actual wind turbines. Measurements have shown that the slowdown can be in excess of 10 m/s for small droplets. The slowdown becomes less significant as the droplet diameter increases. Moreover, in the above-mentioned experiments, the breakup modes of bag, bag-stamen, and shear were observed. The role of such droplet breakup on rain erosion is unknown.

From the results obtained in this study, the following main conclusions can be drawn:

- The slowdown effect leads to significant damage reductions and, consequently, should not be neglected in erosion damage modeling. On actual wind turbines, the slowdown effect varies along the blade but remains significant throughout the erosion-prone region. The conclusions regarding the slowdown in this work are robust with respect to variations in the model parameters, such as the exponents of the damage law.

- Droplet size matters! For the investigated cases, droplets under 0.25 mm diameter are slowed down so much that they contribute only marginally to the erosion damage. Large droplets are thus more damaging than their smaller peers. Furthermore, the droplet slowdown is highly sensitive to the aerodynamics nose radius R_c. Due to an expected difference in trajectory between small and large droplets, the angle of attack correction of $R_c(\alpha)$ is projected to be more significant for smaller droplets. This correction increases the slowdown of smaller droplets.

- Droplet shape matters too! The slowdown effect is already significant for spherical droplets. However, the slowdown of oblate droplets greatly exceeds that of spherical droplets. Therefore, deformation must be taken into account. When studying the impact of droplets on blades, droplets should (at least) be modeled as being oblate. Figure 3.21e can be used as a suggestion for a particular shape.

- Rain intensity matters! This is due to the relationship of rain intensity and droplet size distribution. The slowdown effect is particularly significant for light rain-intensity events. It also shifts the damage accumulation to higher precipitation intensities. Therefore, it may be beneficial to reduce the tip-speed of turbines only during heavy precipitation events to avoid erosion.

Due to the importance of the droplet slowdown effect on the erosion lifetime of the wind turbine blades, additional research is recommended:

1. Rotating-arm erosion test-rigs might also encounter a slowdown effect. This effect would then need to be taken into account in order to find the true impact-speed for a given free-stream velocity.

2. It is conceivable that droplets might break up in a cascade decay. Additionally, it has been shown that droplets prior to impact can represent a water mass that has a non-homogeneous velocity. The potential implications of these two effects need to be better understood.

3. In general, more research needs to be conducted on the dynamics of droplet breakup when droplets are subjected to a transient slip velocity field. For example, when approaching an airfoil. Especially the exact conditions and non-dimensional numbers that promote the various breakup modes need to be further understood. Based on such findings, a catalog of droplet shapes just prior to impact would be beneficial, as it could be used in further studies that concern the collision of droplets with wind turbine blades as well as applications beyond wind energy.

3

Bibliography

Badger, M., Zuo, H., Hannesdóttir, A., Owda, A., and Hasager, C.: Lifetime prediction of turbine blades using global precipitation products from satellites, Wind Energy Science, 7, 2497–2512, https://doi.org/10.5194/wes-7-2497-2022, 2022.

Barfknecht, N., Kreuseler, M., de Tavernier, D., and von Terzi, D.: Performance analysis of wind turbines with leading-edge erosion and erosion-safe mode operation, Journal of Physics: Conference Series, 2265, 032 009, https://doi.org/10.1088/1742-6596/2265/3/032009, 2022.

Bech, J. I., Hasager, C. B., and Bak, C.: Extending the life of wind turbine blade leading edges by reducing the tip speed during extreme precipitation events, Wind Energy Science, 3, 729–748, https://doi.org/10.5194/wes-3-729-2018, 2018.

Bech, J. I., Johansen, N. F.-J., Madsen, M. B., Hannesdóttir, Á., and Hasager, C. B.: Experimental study on the effect of drop size in rain erosion test and on lifetime prediction of wind turbine blades, Renewable Energy, 197, 776–789, https://doi.org/10.1016/j.renene.2022.06.127, 2022.

Best, A. C.: The size distribution of raindrops, Quarterly journal of the royal meteorological society, 76, 16–36, https://doi.org/10.1002/qj.49707632704, 1950a.

Best, A. C.: Empirical formulae for the terminal velocity of water drops falling through the atmosphere, Quarterly Journal of the Royal Meteorological Society, 76, 302–311, https://doi.org/10.1002/qj.49707632905, 1950b.

Brandes, E. A., Zhang, G., and Vivekanandan, J.: Experiments in Rainfall Estimation with a Polarimetric Radar in a Subtropical Environment, Journal of Applied Meteorology, 41, 674 – 685, https://doi.org/10.1175/1520-0450(2002)041%3C0674:EIREWA%3E2.0.CO;22, 2002.

Feo, A., Vargas, M., and Sor, A.: Rotating Rig Development for Droplet Deformation/Breakup and Impact Induced by Aerodynamic Surfaces, Technical Report NASA/TM—2012-217721, National Aeronautics and Space Administration, 2012.

Fæster, S., Johansen, N. F.-J., Mishnaevsky Jr, L., Kusano, Y., Bech, J. I., and Madsen, M. B.: Rain erosion of wind turbine blades and the effect of air bubbles in the coatings, Wind Energy, 24, 1071–1082, https://doi.org/10.1002/we.2617, 2021.

Gaertner, E., Rinker, J., Sethuraman, L., Zahle, F., Anderson, B., Barter, G. E., Abbas, N. J., Meng, F., Bortolotti, P., Skrzypinski, W., et al.: Definition of the IEA 15-Megawatt Offshore Reference Wind Turbine, Tech. rep., National Renewable Energy Lab.(NREL), Golden, CO (United States), 2020.

3

García-Magariño, A.: Water droplet deformation and breakup in the vicinity of the leading edge of an incoming airfoil, Ph.D. thesis, Technical University of Madrid, https://doi.org/10.20868/UPM.thesis.44231, 2016.

García-Magariño, A., Sor, S., and Velazquez, A.: Droplet Ratio Deformation Model in Combination with Droplet Breakup Onset Modeling, Journal of Aircraft, 58, 310–319, https://doi.org/10.2514/1.C035942, 2021.

Hoksbergen, N., Akkerman, R., and Baran, I.: The Springer model for lifetime prediction of wind turbine blade leading edge protection systems: A review and sensitivity study, Materials, 15, 1170, https://doi.org/10.3390/ma15031170, 2022.

Hoksbergen, T., Akkerman, R., and Baran, I.: Liquid droplet impact pressure on (elastic) solids for prediction of rain erosion loads on wind turbine blades, Journal of Wind Engineering and Industrial Aerodynamics, 233, 105 319, https://doi.org/10.1016/j.jweia.2023.105319, 2023.

Hsiang, L.-P. and Faeth, G.: Drop deformation and breakup due to shock wave and steady disturbances, International Journal of Multiphase Flow, 21, 545–560, https://doi.org/10.1016/0301-9322(94)00095-2, 1995.

Jackiw, I. M. and Ashgriz, N.: On aerodynamic droplet breakup, Journal of Fluid Mechanics, 913, A33, https://doi.org/10.1017/jfm.2021.7, 2021.

Jackiw, I. M. and Ashgriz, N.: Prediction of the droplet size distribution in aerodynamic droplet breakup, Journal of Fluid Mechanics, 940, A17, https://doi.org/10.1017/jfm.2022.249, 2022.

Jones, B., Saylor, J., and Testik, F.: Raindrop morphodynamics, Rainfall: State of the Science, 191, 7–28, https://doi.org/10.1029/2009GM000928, 2010.

Jonkman, J., Butterfield, S., Musial, W., and Scott, G.: Definition of a 5-MW reference wind turbine for offshore system development, Tech. rep., National Renewable Energy Lab.(NREL), Golden, CO (United States), 2009.

Keegan, M. H., Nash, D., and Stack, M.: Modelling rain drop impact on offshore wind turbine blades, ASME Turbo Expo 2012, pp. 887–898, https://doi.org/10.1115/GT2012-69175, 2012.

KNMI: Uurgegevens van het weer in Nederland - 235 - De Kooy, Website accessed 01.02.2022, 2020, https://cdn.knmi.nl/knmi/map/page/klimatologie/gegevens/uurgegevens/uurgeg_235_2021-2030.zip.

Lopez-Gavilan, P., Velazquez, A., García-Magariño, A., and Sor, S.: Breakup criterion for droplets exposed to the unsteady flow generated by an incoming aerody-

namic surface, Aerospace Science and Technology, 98, 105 687, https://doi.org/10.1016/j.ast.2020.105687, 2020.

Nicholson, J. E.: Drop breakup by airstream impact, Tech. rep., Mithras Inc., Cambridge, Massachusetts, 1968.

Prieto, R. and Karlsson, T.: A model to estimate the effect of variables causing erosion in wind turbine blades, Wind Energy, 24, 1031–1044, https://doi.org/10.1002/we.2615, 2021.

Schmehl, R.: Tropfendeformation und Nachzerfall bei der technischen Gemischaufbereitung, Ph.D. thesis, Karlsruhe Institute of Technology, 2004.

Shankar Verma, A., Jiang, Z., Ren, Z., Caboni, M., Verhoef, H., van der Mijle-Meijer, H., Castro, S. G., and Teuwen, J. J.: A probabilistic long-term framework for site-specific erosion analysis of wind turbine blades: A case study of 31 Dutch sites, Wind Energy, 24, 1315–1336, https://doi.org/10.1002/we.2634, 2021.

Sichani, A. B. and Emami, M. D.: A droplet deformation and breakup model based on virtual work principle, Physics of Fluids, 27, 032 103, https://doi.org/10.1063/1.4913809, 2015.

Sommerfeld, M., van Wachem, B., and Oliemans, R.: Best Practice Guidelines for Computational Fluid Dynamics of Dispersed Multiphase Flows, Tech. rep., ERCOFTAC - European Research Community On Flow, Turbulence And Combustion and SIAMUF, Swedish Industrial Association for Multiphase Flows, 2008.

Sor, S.: Theoretical model for droplet deformation and trajectory in continuously accelerating flows, Ph.D. thesis, Technical University of Madrid, https://doi.org/10.20868/UPM.thesis.45721, 2017.

Sor, S. and García-Magariño, A.: Modeling of droplet deformation near the leading edge of an airfoil, Journal of Aircraft, 52, 1838–1846, https://doi.org/10.2514/1.C033086, 2015.

Sor, S. and García-Magariño, A.: Correction: Modeling of Droplet Deformation Near the Leading Edge of an Airfoil, Journal of Aircraft, 58, 1–1, https://doi.org/10.2514/1.C033086.c1, 2021.

Sor, S., García-Magariño, A., and Velazquez, A.: Model to predict water droplet trajectories in the flow past an airfoil, Aerospace Science and Technology, 58, 26–35, https://doi.org/10.1016/j.ast.2016.07.015, 2016.

Sor, S., García-Magariño, A., and Velazquez, A.: Droplet in the Shoulder Region of an Incoming Airfoil. Part II: Droplet Breakup, in: AIAA Aviation 2019 Forum, p. 3307, https://doi.org/10.2514/6.2019-3307, 2019.

Springer, G. S. and Baxi, C. B.: A model for rain erosion of homogeneous materials, Tech. Rep. AFML-TR-72-106, Air Force Materials Laboratory, 1972.

Vargas, M. and Feo, A.: Deformation and breakup of water droplets near an airfoil leading edge, Journal of Aircraft, 48, 1749–1765, https://doi.org/10.2514/1.C031363, 2011.

Vargas, M., Sor, S., and García-Magariño, A.: Mechanism of Water Droplet Breakup Near the Leading Edge of an Airfoil, Technical Report NASA/TM—2012-217704, National Aeronautics and Space Administration, 2012.

Verma, A. S., Castro, S. G., Jiang, Z., and Teuwen, J. J.: Numerical investigation of rain droplet impact on offshore wind turbine blades under different rainfall conditions: A parametric study, Composite structures, 241, 112 096, https://doi.org/10.1016/j.compstruct.2020.112096, 2020.

Visbech, J., Göçmen, T., Hasager, C. B., Shkalov, H., Handberg, M., and Nielsen, K. P.: Introducing a data-driven approach to predict site-specific leading-edge erosion from mesoscale weather simulations, Wind Energy Science, 8, 173–191, https://doi.org/10.5194/wes-8-173-2023, 2023.

3

4

Drop-size-dependent effects and erosion-safe mode operation

In the previous chapter, it was shown that droplets in the vicinity of turbine blades slow down, deform and break up. This behavior is governed by the droplet diameter. Hence, droplet slowdown and deformation is a drop-size-dependent effect. The question arises as to whether there are other drop-size-dependent effects as well. This chapter identifies several effects and implements them in a holistic erosion damage forecasting model. Subsequently, the damage model is used to study the influence of drop-size-dependent effects on leading-edge erosion and erosion-safe mode operation in particular.

Local table of contents

4.1. Introduction

Understanding the conditions that promote the development of erosion is fundamental to developing and applying any mitigation strategy, whether in the form of protective solutions or operational adjustments. The parameter space of erosion is vast: Turbines have varying tip-speeds, the wind conditions differ per site and so does the precipitation. Rain is heterogeneous. It is composed of droplets of varying diameters. The statistical distribution of the rain droplets is described with a drop-size distribution, with typical choices being the Best or Marshall-Palmer distributions. In practice, the drop-size distribution is site-dependent (Pryor et al., 2022). Determining the erosivity of a rain event requires knowledge about the drop-size distribution and the erosion damage associated with every droplet diameter.

So far, there is still considerable uncertainty on how the diameter influences the erosivity of droplets. It is also unknown whether the implementation and viability of the ESM might be affected by this lack of knowledge. Bech et al. (2022) performed measurements in an erosion test rig. They found that, depending on the impact speed, either smaller or larger diameters are more damaging. Verma et al. (2020) performed numerical simulations in which a water droplet impacts a composite target. They found that the maximum coating stress increases with the droplet size. Amirzadeh et al. (2017) performed similar simulations but assumed that the impact target was solid. In contrast to Verma et al. (2020), they found that the maximum impact pressure is invariant with the droplet diameter. In Barfknecht and von Terzi (2023), it was shown that droplets in the proximity of wind turbine blades are expected to slow down. Their analysis suggests that large droplets are significantly more damaging than small droplets.

This chapter aims at providing answers to the following research questions:

1. How does the drop size influence the erosivity?

2. Is a thorough understanding of drop-size effects important for the design of the erosion-safe mode?

The term *drop-size effect* refers to physical processes where the droplet diameter influences the erosivity, especially those effects that persist even when accounting for droplet volume or mass. To answer these research questions, a turbine, a site, and a leading-edge material must be considered. In this study, a typical combination of these is chosen. Therefore, some results might only pertain to this particular combination. In this study, the IEA 15MW reference turbine is used (Gaertner et al., 2020). Where applicable, results for the non-dimensional blade span $r/R_{\text{blade}} = 0.9$ are shown. This location was chosen based on the fact that leading-edge protection solutions are generally applied on a length of 10 to 20 m when measured from the tip (Verma et al., 2021). The blade span of the IEA 15MW is approximately 120 m. The turbine was assumed to be located at the coastal site De Kooy (Den Helder) in the Netherlands at coordinates (52.924, 4.780).

The chapter is organized in two parts. Every part pertains to one research question. Linked to this chapter is an extensive appendix that develops and formalizes concepts that are used in this study but are not directly related to the research questions. The first part starts in Sections 4.2.1 and 4.2.2 by developing an erosion damage model based on the impingement metric. Subsequently, in Section 4.2.3, the drop-size effects contained in the model are identified, and their relevance is quantified for each effect individually. In Section 4.2.4, the drop-size effects are analyzed holistically and combined to find an answer to the first research question. Section 4.2.5 synthesizes the results in preparation for the second research question. The second part, presented in Section 4.3, establishes the influence of drop-size effects on the implementation and viability of the ESM. The conclusions of this chapter are presented in Section 4.4. Appendix A gives a formal derivation of the impingement damage metric. In Appendix B, the operational regime of the ESM is defined together with a method to derive optimal ESM strategies.

4.2. Drop-size-dependent effects

The methodology of this section consists of two main parts. First, this study's damage model is derived. It is used to calculate the lifetime of the the blade under various operating conditions. In the second part, the drop-size effects, that are contained within the damage model, are identified and discussed.

4.2.1. Derivation of the damage model

Damage rule and metric

The damage model is built on the linear Palmgren-Miner damage rule. The damage metric that is used is impingement H. It represents the water column that is caught

be the wind turbine's blade during operation. One obtains

$$D = T_{\text{rain}} \int_0^\infty \int_0^\infty \int_{0°}^{360°} \int_0^\infty \frac{\partial_t H_{I,V_{\text{wind}},\theta,\phi}}{H_{\text{allowed}}} d\phi d\theta dV_{\text{wind}} dI, \tag{4.1}$$

where D is the damage accumulated in one year of operation. H_{allowed} is the impingement that can be collected by the blade before damage can be observed on the blade's coating. $\partial_t H_{I,V_{\text{wind}},\theta,\phi}$ is the rate at which impingement is collected during operation. ∂_t is a shorthand notation for the operator $\partial/\partial t$. A detailed derivation of impingement is given in Appendix A.1. T_{rain} is the duration of rain during a year and is given by

$$T_{\text{rain}} = T_{\text{year}} p_{\text{rain}}, \tag{4.2}$$

where T_{year} is the time in a year and p_{rain} is the probability of rain at the wind turbine site. For De Kooy in the Netherlands $p_{\text{rain}} = 6.7\,\%$ (KNMI, 2020).

The equation integrates over four statistically distributed variables, the rain intensity I, the wind speed V_{wind}, the blade's rotational position θ and the rain droplet size ϕ. The equation assumes an elastic behavior of the leading-edge material. The lifetime in years is

$$L = \frac{1}{D}. \tag{4.3}$$

In this study the continuous integrals were discretized and integrated numerically using the trapezoidal rule. The discretization was performed carefully so that the results are grid-converged with respect to the significant digits.

Impingement until end of incubation
The impingement that can be collected by the blade until the end of the incubation period (allowed impingement) is modeled using a power law.

$$H_{\text{allowed}} = \frac{\alpha}{V_{\text{impact}}^\beta}, \tag{4.4}$$

where α and β are two coefficients and V_{impact} is the water droplet impact velocity with the blade. Here α is not an angle. Instead of determining these parameters from, e.g., a semi-empirical relation as used in the Springer model (Hoksbergen et al., 2022), we choose to determine the parameters directly from experimental data instead. Bech et al. (2022) performed tests of a commercial polyurethane-based leading-edge coating in a rotating-arm test-rig. The coating was subjected, in independent tests, to four different droplet sizes of 0.76, 1.90, 2.38 and 3.50 mm. The 0.76 mm droplets were created by spraying, leading to a variance in the diameter of the produced droplets. This is discussed in more detail in the original reference. The test-rig with its test specimen was stopped at regular intervals and new damage spots were recorded. Most damage was observed directly at the

leading edge. It was, therefore, assumed that Equation 4.4 gives the allowed impingement for droplets colliding head-on. The resulting measurements are shown as points in Figure 4.1. From these, two damage laws are derived.
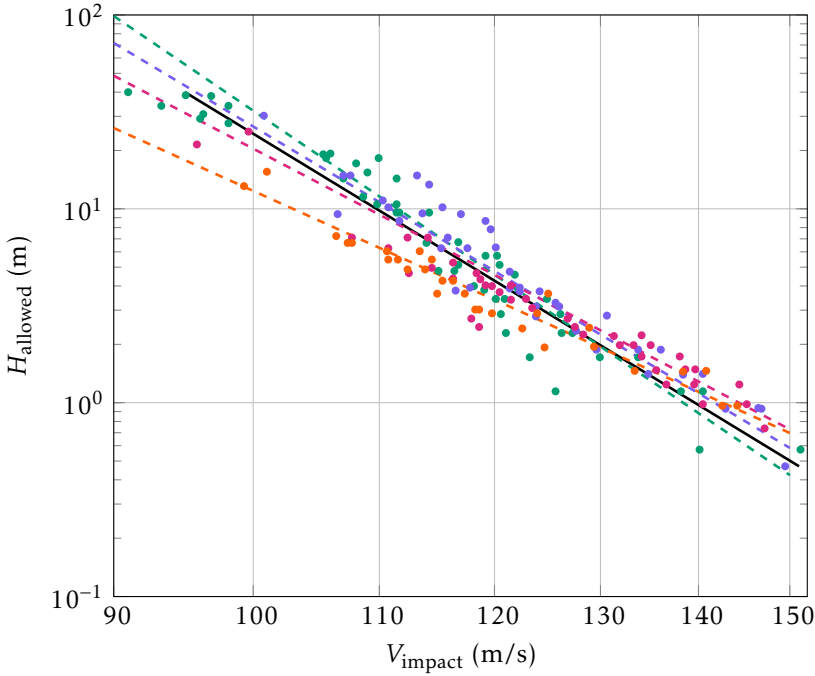
Figure 4.1: Erosion test-rig results by Bech et al. (2022) that relate impact velocity to impingement; droplet diameters are 0.76 mm: •, 1.90 mm: •, 2.38 mm: •, 3.50 mm: •; averaged law by Barfknecht and von Terzi (2023): ——; drop-size-dependent law for 0.76 mm: - - -, 1.90 mm: - - -, 2.38 mm: - - -, 3.50 mm: - - -; note that the figure is a log-log plot.

Averaged law The averaged law is obtained by fitting a curve through the measurements of Bech et al. (2022). It was first described in Barfknecht and von Terzi (2023). The resulting curve is shown in Figure 4.1. The averaged model serves as a baseline for comparing the drop-size-dependent law. The best-fit parameters are

$$\alpha = 3.4860 \times 10^{20}, \qquad \beta = 9.5774. \qquad (4.5)$$

Drop-size-dependent law The drop-size-dependent law is directly taken from Bech et al. (2022). It accounts for drop-size-dependent performance differences in the coating by utilizing a heuristic softsign function. It reads

$$H_{100} = \frac{a\Delta\phi}{1 + |\Delta\phi|} + b, \qquad (4.6)$$

with $\Delta\phi = \phi - \phi_0$, $\phi_0 = 2.3$ mm, $a = -17.1$ and $b = 21.7$. Further,

$$\beta = \frac{a\Delta\phi}{1 + |\Delta\phi|} + b, \tag{4.7}$$

with $a = -3.1$, $b = 8.9$ and $\phi_0 = 2.1$ mm. ϕ needs to be substituted in millimeters! α is given by

$$\alpha = 100^\beta H_{100}. \tag{4.8}$$

Like the averaged law, it is visualized in Figure 4.1.

It should be noted that the parameters of both laws depend on the considered leading-edge material. Therefore, other materials might behave differently, especially with respect to the drop size. The authors of this study consider the results from Bech et al. (2022) to be the best available erosion test-rig data set in the public domain and view them as a good representation of the current state-of-the-art.

Calculation of the accumulated impingement
The impingement rate is the last missing term in Equation 4.1 that needs to be defined. It is given by

$$\partial_t H_{I,V_{\text{wind}},\theta,\phi} = \underbrace{\frac{I f_{\phi,\text{plane}}}{V_\phi}}_{\text{(1)}} \underbrace{V_{\text{collection}}}_{\text{(2)}} f_I f_{V_{\text{wind}}} f_\theta, \tag{4.9}$$

where $V_{\text{collection}}$ is the speed at which rain is accumulated and V_ϕ is the droplet terminal fall velocity. Note that the dimension of $\partial_t H_{I,V_{\text{wind}},\theta,\phi}$ is $[\text{LT}^{-1}]$. The derivation and additional clarification of Equation 4.9 is provided in Appendix A.1. (1) represents the volume of water per volume of air, and (2) represents the swept line (volume) of air per unit time. It is dependent on four statistically distributed variables that will be discussed in the following.

The first distribution $f_{\phi,\text{plane}}$ should not be interpreted as a time fraction, but rather stems from the fact that, at every instant in time, a wide range of droplet sizes impact on the blade. In particular, it describes the amount of water associated with every droplet diameter that passes through an imaginary plane in the air. In this study $f_{\phi,\text{plane}}$ is derived using the Best drop-size distribution (Best, 1950a). Best gives a probability density function (pdf) that describes the water mass associated with every droplet diameter in a volume of air. It reads

$$f_{\phi,\text{air}} = 2.25 \left(\frac{1}{1.3 I^{0.232}} \right)^{2.25} \phi^{2.25-1} e^{-\left(\frac{\phi_0}{1.3 I^{0.232}} \right)^{2.25}}. \tag{4.10}$$

Best's distribution requires the rain intensity I to be given in millimeters per hour and the droplet diameter ϕ must be substituted in millimeters. To convert the distribution into $f_{\phi,\text{plane}}$, the following equation is used

$$f_{\phi,\text{plane}} = \frac{f_{\phi,\text{air}} V_\phi}{\int_0^\infty f_{\phi,\text{air}} V_\phi d\phi}. \tag{4.11}$$

To find the rain intensity distribution f_I, the hourly precipitation data of the automatic KNMI rain gauge station at De Kooy are used. The data from the 10-year window ranging from 2011 to 2020 were used to find the coefficients of f_I in the form of a lognormal distribution. The formula for the lognormal distribution reads

$$f_I = \frac{1}{I\sigma\sqrt{2\pi}} e^{-\frac{(\ln I - \mu)^2}{2\sigma^2}}. \tag{4.12}$$

The coefficients were found using Matlab's *lognfit* function. μ is the mean and σ is the standard deviation. They read $\sigma = 0.9693$ and $\mu = -0.1987$ or $\mu = -15.29$, depending on whether I is considered to be in millimeters per hour or in meters per second.

The distribution of the wind was calculated using a Weibull distribution. It reads

$$f_{\text{wind}} = \frac{k}{c}\left(\frac{V_{\text{wind}}}{c}\right)^{k-1} e^{-(V_{\text{wind}}/c)^k}, \tag{4.13}$$

where c is the scale parameter and k is the shape parameter. Both parameters were obtained for the De Kooy location using the Dutch Offshore Wind Atlas at the height of 150 m (DOWA, 2020). They read $c = 10.5$ m/s and $k = 2.24$. The mean wind speed is $V_{\text{mean}} = 9.2$ m/s.

Note that it is assumed that the wind speed and the rain intensity are *not* statistically correlated. In general, this assumption is not true as, e.g., shown in Letson et al. (2020). In the 2011 to 2020 time frame, the De Kooy mean wind speed at 10 m height above ground during rain was 6.80 m/s, whereas during dry conditions, the mean wind speed was 5.32 m/s (KNMI, 2020). However, for the purpose of this study, this assumption is deemed to be acceptable. Results, for De Kooy, that use actual wind and precipitation measurements as input for the ESM are presented in Barfknecht and von Terzi (2024).

The probability density function of the blade position f_θ is given by the equation

$$f_\theta = \frac{1}{360°}. \tag{4.14}$$

During operation, the turbine spins continuously, hence every blade position is equally likely to occur. It is also assumed that during a standstill, the parking position is random.

Calculation of the drop impact velocity

The key driver for the erosion damage is the impact velocity V_{impact} of the rain droplets. It is used in Equation 4.4, where it has a significant effect on the lifetime due to the size of the parameter β. Small variations in the calculated impact velocity will yield very different H_{allowed}. Secondly, the closely related sibling $V_{\text{collection}}$ is used in Equation 4.9 for the calculation of the impingement rate $\partial_t H_{I,V_{\text{wind}},\theta,\phi}$.
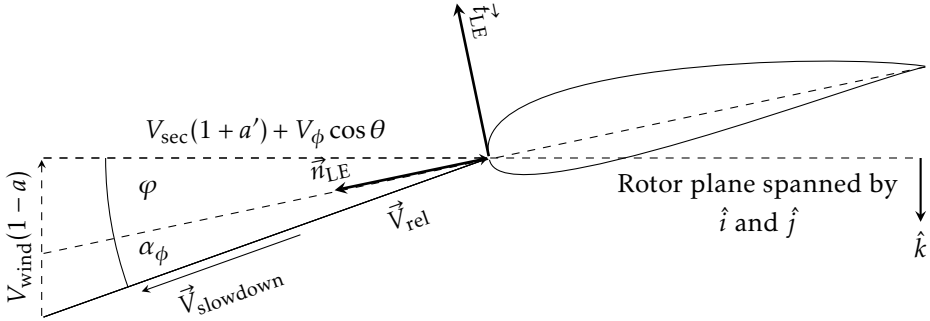
(a) Rain droplet velocity components as seen by a blade section.
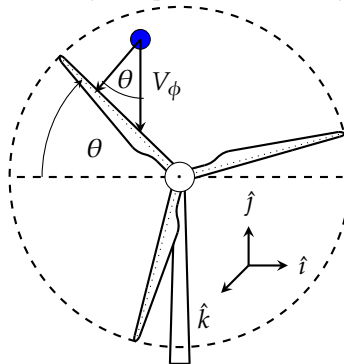
(b) Definition of the angular blade position θ and its influence on the surface normal component of the terminal droplet velocity V_ϕ.

Figure 4.2: Velocity components and angle definitions that constitute V_{impact}.

The following assumptions are made for the derivation of the impact velocity:

- Rain droplets are advected with the local wind vector, which is comprised of the wind speed and the wind turbine's induction factors.

- There are no wind veer, shear, turbulence and gust effects.

- The rotor plane is two-dimensional, i.e., there is no pre-cone and blade bending.

- The blade is rigid.
- The leading edge from root to tip lies in a straight line.
- The droplet slowdown as described in Barfknecht and von Terzi (2023) can be modeled as a one-dimensional problem and the droplets follow a ballistic path. Other assumptions regarding the slowdown effect made in the same reference also apply.

The impact velocity is defined as

$$V_{\text{impact}} = (\vec{V}_{\text{sec}} - \vec{V}_{\text{rain}}) \cdot \vec{n}_{\text{LE}}, \tag{4.15}$$

where $\vec{V}_{\text{sec}}$ is the velocity vector of the blade section. $\vec{V}_{\text{rain}}$ is the velocity vector of the rain (droplets). $\vec{n}_{\text{LE}}$ is the surface normal vector of the leading edge. Figure 4.2 visualizes all velocity components that are considered in this study.

Using the the velocity diagrams of Figure 4.2, one obtains

$$\vec{V}_{\text{sec}} = \begin{bmatrix} \sin\theta V_{\text{sec}} \\ \cos\theta V_{\text{sec}} \\ 0 \end{bmatrix}, \tag{4.16}$$

and

$$\vec{V}_{\text{rain}} = \begin{bmatrix} -\sin\theta V_{\text{sec}} a' \\ -\cos\theta V_{\text{sec}} a' - V_\phi \\ -V_{\text{wind}}(1-a) \end{bmatrix} - \vec{V}_{\text{slowdown}}, \tag{4.17}$$

with

$$\vec{V}_{\text{slowdown}} = V_{\text{slowdown}} \frac{-\vec{V}_{\text{rel}}}{|\vec{V}_{\text{rel}}|}. \tag{4.18}$$

Inserting into Equation 4.15 yields

$$V_{\text{impact}} = \begin{bmatrix} \sin\theta V_{\text{sec}}(1+a') \\ \cos\theta V_{\text{sec}}(1+a') + V_\phi \\ V_{\text{wind}}(1-a) \end{bmatrix} \cdot \underbrace{\begin{bmatrix} \sin\theta\cos\varphi \\ \cos\theta\cos\varphi \\ \sin\varphi \end{bmatrix}}_{\vec{n}_{\text{LE}}} + V_{\text{slowdown}} \frac{-\vec{V}_{\text{rel}}}{|\vec{V}_{\text{rel}}|} \cdot \begin{bmatrix} \sin\theta\cos\varphi \\ \cos\theta\cos\varphi \\ \sin\varphi \end{bmatrix}$$
$$\tag{4.19}$$

$$= V_{\text{sec}}(1+a')\cos\varphi + V_\phi\cos\theta\cos\varphi + V_{\text{wind}}(1-a)\sin\varphi - V_{\text{slowdown}}\cos\alpha_\phi. \tag{4.20}$$

According to Figure 4.2a, $\vec{V}_{\text{rel}}$ is the relative droplet velocity in the plane of the considered airfoil cross-section. In Appendix A.2 it is shown that

$$V_{\text{collection}} = V_{\text{sec}}(1+a')\cos\varphi + V_\phi\cos\theta\cos\varphi + V_{\text{wind}}(1-a)\sin\varphi, \tag{4.21}$$

hence, the collection velocity is the impact velocity but without the slowdown.

The first two terms in Equation 4.20 represent the surface normal component of the circumferential velocity. That is

$$V_{\text{circumferential}} = V_{\text{sec}}(1 + a') + V_\phi \cos\theta, \tag{4.22}$$

with V_{sec} being the speed of the blade section. At the tip, $V_{\text{sec}} = V_{\text{tip}}$. a' is the radial (tangential) induction factor. In contrast to common inflow velocity diagrams for wind turbines, an extra term reading $V_\phi \cos\theta$ can be found in Equation 4.22. This term represents the velocity component due to the terminal velocity of the rain droplet V_ϕ, as shown in Figure 4.2b. It is calculated with the relation from Best (1950b) and reads

$$V_\phi = 9.32 e^{0.0405h} \left(1 - e^{-(0.565\phi)^{1.147}}\right). \tag{4.23}$$

It is shown in Figure 4.3. h is the height above ground in kilometers and ϕ the droplet diameter in millimeters! The height is

$$h = h_{\text{hub}} + r\cos\theta, \tag{4.24}$$

where h_{hub} is the turbine's hub height and r is the position along the blade span. At the tip, r becomes the blade length R_{blade}, that is $r = R_{\text{blade}}$.
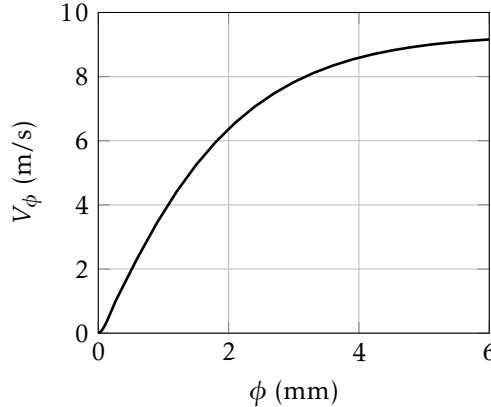
Figure 4.3: Terminal velocity for falling water droplets as a function of the droplet diameter; values for $h = 0$ km, i.e., sea level.

The third term of Equation 4.20 represents the surface normal component of the inflow velocity. It reads

$$V_{\text{inflow}} = V_{\text{wind}}(1 - a), \tag{4.25}$$

where V_{wind} is the wind velocity and a is the axial induction factor. With the

abovementioned assumptions in mind, V_{wind} is constant throughout the entire rotor plane and the droplets will be advected perfectly with this velocity.

The last term is the so-called slowdown velocity as described in Barfknecht and von Terzi (2023). The velocity field of the airfoil interacts aerodynamically with the rain droplets and, when seen from the airfoil, slows them down, thus making them significantly less erosive. The slowdown results from the velocity differential between the velocity field of the blade and the rain droplet. This creates a drag force, leading to a reduction in velocity. Approaching droplets undergo deformation and can break up as shown in Figure 4.4. The deformation and breakup heavily influence the impact speed of the droplets.
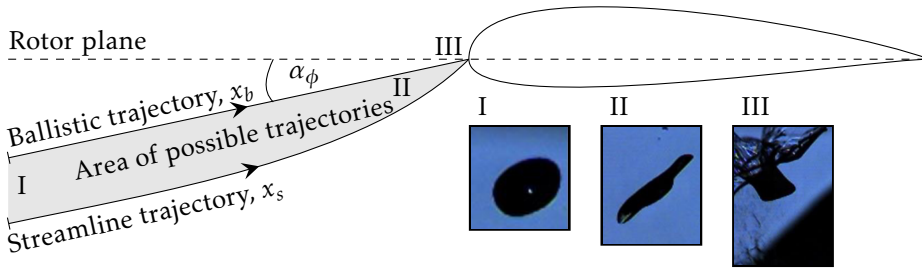
Figure 4.4: Ballistic and streamline trajectory of a droplet approaching an airfoil (at an angle α_ϕ); φ is set to zero in this illustration; far away from the blade, at station (I), droplets have a shape resembling a spheroid; as the droplets approach the leading edge, they deform (II) and eventually break up into specific breakup patterns (III); the high-speed images are reproduced from Sor et al. (2019); the illustration itself is taken from Barfknecht and von Terzi (2023).

Droplets that impact with the leading edge can either travel on a ballistic (in the direction of $\vec{V}_{\text{rel}}$) or a streamline trajectory. The latter assumes that the rain droplets follow the flow perfectly, something that should be true for $\phi \to 0$ mm. Droplets with diameters of $\phi \to \infty$ mm should follow a ballistic trajectory. This study assumes that the droplets follow a ballistic trajectory. In Barfknecht and von Terzi (2023), it was shown that droplets that follow a streamline trajectory experience more slowdown. Hence, assuming a ballistic trajectory underpredicts the slowdown of small droplets. As will be shown in the remainder, this is a conservative assumption regarding the conclusions of this work.

The slowdown velocity V_{slowdown} is obtained by using the methodology from Barfknecht and von Terzi (2023) where an existing Lagrangian model was extended to accurately predict the velocity of droplets in the vicinity of the leading edge of

a wind turbine blade. Two equations of motion are solved that describe the one-dimensional approach of the rain droplets toward the blade:

$$m\frac{d^2x}{dt^2} = F_{\text{drag}},$$ (4.26)

$$\frac{3}{16}m\frac{d^2a}{dt^2} = F_\sigma + F_p,$$ (4.27)

where Equation 4.26 represents the deceleration of the droplet and Equation 4.27 describes the droplet's deformation from a spheroid to an oblate spheroid. The method cannot predict the actual (broken up) droplet shape. However, the results in Barfknecht and von Terzi (2023) showed that approximating the droplet as an oblate spheroid is sufficient to accurately determine the slowdown.

The forces that are acting on the droplet are the drag force F_{drag}, the surface tension F_σ and the pressure force F_p. F_p drives deformation, while F_σ counteracts droplet deformation. Here, a is the semi-major axis of the oblate spheroid. m is the droplet mass and x is the droplet position along its path.

The slowdown velocity is then calculated as

$$V_{\text{slowdown}} = \left(\frac{dx}{dt}\right)_{\text{at impact}}.$$ (4.28)

The background velocity V_{air} field is calculated with:

$$\frac{V_{\text{air}}}{|\vec{V}_{\text{rel}}|} = 1 - \frac{1}{\left(1 - \frac{\Delta x}{R_c}\right)^n},$$ (4.29)

where Δx is the distance between the droplet and blade. At $r/R_{\text{blade}} = 0.9$ the IEA 15MW turbine has an aerodynamic nose-radius $R_c = 0.064$ m and an exponent $n = 1.097$ (Barfknecht and von Terzi, 2023). The reader is referred to Barfknecht and von Terzi (2023) for a detailed description of the slowdown model and how to implement it.

The angle φ is

$$\varphi = \varphi_{\text{pitch}} - \varphi_{\text{twist}},$$ (4.30)

where φ_{pitch} is the pitch angle of the blade. The determination of the pitch angle and also the induction factors is described in further detail in Appendix 4.2.2. φ_{twist} is the local twist angle. At $r/R_{\text{blade}} = 0.9$, $\varphi_{\text{twist}} = -2.1°$. Subsequently, $\cos\alpha_\phi$ can be calculated using

$$\cos\alpha_\phi = \frac{\vec{V}_{\text{rel}}}{|\vec{V}_{\text{rel}}|} \cdot \vec{n}_{\text{LE}} = \cos\left(\arctan\left(\frac{V_{\text{inflow}}}{V_{\text{circumferential}}}\right) - \varphi\right).$$ (4.31)

It is important to note here that α_ϕ, while similar, is not the angle of attack of the blade element, but should rather be considered as the drop impact angle. It should also be mentioned that, depending on the application, it might be more convenient to write V_{impact} in its alternative form, that is

$$V_{\text{impact}} = \cos \alpha_\phi \left(\sqrt{V_{\text{inflow}}^2 + V_{\text{circumferential}}^2} - V_{\text{slowdown}} \right), \qquad (4.32)$$

and concurrently

$$V_{\text{collection}} = \cos \alpha_\phi \sqrt{V_{\text{inflow}}^2 + V_{\text{circumferential}}^2} \,. \qquad (4.33)$$

In this study the impact velocity was determined for the leading edge of the blade. It can also be determined for other locations by adjusting the surface normal vector. This can be desirable since, in practice, the point with the highest erosion can lie slightly off the leading edge in the direction of the stagnation point.

On a final note, the careful reader might argue that some droplets get deflected and do not hit the blade and that this aspect is missing. However, in practice, droplets only miss the blade when they tend to follow a streamline trajectory and when that streamline is located toward the top or bottom of the airfoil, see the results of Sor et al. (2021).

Closely related is the concept of collection efficiency, as known from aircraft icing. For a streamtube, it is the ratio of surface to free-stream water flux as shown in Gent et al. (2000). Two effects influence this ratio. Firstly, the streamtube can widen toward the airfoil. In the region of the leading edge, the widening merely distributes the rain droplets onto a larger blade area, reducing the surface water flux. Sor et al. (2021) showed that at the leading edge, this reduction is in the order of 10 % for the relevant droplet sizes. The effect becomes more pronounced as droplets become smaller. When moving far away from the leading edge, the widening can, indeed, become so large that some droplets start to miss the blade. Secondly, the collection efficiency is comprised of the reduction in surface water flux due to a non-orthogonal impact with the airfoil's leading edge. This aspect is modeled in this study since $(\vec{V}_{\text{sec}} - \vec{V}_{\text{rain}})$ is projected onto $\vec{n}_{\text{LE}}$.

It is important to realize that neglecting the streamtube widening is a conservative assumption regarding the conclusions of this study. The assumptions lead to a higher surface water flux and impingement for smaller droplets. Hence, smaller droplets appear to be more erosive than they actually are. This effect could be included in future works. It, however, at least necessitates Lagrangian particle simulations in a two-dimensional domain, which is computationally costly.

4.2.2. Calculation of the AEP and pitch angle

The method to compute the turbine's power is important for the ESM and, as will be shown, also the damage calculation. At the core of the formula for the power P is

$$P = Q\omega, \tag{4.34}$$

where Q and ω are the rotors' torque and rotational speed, respectively. There exists a maximum generator torque Q_{max} that cannot be exceeded. Therefore, at all times, the following condition must hold:

$$Q \leq Q_{max}. \tag{4.35}$$

For maximum power, Q should be maximized at all times without exceeding Q_{max}. The torque coefficient is found with the following formula:

$$C_Q(\lambda) = \begin{cases} M(\lambda) & \text{if } M(\lambda) < \left(C_{Q_{max}} = \frac{Q_{max}}{qAR} \right), \\ \left(C_Q(\lambda, \varphi_{pitch}) = C_{Q_{max}} \right) & \text{if } M(\lambda) \geq C_{Q_{max}}, \end{cases} \tag{4.36}$$

where $M(\lambda) = \max(C_Q(\lambda, \varphi_{pitch}))$ and λ is the tip-speed ratio. q is the dynamic pressure of the wind, A is the rotor disk area and R is the rotor radius. φ_{pitch} is found by either determining where C_Q is maximum or by determining where $C_Q = C_{Q_{max}}$. The resulting pitch is used in the calculation of the damage, see Equations 4.20 and 4.30. From the tip-speed ratio, the pitch angle, and the position along the blade, the corresponding local induction factors can be found. This study assumes that the wind shear exponent is zero. Hence, the V_{wind} is constant over the rotor disk. If the wind shear exponent is included, it leads to local changes in the tip-speed ratio and will make the local induction factors a function of the blade angular position.

CCBlade, in conjunction with IEA 15MW's yaml ontology file, was used to find the torque coefficient as a function of the tip-speed ratio and the blade pitch angle Ning (2014). The induction factors are also given in the output of CCBlade. The torque coefficient and pitch angle are plotted in Figure 4.5. The torque coefficient is decreased when the turbine enters the rated power region. This is done by adjusting the pitch angle so that the maximum generator torque is not exceeded. The figure shows that pitch angles of over 30° are encountered. Angles of this magnitude impact the damage significantly, see Equations 4.30, 4.31 and 4.42. Therefore, the pitch angle needs to be properly accounted for.

The resulting AEP can be calculated using

$$\text{AEP} = T_{year} \int_0^\infty \int_0^\infty P f_I f_{wind} dV_{wind} dI. \tag{4.37}$$

For normal turbine control, or an ESM that is solely controlled based on the wind speed, the integral (and corresponding probability density function) over the rain intensity can be omitted.

(a) Torque coefficient, C_Q (-)

(b) Pitch angle, φ_{pitch} (°)
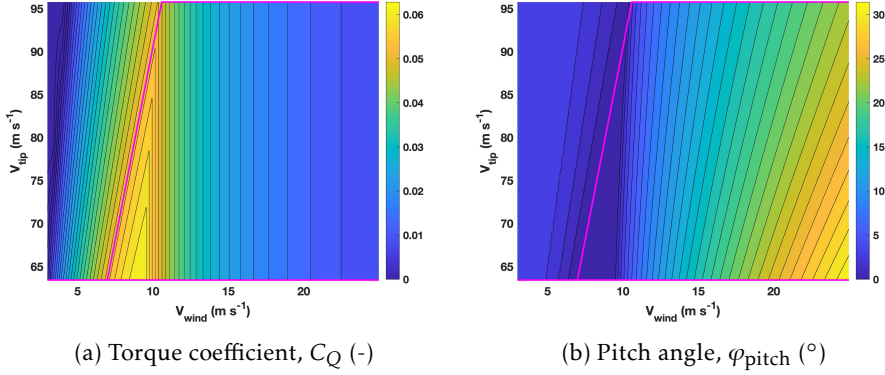
Figure 4.5: Contour plots of the torque coefficient and pitch angle as a function of wind speed and tip-speed; the magenta curves enclose the operational regime of the turbine; IEA 15MW turbine.

4.2.3. Discussion of the drop-size effects in the damage model

This section investigates which deductions can be made from the equations within the previously derived damage model. Different drop-size-dependent effects are derived from the model and discussed. In particular, it is shown that, due to the drop-size-dependent effects, the damage model suggests that:

1. Large droplets are more damaging than small droplets.

2. Large droplets become more frequent as the rain intensity increases.

3. As a consequence of the above, for equal amounts of impingement, higher rain intensities are more damaging than lower intensities.

At the core of these deductions is that V_{impact} and $V_{\text{collection}}$ are the key drivers for erosion. The damage components of Equation 4.1 are

$$\partial_t D_{I,V_{\text{wind}},\theta,\phi} = \frac{\partial_t H_{I,V_{\text{wind}},\theta,\phi}}{H_{\text{allowed}}}. \tag{4.38}$$

Here it is important to realize that V_{impact} is contained in the denominator and $V_{\text{collection}}$ in the numerator, see Equations 4.4 and 4.9! Substituting leads to

$$\partial_t D_{I,V_{\text{wind}},\theta,\phi} \propto V_{\text{impact}}^{\beta} V_{\text{collection}} \approx V_{\text{impact}}^{\beta+1}. \tag{4.39}$$

This equation shows that a faster droplet is much more damaging than a slower droplet. First, a high $V_{\text{collection}}$ leads to a higher rate of impingement accumulation. This effect is linear under the assumptions of this study. Secondly, a high V_{impact} leads to significantly less H_{allowed} due to the large magnitude β, which can be in the order of ten. This effect is very severe and highly non-linear.

Influence of the rotation and terminal velocity on the impact velocity
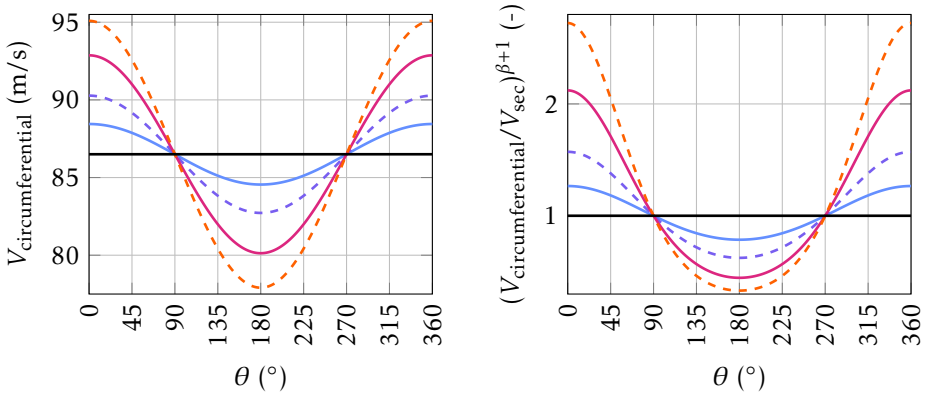
(a) Circumferential velocity

(b) Non-dimensional damage
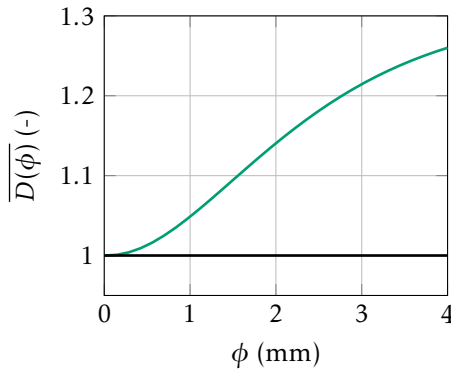
(c) Average damage over one blade rotation

Figure 4.6: Circumferential velocity and non-dimensional damage as a function of angular blade position for different droplet diameters; the induction factors were neglected; $\beta = 9.58$; $V_{\text{sec}} = 86.5$ m/s; without terminal velocity: ——; droplets of 0.5 mm: ——, 1.0 mm: - - -, 2.0 mm: ——, 4.0 mm: - - -; averaged damage over one rotation with terminal velocity included: ——.

The terminal velocity of rain droplets causes an oscillation in impact speed over one blade rotation. In Equation 4.22, the surface normal component of the droplet

terminal velocity is not constant over one blade rotation but is a function of $\cos\theta$. The influence of θ on $V_{\text{circumferential}}$ is shown in Figure 4.6a. $V_{\text{circumferential}}$ is maximum at $\theta = 0°$, i.e., when the blade-section speed and the droplet's terminal velocity directly oppose each other. Correspondingly, $V_{\text{circumferential}}$ is minimum at $\theta = 180°$. Since the droplet terminal velocity is a function of the droplet diameter, as shown in Figure 4.3, this effect becomes more pronounced as the droplet diameter increases. It is noteworthy that the circumferential velocity averaged over one rotation is constant. However, due to the highly non-linear character of Equation 4.39, some impacts at a lower and some impacts at a higher impact speed will, in total, yield a higher damage. Figure 4.6b plots the non-dimensional damage $(V_{\text{circumferential}}/V_{\text{sec}})^{\beta+1}$ over one blade rotation. Here it is assumed that there are no induction factors, $V_{\text{slowdown}} = 0$ and $V_{\text{wind}} = 0$. At $\theta = 90°$ and $\theta = 270°$ the surface normal component of the terminal velocity is zero. Hence, the normalized damage is unity since $V_{\text{circumferential}} = V_{\text{sec}}$. The maximum damage is found at $\theta = 0°$ and the minimum at $\theta = 180°$, coinciding with the locations of maximum and minimum $V_{\text{circumferential}}$. The non-dimensional average damage over one rotation as a function of droplet diameter is shown in Figure 4.6c. It reads

$$\overline{D(\phi)} = \int_0^{360} f_\theta \left(\frac{V_{\text{circumferential}}}{V_{\text{sec}}} \right)^{\beta+1} d\theta. \tag{4.40}$$

The damage is 1.013 for a droplet of 0.5 mm and 1.260 for a droplet of 4.0 mm, so the 4 mm droplet creates about 24.4 % more damage. This shows that the effect is significant and needs to be accounted for.

INFLUENCE OF THE ROTATION AND TERMINAL VELOCITY ON THE IMPACT ANGLE

The drop impact angle α_ϕ varies with the blade position because it depends on $V_{\text{circumferential}}$, see Equation 4.31. During the upstroke of the blade, the term $V_\phi \cos\theta$ is positive and decreases the angle α_ϕ. During the downstroke, the sign becomes negative and α_ϕ increases. The variation in α_ϕ becomes stronger as the droplet diameter increases. α_ϕ is shown in Figure 4.7a. It can be decomposed into

$$\alpha_\phi = \alpha + \alpha(\theta)'. \tag{4.41}$$

The impact angle is, therefore, a combination of the classical angle of attack of the blade and an oscillating component that is dependent on the angular blade position θ.

Equations 4.32 and 4.39 imply that

$$\partial_t D_{I,V_{\text{wind}},\theta,\phi} \propto \cos(\alpha_\phi)^{\beta+1}. \tag{4.42}$$

This equation is shown in its non-dimensional form in Figure 4.7b. As before, the damage oscillates once over one single rotation. On first glance, Figure 4.7b ap-

pears to be similar to Figure 4.6b. During the upstroke, the damage production is increased, whereas during the downstroke of the blade, the damage is reduced. However, the magnitude of the effect is very small, with the amplitude being only about 1.5 % for a droplet of 4 mm diameter. Calculating, similar to Equation 4.40, the averaged non-dimensional damage over one rotation yields Figure 4.7c. The damage is approximately unity for a droplet of 0.5 mm and about 0.999 for a droplet of 4.0 mm. Hence, a slight reduction in the damage can be observed due to α' being asymmetrical with the blade position, i.e., for a droplet of 4 mm diameter $\alpha(0°)' = -0.54°$ and $\alpha(180°)' = 0.66°$. However, considering that the averaged damage is near unity for all droplet diameters, one can conclude that this effect is not significant and can be neglected.
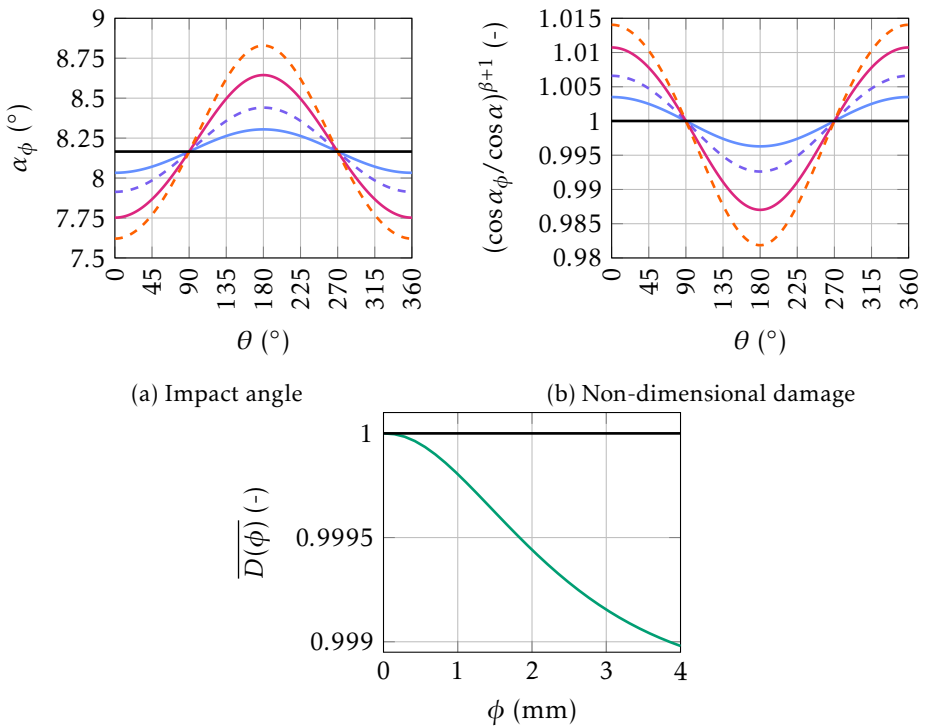
(a) Impact angle

(b) Non-dimensional damage

(c) Average damage over one blade rotation

Figure 4.7: Impact angle and non-dimensional damage as a function of angular blade position for different droplet diameters; the induction factors were neglected; $\beta = 9.58$, $V_{sec} = 86.5$ m/s, $V_{wind} = 9.2$ m/s, $\varphi_{twist,r/R_{blade}=0.9} = -2.10°$, $\varphi_{pitch,9.2 \text{ m/s}} = 0°$; without terminal velocity: ——; droplets of 0.5 mm: - - -, 1.0 mm: ——, 2.0 mm: - - -, 4.0 mm: ——; averaged damage over one rotation with terminal velocity included: ——.

Drop-size-dependent damage law

The drop-size-dependent damage law of Bech et al. (2022) suggests that the performance of a wind turbine coating is dependent on the droplet diameter. The law is given by Equations 4.6, 4.7 and 4.8 and is plotted for four different droplet diameters in Figure 4.1. The spread in the curves for small and large droplets closes with increasing impact speed. At about 116 m/s, a crossover point exists. At that point, droplets of 0.76 and 1.90 mm have the same H_{allowed}. Beyond that point, smaller droplets become more damaging than larger droplets. As the impact speed increases, the spread starts to grow again. For diameters above approximately 2 mm the crossover point is delayed to higher speeds, where the exact location is dependent on the particular diameter.
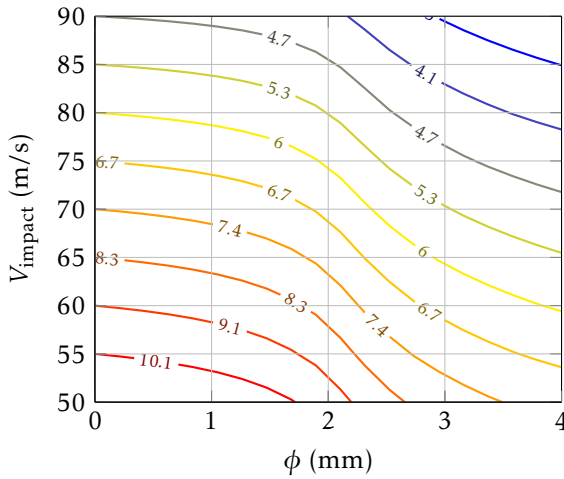
Figure 4.8: Contour lines of $\ln(H_{\text{allowed}})$ according to Equations 4.6, 4.7 and 4.8 for different droplet diameters and impact velocities; contour levels are spawned at $\phi \to 0$ mm, for impact velocities in 5 m/s increments.

The drop-size dependency is shown in more detail in Figure 4.8. The figure shows the natural logarithm of H_{allowed} for a combination of relevant droplet sizes and impact speeds. The shape of the softsign function is clearly visible within the contour plot. The allowed impingement drops sharply above diameters of about 1 mm and continues with a steep decline up to 3 mm, where it then starts to slowly become shallower again. The drop-size effect is significant which can be seen by following a contour. A small droplet $\phi \to 0$ mm has the same allowed impingement at 85 m/s as a 4 mm droplet at about 65.6 m/s. When considering a constant impact speed of 85 m/s, a droplet $\phi \to 0$ mm has an allowed impingement of 201 m, while a 4 mm droplet will already lead to failure after 34 m impingement.

α and β govern the drop-size dependency. As the droplet diameter decreases, α increases, leading to a longer lifetime for small droplets at low impact speeds. Further, as the droplet diameter decreases, β increases, resulting in smaller droplets having a higher sensitivity (slope) with respect to the impact velocity. Consequently, H_{allowed} for small droplets starts high but decreases rapidly with increasing impact speeds. In contrast, for large droplets, H_{allowed} is initially lower but decreases more gradually. These differing behaviors cause the curves for small and large droplets to intersect. The first crossover point occurs at approximately 116 m/s, which is above the typical impact speeds encountered in current wind turbine applications. Therefore, under these conditions, the damage law suggests that small droplets cause less damage than larger ones.

Droplet slowdown

Rain droplets slow down when approaching the leading edge of an airfoil, as shown in Figure 4.9a. It can be seen that the slowdown for droplets of 0.49 mm diameter approaching at 90 m/s is about 10 m/s. The figure also shows that most of the slowdown is taking place close to the leading edge. In this particular case, most of the slowdown is happening at a distance of less than 5 cm to the leading edge. The slowdown is influenced by $|V_{\text{rel}}|$ and the droplet size. As $|V_{\text{rel}}|$ increases, so does the slowdown velocity. This is shown in Figure 4.9a. Figure 4.9b shows that smaller droplets encounter significantly more slowdown than larger ones.
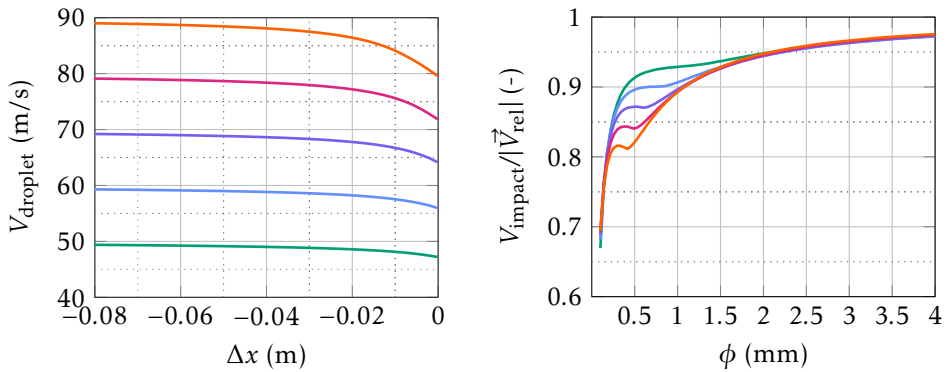
(a) Relative velocity of 0.49 mm diameter droplets versus distance to the leading edge Δx.

(b) Non-dimensional impact velocity as a function of droplet diameter.

Figure 4.9: Relative velocity before impact and non-dimensional impact velocity for droplets approaching the leading edge of an airfoil; plot is reproduced from Barfknecht and von Terzi (2023); $|\vec{V}_{\text{rel}}|$ of 50 m/s: ——, 60 m/s: ——, 70 m/s: ——, 80 m/s: ——, 90 m/s: ——.
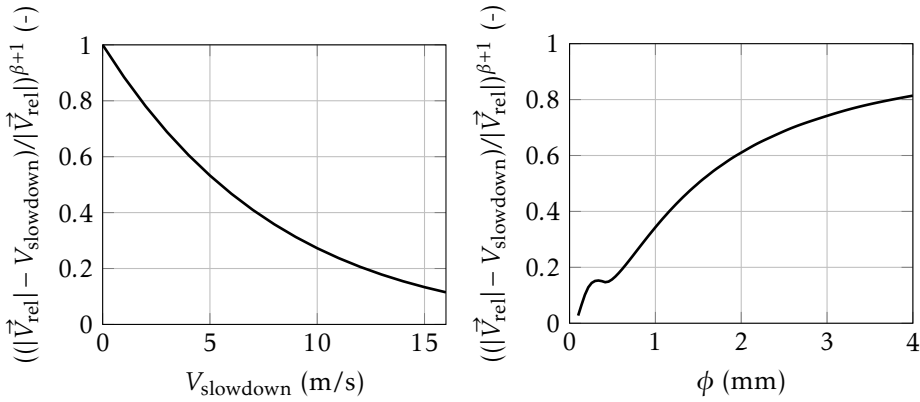
Figure 4.10: Non-dimensional damage due to the slowdown effect versus slow-down velocity and droplet diameter; $\beta = 9.58$, $|\vec{V}_{\text{rel}}| = 86.5$ m/s, $R_c = 0.064$ m and $n = 1.097$.

The damage reduction due to the slowdown effect is visualized in Figure 4.10. Due to the high sensitivity of the damage law, a moderate slowdown of 5.5 m/s reduces the erosion damage already by half. The figure also shows the damage reduction that is associated with different droplet diameters. The slowdown effect suggests a damage reduction of about 20 % for droplets of 4 mm. For droplets of 0.5 mm a damage reduction of 84 % is predicted. Hence, the slowdown is highly drop-size-dependent and overall leads to a significant reduction in the absolute erosion damage.

4.2.4. Composition of the total erosion damage

With the described damage model and the identified drop-size effects, the total erosion damage can be calculated for the considered sample site and turbine. Sub-sequently, it can be decomposed into its components to quantify the influence of the drop-size effects. The damage is decomposed with respect to the droplet diameter, the angular position of the blade, the wind speed and the rain intensity. Equation 4.1 can be modified into

$$D(\phi) = T_{\text{rain}} \int_0^\infty \int_0^\infty \int_0^{360} \partial_t D_{I,V_{\text{wind}},\theta,\phi} d\theta \, dV_{\text{wind}} \, dI. \tag{4.43}$$

Then $D(\phi)$ is normalized into $f_D(\phi)$ so that

$$\int_0^\infty f_D(\phi) d\phi = 1. \tag{4.44}$$

Similarly, $f_D(I)$, $f_D(\theta)$ and $f_D(V_{\text{wind}})$ can be found. By normalizing D, influences of drop-size effects on the absolute lifetime are excluded. This makes the comparison of drop-size effects easier. $f_D(\phi)$ represents a probability density function. Consequently, $F_D(\phi) = \int_0^\phi f_D(\phi')d\phi'$ represents the cumulative distribution function (cdf). The decomposition of the damage in its pdf and cdf is shown for all four independent variables in Figure 4.11.

(a) Rain droplet diameter

(b) Rain intensity

(c) Angular position of the blade

(d) Wind speed
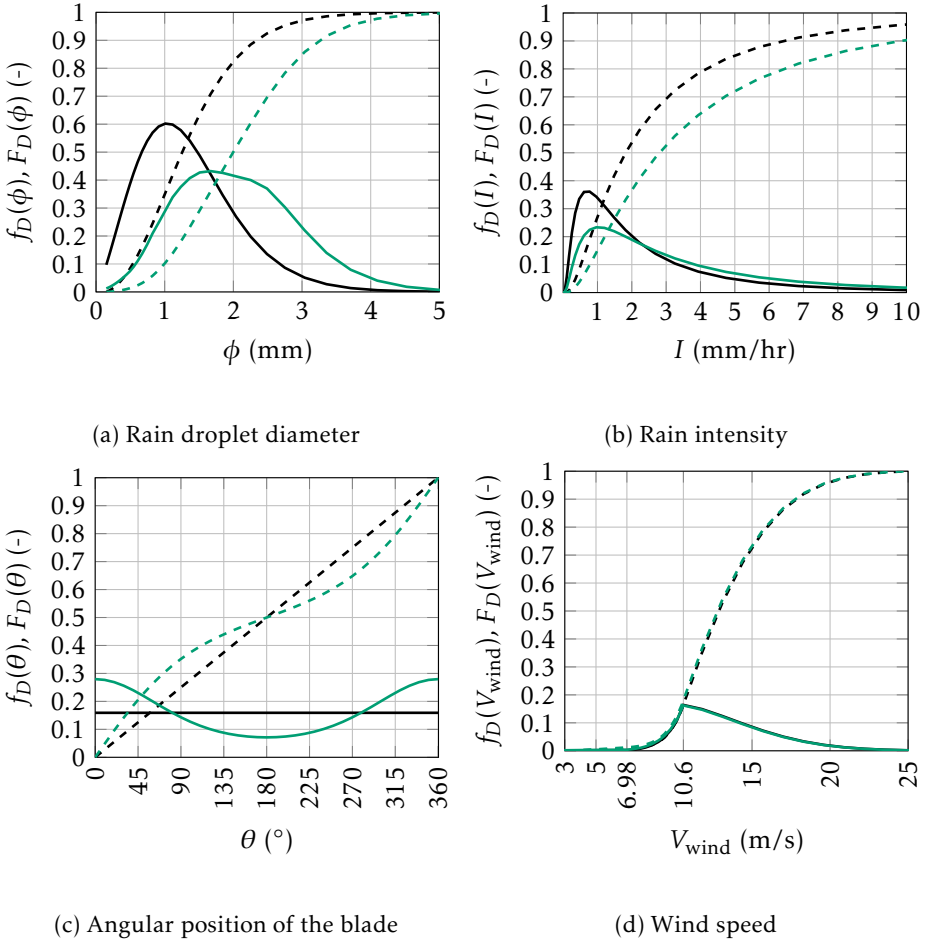
Figure 4.11: Composition of the normalized erosion damage with respect to the four independent variables; IEA 15MW turbine located at De Kooy; without drop-size effects: pdf: ——, cdf: - - -; with drop-size effects: pdf: ——, cdf: - - -.

Figure 4.11a shows the decomposition with respect to the droplet diameter. It is important to note here, that the figure shows the damage that is associated with the total water volume comprised by all droplets of a particular diameter. It does

not show the damage for a single droplet! The figure shows that when drop-size effects are excluded, droplets of around 1 mm contribute the most toward erosion damage. Half of the total erosion damage is created by droplets of 1.26 mm and below. 97.0 % of the entire damage is created by droplets up to a size of 3 mm. The inclusion of drop-size effects causes a shift toward larger droplet diameters. The droplet diameter contributing the most toward erosion damage becomes then 1.67 mm. The probability density function with drop-size effects has a plateau region. Therefore, a wider range of droplets becomes important for erosion. Half of the erosion damage is created by droplets of 2.00 mm and below. Droplets up to 3 mm diameter create 84.8 % of the erosion damage. Hence, droplets over 3 mm diameter become significant for erosion when drop-size effects are properly accounted for.

Figure 4.11b shows how the drop-size effects influence the decomposition of the erosion damage with respect to the rain intensity. Similar to Figure 4.11a, the inclusion of the drop-size effects shifts damage production to higher rain intensities. Without drop-size effects, 50 % of the total damage is produced by rain intensities of 1.82 mm/hr and below. With the inclusion of the drop size, this value changes to 2.81 mm/hr. The probability density functions show that the damage contribution is reduced for precipitation events of approximately 2.2 mm/hr and below, whereas above this value, the damage contribution is increased.

The decomposition of the damage with respect to the blade's angular position is shown in Figure 4.11c. Without any drop-size effects, the damage production is constant for all blade positions, and hence, the damage accumulates linearly toward unity. When drop-size effects are included, one can see that, during the upstroke ($-90° < \theta < 90°$, see Figure 4.2b), damage production is higher than during the downstroke ($90° < \theta < 270°$). The difference is significant. At $\theta = 0°$, the damage is about three times higher than at $\theta = 180°$. Therefore, most erosion damage is created during the upstroke of the blade.

As shown in Figure 4.11d, drop-size effects have a negligible influence on the decomposition with respect to the wind speed. With drop-size effects, the variable load region contributes slightly more toward the erosion damage.

Previously, in Figure 4.11a, the damage associated with all droplets of a particular size was shown. However, it is also possible to compute the damage associated with a single droplet. Firstly, one can calculate the damage per droplet *normalized* by water mass. This excludes differences in erosion damage due to small and large droplets having different volumes. Secondly, the water volume can be added to obtain the *absolute* damage for a single water droplet.

The *normalized damage* for a droplet of a particular diameter is given by

$$\frac{D(\phi)}{H(\phi)} = \frac{\int_0^\infty \int_0^\infty \int_0^{360} \partial_t D_{I,V_{\text{wind}},\theta,\phi} d\theta \, dV_{\text{wind}} dI}{\int_0^\infty \int_0^\infty \int_0^{360} \partial_t H_{I,V_{\text{wind}},\theta,\phi} d\theta \, dV_{\text{wind}} dI}. \tag{4.45}$$

This is equal to the damage that is created per 1 m impingement of droplets of a particular size. Similarly, the *absolute damage* accounting for differences in water volume, is given by

$$\text{Vol}_\phi \frac{D(\phi)}{H(\phi)} = \frac{D(\phi)}{n_\phi/dA}, \tag{4.46}$$

where the relation is used that $H(\phi) = n_\phi \text{Vol}_\phi/dA$, where Vol_ϕ is the volume of a droplet with diameter ϕ. n_ϕ is the number of droplets of a particular diameter and dA is a surface element of the blade, see Appendix A.1. Hence, Equation 4.46 is the damage created per droplet on a surface area element dA.
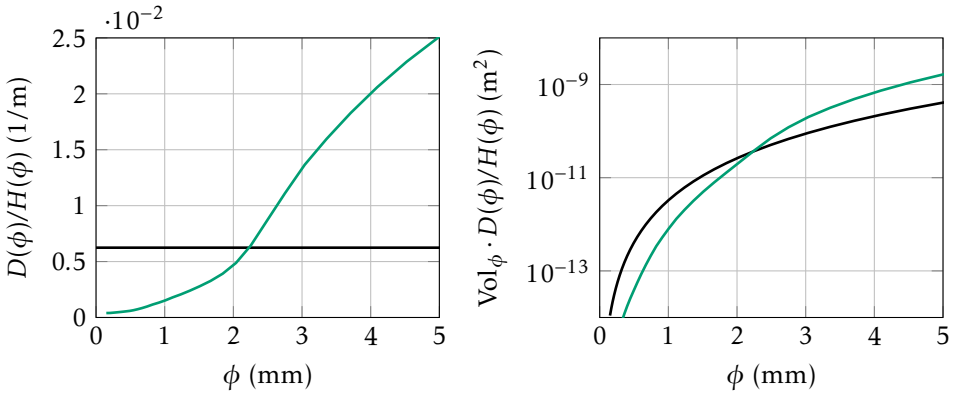
(a) Damage per meter impingement   (b) Damage per droplet on area dA

Figure 4.12: Normalized and absolute erosion damage for a single droplet at varying diameters; IEA 15MW turbine located at De Kooy; without drop-size effects: ——; with drop-size effects: ——.

The metrics of Equations 4.45 and 4.46 are shown in Figure 4.12. It is important to note that the numerical values of the curves with and without drop-size effects cannot be directly compared. The reason is that drop-size effects also influence the absolute lifetime. This aspect is further discussed in Section 4.3 and, particularly, in Table 4.1. Hence, only the behavior of the curves is of interest here.

In Figure 4.12a, the damage caused by all drop sizes is constant when drop-size-dependent effects are neglected. With drop-size effects, it is visible that large droplets produce significantly more damage for the same amount of water. For example, the damage produced, for equal amounts of water, by 4 mm droplets is about 14 times higher than that of 1 mm droplets. In Figure 4.12b, the absolute damage for a single droplet is given. Including the water volume significantly amplifies the difference in damage production between a small and a large droplet. Without

drop-size effects, a 4 mm droplet is, as expected, 64 times more damaging than a droplet of 1 mm diameter. If drop-size effects are included, this increases to 896 times.

4.2.5. Synthesis

The analysis presented in this section revealed that the following relevant drop-size-dependent effects are contained within the assumed damage model:

- Rotation of the blade: Larger droplets have a higher terminal velocity. This, averaged over one rotation, leads to more damage due to the non-linear nature of the damage model.

- The slowdown effect: Large droplets have less slowdown than small droplets. Hence, large droplets have a higher impact speed.

- Damage law: Large droplets have a lower allowed impingement in the relevant impact-speed range for current wind turbines.

From these effects, it was concluded that, for the same impingement, large rain droplets must be more damaging than small droplets. The drop-size distribution of Equation 4.11 is visualized in Figure 4.13. It states that rain becomes comprised of larger and larger droplets with increasing rain intensity. Hence, for the same amount of impingement, higher rain intensity events should create more erosion damage.
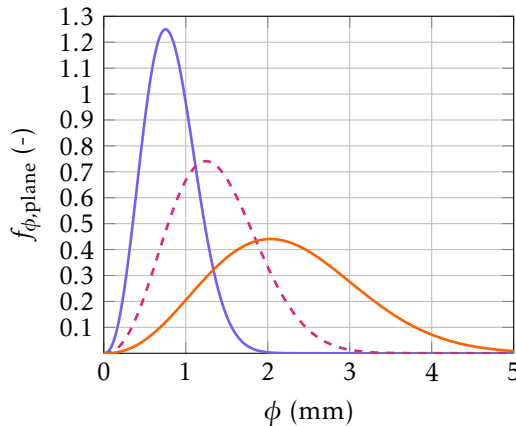
Figure 4.13: Best's distribution for a plane as a function of droplet diameter in millimeters for different rain intensities; rain intensities 0.1 mm/hr: ——, 1 mm/hr: - - -, 10 mm/hr: ——; the figure is partly reproduced from Barfknecht and von Terzi (2023).

The erosion damage per meter impingement of a particular rain intensity is given in Figure 4.14. The formula for the damage is analogous to Equation 4.45. As before, the damage is not equal for both curves. When no drop-size effects are included, the erosiveness is constant across the rain intensities. It is noteworthy that the value of $D(I)/H(I) = 0.624 \cdot 10^{-3}$ 1/m is equal to the one in Figure 4.12a. Hence, when drop-size effects are excluded, the normalized damage is invariant with respect to the droplet diameter and rain intensity. As predicted, when the drop-size effects are included, the erosiveness rapidly increases with increasing rain intensity. This corroborates statement three in Section 4.2.3. These findings directly influence the operation of the ESM. This aspect is discussed in the next section.
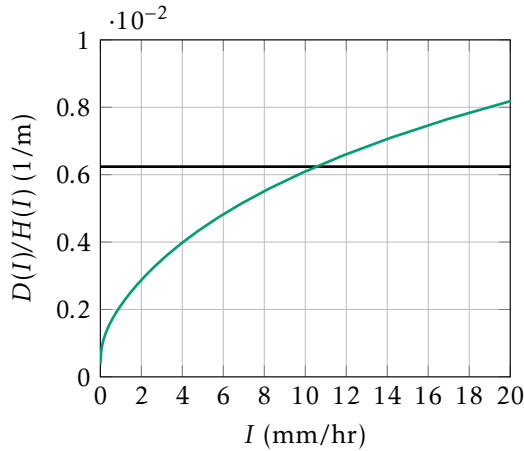
Figure 4.14: Normalized erosion damage per meter of impingement at various rain intensities; IEA 15MW turbine located at De Kooy; without drop-size effects: ——; with drop-size effects: ——.

4.3. Influence of drop-size-dependent effects on ESM operation

Drop-size effects cause a shift of erosion damage production to higher rain intensities. As a consequence, the viability of the ESM is affected. As Equation 4.12 shows, high rain-intensity events are rare. With this in mind, it might be possible to avoid a sizeable portion of the erosion damage, at minimum AEP loss, by operating in the ESM only during these rare but highly damaging events. Such an ESM variant would then increase its economic viability. In this section, first, the significance of the drop-size effects on the general ESM operation is established. Then, the influence of the drop-size effects on two optimal ESM designs is investigated. Some of the concepts used in this section, such as the operating regime of the ESM,

an optimal ESM strategy as well as the detailed derivations of the considered ESM variants, are discussed in the Appendix B.2.
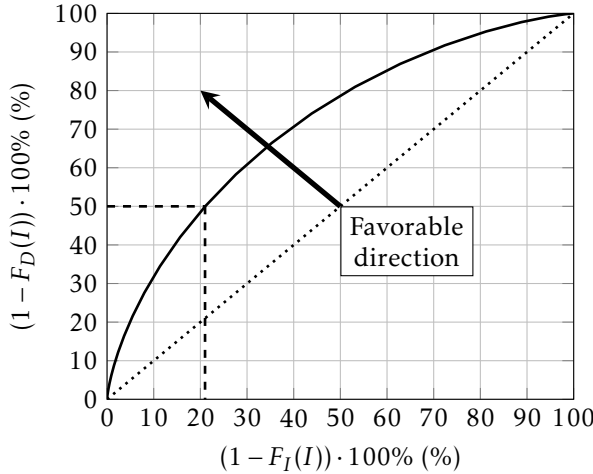
Figure 4.15: Non-dimensional damage that can be avoided by stopping the turbine (S-ESM) against the X % of highest intensity rain events; without drop-size effects; dotted line for reference for equal contribution.

Figure 4.15 is created to understand which rain events are causing damage. The data on the x-axis are defined as

$$(1 - F_I(I)) \cdot 100\% = \left(1 - \int_0^I f_I(I')dI'\right) \cdot 100\%. \tag{4.47}$$

The graph should be interpreted in the following way:

- x-axis: Stopping the turbine during the X % highest rain intensity events

- y-axis: will save Y % of damage.

For example, fully stopping the turbine during the ≈ 21 % highest rain intensity events will avoid 50 % of the total erosion damage. In the following, fully stopping the turbine during precipitation will be referred to as STOP-ESM or, in short, S-ESM.

The figure shows that the damage follows a concave curve. For better visualization, a 1:1 line is also given. From an ESM perspective, it would be advantageous if the curve was pulled in the direction of the arrow, i.e., make it more concave. Most damage would then be created during a few heavy rain events during the year.

Table 4.1: Summary showing the influence of the drop-size-dependent effects on the lifetime and percentage time a turbine needs to stop (S-ESM) during precipitation to realize a particular LX. Normalized lifetime is defined as $\overline{L} = L/L_{\text{All-off}}$; results for the De Kooy site.

LX = 2	LX = 5	LX = 10	$\overline{L}$ (-)	Rot.	Imp. angle	Dmg. law	Slowd.
21.04 %	51.86 %	68.96 %	1.00	off	off	off	off
20.42 %	51.06 %	68.25 %	0.92	on	off	off	off
20.42 %	51.06 %	68.25 %	0.92	on	on	off	off
15.61 %	45.14 %	63.23 %	1.13	off	off	on	off
17.02 %	45.52 %	62.73 %	2.27	off	off	off	on
10.65 %	35.04 %	52.87 %	2.03	on	on	on	on

A series of computations were performed to study the influence of the drop-size effects on the curve from Figure 4.15. First, the influence of the four drop-size-dependent effects from Section 4.2.3 is quantified independently. Subsequently, the effects are combined. Three distinct points on the curve were chosen to represent the curve in a convenient and condensed format. They are the 50, 80, and 90 % damage avoidance points. These correspond to a lifetime extension (LX = $L_{\text{ESM}}/L_{\text{no ESM}}$, L is the incubation time) of factors 2, 5, and 10. Table 4.1 shows the corresponding values of Equation 4.47 for these three reference points. The first row in the table sets a benchmark with all drop-size-dependent effects deactivated. The four independent simulations are:

1. Rotation — On: $V_{\text{circumferential}}$ is calculated according to Equation 4.22; Off: Blade is fixed at $\theta = 90°$ thus $V_{\text{circumferential}} = V_{\text{sec}}(1 + a')$; notice, *Impact angle* is set to *Off*; see next point and Table 4.1!

2. Impact angle — On: $\cos\alpha_\phi$ is calculated with Equation 4.22 in Equation 4.31; Off: $\cos\alpha_\phi$ is calculated with $V_{\text{circumferential}} = V_{\text{sec}}(1 + a')$ and, hence, $\cos\alpha_\phi = \cos\alpha$, where α is the angle of attack.

3. Damage law — On: Drop-size-dependent damage law given by Equations 4.6, 4.7 and 4.8; Off: Averaged damage law given by Equation 4.5.

4. Slowdown — On: V_{slowdown} is calculated; Off: $V_{\text{slowdown}} = 0$.

Without any drop-size effects, the damage model predicts that turning off (S-ESM) the turbine during the 21.04 % heaviest rain events will avoid 50 % of the total erosion damage. Activating the *Rotation* effect decreases this value slightly to 20.42 %. The influence on the absolute lifetime is stronger. Here, the normalized lifetime $\overline{L}$ is decreased from 1.00 to 0.92. As previously predicted in Section 4.2.3, *Impact angle* has no measurable influence on the results. A much more significant

impact can be observed from the drop-size-dependent damage law and the slow-down effect. The *Damage law* and *Slowdown* shift the values for the 50 % point to 15.61 % and 17.02 %, respectively. When combined, the 50 % point is shifted to 10.65 %. An even larger influence can be observed for the 80 % point, where the percentages change from 51.86 to 35.04 %. The *All-off* and *All-on* cases are plotted in Figure 4.16. Compared to the *All-off* curve, the *All-on* curve has shifted significantly to the upper left corner of the figure. When looking at the LX, one can see that, at 50 % (x-axis), the lifetime increases from approximately a factor 5 to a factor 9, almost doubling.

(a) Damage avoidance

(b) Lifetime extension
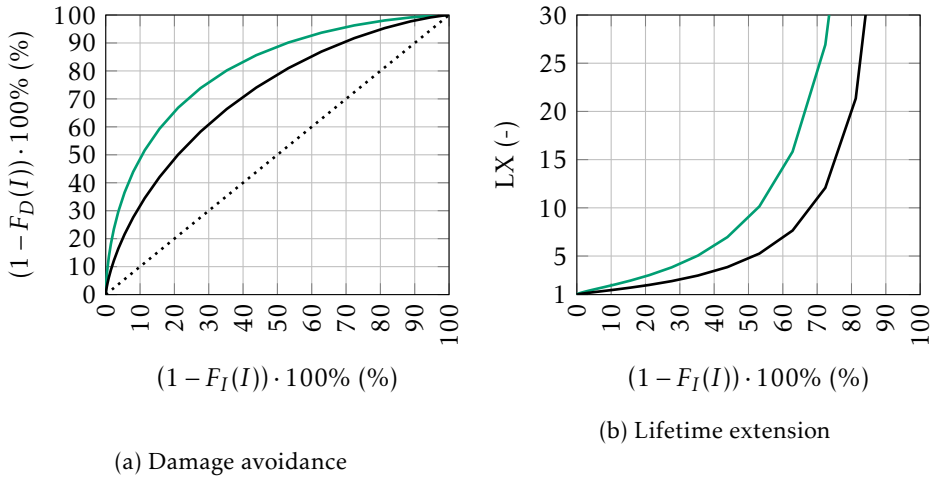
Figure 4.16: Curves showing the damage avoidance and lifetime extension factor against the X % of heaviest rain events; this is equivalent to operating in a S-ESM; all on: ——, all off: ——.

It can be concluded that including drop-size effects within the damage model strongly influences the absolute lifetime. Additionally, the damage production is significantly shifted to higher rain intensities. To illustrate this point further, assume a turbine was to follow an ESM strategy of stopping during precipitation events with the aim of reducing erosion damage by 50 %. If the ESM design was based on a damage model without drop-size effects, then it would stop during approximately 21 % of all precipitation events. However, with drop-size-dependent effects adequately taken into account, it was actually only required to stop during the 10.65 % highest rain intensity events. As a consequence, the ESM would overshoot on its intended LX at the cost of increased AEP losses. Therefore, an ESM needs to be based on an accurate prediction from an erosion damage model. Otherwise, it is not possible to objectively determine which conditions are erosive. If the damage model neglects drop-size effects, the ESM strategy will be sub-optimal. Compared to other strategies, the S-ESM can only provide a minor increase in LX

for a particular AEP loss. Methods that *gradually* adjust the tip-speed based on weather conditions perform significantly better. Two options from this group are the V-ESM and VI-ESM. The former regulates the tip-speed based on the wind speed V_{wind}, whereas the latter additionally considers the rain intensity I. For an explanation and derivation of both strategies, see Appendix B.2.

The low performance of the S-ESM in comparison to the V-ESM and VI-ESM becomes apparent when looking at their Pareto fronts in Figure 4.17a. A Pareto front represents the maximum LX that can be achieved for a particular AEP loss. In the figure, all curves are normalized with the nominal erosion lifetime in the absence of any ESM. Therefore, all curves start at 0 % AEP loss and at an LX of unity. The S-ESM performs poorly and can only provide a maximum LX of 2.5 for an AEP loss of about 1 %. While the V-ESM and VI-ESM perform much better, there are also striking performance differences between them, where the latter is clearly superior. For further detail on the concept of the Pareto front of an ESM, the reader should consult Appendix B.1 and especially Figure B.1.

(a) Lifetime extension

(b) Scaled lifetime extension
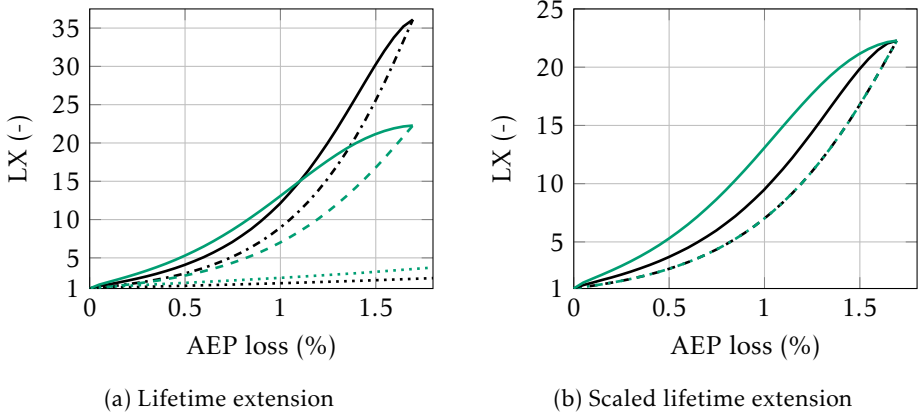
Figure 4.17: Pareto curves of lifetime extension as a function of the AEP loss; without drop-size effects, S-ESM: ······, V-ESM: -·-·-, VI-ESM: ——; with drop-size effects, S-ESM: ······, V-ESM: - - -, VI-ESM: ——; for more information on how to interpret this figure the reader should consult Figure B.1 and B.5 and their corresponding explanation in the text; IEA 15MW turbine located at De Kooy.

Due to the poor performance, the S-ESM represents merely a *theoretical* strategy. In contrast, the V-ESM and VI-ESM are much more suitable for a *practical* implementation. The question arises of how drop-size effects influence the performance of the VI-ESM. Since it is based on the rain intensity, it should profit from the more accurate relation between damage accumulation and rain intensity. Figure 4.17a shows that also the VI-ESM's performance is significantly increased when drop-size effects are properly accounted for. This is visible by the spread, i.e., the hor-

izontal distance between the Pareto fronts of the V-ESM and VI-ESM. The ESM strategies with drop-size effects show a much wider spread.
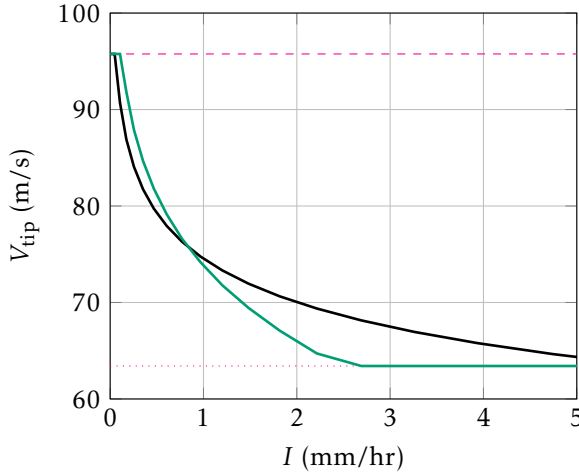
Figure 4.18: Slice of the tip-speed surface of the VI-ESM mode at 1 % AEP loss as a function of rain intensity; the figure shows a slice analogous to Figure B.4c that intersects the tip-speed control surface at $V_{\text{wind}} = 15$ m/s; without drop-size effects: ——, with drop-size effects: ——; minimum tip-speed $V_{\text{tip, min}}$: ·······, maximum tip-speed $V_{\text{tip, max}}$: – – –.

Drop-size effects also influence the prediction of the absolute lifetime. To remove this factor and to be able to better compare the influence of the drop-size effects on the shape of the Pareto fronts, a rescaling operation was performed. For that purpose, the Pareto front of V-ESM without drop-size effects was rescaled so that it became equal to the Pareto front of V-ESM with drop-size effects. The found scaling values were then applied to the Pareto front of the VI-ESM without drop-size effects. For clarification, the rescaling of the VI-ESM was performed with

$$LX_{\text{VI-ESM, rescaled, all-off}} = LX_{\text{VI-ESM, all-off}} \frac{LX_{\text{V-ESM, all-on}}}{LX_{\text{V-ESM, all-off}}}. \tag{4.48}$$

The result is shown in Figure 4.17b. It can be seen that both V-ESM curves become identical. The horizontal spread between V-ESM and VI-ESM approximately doubles when drop-size effects are taken into account. At 1 % AEP loss, the V-ESM has an LX of about 7, while the VI-ESM without drop-size effects has a lifetime extension of 9.5. However, when drop-size effects are properly modeled, the figure reveals that the VI-ESM can actually achieve an LX of 13.1! Therefore, failing to properly account for drop-size effects will make the VI-ESM look significantly worse, potentially indicating that a ESM might not be feasible, while in reality it

may well be.

Figure 4.18 shows the influence of the drop-size effects on the VI-ESM's tip-speed surfaces, which is the tip-speed as a function of the wind speed and rain intensity, i.e., $g(V_{\mathrm{wind}}, I)$, for reference see Equation B.5. The resulting surface for a target AEP loss of 1 % was chosen. Only a slice through the surface at $V_{\mathrm{wind}} = 15$ m/s is shown. As expected, the curve of the ESM without drop-size effects has a higher tip-speed at higher rain intensities ($\approx 1-5$ mm/hr). This is because, without drop-size effects in the damage model, the amount of erosion these intensities cause is underpredicted. On the contrary, the curve of the ESM with drop-size effects reduces the tip-speed in this region up to the minimum tip-speed. As compensation, it retains the maximum tip-speed a bit longer at lower rain intensities.

4.4. Conclusions

In this chapter, an erosion damage model for wind turbines was developed that is based on the impingement metric. Several drop-size-dependent effects were shown to be included within the proposed model. The importance of these effects was demonstrated for a typical combination of wind turbine, leading-edge material and site. The sensitivity of the ESM design to the drop-size-dependent effects was characterized. The two research questions posed in this chapter are:

1) How does the drop size influence the erosivity?

- Four drop-size effects were identified inside the developed damage model. The two dominant effects are the drop-size-dependent damage law from Bech et al. (2022) and the slowdown effect from Barfknecht and von Terzi (2023). It was found that, normalized for water volume, large droplets are significantly more damaging than small droplets. It was also found that the exclusion of drop-size effects leads to a severe underestimation in the projected erosion lifetime.

- The higher erosivity of large droplets can be attributed to their higher impact-velocity. Additionally, the damage model from Bech et al. (2022) suggests that, in the relevant impact-velocity range, the allowed impingement reduces with an increase in droplet diameter.

- The parameter space of leading-edge erosion is affected by drop-size effects. Without such effects, 50 % of damage is created by droplets below 1.26 mm diameter, whereas, with drop-size effects, this value is shifted to 2.00 mm. These effects need to be taken into account when determining the relevant parameters for theoretical and experimental studies in erosion research.

2) Is a thorough understanding of drop-size-related effects important for the design of the erosion-safe mode?

- Drop-size effects push the damage production to higher rain-intensities. It was found that, without drop-size effects, 50 % of the erosion damage is caused by ca. 21 % of the highest intensity rain events. However, with drop-size effects, this value was roughly halved (10.65 %).

- The VI-ESM strategy is highly sensitive to drop-size effects. For the considered turbine and sample site, it was found that the damage model indicated, for 1 % AEP loss, an LX of 9.5 without drop-size effects. However, with the proper modeling of the droplet behavior, it was shown that the actual LX is 13.1.

To conclude, it is indeed very important for the design of the ESM to use a damage model that includes drop-size effects properly. Failing in this respect will make the ESM appear less performant than it actually is, or it will lead to a suboptimal strategy that will suffer from overshoots in the targeted LX at a cost of significantly higher AEP loss than intended.

The largest uncertainty of this study concerns the drop-size dependency of the leading-edge material. Currently, to the authors best knowledge, Bech et al. (2022) published the only study that independently tested a coating for various drop sizes. The importance of the slowdown effect is projected to grow in the future. The slowdown depends on the aerodynamic nose radius R_c and the tip-speed. Both are expected to grow as wind turbine blades become larger.

Several other findings and conclusions were made as a byproduct of this research. These are included in the appendix. It was shown that for impingement, the damage scales according to $\propto V_{\text{impact}}^{\beta} V_{\text{collection}} \approx V_{\text{impact}}^{\beta+1}$. Additionally, the operational regime of the ESM was defined and a method for finding optimal ESM strategies was proposed. In particular, it can be concluded that:

- The VI-ESM is substantially more powerful than the V-ESM. Even without properly modeling drop-size effects, the VI-ESM can provide significantly more life extension for the same AEP loss.

- The drop-size distribution $f_{\phi,\text{plane}}$ is crucial. The drop-size effects are only relevant because large droplets become more frequent at higher rain intensities. For using the ESM in the field, the assumed drop-size distribution must reflect the actual drop-size distribution at the considered wind turbine site.

- The VI-ESM η-contours are not dependent on the rain intensity and wind speed probability density functions.

Bibliography

Amirzadeh, B., Louhghalam, A., Raessi, M., and Tootkaboni, M.: A computational framework for the analysis of rain-induced erosion in wind turbine blades, part I: Stochastic rain texture model and drop impact simulations, Journal of Wind Engineering and Industrial Aerodynamics, 163, 33–43, https://doi.org/10.1016/j.jweia.2016.12.006, 2017.

Barfknecht, N. and von Terzi, D.: On the significance of rain droplet slowdown and deformation for leading-edge rain erosion, Wind Energy Science Discussions, 2023, 1–42, https://doi.org/10.5194/wes-2023-169, 2023.

Barfknecht, N. and von Terzi, D.: Mitigating blade erosion damage through nowcast-driven erosion-safe mode control, Journal of Physics: Conference Series, 2024.

Bech, J. I., Johansen, N. F.-J., Madsen, M. B., Hannesdóttir, Á., and Hasager, C. B.: Experimental study on the effect of drop size in rain erosion test and on lifetime prediction of wind turbine blades, Renewable Energy, 197, 776–789, https://doi.org/10.1016/j.renene.2022.06.127, 2022.

Best, A. C.: The size distribution of raindrops, Quarterly journal of the royal meteorological society, 76, 16–36, https://doi.org/10.1002/qj.49707632704, 1950a.

Best, A. C.: Empirical formulae for the terminal velocity of water drops falling through the atmosphere, Quarterly Journal of the Royal Meteorological Society, 76, 302–311, https://doi.org/10.1002/qj.49707632905, 1950b.

DOWA: 10 year average wind speed (F) and Weibull scale (a) and shape parameter (k) for height 150m, Website accessed 02.01.2024, 2020, https://www.dutchoffshorewindatlas.nl/atlas/image-library/image-library/parameters-per-height-150m.

Gaertner, E., Rinker, J., Sethuraman, L., Zahle, F., Anderson, B., Barter, G. E., Abbas, N. J., Meng, F., Bortolotti, P., Skrzypinski, W., et al.: Definition of the IEA 15-Megawatt Offshore Reference Wind Turbine, Tech. rep., National Renewable Energy Lab.(NREL), Golden, CO (United States), 2020.

Gent, R. W., Dart, N. P., and Cansdale, J. T.: Aircraft icing, Philosophical Transactions of the Royal Society of London. Series A: Mathematical, Physical and Engineering Sciences, 358, 2873–2911, https://doi.org/10.1098/rsta.2000.0689, 2000.

Hoksbergen, N., Akkerman, R., and Baran, I.: The Springer model for lifetime prediction of wind turbine blade leading edge protection systems: A review and sensitivity study, Materials, 15, 1170, https://doi.org/10.3390/ma15031170, 2022.

KNMI: Uurgegevens van het weer in Nederland - 235 - De Kooy, Website accessed 01.02.2022, 2020, https://cdn.knmi.nl/knmi/map/page/klimatologie/gegevens/uurgegevens/uurgeg_235_2021-2030.zip.

Letson, F., Barthelmie, R. J., and Pryor, S. C.: Radar-derived precipitation climatology for wind turbine blade leading edge erosion, Wind Energy Science, 5, 331–347, https://doi.org/10.5194/wes-5-331-2020, 2020.

Ning, S. A.: A simple solution method for the blade element momentum equations with guaranteed convergence, Wind Energy, 17, 1327–1345, https://doi.org/10.1002/we.1636, 2014.

Pryor, S. C., Barthelmie, R. J., Cadence, J., Dellwik, E., Hasager, C. B., Kral, S. T., Reuder, J., Rodgers, M., and Veraart, M.: Atmospheric Drivers of Wind Turbine Blade Leading Edge Erosion: Review and Recommendations for Future Research, Energies, 15, https://doi.org/10.3390/en15228553, 2022.

Sor, S., García-Magariño, A., and Velazquez, A.: Droplet in the Shoulder Region of an Incoming Airfoil. Part II: Droplet Breakup, in: AIAA Aviation 2019 Forum, p. 3307, https://doi.org/10.2514/6.2019-3307, 2019.

Sor, S., García-Magariño, A., Morote, P., and Olalla, J. M.: Influence of the deformation in the collection efficiency on a profile applying DRD model, AIAA AVIATION 2021 FORUM, https://doi.org/10.2514/6.2021-2642, 2021.

Verma, A. S., Castro, S. G., Jiang, Z., and Teuwen, J. J.: Numerical investigation of rain droplet impact on offshore wind turbine blades under different rainfall conditions: A parametric study, Composite structures, 241, 112 096, https://doi.org/10.1016/j.compstruct.2020.112096, 2020.

Verma, A. S., Noi, S. D., Ren, Z., Jiang, Z., and Teuwen, J. J. E.: Minimum Leading Edge Protection Application Length to Combat Rain-Induced Erosion of Wind Turbine Blades, Energies, 14, https://doi.org/10.3390/en14061629, 2021.

4

5

Nowcast-driven erosion-safe mode control

At this point, the thesis has shown that the ESM can deliver, for a coastal site in the Netherlands, an attractive lifetime extension factor of about 13 for an AEP loss of about 1 %. However, these numbers were obtained under ideal conditions that can only be reached with a perfect weather forecast. This chapter aims to investigate the ESM's performance when it is driven with a state-of-the-art weather-radar-based probabilistic rainfall nowcast provided by the Royal Netherlands Meteorological Institute (KNMI). The results will show whether the improvements made in this thesis to the ESM have already made the ESM an attractive option for erosion mitigation.

Local table of contents

5.1. Introduction

For the application of the ESM in the field, an accurate short-term forecast, ideally in the order of minutes to hours, is required[1]. This time frame is currently covered by state-of-the-art meteorological nowcasting products, where radar-based observations are extrapolated in time using a variety of statistical and advection-based methods (Lin et al., 2005).

Tilg et al. (2020) argue that several challenges exist with classical radar-based precipitation forecasts for offshore applications, such as radar clutter caused by wind farms. They, therefore, propose using a micro-rain radar placed in the vicinity of a turbine to collect the required data. However, this necessitates extra hardware, which needs to be operated and maintained, and it requires the construction of a well-performing rainfall product out of the radar reflectivity measurements. This adds complexity and cost, which is not always feasible. Therefore, it seems beneficial if, ideally, standard *off-the-shelf* forecasting products could be used to drive the ESM. An advantage of the Netherlands is that one of the C-band weather radars is located at the coast in the vicinity of the largest offshore wind farms, see Figure 5.1. Together with a recent reduction in clutter in the Dutch radar composite (Overeem et al., 2020), this lowers the systematic errors in the radar product, as mentioned by Tilg et al. (2020).

The objective of the present study is to investigate whether a state-of-the-art weather-radar-based precipitation nowcast product can be used to effectively drive

---

[1]A rain forecast is required to give the turbine enough time to change its speed. Additionally, the energy that a power plant will produce is usually sold ahead of time, for example, by trading contracts on an energy exchange. The shortest contract offered on EPEX (European Power Exchange) SPOT is the 15-minute intraday contract. It can be traded up to five minutes before delivery. Any failure to deliver contractually obliged energy needs to be resolved through the balancing market managed by the transmission system operators. Balancing typically incurs additional costs, such as imbalance charges or the need to procure energy at potentially higher market rates to fulfill obligations.

the erosion-safe mode. To this end, the performance of the ESM is compared for being driven by the nowcast with being driven by rainfall measurements.

5.2. Methodology

5.2.1. Forecast products

Two weather-radar-based products are used. One serves as the ground truth of *true rain*. The other represents the nowcast used to determine the speed at which the wind turbine should operate.

rad_nl25_rac_mfbs_5min: The true rain was obtained from KNMI's rad_nl25 _rac_mfbs_5min product (KNMI, 2023b). It is a rain-gauge-corrected quality-controlled radar-based dataset that provides precipitation accumulations for the land area of the Netherlands on a grid with a 1x1 km resolution. This dataset is not available in real time, but it is generally considered a high-quality data set that can be used for reference purposes (Imhoff et al., 2020).

precipitation_NL_ensemble_nowcast_5min: For the forecast, KNMI's new state-of-the-art precipitation_NL_ensemble_nowcast_5min product was chosen (KNMI, 2023a). The product is based on the open-source pySTEPS package, representing a probabilistic forecast of 20 ensembles (KNMI, 2023a; Imhoff et al., 2020; Pulkki-nen et al., 2019). It provides rainfall nowcasts in 5-minute increments up to 120 minutes in advance with a spatial resolution of 1x1 km. Its fine resolution provides the potential to control every turbine in a wind park individually based on the expected rainfall. Due to its novelty, the product data series has only a span of about ten months, running from 04:45 04/07/2022 to 01:55 07/05/2023 (time format: hh:mm DD/MM/YYYY). This range includes 77916 forecasts that were analyzed in this study. This product is termed *the nowcast* in the following.

The domain of both products is shown in Figure 5.1. It can be seen that the products span the entirety of the landmass of the Netherlands and, importantly, also the parts of the Dutch North Sea that are being developed for offshore wind parks.

For the purpose of this study, one important assumption with regard to the weather products was made. Both products indicate the rain at an altitude of 1500 m. As calculated in Tilg et al. (2020), droplets require about 5 minutes to reach the ground from such altitude. Here, it is assumed that this time delay does not exist.

5.2.2. Wind turbine and sample sites

A model turbine is required for the evaluation of the ESM. For this purpose, the IEA 15MW reference wind turbine (RWT) was chosen since it represents the current generation of large offshore wind turbines (Gaertner et al., 2020). Three sample sites are chosen for this investigation: The KNMI stations of De Kooy (#235), Herwijnen (#356) and Maastricht (#380). The number in parenthesis provides the
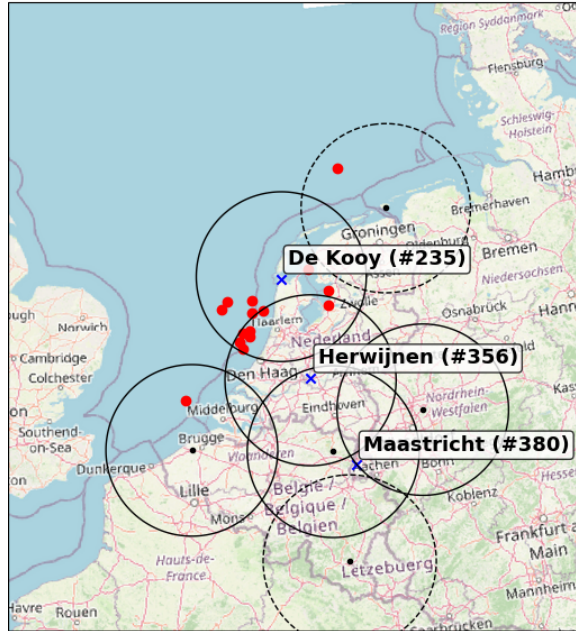
Figure 5.1: The figure shows the entire coverage area of the nowcast plotted in a stereographic projection; height of 765 km; width of 700 km; the three sample sites are indicated with a blue cross; current Dutch offshore wind farms are indicated with a red dot; the 100 km radius around weather radars is indicated by a solid black circle, outside this range a radar-based product usually degrades (Imhoff et al., 2021); the dashed circles represent the German Borkum and Belgian Wideumont radars that are since recently used in some KNMI products; the background map is taken from OpenStreetMap released under the ODbL license.

KNMI station identifier. The De Kooy station represents a coastal site. The Maastricht station lies far inland in the Dutch province of Limburg. The Herwijnen station can be seen as an *in-between* station. The location of all three stations is shown in Figure 5.1.

For the official KNMI stations, wind data are provided as an hourly mean at a height of ten meters (KNMI, 2023c). It is assumed that the wind stays constant in the given hourly interval. The wind speed at the IEA RWT's 150 m hub height is obtained by scaling the measured wind speed so that the mean wind speed coincides with the data provided by the Dutch Offshore Wind Atlas (DOWA) for 150 m height (DOWA, 2020). It was found that using a power law correction, as, for example, suggested by Shankar Verma et al. (2021), yields a mean wind speed that greatly differs from the ones given by the DOWA. DOWA's data are deemed more reliable. The scaling coefficients applied to the 10 m wind measurements are 1.7742 (De Kooy, #235), 2.0157 (Herwijnen, #356) and 1.9386 (Maastricht, #380).

The IEA 15MW RWT is designed for a mean wind speed at hub height of 10 m/s
(Gaertner et al., 2020). However, the chosen sites have mean wind speeds of 9.2
(#235), 7.65 (#356) and 7.42 m/s (#380). Hence, the operational time at rated
power is reduced. For a 10 m/s site the turbine would operate 42 % of the time
at rated capacity. For the three sites, this becomes 35 (#235), 22 (#356) and 21 %
(#380).

5.2.3. ESM strategy

The ESM exploits two characteristics of leading edge erosion. Firstly, the damage
production is very sensitive to changes in the speed of the blade, and, secondly,
erosion damage production increases as rain intensity increases (Barfknecht and
von Terzi, 2024). In this study, two distinct ESM strategies are considered: the V-
ESM and the VI-ESM. The V-ESM limits the tip-speed during precipitation events
based on wind speed (V_{wind}). The VI-ESM limits the tip-speed based on wind speed
and rain intensity (I). These strategies were developed in Barfknecht and von Terzi
(2024), where it was shown that they are optimal strategies. They provide the
highest damage reduction for the lowest possible AEP loss.

The ESM strategies can be defined by relations of the form

$$\text{V-ESM} = g_{opt}(V_{wind}), \qquad \text{VI-ESM} = g_{opt}(V_{wind}, I_{nowcast}), \qquad (5.1)$$

where g is a function relating environmental inputs, such as V_{wind} and I, to the
turbine's tip-speed V_{tip}. g_{opt} is defined (for the VI-ESM) as

$$g_{opt} = \{g(V_{wind}, I) \quad \text{subject to} \quad \text{minimize}(|\eta(g(V_{wind}, I)) - K|) \quad \text{for all} \quad (V_{wind}, I)\}, \qquad (5.2)$$

where

$$\eta(g(V_{wind}, I)) = \frac{\frac{\partial P}{\partial V_{tip}}}{\frac{\partial(\partial_t D)}{\partial V_{tip}}} = \frac{\partial P}{\partial(\partial_t D)}, \qquad (5.3)$$

and

$$g(V_{wind}, I) = \left\{ g_{min}(V_{wind}) \le V_{tip} \le g_{normal}(V_{wind}) \text{ for all } (V_{wind}, I) \right\}. \qquad (5.4)$$

P is the power of the turbine and $\partial_t D$ is the erosion damage production rate. Here,
the probabilistic (continuous) formulation of the power and damage production
for a particular site must be used, as explained in Barfknecht and von Terzi (2024).
g_{min} is the turbine's minimum speed. g_{normal} represents the turbine's normal tip-
speed as a function of wind speed. In the method, a constant K is chosen. Sub-
sequently, the tip-speed for every environmental input is chosen such that $\eta = K$,
or when this is not possible, the η closest to K is selected. The resulting tip-speed
for every V_{wind} and I is g_{opt}. η measures which tip-speeds as a function of V_{wind}

and I add the most power for the lowest damage increase. A value of K leads to a particular tuple of AEP loss and damage reduction. By varying K, other tuples can be realized. The reader is referred to the original reference for the full description of the method and key assumptions in the derivation.

5.2.4. Calculation of damage and power

The damage model is based on impingement H, a metric for the accumulated water column by the blade. The damage model was developed in Barfknecht and von Terzi (2024) and incorporates several drop-size-dependent effects, such as the slowdown effect from Barfknecht and von Terzi (2023) and a drop-size-dependent damage law from Bech et al. (2022). Since the wind speed and the precipitation forecast are given as a discrete data set, the hybrid continuous-discrete approach from Barfknecht and von Terzi (2024) is used. It reads

$$D = \sum_{i=1}^{N} \left(\int_{0°}^{360°} \int_{0}^{\infty} \frac{\partial_t H(I_{\text{true rain}}(t_i), V_{\text{wind}}(t_i), \theta, \phi)}{H_{\text{allowed}}(V_{\text{wind}}(t_i), \phi)} f_{\phi,\text{plane}} f_\theta \, d\phi d\theta \right)_i \Delta T_i. \quad (5.5)$$

N is the number of elements in the data series. $f_{\phi,\text{plane}}$ is the drop size (ϕ) distribution through a plane, and f_θ is the uniform distribution of the blade position (θ). $\partial_t H$ is the impingement accumulation rate and H_{allowed} is the impingement until the end of the incubation time. V_{impact} is the impact speed of the droplets and is dependent on V_{tip}, V_{wind} and others. In this formulation the variables θ and ϕ are considered distributed and the variables I and V_{wind} are considered discrete. $\Delta T_i = t_i - t_{i-1}$ is the time step of a particular data frame i with time stamp t_i. For the products used in this study, ΔT_i is five minutes.

The power is calculated as $P = Q\omega$ with

$$C_Q(\lambda) = \begin{cases} M(\lambda) & \text{if } M(\lambda) < \left(C_{Q_{\max}} = \frac{Q_{\max}}{qAR} \right), \\ \left(C_Q(\lambda, \varphi_{\text{pitch}}) = C_{Q_{\max}} \right) & \text{if } M(\lambda) \geq C_{Q_{\max}}, \end{cases} \quad (5.6)$$

where $Q = qARC_Q$ and $\omega = V_{\text{tip}}/R$. $M(\lambda) = \max(C_Q(\lambda, \varphi_{\text{pitch}}))$, ω is the rotational speed, q is the dynamic pressure, A is the rotor disk area, R is the rotor radius and C_Q is the torque coefficient. For any tip-speed ratio λ, the pitch angle φ_{pitch} is chosen such that the torque coefficient is maximized in the partial load region and limited to the rated generator torque $Q_{\max}$ in the rated power region. It is assumed that neither the blade position nor the droplet diameter influence the energy production. Hence, the produced energy becomes:

$$E = \sum_{i}^{N} P_i \Delta T_i. \quad (5.7)$$

Due to these assumptions, the equation becomes a simple summation over all the time steps. The reader should note that the definitions of P and D given in this section are different to those in Equation 5.3. The reader is referred to the original reference for an in-depth explanation.

5.3. Results

The accuracy of the nowcasting product is essential for a successful utilization in the ESM. When the nowcast and the true rain do not correlate well, false-positive and false-negative control decisions are produced. As a consequence, the turbine will operate at reduced performance in dry conditions or will accumulate significant amounts of damage during precipitation events. Figure 5.2 provides an initial assessment of the performance of the nowcasting product at the 1x1 km grid cell above the site De Kooy.
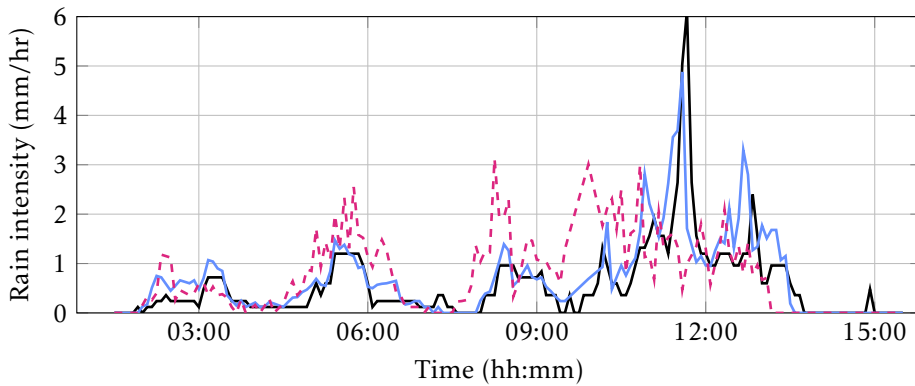
Figure 5.2: Actual rainfall observations and nowcasts for 21-07-2022 between 1:30 and 15:30 at station De Kooy. True rain (radar-corrected): ——, 15-min nowcast (1 ensemble): ——, 60-min nowcast (1 ensemble): - - -.

A rainfall event is shown that occurred in July 2022, when a low pressure area moved over central Netherlands, resulting in widespread rainfall with local convective activity. For this event, the true rainfall, based on the corrected radar product and the rainfall nowcasts for 15 and 60 minutes ahead, is given. The 15-minute nowcast performs well. It can accurately predict the rain intensity as well as the start and end times of the individual precipitation events. A deterioration in performance can be observed for the 60-minute nowcast, especially later during that day, which coincides with heavier rainfall intensities as a result of convective activity. Convective rainfall (thunderstorm) is more challenging to capture far in advance with nowcasting methods. New storms generally form within time spans of 30 minutes and thus cannot yet be part of the observations in the 60-minute

nowcast (Imhoff et al., 2020).

5.3.1. Evaluation of the single-ensemble nowcast

The accuracy of the nowcast is first assessed by considering a single (random) en-semble member. The total damage and energy is calculated for both series of the true rain and the nowcast. By considering a complete sweep of ESM coefficients K, see Equation 5.2, a Pareto front is spanned that shows the maximum attainable lifetime extension (LX = $L_{ESM}/L_{no\ ESM}$, L is the erosion incubation time) for a par-ticular AEP penalty. The best possible Pareto front is obtained when the ESM is controlled with a perfect forecast, i.e., the ground truth rain is used. The goal of any nowcasting-controlled ESM is to approach this front as closely as possible. The nowcast is evaluated at lead times of 0, 5, 15, 30, 60 and 120 minutes. The V-ESM and VI-ESM strategies are considered. The results are shown in Figure 5.3.

Comparing the true rain Pareto fronts of the V-ESM and the VI-ESM shows that the latter performs significantly better. The start and end points of the respective V-ESM and VI-ESM Pareto (——) fronts are equal. The start (1, 0 %) represents an ESM strategy that never slows down the turbine, and the end point indicates a strategy that always slows down the turbine to minimum speed when rain is predicted. Between the start and end points, the considered ESM strategies can perform differently. Barfknecht and von Terzi (2024) obtained the same results but for a completely probabilistic setting. For Herwijnen, the V-ESM can provide an LX of three for a 1 % AEP penalty. Whereas the VI-ESM strategy provides for the same AEP loss an LX of seven.

A comparison of the Pareto fronts across the three considered sites shows a re-duction in maximum attainable LX when moving inland. This is caused by the reduced mean wind speed that causes the turbine to spin more frequently at min-imum rotational speed. Hence, during (some) precipitation events, the turbine speed cannot be reduced further. However, it should also be noted that for lower mean wind speed, the absolute accumulated damage, even in the absence of the ESM, is reduced. It is also visible that moving inland increases the maximum AEP loss. Interestingly, the maximum LX for the 5 to 120-minute nowcasts is surpris-ingly similar across all sites, whereas pronounced differences exist for the 0-minute nowcast.

The curves of the nowcasts approach the Pareto front as the lead times are re-duced, which is expected given the increasing quality of the nowcasts for shorter lead times (Lin et al., 2005; Imhoff et al., 2020). The 0-minute nowcast represents the current rain conditions. Ideally, it would perform similarly to the ground truth product. This is not the case due to the absence of quality-controlled rain gauge corrections in the operational radar product used in the nowcast, while such cor-rections are present in the ground truth reference product. Hence, a considerable

(a) V-ESM, De Kooy

(b) VI-ESM, De Kooy

(c) V-ESM, Herwijnen

(d) VI-ESM, Herwijnen

(e) V-ESM, Maastricht

(f) VI-ESM, Maastricht
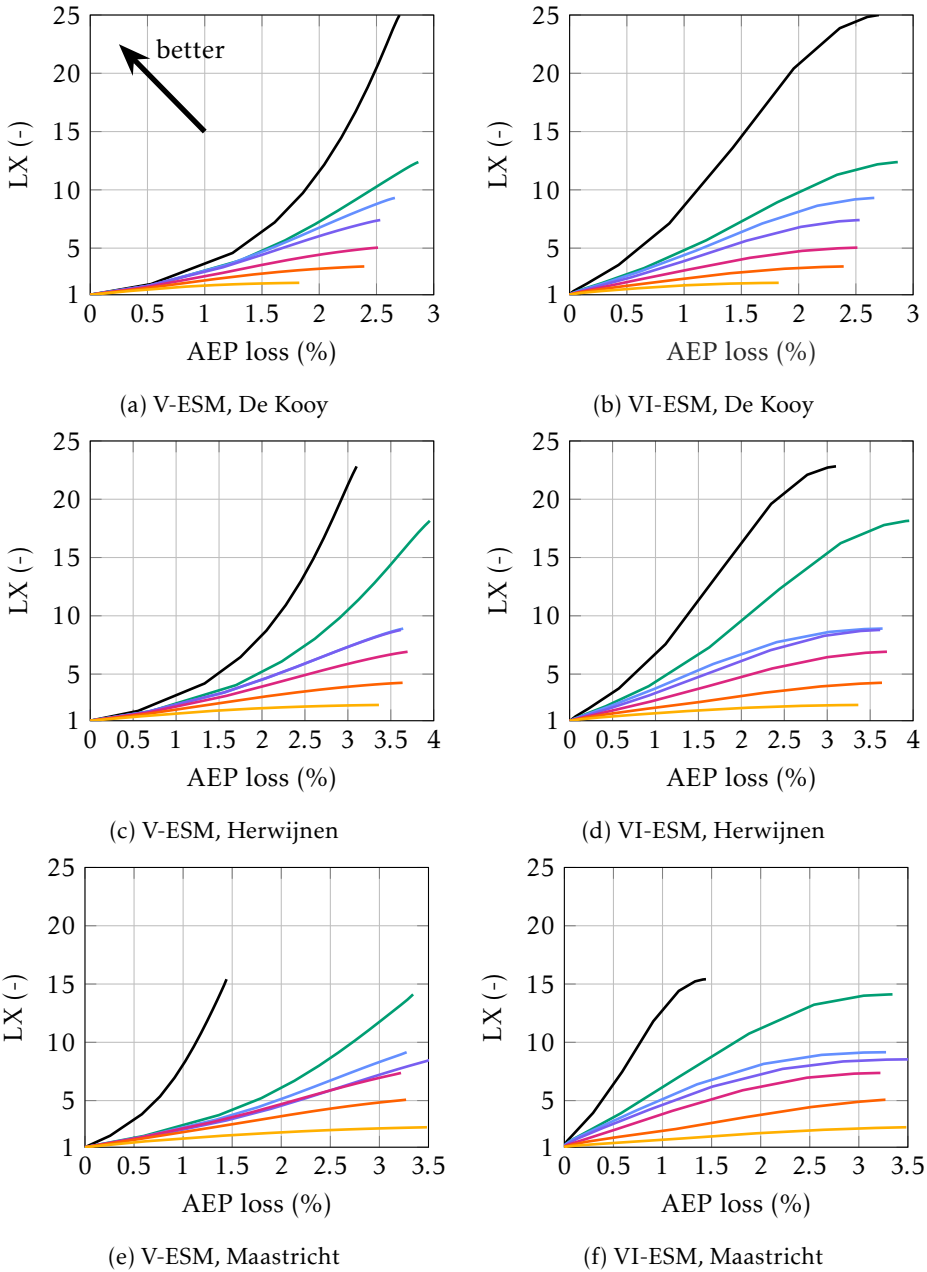
Figure 5.3: Single-ensemble results (Lifetime extension factor versus AEP loss) for the V-ESM and VI-ESM; three different sites were considered; Pareto front with perfect ground truth precipitation data: ——; Curves obtained using nowcast of 0-min: ——, 5-min: ——, 15-min: ——, 30-min: ——, 60-min: ——, 120-min: ——.

gap exists between the ground truth Pareto front and the curve of the 0-minute nowcast. Nevertheless, the 0-minute nowcast can still achieve an LX of about five for a roughly 1 % AEP loss when the VI-ESM is used. The 5 and 15-minute nowcasts are generally close together and sometimes even overlap, as is the case for the Herwijnen station. The 30-minute nowcasts already show a considerable degradation in the performance. The 60 and 120-minute nowcasts perform poorly. For example, the 120-minute nowcasts can only achieve an LX of about two. This is an expected result, as it has been found in the literature that the maximum skillfulness for a nowcast is limited to around 120 minutes (Imhoff et al., 2020). From the results, it appears to be realistic to make ESM control decisions up to 15 minutes in advance.

Table 5.1: Contingency table for the De Kooy (#235) station; nowcast data are given for the entire period from 04/07/2022 until 07/05/2023 (DD/MM/YYYY); monthly values are given for the 15-minute nowcast; for the analysis by month note that the data length of July is slightly reduced due to the start date; the month of May was omitted since only 7 days of data were available; false positive (FP), false negative (FN), true positive (TP), true negative (TN), hit rate (HR), false positive rate (FPR), rain column predicted by the nowcast (H_{now}), true rain column (H_{true}), data completeness (DC). All data except H are given in %. H is given in mm.

Nowcast	FP	FN	TP	TN	HR	FPR	H_{now}	H_{true}	DC
perfect	0.00	0.00	7.50	92.50	100.00	0.00	727	727	100.0
0-min	1.43	0.88	6.62	91.07	88.23	1.55	519	631	88.2
5-min	1.32	1.21	6.27	91.20	83.85	1.42	509	629	88.2
15-min	1.41	1.56	5.92	91.11	79.15	1.52	455	628	88.2
30-min	1.70	2.11	5.38	90.81	71.82	1.83	479	627	88.2
60-min	2.17	3.03	4.45	90.35	59.51	2.35	365	633	88.2
120-min	2.00	4.53	2.99	90.48	39.78	2.16	204	624	88.2
Jul '22	0.37	0.56	2.53	96.54	81.90	0.39	16	17	93.0
Aug	0.22	0.32	1.57	97.89	83.13	0.23	50	41	94.6
Sep	2.81	2.01	8.68	86.50	81.24	3.14	90	113	91.2
Oct	0.98	0.86	2.72	95.44	75.97	1.01	17	33	96.5
Nov	2.47	2.53	11.73	83.27	82.24	2.88	98	155	89.1
Dec	1.51	2.18	5.40	90.91	71.27	1.63	36	55	92.0
Jan '23	2.24	2.06	8.35	87.35	80.20	2.50	42	64	74.4
Feb	0.55	1.17	2.18	96.10	65.13	0.57	4	13	72.2
Mar	2.36	2.80	10.41	84.43	78.80	2.71	52	78	83.2
Apr	0.82	1.42	6.18	91.58	81.29	0.88	47	57	99.2

Table 5.1 gives the values of the contingency table metrics for KNMI's De Kooy station for different nowcast lead times and months. The nowcasts have some gaps

in the analyzed time span. Therefore, the data completeness is given. The 0 to 15-minute nowcasts retain good performance with hit rates above 79 %. The performance drops starting from the 30-minute nowcast due to increasing FN (false negative) values. The FP (false positive) values stay fairly constant across all lead times. Hence, the degradation of the nowcast performance can be attributed to the increase in FN as the lead times increase. This is shown in Figure 5.3. High FN values are associated with missed rain events. As the lead times increase, the AEP loss is reduced since the turbine fails to slow down due to missed events. This is accompanied by a reduction in the maximum LX. The table also shows that the single-ensemble nowcasts underestimate the total precipitation column. Note that the rain column reference values slightly differ due to the gaps in the dataset and the way the values are stored in the separate files that the KNMI provides.

The second part of the table analyzes the 15-minute nowcast values by month. A relatively constant hit rate can be observed with exceptions being the months of December 2022 and February 2023. However, during the latter hardly any precipitation occurred and only 4 out of 13 mm of rainfall was forecasted. In the tested period, there was more rain in the winter than in the summer months and also the probability of having rain was higher during winter. It is noteworthy that the summer months of 2022 were unusually dry in the Netherlands and usually the precipitation column is rather constant across the months. During these months the TP rate is increased since more rain events are correctly forecasted. However, also the FP and FN rates are increased, which is caused by the higher number of precipitation events in winter.

5.3.2. Evaluation of the multiple-ensemble nowcast

The nowcast contains 20 ensembles, i.e., for every lead time, the nowcast predicts 20 possible outcomes. It, therefore, contains probabilistic information, capturing the uncertainty in the rainfall forecast. These could be used for the ESM. The aim can be simply to optimize the nowcast curves so that they approach the Pareto front. Another aim could be to make the ESM more well-behaved. In a practical implementation, the choice of constant K is based on the intended LX and AEP loss as given by the ground truth Pareto front. Without prior knowledge, there is no guarantee that this tuple of values can be achieved. Here it is argued that, from an operator perspective, it is advantageous if one value of the tuple is preserved. For example, the operator wants to be certain that a particular LX is achieved accepting a higher AEP loss, or, vice versa, the operator defines a particular AEP loss hoping for the best possible LX. A value of K with a completely unpredictable {AEP loss, LX} tuple seems undesirable.

In Section 5.3.1 just one ensemble member of the nowcast is used. Here, all 20 ensemble members are analyzed by considering the four operators min, max, mean

and the median, that are applied to the ensemble vector. It is worth noting that the median operator will indicate rain when more than half of the ensembles indicate rain. Hence, it is equal to utilizing the ESM when the rain probability is above 50 %.

Figure 5.4 shows the results of the multi-ensemble nowcast. The results for the 0-minute nowcast are equal for all ensembles, as this is still the latest observation. Hence, the 0-minute results are also equal to the ones from Figure 5.3b. The curves of the max and mean operator perform almost identically, which is likely a result of the skewness of the ensemble members. It appears that a considerable amount of ensemble members indicate either no rainfall or considerable rainfall. It can be seen that in comparison to the single-ensemble VI-ESM (- - -) the curves for the max and mean operator are moved closer to the Pareto front. This is especially true for the 15-minute nowcast. The higher lead time nowcasts can also achieve a significantly higher LX, albeit at the cost of a high AEP loss. The min operator performs poorly. It can also be seen that the end points of the curves are shifted towards lower AEP losses. This comes at a penalty in LX. Overall, the curves of all lead times are moved into a less favorable direction. The median operator performs similarly in comparison to the single-ensemble nowcast. The 15-minute curve, however, is shifted down.

Figure 5.4 also indicates iso-lines (⋯⋯) that connect data points for the same values of K across the Pareto front and the nowcasting curves. The iso-lines of the median operator run almost straight down from the Pareto front to the 0-minute curve. From that point, they only slightly start deviating up to the 60-minute curve. The iso-lines of the mean operator are almost vertical up to the 15-minute curve. For a starting AEP loss of about 1.25 %, the curve then starts to deviate to the left, whereas for the iso-line starting slightly above 2.25 % the lines quickly deviate to the right. It can be said that the mean and median operators allow for the realization of an ESM that can preserve the indicated AEP loss (when the maximum lead time stays less or equal to 30 minutes) but will yield a variable lifetime. The iso-lines of the max operator move sideways, starting from the 0-minute curve. Hence, with this strategy, one has a high certainty about the LX at the penalty of the variable AEP loss. However, since the iso-line first runs straight down from the Pareto front to the 0-minute curve, the max operator suffers from the problem that an initial estimate for the reduction in the lifetime is required.

In Table 5.2, it can be seen that the max operator leads to low FN but increases the FP in comparison to the values in Table 5.1. It is worth noting that the values for FP to TN are equal to the mean operator. A consequence of the fact that both operators will indicate rain when only one single ensemble indicates $I > 0$ mm/h. Differences can be seen in the predicted rain accumulation. In comparison to the max, the min operator shows the opposite behavior. Max and min constitute boundaries for

(a) min

(b) median

(c) max

(d) mean

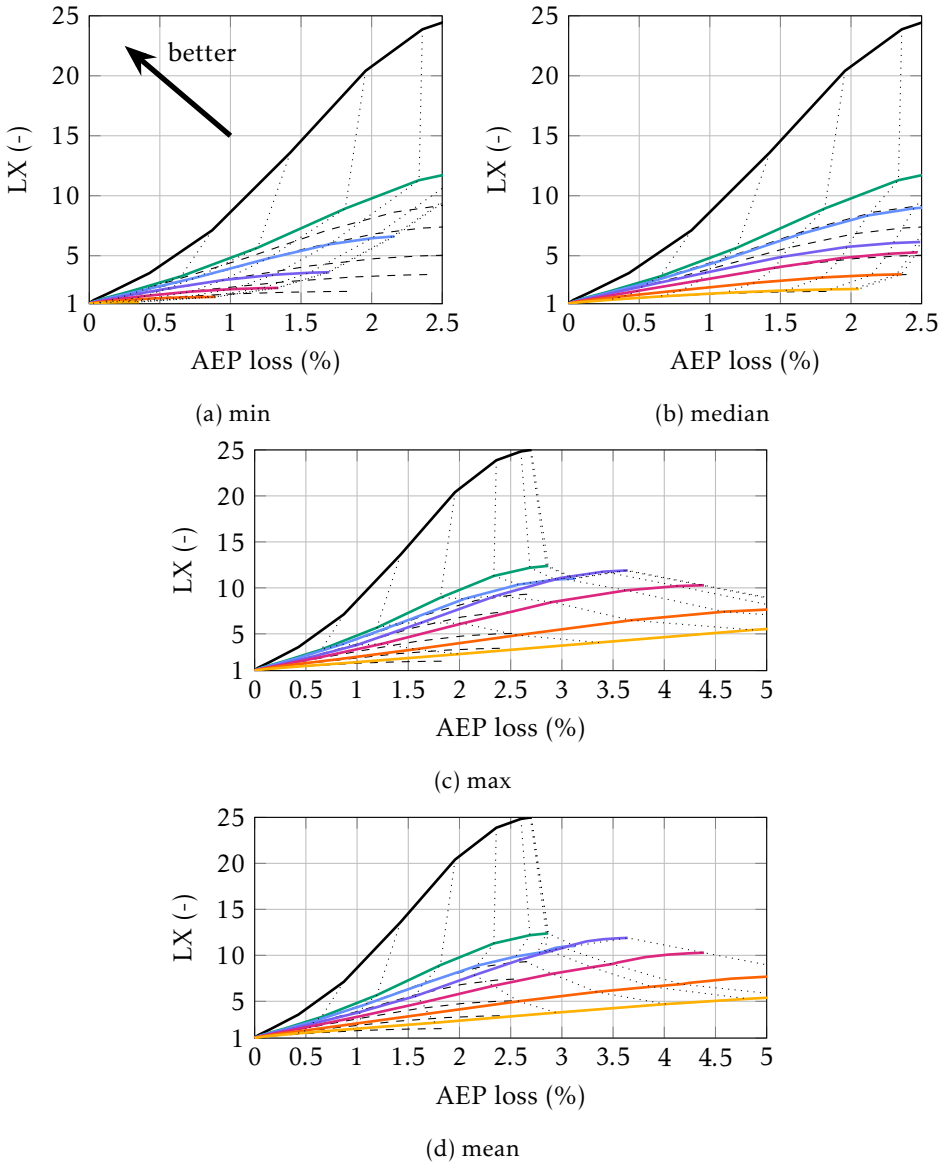Figure 5.4: Multi-ensemble results (Lifetime extension factor versus AEP loss) for the VI-ESM; only the De Kooy (#235) site was considered; Pareto front with perfect ground truth precipitation data: ——; Curves obtained using nowcast of 0-min: ——, 5-min: ——, 15-min: ——, 30-min: ——, 60-min: ——, 120-min: ——; single-ensemble VI-ESM curves from Figure 5.3b for reference: - - -; lines that connect equal K values across curves ⋯⋯.

Table 5.2: Contingency table for the De Kooy (#235) station with different operators applied to the multi-ensemble nowcast; headers and other information are analogue to Table 5.1.

	Nowcast	FP	FN	TP	TN	HR	FPR	H_{now}	H_{true}
	perfect	0.00	0.00	7.50	92.49	100.00	0.00	727	727
max	5-min	2.31	0.86	6.62	90.21	88.53	2.50	815	629
	15-min	4.23	0.77	6.71	88.29	89.69	4.57	1057	628
	120-min	17.09	1.26	6.26	75.39	83.29	18.48	1810	624
min	5-min	0.60	2.09	5.39	91.92	72.06	0.65	271	629
	15-min	0.25	3.25	4.24	92.27	56.60	0.27	174	628
	120-min	0.10	6.81	0.70	92.39	9.34	0.11	15	624
mean	5-min	2.31	0.86	6.62	90.21	88.53	2.50	475	629
	15-min	4.23	0.77	6.71	88.29	89.69	4.57	467	628
	120-min	17.09	1.26	6.26	75.39	83.29	18.48	336	624
median	5-min	1.23	1.31	6.17	91.29	82.48	1.33	459	629
	15-min	1.27	1.64	5.85	91.24	78.14	1.38	423	628
	120-min	1.79	3.89	3.62	90.70	48.21	1.93	196	624

FN and FP, respectively. It should not be possible to achieve lower values (with straightforward methods). The median operator and single-ensemble values are close. However, the latter has slightly better FN values. From the table, it appears that balanced FP and FN values lead to vertical iso-lines, whereas high values for FP shift the iso-lines to the right. Vice-versa, high FN shift iso-lines to the left. To conclude, the min operator is not a good strategy, due to the underestimating tendency of the nowcasting ensemble. Depending on the goal of the turbine owner the median, mean or max operator could be an appropriate choice.

5.4. Conclusions
The results showed that a state-of-the-art nowcasting system can be used to drive an ESM and achieve meaningful lifetime gains with limited AEP loss. The 5-minute and 15-minute lead times of the nowcasts provide sufficient accuracy with enough response time to change the speed of the turbine. However, the nowcast-controlled ESM still operates far from the Pareto front. With the current state-of-the-art, achieving a lifetime increase of a factor of five for a penalty of about 1 % in AEP seems possible. Depending on the AEP losses caused either by erosion and imperfect repairs or by applying leading-edge protection systems, this may be a worthwhile strategy to mitigate rain erosion damage. The results also showed that the VI-ESM significantly outperforms the V-ESM. Hence, even though the VI-ESM requires a forecast of the rain intensity, it should always be the preferred strategy.

The probabilistic information in the multi-ensemble nowcast can be used to improve either the performance or predictability of the ESM. This study also demonstrated that improvements to the skillfulness of nowcasts can drastically improve the viability of the ESM.

5

Bibliography

Barfknecht, N. and von Terzi, D.: On the significance of rain droplet slowdown and deformation for leading-edge rain erosion, Wind Energy Science Discussions, 2023, 1–42, https://doi.org/10.5194/wes-2023-169, 2023.

Barfknecht, N. and von Terzi, D.: Drop-size-dependent effects in leading-edge rain erosion and their impact for erosion-safe mode operation, Wind Energy Science Discussions, 2024, 1–49, https://doi.org/10.5194/wes-2024-33, 2024.

Bech, J. I., Johansen, N. F.-J., Madsen, M. B., Hannesdóttir, Á., and Hasager, C. B.: Experimental study on the effect of drop size in rain erosion test and on lifetime prediction of wind turbine blades, Renewable Energy, 197, 776–789, https://doi.org/10.1016/j.renene.2022.06.127, 2022.

DOWA: 10 year average wind speed (F) and Weibull scale (a) and shape parameter (k) for height 150m, Website accessed 02.01.2024, 2020, https://www.dutchoffshorewindatlas.nl/atlas/image-library/image-library/parameters-per-height-150m.

Gaertner, E., Rinker, J., Sethuraman, L., Zahle, F., Anderson, B., Barter, G. E., Abbas, N. J., Meng, F., Bortolotti, P., Skrzypinski, W., et al.: Definition of the IEA 15-Megawatt Offshore Reference Wind Turbine, Tech. rep., National Renewable Energy Lab.(NREL), Golden, CO (United States), 2020.

Imhoff, R. O., Brauer, C. C., Overeem, A., Weerts, A. H., and Uijlenhoet, R.: Spatial and Temporal Evaluation of Radar Rainfall Nowcasting Techniques on 1,533 Events, Water Resources Research, 56, e2019WR026 723, https://doi.org/10.1029/2019WR026723, 2020.

Imhoff, R. O., Brauer, C., van Heeringen, K.-J., Leijnse, H., Overeem, A., Weerts, A., and Uijlenhoet, R.: A climatological benchmark for operational radar rainfall bias reduction, Hydrology and Earth System Sciences, 25, 4061–4080, https://doi.org/10.5194/hess-25-4061-2021, 2021.

KNMI: Precipitation - radar/gauge 5-minute ensemble nowcast of precipitation over the Netherlands, Website accessed 01.09.2023, 2023a, https://dataplatform.knmi.nl/dataset/precipitation-nl-ensemble-nowcast-5min-1-0.

KNMI: Precipitation - 5 minute precipitation accumulations from climatological gauge-adjusted radar dataset for The Netherlands (1 km) in KNMI HDF5 format, Website accessed 01.09.2023, 2023b, https://dataplatform.knmi.nl/dataset/rad-nl25-rac-mfbs-5min-2-0.

KNMI: Uurgegevens van het weer in Nederland, Website accessed 01.09.2023, 2023c, https://www.knmi.nl/nederland-nu/klimatologie/uurgegevens.

Lin, C., Vasić, S., Kilambi, A., Turner, B., and Zawadzki, I.: Precipitation forecast skill of numerical weather prediction models and radar nowcasts, Geophysical Research Letters, 32, https://doi.org/10.1029/2005GL023451, 2005.

Overeem, A., Uijlenhoet, R., and Leijnse, H.: Full-year evaluation of nonmeteorological echo removal with dual-polarization fuzzy logic for two C-band radars in a temperate climate, Journal of Atmospheric and Oceanic Technology, 37, 1643–1660, https://doi.org/10.1175/JTECH-D-19-0149.1, 2020.

Pulkkinen, S., Nerini, D., Pérez Hortal, A. A., Velasco-Forero, C., Seed, A., Germann, U., and Foresti, L.: Pysteps: an open-source Python library for probabilistic precipitation nowcasting (v1.0), Geoscientific Model Development, 12, 4185–4219, https://doi.org/10.5194/gmd-12-4185-2019, 2019.

Shankar Verma, A., Jiang, Z., Ren, Z., Caboni, M., Verhoef, H., van der Mijle-Meijer, H., Castro, S. G., and Teuwen, J. J.: A probabilistic long-term framework for site-specific erosion analysis of wind turbine blades: A case study of 31 Dutch sites, Wind Energy, 24, 1315–1336, https://doi.org/10.1002/we.2634, 2021.

Tilg, A.-M., Hasager, C. B., Kirtzel, H.-J., and Hummelshøj, P.: Brief communication: Nowcasting of precipitation for leading-edge-erosion-safe mode, Wind Energy Science, 5, 977–981, https://doi.org/10.5194/wes-5-977-2020, 2020.

5

6

Conclusions

6.1. Summary

The objective of this thesis was to:

> Understand which precipitation conditions and physics promote erosion and how this gained understanding can be used in the erosion-safe mode.

From this, four key research questions were formulated in Section 1.3 that together form the thesis arc. These are answered in the following.

Chapter 2: Does the erosion-safe mode have the potential to be a viable erosion mitigation strategy?

The results have shown that the ESM can lead to a lower AEP loss than a mildly eroded blade (or a blade that is equipped with a LEP system that leads to a similar loss). However, this result is enormously dependent on the site characteristics. Frequent (damaging) rain and higher site mean wind speeds reduce the ESM's viability.

Leading-edge erosion only causes a small loss in AEP for high-mean wind speed sites. For such sites, the turbine operates for a significant amount of time in the rated power region. However, the viability of the ESM increases as the mean wind speed decreases due to more operation in the partial load region. While AEP loss estimation using XFoil is simplistic, it nevertheless is able to provide trends. These trends highlight the need to understand which precipitation conditions contribute to erosion, as not all precipitation events cause the same degree of damage. For example, the ESM might be a good strategy if most of the total rain column falls in a short time (during a year).

The results are conservative since repair costs were neglected. Only costs due to AEP loss were considered. This assumption plays in the favor of the ESM, which, in

theory, does not necessitate maintenance and repair. Or, in the worst-case scenario, it only requires repair less than a handful of times during the entire lifetime of the blade. To conclude, it was shown that the selection of the most suitable LEP solution is the result of a trade-off.

Chapter 3: How do rain droplets behave in the vicinity of the blade and how does this behavior influence leading-edge erosion?
Rain droplets and wind turbine blades interact aerodynamically as they approach each other. Shortly before impact, droplets undergo considerable deformation into the shape of an oblate spheroid. Depending on the Weber number, droplets will transition into one of the several distinct droplet breakup modes. Hence, impacting rain droplets are not circular.

The interaction reduces the relative speed between the blade and the droplet. When viewed from the blade, an incoming droplet appears to slow down. The deformation and breakup greatly increase the slowdown of the droplet in comparison to droplets that were assumed to remain circular. The droplet slowdown can be over 10 m/s.

The slowdown profoundly influences the formation of erosion damage. Neglecting it will underestimate the erosion lifetime of a particular coating by up to a factor of two. The slowdown effect is highly sensitive to the droplet diameter and the aerodynamic nose radius of the blade's airfoil. Smaller droplets and larger aerodynamic nose radii lead to significantly more slowdown. Due to its dependency on the droplet diameter, the slowdown and deformation effect can be called a drop-size effect. Since the number of larger droplets increases as the rain intensity goes up, the slowdown effect suggests that, for the same water column, rain intensities do not contribute equally toward damage formation. This hints at a potential lever for the ESM.

Chapter 4: How do drop-size-dependent effects influence leading-edge erosion and erosion-safe mode operation?
Drop-size effects suggest that large droplets are much more erosive than their smaller counterparts, even when accounting for the difference in water volume due to the droplet diameter. Neglecting drop-size effects suggests that, for the investigated turbine and site, droplets up to 1.26 mm are responsible for 50 % of all erosion damage. By properly taking into account drop-size effects, this value changes to 2.00 mm.

In total, four individual drop-size effects have been identified. Of these, three proved significant, with the major contributors being the slowdown and deformation effect and the drop-size-dependent damage law of Bech et al. (2022). The higher erosiveness of the larger droplets can be attributed to their higher impact speed and the lower incubation time in the, for wind turbines, relevant impact velocity range.

Drop-size effects increase the viability of the erosion-safe mode. They resolve deficiencies in the modeling of the erosiveness of high rain-intensity events. In particular, with proper modeling of drop-size effects, 50 % of the erosion damage is caused by the 10.65 % highest rain-intensity events. Without proper modeling, this value is about 21 %. Drop-size effects also influence the viability of the optimal ESM strategies. An ESM that controls the turbine based on wind speed and rain intensity can provide a lifetime extension factor of 9.5 when drop-size effects are neglected. Accounting for them increases the ESM's lifetime extension factor (LX) to 13.1.

Chapter 5: Can state-of-the-art precipitation nowcasting be used to effectively drive the erosion-safe mode?

The investigated nowcast, which is representative of the current state-of-the-art, provided a skillful prediction of the weather up to 30 minutes ahead. Longer lead times lead to a considerable reduction in performance. This can be attributed to an increase in false negative predictions. Said differently, the nowcast fails to predict rain as the lead times increase. These false negative predictions above a 30-minute lead time can be attributed to missed convective precipitation events (thunderstorms), which form in a time frame of 30 minutes and less and thus cannot be captured by a mainly extrapolation-based nowcast.

The five and 15-minute predictions lead to an attainable lifetime extension factor of about five for an AEP loss of 1 %. The Pareto front suggests a maximum LX of 8.6 for this AEP loss. This is considerably lower than the 13.1 reported in Chapter 4. However, this difference can be attributed to some degree to the short time frame of less than a year. Nevertheless, the results indicate that a considerable difference still exists between the theoretical and practical achievable LX. It was also shown that the choice of a target {AEP loss, LX} tuple could, when the ESM is fed with an actual nowcast, lead to a different tuple (position) on the Pareto front. Hence, how well an ESM *behaves* is of concern.

It was possible to extract useful behavior from the probabilistic information within the nowcast by using some straightforward mathematical operators. These can be used to either improve the performance of the ESM or steer its behavior with respect to the tuple setpoint. To conclude, it was shown that already, with the advancements made in this thesis, it is possible to operate in an ESM and achieve meaningful LX for a moderate AEP loss.

6.2. Implications

The results of this thesis have profound implications for the field of leading-edge erosion.

Erosion testing and research: The investigated drop-size effects change the parameter space of erosion by shifting the origin of damage to higher droplet diameters. This needs to be taken into account when performing experimental or

numerical research by choosing the proper droplet size. Drop-size effects are also site-dependent due to their reliance on the wind, droplet and rain intensity distributions. Hence, different sites have different parameter spaces that need to be accounted for. Thus, to ensure accuracy in erosion forecasting models, drop-size effects must be included.

The deformation and slowdown effect, in particular, cannot be neglected. The current assumption of impacting rain droplets being circular is insufficient. The slowdown effect is most likely also occurring in rotating-arm test-rigs, albeit at a lower magnitude than on full-scale blades. This needs to be accounted for by, for example, correcting the V-H curves.

Design of the ESM: The ESM cannot be used efficiently without accurately quantifying drop-size effects. The entire idea of the ESM is to curtail the turbine only during the specific precipitation events that contribute significantly toward erosion. Without properly modeling drop-size effects, these events cannot be characterized accurately. This thesis made several conservative assumptions concerning the drop-size effects. Hence, the actual performance of the ESM is most likely still underestimated. More research is required to identify the ESM's true performance.

The ESM cannot be employed without a weather forecast. Current state-of-the-art nowcasts provide a skillfulness that already enables the usage of the ESM. However, these nowcasts still shed significant performance, which can only be recovered by improving their accuracy, especially for longer lead times.

To summarize, the ESM depends on two aspects. First, there is the ESM strategy, i.e., the decision on how to curtail based on the site characteristics, turbine, and weather. Here, the drop-size effects play a significant role. Second, there is the practical implementation, where weather prediction is arguably the most important aspect.

Hail and dust: Another aspect is the potential applicability of the slowdown effect to hail and dust erosion. In principle, both should also interact aerodynamically with the blade, but a different parameter space applies. Deformation does not occur, potentially reducing the expected slowdown. Hail, which is per definition larger than 5 mm, has a slightly lower density than rain. It is not necessarily round but can have random shapes, including shapes that resemble a flattened oblate spheroid (Allen et al., 2020). In the case of hail, the slowdown can probably be neglected due to the parameter space. However, hail features a high terminal velocity, which is important for the drop-size effect discussed in Section 4.2.3. Airborne dust, on the other hand, might be more affected due to its smaller size. Typical sizes are $62.5 \leq \phi_{\text{sand}} < 2000$ μm and $4 \leq \phi_{\text{silt}} < 62.5$ μm, where most airborne dust is composed of silt (Attiya and Jones, 2020). The density of dust $\rho_{\text{quartz}} = 2650$ kg/m^3 is, however, higher.

Design of blades: The high sensitivity of the slowdown effect implies that erosion is not only specific to the leading-edge material but also specific to the aerodynamic design of the turbine. The sensitivity to the aerodynamic nose radius R_c opens a path to erosion-resistant blade design. The impact speed of rain droplets can be reduced by increasing R_c, either by increasing the chord or choosing airfoils with a larger R_c/c. The lever for the latter is mostly the thickness of the airfoil. However, optimizing R_c/c for airfoils of equal thickness should also be possible. It is important to note that potential gains in erosion resistance must be weighed against potential aerodynamic losses or other structural aspects.

6.3. Outlook

At the end of this thesis, the author would like to express his opinions and provide an outlook for the future, particularly on two topics in leading-edge erosion. First, it is argued that research in erosion mitigation will stay relevant in the future. Secondly, the future role of the erosion-safe mode is discussed by briefly highlighting some of its opportunities and threats.

A question discussed in the erosion community is: Will research in leading-edge erosion, as improvements are made, be relevant in the future, or is the problem (soon) going to be solved? At conferences, it is often heard (as a sales pitch) that a particular LEP solution never debonds, does not degrade, and does not cause an AEP loss. Solving erosion would, therefore, be merely an act of equipping all blades with that (perfect) LEP solution. Whether these claims are true or not is hard to verify. However, even if a particular LEP solution is near perfect for a present turbine, this must not hold true for future turbines.

A closer look at the design-tip-speed of a turbine is taken to understand this aspect. In the past, the size of turbines steadily increased along with their tip-speed. The IEA 10MW has a tip-speed of 90 m/s. The tip-speed of the newer IEA 15MW is 95 m/s and for the newest IEA 22MW a tip-speed of 105 m/s was chosen. An increase in the turbine's tip-speed is often regarded as advantageous since it allows for a lower generator torque at the same turbine power. This reduces the size and mass of the drivetrain, which leads to positive trickle-down effects in the design of the nacelle and tower. Certain requirements can also limit that growth in speed, for example, onshore, where acoustic considerations play an important role. In offshore applications, noise is of far lesser importance, and hence, the speeds can be higher and growth is permissible. Based on the findings in this thesis, the argument is made that erosion considerations also limit the tip-speed since erosion lifetime drastically decreases with increasing droplet impact speeds. If the tip-speed is chosen too high, the erosion lifetime might be so low that constant repairs are required, driving a particular turbine design in a non-economical direction. Recall, with $\beta = 10$ in Equation 3.1, a moderate increase of about 7 % in

the tip-speed reduces the erosion lifetime by half. The hypothesis is formed that a currently satisfactory LEP solution will give the turbine designer the desire to increase the tip-speed to improve the turbine design holistically, necessitating better LEP systems. Thus, a feedback loop is formed between the turbine designer on one side and LEP developers on the other. This aspect is visualized in Figure 6.1.
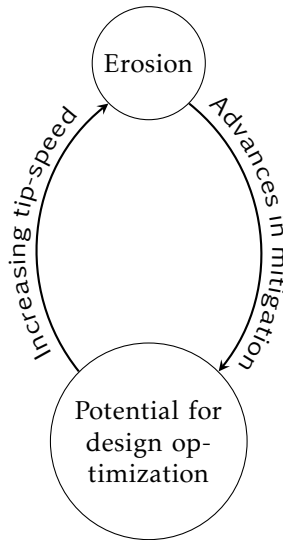
Figure 6.1: Repeating cycle of advances in erosion mitigation and increasing tip-speeds.

New aspects are also continuously introduced into the erosion community, necessitating new research. Two novel aspects of erosion were presented at the 5th International Symposium on Leading Edge Erosion of Wind Turbine Blades. Leon Mishnaevsky (DTU) presented *Project Premise*, which plans to investigate offshore microplastic pollution due to erosion. At the same conference, Allen Hall (Weather Guard Lightning Tech) argued that he could see from field observations that eroded blades are much more susceptible to lightning-induced damage. The future will tell whether these aspects are relevant. But they illustrate that there is a *beyond current research* and that, in the author's opinion, erosion research will be required for many years to come.

This thesis has shown that the erosion-safe mode can be an attractive method for mitigating erosion. The question is how good the ESM needs to be so that a natural desire is created for its utilization. To this end, the author argues that a lifetime extension of around ten should be achieved for *acceptable cost*. Acceptable cost could be defined as the cost that are equal or less to the cost associated with maintenance and AEP loss of an LEP solution or the associated cost of a blade that is operated with the *let it erode and repair when necessary* strategy. The lifetime extension of

ten is based on the conservative assumption that an unprotected blade will last for about one year in the field before signs of erosion appear. If the lifetime of a turbine is set to 30 years, then blade repair is merely required two times during its entire lifespan, a number that certainly seems attractive. If the lifetime of an unprotected blade can be increased to three years, e.g., by advances in materials and coatings, then the ESM will mitigate erosion over the turbine's entire lifetime. Additionally, the erosion lifetime is not constant over the entire blade length but increases toward the root of the blade. Hence, a blade section located further inboard might have a significantly higher lifetime in its unprotected state, so the ESM will always fully protect that section over the entire turbine's lifetime. Repairs are then only necessary in small regions outboard of the blade.

However, the ESM suffers from a *psychological* component that does not play in its favor. The following quote summarizes the problem nicely:

> *"AEP loss is guaranteed, damage reduction is expected."*
>
> - Jens Visbech Madsen (DTU), *5th Int. Symp. on LEE of WT Blades, 2024*

The exact AEP loss that is associated with erosion is still debated. The consensus in the research community is currently that the AEP loss can be up to several percent. However, measuring the AEP loss in the field can be challenging. So, a situation is created in which there is uncertainty about AEP loss due to erosion but certainty about the AEP loss due to the ESM. This, mixed with uncertainty about the expected damage reduction, makes many in the field of erosion skeptical about the ESM.

To make the ESM a success, the erosion community needs certainty. This can come only by continuing the (multidisciplinary-)research but also by having an open-mindedness for new ideas along with the imagination to see their potential.

BIBLIOGRAPHY

Allen, J. T., Giammanco, I. M., Kumjian, M. R., Jurgen Punge, H., Zhang, Q., Groenemeijer, P., Kunz, M., and Ortega, K.: Understanding Hail in the Earth System, Reviews of Geophysics, 58, e2019RG000 665, https://doi.org/10.1029/2019RG000665, 2020.

Attiya, A. and Jones, B.: Assessment of mineralogical and chemical properties of airborne dust in Iraq, SN Applied Sciences, 2, 1614, https://doi.org/10.1007/s42452-020-03326-5, 2020.

Bech, J. I., Johansen, N. F.-J., Madsen, M. B., Hannesdóttir, Á., and Hasager, C. B.: Experimental study on the effect of drop size in rain erosion test and on lifetime prediction of wind turbine blades, Renewable Energy, 197, 776–789, https://doi.org/10.1016/j.renene.2022.06.127, 2022.

6

A

The impingement collected by a wind turbine blade

This appendix provides a formal derivation for the impingement collected by a blade. Impingement is the damage metric used in this study's damage model. Previous studies have not shown such a derivation, leaving potential ambiguity in how impingement should be computed (López et al., 2023; Visbech et al., 2023). Additional clarification has become necessary due to the introduction of the slowdown effect in leading-edge erosion (Barfknecht and von Terzi, 2023). The first part gives a general derivation of impingement and discusses several solution approaches. The second part determines $V_{collection}$.

The content of this chapter was published in:

A.1. Derivation of the impingement equation and evaluation approaches

Impingement is the amount of water collected by a blade. The concept can be viewed in a more tangible way by considering a bucket mounted to the leading edge of a wind turbine blade. The water inside the bucket, after a certain operational time, is the impingement. Two different impingement metrics can be defined: $H^{(3)}$ and $H^{(1)}$. The former represents the intercepted water volume, while the latter represents the intercepted water column $H^{(1)}$. In particular, $H^{(1)} = H^{(3)}/dA$, where dA is an (infinitesimal) surface element of the blade. Therefore, we find for the dimensions $[H^{(1)}] = L$ and $[H^{(3)}] = L^3$.
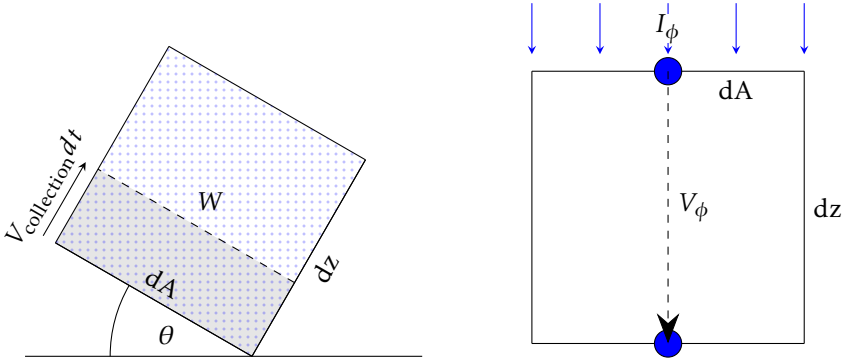
(a) Flow domain of air with rain (blue dots); it is oriented at an arbitrary blade angle θ and is swept by a wind turbine blade section dA; the swept volume during dt is indicated in light gray.

(b) Control volume for the derivation of W; rain enters at the top of the control volume; it subsequently falls through the volume until it reaches the lower boundary.

Figure A.1: Representation of the flow domain and control volume used for deriving $H^{(3)}$.

The general form of impingement for a blade sweeping a flow domain of air that contains rain is

$$H^{(3)} = \int_0^T \frac{\partial H^{(3)}}{\partial t} dt, \tag{A.1}$$

where t is the time and $\partial H^{(3)}/\partial t$ is the volume of water collected per unit time. From Figure A.1a one can see that

$$\frac{\partial H^{(3)}}{\partial t} = W V_{\text{collection}} dA, \tag{A.2}$$

where $V_{\text{collection}}$ is the speed at which the flow domain is swept by the blade. dA is an (infinitesimal) surface element on the leading edge and W is the volume of

water (rain) contained per volume of air. W can also be named the water volume fraction. Per definition,

$$W = \frac{d\mathrm{Vol_{water}}}{d\mathrm{Vol_{air}}}. \tag{A.3}$$

To find W we consider Figure A.1b. The volume of air is given by

$$d\mathrm{Vol_{air}} = dA dz = dx dy dz. \tag{A.4}$$

The volume of water contained inside the control volume can be calculated by first considering the control volume to be empty. Water is entering the volume via its top face. The time is recorded when the water reaches the lower boundary. At that time, the fluxes from the top and bottom face cancel out. Hence,

$$\mathrm{dVol_{water}} = I dA dt_{\mathrm{fall\ through}}. \tag{A.5}$$

I is the rain intensity, or interpreted differently, it is the normalized surface flux of water (volume) in the dimensions $[LT^{-1}]$. $dt_{\mathrm{fall\ through}}$ is the fall-through time of the rain. From Figure A.1b,

$$dt_{\phi,\mathrm{fall\ through}} = \frac{dz}{V_\phi}. \tag{A.6}$$

V_ϕ is the terminal velocity of the rain. However, as shown in Figure 4.3, the terminal velocity is a function of the droplet diameter and thus not universal. Hence, W is dependent on ϕ. We need to find W_ϕ, the water volume fraction as a function of the droplet diameter. For that, we consider the rain intensity of every droplet diameter, which is

$$I_\phi = f_{\phi,\mathrm{plane}} I. \tag{A.7}$$

$f_{\phi,\mathrm{plane}}$ is the distribution of water (mass) through a plane as a function of the drop diameter, see Equation 4.11. Note that $\int_0^\infty f_{\phi,\mathrm{plane}} d\phi = 1$. By combining Equations A.3, A.4, A.5, A.6 and A.7, we obtain

$$W_\phi = \frac{f_{\phi,\mathrm{plane}} I}{V_\phi}. \tag{A.8}$$

Inserting into Equation A.2 yields

$$\frac{\partial H_\phi^{(3)}}{\partial t} = W_\phi V_{\mathrm{collection}} dA = \frac{f_{\phi,\mathrm{plane}} I}{V_\phi} V_{\mathrm{collection}} dA. \tag{A.9}$$

Later it will be shown that $V_{\mathrm{collection}}$ is also a function of the droplet diameter! By

A

integrating over the droplet diameter, we obtain

$$\partial_t H^{(3)} = dA \int_0^\infty \frac{f_{\phi,\text{plane}} I}{V_\phi} V_{\text{collection}} d\phi, \tag{A.10}$$

or

$$\partial_t H^{(1)} = \int_0^\infty \frac{f_{\phi,\text{plane}} I}{V_\phi} V_{\text{collection}} d\phi. \tag{A.11}$$

For conciseness, we define $\partial H/\partial t = \partial_t H$. Finally, $H^{(1)}$ and analogously $H^{(3)}$ can be obtained by

$$H^{(1)} = \int_0^T \partial_t H^{(1)} dt, \tag{A.12}$$

where T is the time that rain is collected. The full version of Equation A.11 is obtained by substituting $V_{\text{collection}}$. It is determined in the next section. For the definition of $V_{\text{collection}}$ see Equation 4.21. The equation becomes

$$\partial_t H^{(1)}(I, V_{\text{wind}}, \theta) = \int_0^\infty \frac{f_{\phi,\text{plane}} I}{V_\phi} \bigg(V_{\text{sec}}(1 + a') \cos\varphi + V_\phi \cos\theta \cos\varphi \tag{A.13}$$
$$+ V_{\text{wind}}(1 - a) \sin\varphi \bigg) d\phi,$$

where in parenthesis the independent variables are given that change during turbine operation. From this equation, simplified versions can be derived. Noting that V_{sec} is significantly larger than all other summands and $\cos\varphi \approx 1$, one obtains

$$\partial_t H^{(1)} \approx V_{\text{sec}} \int_0^\infty \frac{f_{\phi,\text{plane}} I}{V_\phi} d\phi = V_{\text{sec}} \int_0^\infty W_\phi d\phi = W V_{\text{sec}}. \tag{A.14}$$

For $V_{\text{wind}} = 0$, $V_{\text{sec}} = 0$, $\varphi = 0°$ and a blade position of $\theta = 0°$, Equation A.13 reduces to

$$\partial_t H^{(1)} = I \int_0^\infty f_{\phi,\text{plane}} d\phi = I, \tag{A.15}$$

which is simply the rate of rain falling through an imaginary plane, or expressed differently, the rate of rain caught by a rain gauge located on the ground under ideal conditions.

Equation A.12 requires the continuous time integration over $\partial_t H^{(1)}$. However, it is too difficult or potentially even impossible to calculate this definite integral. A solution approach is to discretize this equation by

$$H^{(1)} = \sum_{i=1}^N \Big(\partial_t H^{(1)}(I(t_i), V_{\text{wind}}(t_i), \theta(t_i)) \Big)_i \Delta T_i, \tag{A.16}$$

where ΔT_i is a fixed time-interval. However, for studies that do not use discrete input data (like this one), it is more convenient to express the time integral probabilistically using probability density functions. According to the law of large numbers the mean converges to the expected value, i.e.,

$$\frac{1}{T}\int_0^T y(x(t))dt = \int_{x_L}^{x_U} y(x)f_x dx, \tag{A.17}$$

where y is a function. $x(t)$ is variable depending on t, for example, the rain intensity. f_x is the pdf of x so that $\int_{x_L}^{x_U} f_x dx = 1$. Subscripts U and L indicate the upper and lower bounds of integration. With this, one can rewrite Equation A.12 as

$$H^{(1)} = \int_0^T \partial_t H^{(1)}(x_1(t),...,x_n(t))dt \tag{A.18}$$

$$= T\int_{x_{1_L}}^{x_{1_U}} ... \int_{x_{N_L}}^{x_{N_U}} \partial_t H^{(1)}(x_1,...,x_n)f_{x_1}...f_{x_N}dx_1...dx_N$$

$$= T\int_{x_{1_L}}^{x_{1_U}} ... \int_{x_{N_L}}^{x_{N_U}} \partial_t H^{(1)}_{x_1,...,x_N}(x_1,...,x_n)dx_1...dx_N.$$

Note that $\partial_t H^{(1)}(x_1(t),...,x_n(t)) \neq \partial_t H^{(1)}(x_1,...,x_n)$. Additionally, the definition

$$\partial_t H_x^{(1)}(x) = \partial_t H^{(1)}(x)f_x \tag{A.19}$$

is used. In this study four integrals over the variables $I, V_{\text{wind}}, \theta, \phi$ need to be evaluated. However, the integral over ϕ is not directly visible in Equation A.18 but is somewhat hidden in Equation A.13. Additionally, both equations have a similar form, since they both integrate over at least one pdf. To improve readability, we define, similar to Equation A.9,

$$\partial_t H_\phi^{(1)}(\phi) = \partial_t H^{(1)}(\phi)f_{\phi,\text{plane}}, \tag{A.20}$$

with

$$\partial_t H^{(1)}(\phi) = \frac{I}{V_\phi}V_{\text{collection}}. \tag{A.21}$$

Notice that $\partial_t H^{(1)} \neq \partial_t H^{(1)}(\phi)$! By transferring Equation A.12 into the probabilistic

form, one obtains the equation for impingement used in this study. It reads

$$H^{(1)} = T \int_0^\infty \int_0^\infty \int_{0°}^{360°} \int_0^\infty \partial_t H_{I,V_\text{wind},\theta,\phi}(I,V_\text{wind},\theta,\phi)d\phi d\theta dV_\text{wind}dI \qquad \text{(A.22)}$$

$$= T \int_0^\infty \int_0^\infty \int_{0°}^{360°} \int_0^\infty \partial_t H(I,V_\text{wind},\theta,\phi)f_I f_{V_\text{wind}} f_\theta f_{\phi,\text{plane}}d\phi d\theta dV_\text{wind}dI. \tag{A.23}$$

Substituting Equations A.21 and 4.21 leads to

$$H^{(1)} = T \int_0^\infty \int_0^\infty \int_{0°}^{360°} \int_0^\infty \frac{I}{V_\phi}\bigg(V_\text{sec}(1+a')\cos\varphi + V_\phi \cos\theta\cos\varphi \qquad \text{(A.24)}$$

$$+ V_\text{wind}(1-a)\sin\varphi\bigg)f_I f_{V_\text{wind}} f_\theta f_{\phi,\text{plane}}d\phi d\theta dV_\text{wind}dI. \tag{A.25}$$

This equation is similar to the Palmgren-Miner damage rule from Equation 4.1. In the main body of this study, the superscript is omitted. For all practical purposes, the integrals, once again, need to be evaluated numerically, for example, with a simple trapezoidal rule.

When it is required to compute the impingement directly from time-dependent meteorological data, it might be more convenient to formulate $H^{(1)}$ in a hybrid continuous-discrete form. The rain intensity I and the wind speed V_wind are usually readily available as discrete meteorological data sets. Hence, I and V_wind are considered to be discrete and constant over one time-interval ΔT_i. However, for θ and for ϕ usually no time-dependent data sets are available. For example, it is unlikely that discrete measurements are taken multiple times during one blade rotation. Hence, they should be considered continuous and instead described by their respective probability density function. As a result, one obtains

$$H^{(1)} = \sum_{i=1}^N \left(\int_{0°}^{360°} \int_0^\infty \partial_t H^{(1)}_{\theta,\phi}(I(t_i),V_\text{wind}(t_i),\theta,\phi)d\phi d\theta\right)_i \Delta T_i. \tag{A.26}$$

A.2. Determination of $V_\text{collection}$

In this section, $V_\text{collection}$ is determined, which is slightly different from V_impact. The correct determination is important since any error linearly propagates into the accumulated impingement.

Figure A.2a shows a control volume that is fixed in space (air) and contains rain. The volume is swept by a blade section with area dA and speed $\vec{V}_\text{sec} \cdot \vec{n}_\text{LE}$. It is aligned with the blade's leading edge in such a way that $\vec{n}_\text{LE} = \vec{u}$ where $d\vec{U} = \vec{u}dA$. $\vec{F}$ is the flux vector across the control volume's boundaries. The flux describes the
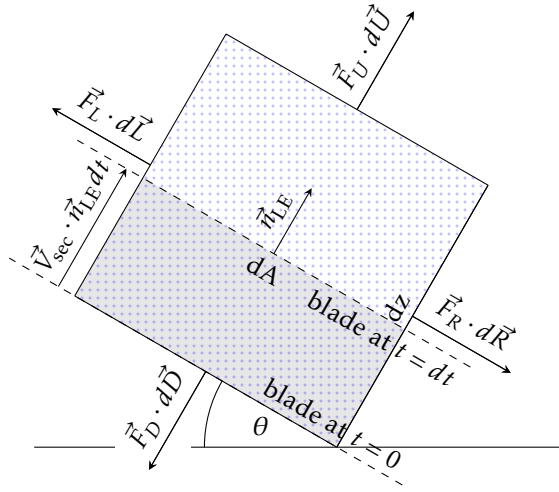
(a) Control volume fixed in the air; it is swept by a wind turbine blade section dA; the swept volume during dt is indicated in light gray.
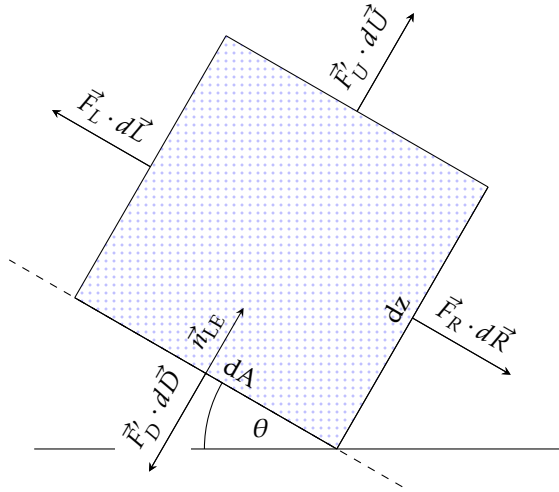
(b) Control volume mapped to reference frame of the blade; the boundary D has become the leading-edge of the blade.

Figure A.2: Control volume of air containing rain with blade section; oriented at an arbitrary blade angle θ.

rain that enters and leaves the control volume. It is more convenient to map the problem into the reference frame of the blade by defining the adjusted fluxes $\vec{F}'_U$ and $\vec{F}'_D$, yielding Figure A.2b.

For the mapped problem, one can write the continuity equation of the control volume as

$$\frac{\partial m}{\partial t} = \iint_S \vec{F} \cdot d\vec{S}, \tag{A.27}$$

where m is the mass of water inside the control volume and $\vec{S}$ is the surface vector of the control volume. $\partial m / \partial t$ is the net rate of change of the mass inside the control volume. $\iint_S \vec{F} \cdot d\vec{S}$ is the mass entering or leaving the control volume due to the velocity of the rain field.

The surface integral over the boundary S is evaluated by integrating over all four sides separately, that is

$$\iint_S \vec{F} \cdot d\vec{S} = \iint_R \vec{F}_R \cdot d\vec{R} + \iint_L \vec{F}_L \cdot d\vec{L} + \iint_U \vec{F}'_U \cdot d\vec{U} + \iint_D \vec{F}'_D \cdot d\vec{D}. \tag{A.28}$$

It is assumed that, for the length scale of the control volume, the rain field is constant; this implies amongst other $\vec{F}_R = \vec{F}_L = $ const. The fluxes of the left and right faces are, therefore, equal in magnitude and direction. The surface normals are, however, opposite in sign, hence,

$$0 = \iint_R \vec{F}_R \cdot d\vec{R} + \iint_L \vec{F}_L \cdot d\vec{L}. \tag{A.29}$$

Additionally, the bottom boundary boundary is aligned and coincidental with the blade's leading-edge, so that $\vec{d} = -\vec{n}_{LE}$. Thus, the boundary D can be considered as the blade's leading edge. It follows that D is impermeable,

$$\iint_D \vec{F}'_D \cdot d\vec{D} = 0. \tag{A.30}$$

The surface integral becomes

$$\iint_S \vec{F} \cdot d\vec{S} = \iint_U \vec{F}'_U \cdot d\vec{U}. \tag{A.31}$$

Therefore, the net rate of change of mass inside the control volume is

$$\frac{\partial m}{\partial t} = \iint_U \vec{F}'_U \cdot d\vec{U}, \tag{A.32}$$

which can also be interpreted as the rate of mass that is intercepted by the blade. By assuming incompressibility and thus dividing by the density of water ρ, assuming

that $\vec{F}'_U$ is constant over the boundary patch and dividing by the surface area $|\vec{U}|$, one obtains:

$$\partial_t H^{(1)} = \frac{1}{\rho|\vec{U}|} \iint_U \vec{F}'_U \cdot d\vec{U}. \tag{A.33}$$

Due to the transformation of the problem the modified surface flux is

$$\vec{F}'_U \cdot d\vec{U} = \vec{F}_U \cdot d\vec{U} - \vec{F}_{\text{sec}} \cdot d\vec{A}, \tag{A.34}$$

with

$$\vec{F}_U \cdot d\vec{U} = -\rho \left(\int_0^\infty W_\phi \vec{V}_{\text{water}} d\phi \right) \cdot d\vec{U}, \tag{A.35}$$

and

$$\vec{F}_{\text{sec}} \cdot d\vec{A} = -\rho \left(\int_0^\infty W_\phi d\phi \right) \vec{V}_{\text{sec}} \cdot \vec{n}_{\text{LE}} dA. \tag{A.36}$$

The minus signs are required so that mass entering the control volume is positive. Substituting and with $d\vec{U} = dA\vec{u} = dA\vec{n}_{\text{LE}}$:

$$\partial_t H^{(1)} = -\left(\int_0^\infty W_\phi \vec{V}_{\text{water}} d\phi \right) \cdot \vec{n}_{\text{LE}} + \left(\int_0^\infty W_\phi d\phi \right) \vec{V}_{\text{sec}} \cdot \vec{n}_{\text{LE}} \tag{A.37}$$

$$= \int_0^\infty W_\phi \left(\vec{V}_{\text{sec}} - \vec{V}_{\text{water}} \right) \cdot \vec{n}_{\text{LE}} d\phi. \tag{A.38}$$

$\vec{V}_{\text{sec}}$ is given by Equation 4.16. $\vec{V}_{\text{water}}$ can be determined using Figure 4.2 which yields

$$\vec{V}_{\text{water}} \cdot \vec{n}_{\text{LE}} = \begin{bmatrix} -\sin\theta V_{\text{sec}} a' \\ -\cos\theta V_{\text{sec}} a' - V_\phi \\ -V_{\text{wind}}(1-a) \end{bmatrix} \cdot \begin{bmatrix} \sin\theta\cos\varphi \\ \cos\theta\cos\varphi \\ \sin\varphi \end{bmatrix} \tag{A.39}$$

$$= -\left(V_{\text{sec}} a' \cos\varphi + V_\phi \cos\theta \cos\varphi + V_{\text{wind}}(1-a)\sin\varphi \right). \tag{A.40}$$

Here, it is assumed that the rain droplets are advected with the radial and axial induction factor, the wind speed and the terminal velocity. Inserting into Equation A.38 gives

$$\partial_t H^{(1)} = \int_0^\infty W_\phi \left(V_{\text{sec}} \cos\varphi + V_{\text{sec}} a' \cos\varphi + V_\phi \cos\theta \cos\varphi + V_{\text{wind}}(1-a)\sin\varphi \right) d\phi dA. \tag{A.41}$$

Comparing with Equation A.11, one obtains

$$\partial_t H^{(1)} = \int_0^\infty W_\phi V_{\text{collection}} d\phi. \tag{A.42}$$

with

$$V_{\text{collection}} = V_{\text{sec}}(1 + a')\cos\varphi + V_\phi \cos\theta\cos\varphi + V_{\text{wind}}(1 - a)\sin\varphi. \qquad \text{(A.43)}$$

In comparison to V_{impact}, $V_{\text{collection}}$ does not contain the slowdown velocity. It is possible to define $V'_{\text{collection}} = V_{\text{impact}}$. However, in that case, W_ϕ needs to be corrected. The slowdown is a local phenomenon that occurs in the proximity of the leading edge on the length scale of the aerodynamic nose radius R_c. It reduces the local velocity of the rain droplets but, at the same time, increases the droplet concentration per volume of air. When both factors are accounted for, the flux remains unchanged. The correction for the case $V'_{\text{collection}} = V_{\text{impact}}$ is

$$W'_\phi = \frac{V_{\text{collection}}}{V_{\text{collection}} - V_{\text{slowdown}}\cos\alpha_\phi}. \qquad \text{(A.44)}$$

The conclusion is, therefore, that the slowdown effect decreases the impact speed but does not influence the impingement accumulation rate.

A

BIBLIOGRAPHY

Barfknecht, N. and von Terzi, D.: On the significance of rain droplet slowdown and deformation for leading-edge rain erosion, Wind Energy Science Discussions, 2023, 1–42, https://doi.org/10.5194/wes-2023-169, 2023.

López, J. C., Kolios, A., Wang, L., and Chiachio, M.: A wind turbine blade leading edge rain erosion computational framework, Renewable Energy, 203, 131–141, https://doi.org/10.1016/j.renene.2022.12.050, 2023.

Visbech, J., Göçmen, T., Hasager, C. B., Shkalov, H., Handberg, M., and Nielsen, K. P.: Introducing a data-driven approach to predict site-specific leading-edge erosion from mesoscale weather simulations, Wind Energy Science, 8, 173–191, https://doi.org/10.5194/wes-8-173-2023, 2023.

B

The ESM regime and a method for finding optimal ESM strategies

This appendix aims to develop some of the concepts pertaining to the ESM used in Section 4.3. In Appendix B.1, the operational regime of the ESM is defined. Appendix B.2 provides a semi-analytical approach for finding optimal ESM strategies.

The content of this chapter was published in:

B

B.1. The operational regime of the ESM

For a practical ESM design, it is not desirable to fully stop the turbine (S-ESM) as the erosion damage savings come at a large AEP penalty. This was shown in Figure 4.17a. With the high value of β in mind, a small reduction in the tip-speed can already greatly increase the erosion lifetime of the blade, while maintaining a decent amount of power production. Hence, a practical ESM strategy will attempt to mitigate erosion by only slightly but sufficiently reducing the tip-speed of a turbine. To this end, it is useful to first understand the operational regime of the ESM before a good strategy can be chosen.

The concept of the ESM can be visualized in an {AEP loss, lifetime extension (LX)} diagram. By reducing the tip-speed during precipitation events, a turbine operating in an ESM trades AEP for an extension in its lifetime, i.e., the AEP decreases while the erosion lifetime increases. The regime in which this trade takes place is visualized in Figure B.1. In this figure, the points A, B, C and D and their connecting curves form an operational regime. The turbine can only operate within this regime. Point A represents a turbine during normal operation. This means no ESM is utilized during precipitation events. Hence, the turbine experiences no AEP loss (a potential performance loss due to erosion is not considered here) and, as a result, the normalized lifetime is unity. The turbine operates at Point B when it spins at its minimum rotational-speed (5 rpm for the IEA 15MW reference turbine) during all precipitation events. It is important to note that point B implies that there is a perfect knowledge of the incoming precipitation. Additionally, the turbine must also be able to react infinitely fast to changing precipitation conditions. The region is closed by two highly undesirable operating points. Point C represents the operation at the minimum turbine-speed at all times, including dry (no rain) conditions. As with point B, point C offers the highest LX. However, this comes at the cost of very high AEP losses because the turbine's speed is permanently reduced, effectively de-rating the turbine. The turbine operates at point D when the wind turbine's speed is reduced to its minimum during dry events only, but keeps its nominal speed during precipitation events. Here, no increase in lifetime is achieved. However, a large reduction in AEP is realized, albeit somewhat lower than for point C.

Points A, B, C and D can also be interpreted with respect to the quality of the weather forecast. Point B is realized with a perfect forecast. Point C represents a forecast that indicates precipitation at all times. Point D represents a perfectly inverted forecast. Hence, a forecast that indicates no rain when it actually rains and indicates rain when it is actually dry. Point A can be interpreted as a turbine that is controlled by a weather forecast that never indicates precipitation.

It is straightforward to see that the best ESM is realized when operating on the curve from point A to B, called $\overline{AB}$. It represents the Pareto front of an ESM strat-

egy under the assumption of perfect rain-knowledge and instantaneous turbine-control. The front represents the highest possible lifetime extension for a minimum of AEP loss. In practice, neither perfect knowledge of precipitation nor instantaneous turbine-control can be achieved. Any practical ESM implementation aims to operate as closely as possible to the Pareto front under the practical limitations. The ESM becomes more viable, i.e., more lifetime for a lower AEP loss, if a new Pareto front can be found that is shifted in the direction of the arrow in Figure B.1. The concept is similar to Figure 4.15 and similar conclusions hold.
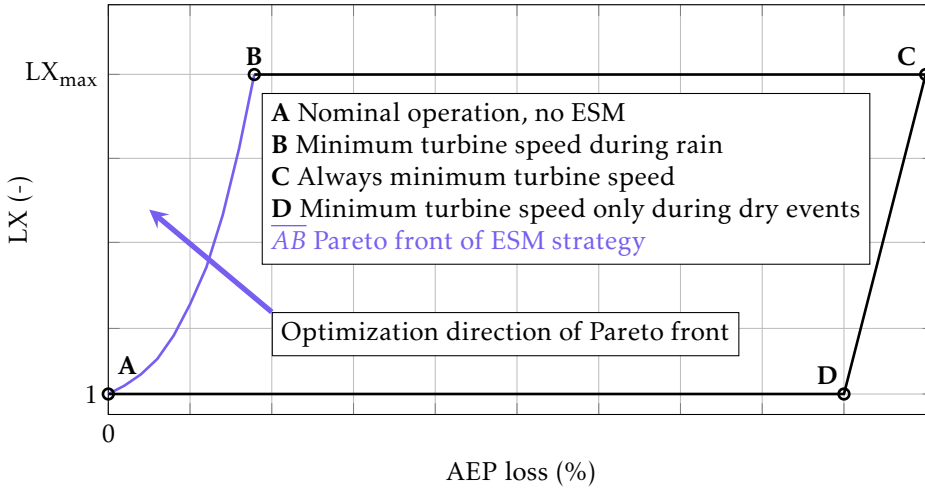
Figure B.1: Operational regime of the ESM spanned by the AEP loss and the lifetime extension.

B.2. A method for finding optimal ESM control strategies

This section describes a semi-analytical approach that can be used to find ESM control strategies that lead to optimal Pareto fronts (see Figure B.1). The ESM strategies that have been presented in the literature were, up to now, heuristic (Barfknecht et al., 2022; Bech et al., 2018). Finding the optimal strategy has not yet been described in the literature. Additionally, by using the optimal strategy for investigating the drop-size effects, ambiguity in the results concerning the *goodness* of the Pareto front is eliminated. The approach presented here is straightforward to implement and computationally light, requiring only a few seconds of wall-clock time to compute.

An ESM strategy is a function determining how the turbine operates under precipitation conditions with the aim to maximize lifetime, i.e., to minimize the rain

B
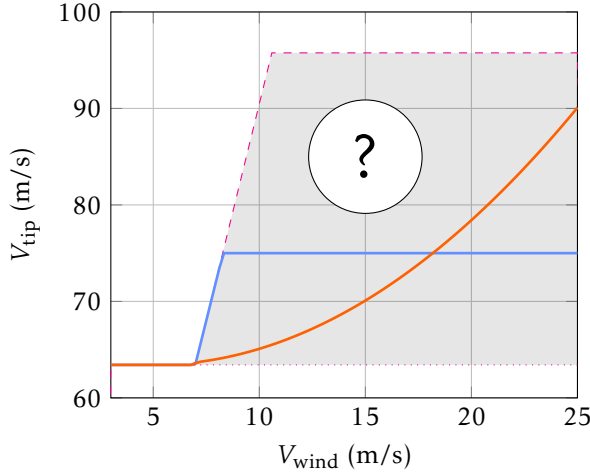
Figure B.2: Operational tip-speed regime of the IEA 15MW turbine as a function of the instantaneous wind speed; $g_{min}(V_{wind})$: ········, $g_{normal}(V_{wind})$: - - - , ESM based on limit (C-ESM): ——, ESM based on a parabolic equation: ——.

erosion damage, and to minimize AEP loss. Understanding that every ESM strategy leads to a unique Pareto front is important. Hence, some strategies are more optimal than others. At the core is a function that relates the turbine's tip-speed to environmental variables. For example,

$$g(V_{wind}, I, ...) = \left\{ g_{min}(V_{wind}) \leq V_{tip} \leq g_{normal}(V_{wind}) \text{ for all } (V_{wind}, I, ...) \right\}, \quad (B.1)$$

where $g_{min}(V_{wind}) = V_{tip, min}$ is the minimum tip-speed and $g_{normal}(V_{wind})$ is the normal piecewise-linear control function of the turbine. Both are shown in Figure B.2 and span an operational regime colored in gray. An ESM strategy is a curve in this regime. Theoretically, a turbine could spin over the entire wind speed range at the maximum tip-speed. However, it will be shown in the following that this is not desirable.

Two straightforward ESM strategies can be derived called the C-ESM and S-ESM. The C-ESM defines a constant upper threshold C to the tip-speed and applies this threshold to the normal control curve when precipitation occurs. That is

$$\text{C-ESM} = \begin{cases} g_{normal}(V_{wind}) & \text{if } I = 0, \\ \min(g_{normal}(V_{wind}), C) & \text{if } I > 0. \end{cases} \quad (B.2)$$

The S(TOP)-ESM reduces the tip-speed of the turbine to zero when the rain inten-

sity exceeds a particular threshold I_{th}. That is

$$
\text{S-ESM} = \begin{cases} g_{\text{normal}}(V_{\text{wind}}) & \text{if } I \leq I_{\text{th}}, \\ 0 & \text{if } I > I_{\text{th}}. \end{cases} \tag{B.3}
$$

B

These methods are heuristic and, in general, do not represent an optimal ESM strategy. Optimal is defined as the curve that provides the maximum lifetime extension for the minimum AEP loss for a particular set of independent environmental variables ($V_{\text{wind}}, I, ...$). For example, the C-ESM is an optimal strategy only when either $C = V_{\text{tip, min}}$ or $C = V_{\text{tip, max}}$.
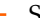
The V-ESM, which only considers the wind speed, is the first strategy that creates an entire optimal Pareto front. It is defined as

$$
\text{V-ESM} = \begin{cases} g_{\text{normal}}(V_{\text{wind}}) & \text{if } I = 0, \\ g_{\text{opt}}(V_{\text{wind}}) & \text{if } I > 0, \end{cases} \tag{B.4}
$$

where g_{opt} is the curve that leads to an optimal strategy. The VI-ESM represents a more advanced strategy that also includes the rain intensity I as another environmental input. The VI-ESM is defined as

$$
\text{VI-ESM} = \begin{cases} g_{\text{opt}}(V_{\text{wind}}, 0) = g_{\text{normal}}(V_{\text{wind}}) & \text{if } I = 0, \\ g_{\text{opt}}(V_{\text{wind}}, I) & \text{if } I > 0. \end{cases} \tag{B.5}
$$

That is, when $I = 0$, the strategy follows the normal tip-speed control curve. If other environmental conditions were to significantly promote erosion, like ambient temperature, UV radiation, etc., then more advanced strategies could be considered.

The question is how to find the optimal curve g_{opt} within the operational regime. One could heuristically guess a function leading to a strategy such as the C-ESM, which is shown as the curve —— in Figure B.2. Alternatively, one could consider any other arbitrary function, such as the parabolic curve ——. Subsequently, the coefficients of these functions could be optimized. However, no guessed function is guaranteed to lead to the optimal strategy. It is possible to use high-order polynomials. For a sufficiently high order, these could approximate the optimal function closely. However, optimizing for many coefficients is a non-trivial task, especially when g is of high order and a function of many environmental variables.

Here, it is argued that an ESM strategy is optimal inside the region spanned by $g_{\text{min}}(V_{\text{wind}})$ and $g_{\text{normal}}(V_{\text{wind}})$ when

$$
g_{\text{opt}} = \{g(V_{\text{wind}}, I, ...) \quad \text{subject to} \quad \text{minimize}(|\eta(g(V_{\text{wind}}, I, ...)) - K|) \\ \text{for all} \quad (V_{\text{wind}}, I, ...)\}, \tag{B.6}
$$

where

$$\eta(g(V_{\text{wind}}, I, ...)) = \frac{\frac{\partial P}{\partial V_{\text{tip}}}}{\frac{\partial(\partial_t D)}{\partial V_{\text{tip}}}} = \frac{\partial P}{\partial(\partial_t D)}. \tag{B.7}$$

$P(g(V_{\text{wind}}, I, ...))$, abbreviated as P, is the (instantaneous) turbine power and $\partial_t D(g(V_{\text{wind}}, I, ...))$, abbreviated as $\partial_t D$, is the damage accumulation rate. The choice of the variable K determines an operational tuple of {AEP loss, LX} on the Pareto front. By considering all possible values of K, the entire Pareto front is obtained. It is important to note that this method is only optimal with perfect knowledge of the precipitation and assumes that the turbine can react instantaneously to changes in the independent environmental variables.

(a) P (MW)

(b) $\ln(\partial_t D)$ (1/s)

(c) $\ln(\eta)$
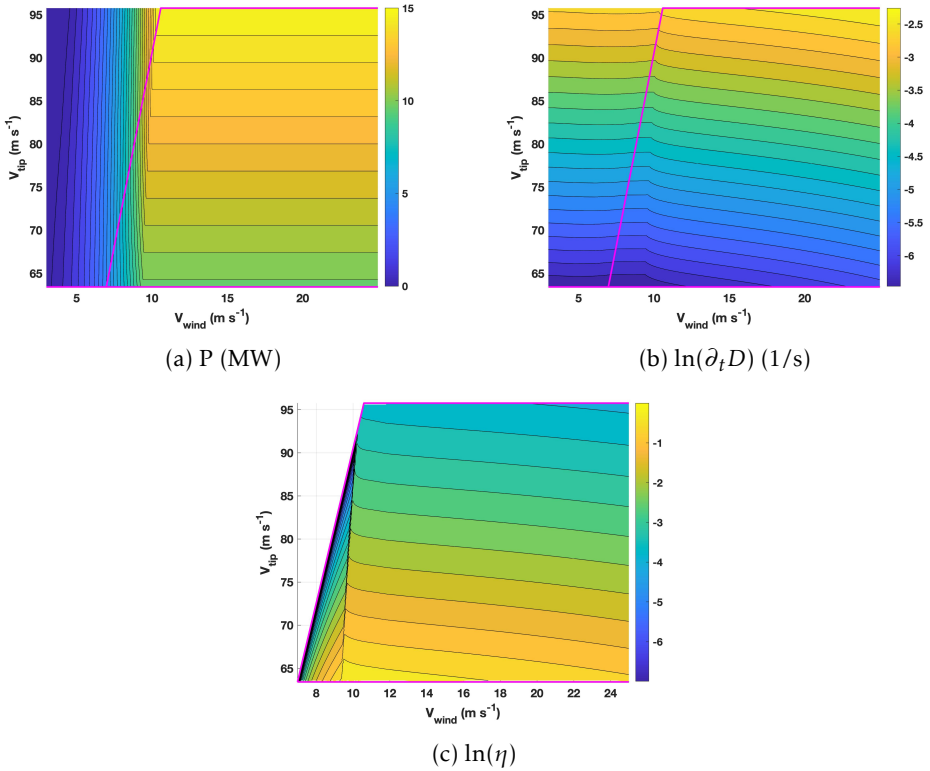
Figure B.3: Turbine power, erosion damage production rate and η as a function of V_{wind} and V_{tip} according to Equation B.7; η was rescaled to a range from zero to one; the natural logarithm was applied to the values of (b) and (c) for improved visualization; the magenta piecewise-linear curves indicate the minimum and maximum allowed speed of the turbine, see also Figure B.2; all drop-size effects are activated; IEA 15MW turbine located at De Kooy.

The method can also be described as follows: Choose a constant K and then determine the tip-speeds for all independent environmental variables (V_{wind}, I, ...) so that $\eta = K$. Since the turbine has a lower and an upper speed limit given by $g_{min}(V_{wind})$ and $g_{normal}(V_{wind})$, respectively, it is not always possible to satisfy $\eta = K$. For these cases, the tip-speed with the corresponding η closest to K should be chosen.

To understand why Equation B.7 leads to the optimal ESM strategy, one should consider Figure B.3c. The figure shows η in the space spanned by V_{wind} and V_{tip}. As per Figure B.1, the operation at the minimum tip-speed during rain represents an optimal strategy (see Point B). However, while providing the highest possible LX, this operational point also comes with a large AEP penalty. In practice, another operational point on the Pareto front is likely to be more desirable. To achieve this, the tip-speed must increase, however, this also increases the erosion damage production. The aim must be to add the highest growth in power for the smallest growth in damage. This is achieved when starting from the minimum tip-speed and then increasing the tip-speed for the independent variables (V_{wind}, I, ...) that have the highest $\partial P/\partial(\partial_t D)$. Since the same value of η might be found for a variety of independent values, contours of η exist. These are shown as black lines in Figure B.3c. Therefore, to find an optimal ESM strategy that satisfies a tuple constraint, one needs to, starting from the minimum tip-speed, continuously advance across the η-levels in the direction of increasing tip-speeds. This process is stopped when the value of K is found, which satisfies the tuple constraint. A contour line thus represents an optimal ESM control curve $g_{opt}(V_{wind}, I, ...)$. The Pareto front is formed when the tuples are recorded for every valid value of K.

The approach of Equation B.6 is valid because the values of η in the region bound by the g_{min} and g_{normal}, are strictly monotonically decreasing with respect to an increasing tip-speed for a particular set of (V_{wind}, I, ...). There are no local minima/-maxima or saddle points in the bound region. In the variable load region, g_{normal} passes through the points of maximum power generation. Above this curve, the power production decreases, even though the tip-speed is increased. Hence, above g_{normal} in the variable load region, the power decreases and η becomes negative. Thus, the turbine produces less power but more damage. This is an operational regime that is clearly undesirable. The discussed properties are true for the IEA 15MW turbine and turbines of similar design. Other turbines might behave differently, and in this case, the approach might require modification. It is also noteworthy that this approach only considers damage and AEP loss. The potential influence of repair strategies and their associated costs are not considered. Last but not least, it should be noted that the pitch angle of the blade is precomputed and set according to the method described in Appendix 4.2.2. The pitch angle is determined so that power production is optimized while at the same time the maximum generator torque is respected. However, since the pitch angle influences P

and $\partial_t D$, it is also possible to consider it as a free variable that can be optimized. Or said differently, an ESM could regulate the tip-speed and pitch angle to mitigate erosion. This route has not been explored any further in this work.

In a practical implementation, the values of η can be precomputed on a large grid that is spanned by $(V_{wind}, I, ...)$ and V_{tip}. Hence, for the V-ESM, η is an array of rank two, while for the VI-ESM, η becomes an array of rank three. The discretization of V_{tip} can far exceed the physical limits of the turbine. Subsequently, the appropriate contour line of $\eta = K$ can be extracted that yields a temporary control curve $g'_{opt}(V_{wind}, I, ...)$. Subsequently, this curve can be clamped with

$$g_{opt}(V_{wind}, I, ...) = \text{clamp}(g'_{opt}(V_{wind}, I, ...), g_{min}(V_{wind}), g_{normal}(V_{wind})), \quad (B.8)$$

where

$$\text{clamp}(x, x_{min}, x_{max}) = \min(\max(x, x_{min}), x_{max}) \quad (B.9)$$

is the clamping operator. The optimization of one value (K) is required to satisfy a particular tuple. Solving this optimization problem is trivial, e.g., by simply calculating all tuples for all K. The computational cost of the proposed approach is minimal and similar to the C-ESM. The derivatives of $\partial P/\partial V_{tip}$ and $\partial(\partial_t D)/\partial V_{tip}$ can be computed by using a simple finite difference scheme. The magnitude of η might not always be convenient since $P \gg \partial_t D$. The power production is in the order of MW, hence $P \approx 10^6$ to $P \approx 10^7$, while the order of the total damage accumulated per year is $D \approx 10^{-2}$ to $D \approx 10^0$. Consequently, assuming the latter, the damage production rate in 1/s becomes $\partial_t D \approx 10^{-8}$. Hence, for the constituents of η, there exists a considerable difference in magnitudes. Therefore, performing a rescaling operation can be advantageous. It is important to note that rescaling does not influence the resulting control curve g_{opt} but is merely a question of convenience in the actual implementation.

The damage rate calculation is dependent on the considered mode. For the V-ESM, the damage rate reads

$$\partial_t D_{V-ESM}(g_{opt}(V_{wind})) = \int_0^\infty \int_{0°}^{360°} \int_0^\infty \partial_t D_{I,\theta,\phi} d\phi d\theta dI. \quad (B.10)$$

For the VI-ESM the damage rate becomes

$$\partial_t D_{VI-ESM}(g_{opt}(V_{wind}, I)) = \int_{0°}^{360°} \int_0^\infty \partial_t D_{\theta,\phi} d\phi d\theta. \quad (B.11)$$

When comparing Equations B.10 and B.11 with Equation 4.1, one can see that for every independent variable that drives the ESM, the respective integral must be removed. Therefore, the V-ESM depends on f_I, f_θ and f_ϕ, plane. Whereas the VI-ESM depends on f_θ and f_ϕ, plane. Conversely, this shows that the distribution of

wind at a particular site does not influence the V-ESM and VI-ESM η-contours. Expanding on this, the VI-ESM η-contours are also independent of the rain intensity distribution of the site! Both ESM strategies depend on the drop-size distribution f_ϕ,plane. In practice, f_ϕ,plane varies per site Pryor et al. (2022). Hence, one can conclude that for an optimal ESM strategy, the site-specific drop-size distribution should be taken into account.

The contours of the V-ESM's power and damage accumulation rate are shown in Figures B.3a and B.3b. In the variable load region, the iso-contour lines of the damage accumulation rate are almost flat. In the rated power region, the iso-contour lines start falling due to the interplay of the increasing wind speed and pitch angle. The iso-contour lines of P are flat in the rated power region. This is due to the turbine being torque limited in this region and an increase in the power can only come from an increase in the rotational speed (see Equation 4.34). In the variable load region, the power iso-contour lines are almost vertical, and hence the power changes rapidly with the tip-speed. For the numerical calculation of the derivatives, it is important to use a sufficiently fine grid in this region. Additionally, any interpolation scheme must have a sufficiently high continuity to avoid erroneous discontinuities in the contour plot of η. The resulting $\eta_{\text{V-ESM}}$ is visualized in Figure B.3c for the operational space. It can be seen that η decreases with increasing tip-speed. Close to the minimum tip-speed, η predicts that an increase in tip-speed will yield a considerable increase in power for only a moderate increase in damage production. However, as the tip-speed increases, due to the high value of β, η reduces rapidly; this is a consequence of the order of the damage and power terms. The damage scales with the tip-speed according to approximately $\beta + 1$ while the power scales with about order one. Therefore, in comparison, a change in the wind speed only marginally affects power but greatly affects erosion damage production.

The extension of the V-ESM to the VI-ESM is straightforward. Instead of Equation B.10, Equation B.11 must be used. Figure B.4a shows a resulting ESM strategy based on an arbitrary value of K. For $I = 0$, i.e., no rain, the ESM strategy retains the original control curve of the turbine. As the rain intensity increases, the curve starts to fall in the direction of increasing rain intensities. The *fall* is similar to a parabolic curve. In the direction of V_{wind}, the VI-ESM strategy is similar to the V-ESM strategy. Two slices through the volumetric data of η are given in Figure B.4. The first slice, given in Figure B.4b, shows η in the V_{wind}-V_{tip}-plane. This slice is very similar to Figure B.3c. Hence, the prior observations pertain to it. In Figure B.4c the slice in the I-V_{tip}-plane is given. It is visible how the iso-contours fall as the rain intensity increases. This aligns with earlier observations that higher rain intensities produce much more damage than lower rain intensities.

Figure B.5 shows the resulting optimal Pareto fronts of the V and VI-ESM. As with any ESM strategy, the start and end points of both modes are equal (see Points A

B
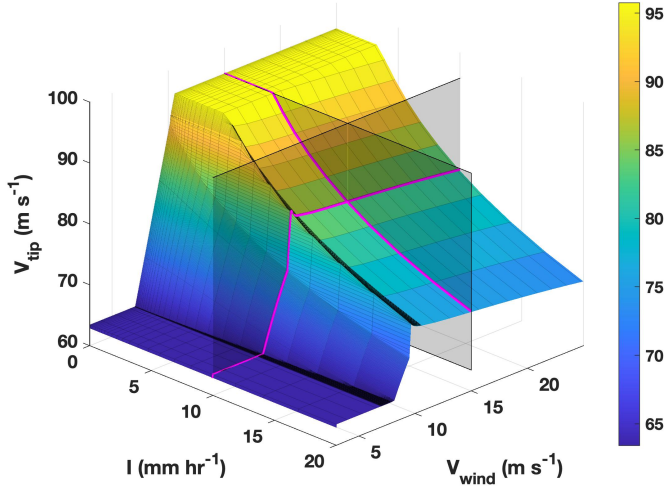
(a) g_{opt} for an arbitrary value of K in Equation B.6.
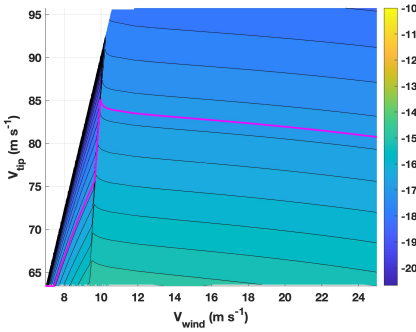
(b) Slice through the volumetric data of η in the V_{wind}-V_{tip}-plane; the black lines show the iso-contours of η.
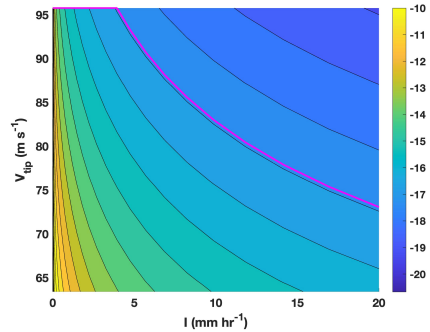
(c) Slice through the volumetric data of η in the I-V_{tip}-plane; the black lines show the iso-contours of η.

Figure B.4: Resultant VI-ESM control curve for a particular K according to Equation B.6 as well as slices through the volumetric data of η as a function of V_{wind} and I; in the slices the magenta-colored curves represent the surface of Figure B.4a; the natural logarithm was applied to η for improved visualization; all drop-size effects are activated; IEA 15MW turbine located at De Kooy.

and B in Figure B.1). In between these points, the VI-ESM can achieve a significantly higher lifetime extension than the V-ESM and can, therefore, be considered superior. For example, at 1 % AEP loss, the V-ESM provides a lifetime extension of about seven, whereas the VI-ESM offers an extension of about 13.1. The increase in performance comes with a shift in shape. The V-ESM produces a convex curve, whereas the graph of the VI-ESM is first convex and then becomes concave toward the maximum lifetime extension. This change in shape is associated with a shift of the Pareto front upwards and to the left, thus in the favorable direction as indicated in Figure B.1.
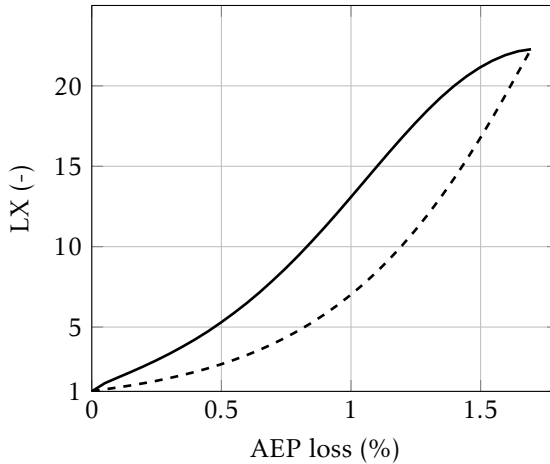
Figure B.5: Resulting Pareto fronts for the V-ESM - - - and VI-ESM ⎯⎯ using the optimal approach from Equation B.6; all drop-size effects are activated; IEA 15MW turbine located at De Kooy.

Heuristic reference ESM strategies are considered to support the claim of Equation B.6. The V-ESM and VI-ESM are tested against the heuristic C-ESM used in Barfknecht et al. (2022). Additionally, two other strategies are considered. The first is a more sophisticated rule where the control curve comprises two piecewise-linear line segments. For that $\Delta V = V_{\mathrm{wind}} - V_{15}$ is defined, where $V_{15} = 6.98$ m/s, which is the wind speed at the end of IEA 15MW's minimum rotor speed control region, see Gaertner et al. (2020). The equation reads

$$
\mathrm{LV\text{-}ESM} = \begin{cases} g_{\mathrm{normal}}(V_{\mathrm{wind}}) & \text{if } I = 0, \\ \mathrm{clamp}\left(\min(C_2 \Delta V + 1, C_1), 1, \frac{g_{\mathrm{normal}}(V_{\mathrm{wind}})}{g_{\mathrm{min}}(V_{\mathrm{wind}})}\right) g_{\mathrm{min}}(V_{\mathrm{wind}}) & \text{if } I > 0. \end{cases}
$$
$$(B.12)$$

The second is an extension that adds a dependency on I. This creates a rule consisting of three piecewise-linear planes. It uses the definition $\Delta I = I - C_4$. The equation

reads

$$\text{LVLI-ESM} = \text{clamp}\left(\min(C_3\Delta I + C_2\Delta V + 1, C_1), 1, \frac{g_{\text{normal}}(V_{\text{wind}})}{g_{\text{min}}(V_{\text{wind}})}\right) g_{\text{min}}(V_{\text{wind}}).$$

(B.13)

B

For both equations, the coefficients $C_1,...,C_4$ are required. LV stands for linear with respect to V_{wind}. The acronym LI stands for linear with respect to I. Matlab's *fmincon* function was used to find the coefficients. A particular target AEP loss was defined, and then the coefficients that led to the highest lifetime extension were selected. This resulted in Figure B.6, which compares the performance of the V-ESM and VI-ESM to the heuristic C-ESM, LV-ESM and LVLI-ESM strategies. The figure plots the difference in lifetime extension $\Delta \text{LX} = LX_{\text{optimal}} - LX_{\text{heuristic}}$ against the corresponding AEP loss.

As shown in Figure B.6a, the C-ESM offers up to 0.8 less LX in comparison to the V-ESM. The LV-ESM performs significantly better, performing almost as well as the V-ESM in some parts. The good performance of the LV-ESM can be explained by its form of two piecewise-linear segments. These allow for a close approximation of η's ideal contour lines as shown in Figure B.3c.

(a) V-ESM as baseline   (b) VI-ESM as baseline
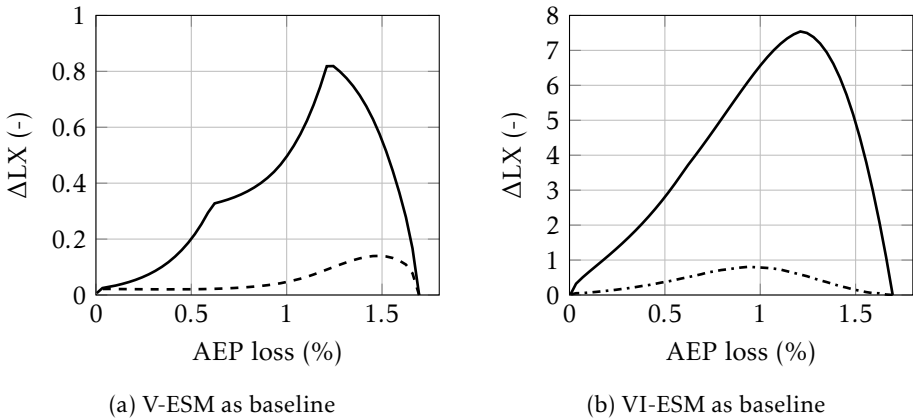
Figure B.6: Difference in lifetime extension between the optimal and heuristic ESM strategies; C-ESM: ——, LV-ESM - - - and LVLI-ESM -·-··; IEA 15MW turbine located at De Kooy.

Figure B.6b shows that the maximum deficit in LX of the LVLI-ESM compared to the VI-ESM is about 0.8. The contours of η in the direction of the rain intensity have the shape of a falling parabolic curve, see for example Figure B.4c. The linear approximation of the LVLI-ESM seems to deliver good performance in this region. To conclude, it is shown that the considered heuristic methods can, in some regions, approach the performance of the optimum ESM, but cannot exceed its performance.

While heuristic methods can provide a reasonably good approximation of the optimal solution, differences still exist. A $\Delta LX = 0.8$ is still significant considering it is merely the result of an offline optimization problem. A further argument for the optimum ESM stems from the following anecdotal evidence: For the authors of this paper, the implementation of the optimum ESM was quite straightforward. However, the optimization of the coefficients of the LV-ESM and LVLI-ESM proved to be challenging. As stated, the optimization was performed with Matlab's fmincon function. Careful considerations had to be paid to the chosen settings. Often, the results would not converge to the optimum set of coefficients. Overall, the optimization of the (less-performing) heuristic curves consumed significantly more time from the authors and required more computational resources.

B

Bibliography

Barfknecht, N., Kreuseler, M., de Tavernier, D., and von Terzi, D.: Performance analysis of wind turbines with leading-edge erosion and erosion-safe mode operation, Journal of Physics: Conference Series, 2265, 032 009, https://doi.org/10.1088/1742-6596/2265/3/032009, 2022.

Bech, J. I., Hasager, C. B., and Bak, C.: Extending the life of wind turbine blade leading edges by reducing the tip speed during extreme precipitation events, Wind Energy Science, 3, 729–748, https://doi.org/10.5194/wes-3-729-2018, 2018.

Gaertner, E., Rinker, J., Sethuraman, L., Zahle, F., Anderson, B., Barter, G. E., Abbas, N. J., Meng, F., Bortolotti, P., Skrzypinski, W., et al.: Definition of the IEA 15-Megawatt Offshore Reference Wind Turbine, Tech. rep., National Renewable Energy Lab.(NREL), Golden, CO (United States), 2020.

Pryor, S. C., Barthelmie, R. J., Cadence, J., Dellwik, E., Hasager, C. B., Kral, S. T., Reuder, J., Rodgers, M., and Veraart, M.: Atmospheric Drivers of Wind Turbine Blade Leading Edge Erosion: Review and Recommendations for Future Research, Energies, 15, https://doi.org/10.3390/en15228553, 2022.

List of Abbreviations

AEP	Annual Energy Production
AOA	Angle Of Attack
CFD	Computational Fluid Dynamics
DDB	Droplet Deformation and Breakup model
DNS	Direct Numerical Simulation
DOWA	Dutch Offshore Wind Atlas
DRD	Droplet Ratio Deformation model
EOL	Erosion Onset Location
EOM	Equations of Motion
EOS	Erosion Onset Speed
ESM	Erosion-Safe Mode
HAWT	Horizontal Axis Wind Turbine
IEA	International Energy Agency
KNMI	Koninklijk Nederlands Meteorologisch Instituut
LX	Lifetime Extension
NLTAB3	Non Linear Taylor Analogy Breakup model
NREL	National Renewable Energy Laboratory
RPM	Revolutions Per Minute
RWT	Reference Wind Turbine
SIMPLE	Semi-Implicit Method for Pressure Linked Equations
STEPS	Short-Term Ensemble Prediction System
TAB	Taylor Analogy Breakup model
TSR	Tip-Speed Ratio
cdf	cumulative density function
pdf	probability density function
C-ESM	ESM with constant maximum tip speed
LV-ESM	heuristic ESM with linear dependency on wind speed
LV-LI-ESM	extension of LV-ESM with linear dependency on rain intensity
S-ESM	Stop-ESM, ESM that stops during rain
V-ESM	optimum wind-speed-based ESM
VI-ESM	optimum wind-speed and rain-intensity-based ESM

LIST OF SYMBOLS

A	rotor disc area
A_a	frontal area of deformed droplet
AEP	annual energy production
$A_{\text{projected}}$	projected droplet area in Springer model
A_s	surface area of oblate spheroid
$A_{s,0}$	surface area of sphere
A_0	frontal area of spherical droplet
$\overline{AB}$	Pareto front of ESM strategy
a	semi-major axis of deformed droplet
a	coefficient in drop-size-dependent damage law
a	axial induction factor
a'	radial induction factor
a_{impact}	droplet semi-major axis at impact
a_{max}	droplet semi-major axis at onset of breakup
a_0	initial droplet semi-major axis
$\bar{a}$	non-dimensional droplet semi-major axis
a_ϕ	droplet semi-major axis at terminal falling conditions
b	droplet semi-minor axis
b	coefficient in drop-size-dependent damage law
C	threshold for C-ESM
C_D	resultant drag coefficient of droplet
$C_{D_{\text{disk}}}$	drag coefficient of a disk
$C_{D_{\text{sphere}}}$	drag coefficient of a sphere
C_{dynamic}	dynamic drag component of droplet
C_l	airfoil lift coefficient
C_p	pressure coefficient driving droplet deformation
C_Q	torque coefficient
$C_{Q_{\text{max}}}$	maximum torque coefficient
C_{static}	static drag component of droplet
C_1	constant of curve fit for angle of attack correction
C_2	constant of curve fit for angle of attack correction
$C_{1 \text{ to } 4}$	coefficients for heuristic ESM strategies

c	Weibull wind speed distribution scale parameter
c	airfoil chord
D	total erosion damage (during a year)
D	lower control volume boundary
D	time format for days
$\vec{D}$	surface vector of lower control volume boundary
$D(I)$	D as a function of I
$\overline{D}$	non-dimensional D
$D(\phi)$	D as a function of ϕ
$\overline{D(\phi)}$	normalized damage over one blade rotation as a function of ϕ
$D_{\text{cumulative}}$	D in cumulative form
$D_{\text{no slowdown}}$	D for when droplets don't have slowdown
D_x	D multiplied with distribution of x
dA	(infinitesimal) blade surface element
$dt_{\text{fall through}}$	time for a droplet to fall through the domain
dx	infinitesimal length in x-direction
dy	infinitesimal length in y-direction
dz	infinitesimal length in z-direction
E	energy produced by turbine
F	impact force in Springer model
$\vec{F}$	water mass surface flux
$\vec{F}_D$	water mass flux of lower boundary
$F_D(I)$	cdf of $f_D(I)$
$F_D(V_{\text{wind}})$	cdf of $f_D(V_{\text{wind}})$
$F_D(\theta)$	cdf of $f_D(\theta)$
$F_D(\phi)$	cdf of $f_D(\phi)$
F_{drag}	drag force on droplet
F_I	cdf of the rain intensity
$\vec{F}_L$	water mass flux of left boundary
F_p	pressure force on droplet driving deformation
$\vec{F}_R$	water mass flux of right boundary
$\vec{F}_U$	water mass flux of upper boundary
F_σ	surface tension force on droplet
$F_{\phi,\text{site}}$	cdf of water of mass associated with a droplet diameter at a particular site
$f_D(I)$	pdf of damage at site w.r.t rain intensity
$f_D(V_{\text{wind}})$	pdf of damage at site w.r.t wind speed
$f_D(\theta)$	pdf of damage at site w.r.t angular position

$f_D(\phi)$	pdf of damage at site w.r.t droplet diameter
f_I	pdf of rain intensity
$f_{V_{\text{wind}}}$	pdf of wind speed
f_x	pdf of dummy variable x
f_θ	pdf of angular blade position
$f_{\phi,\text{air}}$	drop-size distribution in a volume of air
$f_{\phi,\text{plane}}$	drop-size distribution through plane in air
$f_{\phi,\text{site}}$	pdf of water of mass associated with a droplet diameter at a particular site
g	generic $V_{\text{tip}}(V_{\text{wind}})$ curve
g_{min}	minimum $V_{\text{tip}}(V_{\text{wind}})$ curve
g_{normal}	normal $V_{\text{tip}}(V_{\text{wind}})$ curve
g_{opt}	optimum $V_{\text{tip}}(V_{\text{wind}},I)$ curve
H	accumulated impingement
$H^{(1)}$	accumulated impingement column as [L]
$H^{(3)}$	accumulated impingement volume as $[L^3]$ on dA
$H(I)$	H as a function of I
$H(t)$	accumulated impingement as a function of time
$H(\phi)$	H as a function of ϕ
H_{allowed}	allowed impingement until end of incubation
H_{now}	nowcast-predicted precipitation column
H_{true}	true precipitation column
H_x	H multiplied with distribution of x
H_{100}	softsign function in drop-size-dependent damage law
h	height in km for droplet terminal velocity formula
h	blade section height
h	time format for hours
I	rain intensity
I_{th}	rain intensity threshold for S-ESM
I_ϕ	rain intensity for every droplet diameter
i	index for discrete time-interval
K	constant selecting an η contour of optimal ESM
k	calibration constant in DRD model
k	Weibull wind speed distribution shape parameter
L	erosion lifetime
L	left control volume boundary

$\vec{L}$	surface vector of left control volume boundary
$\overline{L}$	normalized erosion lifetime
LX	(L)ifetime e(X)tension factor
LX_{max}	highest possible LX of a particular ESM strategy
M	time format for minutes
$M(\lambda)$	maximum torque coefficient as a function or λ
m	droplet mass
h	time format for minutes
N	XFoil N-crit factor
N	measure for incubation time
N_i^*	number of allowable impacts on one location as per Springer model
n	aerodynamic exponent
n_ϕ	number of droplets of diameter ϕ
$\vec{n}_{LE}$	normal vector of the leading edge
Oh	Ohnesorge number
P	wind turbine power
p_{rain}	probability of rain (at site)
$p_{damaging\ rain}$	probability of damaging rain
p_{wh}	water hammer pressure in Springer model
Q	rotor torque
Q_{max}	maximum rotor torque
q	dynamic pressure
R	rotor blade length
R	right control volume boundary
$\vec{R}$	surface vector of right control volume boundary
R_{blade}	rotor blade length
R_c	aerodynamic nose radius
$R_c(\alpha)$	aerodynamic nose radius as a function of angle of attack
$R_{c,0}$	$R_c(\alpha)$ at 0-degree angle of attack
Re	droplet Reynolds number
R_0	initial droplet radius
r	position along rotor blade
r	distance to impact location in Springer model
r/R	non-dimensional position along rotor blade

r/R_{blade}	non-dimensional position along rotor blade
T	time turbine catches rain
T_{rain}	duration of rain (during a year)
T_{year}	time in a year, number of seconds in a year
$T_{\text{year, spinning}}$	time in a year the turbine spins
t	time
$\vec{t}_{\text{LE}}$	tangent vector of the leading edge
U	upper control volume boundary
$\vec{U}$	surface vector of upper control volume boundary
V_a	expansion velocity of droplet semi-major axis
$V_{a,0}$	start expansion velocity of droplet semi-major axis
V_{air}	velocity of air (in front of the airfoil)
V_{blade}	blade velocity
$V_{\text{circumferential}}$	circumferential velocity component
$V_{\text{collection}}$	water collection velocity for impingement
$V_{\text{ESM,REL}}$	ESM velocity based on V_{wind} and V_{sec}
V_{impact}	impact speed of droplet
V_{inflow}	inflow velocity component
V_{mean}	(hub height) site mean wind speed
$\vec{V}_{\text{rain}}$	rain velocity vector
$\vec{V}_{\text{rel}}$	relative droplet velocity vector
V_{sec}	blade section speed
$\vec{V}_{\text{sec}}$	blade section velocity vector
V_{slip}	velocity difference of droplet and air flow
V_{slowdown}	slowdown velocity
V_{tip}	tip-speed of wind turbine
$V_{\text{tip, min}}$	minimum tip-speed of wind turbine
$V_{\text{tip, max}}$	maximum tip-speed of wind turbine
V_{wind}	wind speed
V_x	droplet velocity in slowdown simulation
$V_{x,0}$	droplet velocity at start of slowdown simulation
V_{15}	wind speed at IEA 15MW's minimum rotor speed control region
V_∞	ΔV far away from the airfoil
V_ϕ	droplet terminal velocity
Vol_{air}	volume of air
$\text{Vol}_{\text{water}}$	volume of water in the air
Vol_ϕ	droplet volume

W	volume of water per volume of air
W_ϕ	W for a particular drop size
We	Weber number
$\text{We}_{\text{impact}}$	Weber number based on V_{impact}
We_∞	Weber number based on V_∞
x	droplet position
x	dummy variable in clamping operator
x_{min}	upper clamping limit
x_{max}	lower clamping limit
$x(t)$	dummy variable in law of large numbers as a function of time
x/c	non-dimensional transition point location along chord
x_b	ballistic droplet trajectory position
x_{blade}	position of the blade in slowdown simulation
$x_{\text{blade},0}$	starting position of the blade in slowdown simulation
x_s	streamline droplet trajectory position
x_0	starting position of droplet
$x_{95\%}$	position at which ΔV reached 95 % of V_∞
$x_{95\%}(\alpha)$	$x_{95\%}$ as function of angle of attack
$x_{95\%,0}$	$x_{95\%}$ at 0-degree angle of attack
Y	time format for years
$y(t)$	dummy variable in law of large numbers as a function of time
α	angle of attack
α	coefficient in damage law
$\alpha(\theta)'$	oscillating component in impact angle
α_ϕ	drop impact angle
β	exponent in damage law
ΔI	difference of I and C_4
ΔLX	difference of optimal and heuristic LX
ΔT_i	length of time-interval i
ΔV	relative velocity between droplet and airfoil
ΔV	difference of V_{wind} and V_{15}
Δx	distance between droplet and airfoil
$\Delta\phi$	difference of ϕ and ϕ_0
ϵ	eccentricity of droplet

η	change in power for a change in damage
θ	angular blade position
λ	tip-speed ratio
μ	mean in lognormal distribution
μ_{air}	dynamic viscosity of air
μ_{water}	dynamic viscosity of water
ρ	density of water in derivation of H
ρ_{air}	density of air
ρ_{water}	density of water
σ	standard deviation in lognormal distribution
σ_{water}	surface tension of water
$\sigma(...)$	stress field in Springer model derivation
ϕ	droplet diameter
ϕ_0	reference diameter in drop-size-dependent damage law
ϕ_0	initial droplet diameter
φ	sum of pitch and twist angle
φ_{pitch}	pitch angle
φ_{twist}	twist angle
ω	angular speed of blade
∂_t	short-hand notation for $\partial/\partial t$
$\partial_t H$	impingement accumulation rate
$\partial_t D_{\text{V-ESM}}$	damage production rate for V-ESM computation
$\partial_t D_{\text{V-ESM}}$	damage production rate for VI-ESM computation v

Glossary

Within this thesis several terms related to the field of leading-edge rain erosion are used. These might not be necessarily universal across the entire field. Therefore, to enhance the readability of this thesis, some of the terms used in this thesis are defined in the following table.

Incubation time	The time of operation until the first erosion damage becomes visible on the blade (specimen). The incubation time can also be defined with respect to other metrics. For example, the number of drop impacts before erosion damage starts to occur.
Damage metric	A quantity that can be used as a proxy for erosion damage. Such as the number of droplet impacts, the amount of transferred kinetic energy or the intercepted water column. This thesis uses impingement as the damage metric.
Damage law	A relation (of measurements) that relates the allowable amount or quantity of the damage metric until the end of the incubation time to another variable, such as the impact speed. For example, a relation that relates the impact speed to the number of droplet impacts until failure, see Equation 4.5.
Damage rule	A relation that is used to make predictions about the lifetime of a material under cyclic loading. This thesis uses the Palmgren-Miner relation which is a linear damage accumulation rule.
Damage model	A framework that combines a damage rule, metric, and law with other information, such as a turbine model or meteorological data, to make predictions about the generated erosion damage. In Section 4.2 a damage model is derived.
Erosion-safe mode (ESM)	Slowing down or stopping the turbine during precipitation events with the aim of reducing or fully avoiding erosion damage.
ESM operation	The process of using the ESM (during precipitation events).

ESM control	The actual control implementation of the ESM on a wind turbine.
ESM strategy	The fundamental working principle, e.g., in terms of a look-up-table, of an ESM variant. ESM strategies are discussed in detail in Section B.2.
Impingement	The water column (or volume when looking at a surface element dA) that is collected by the wind turbine during operation. More tangible, impingement can be seen as the water column or volume that is collected by a bucket mounted on a blade. The formal derivation of impingement is shown in Section A.
Allowed impingement	The impingement that can be collected by the blade until the end of incubation. In this thesis, a damage law relates the impact speed to the allowed impingement as per Equation 3.37.

List of Publications

Journal and conference publications

4. **N Barfknecht**, R Imhoff and D von Terzi. Mitigating blade erosion damage through nowcast-driven erosion-safe mode control. Journal of Physics: Conference Series, 2767(3): 032001, May 2024.

3. **N Barfknecht** and D von Terzi. Drop-size-dependent effects in leading-edge rain erosion and their impact for erosion-safe mode operation. Wind Energy Science Discussions, wes-2024-33:1-49, 2024.

2. **N Barfknecht** and D von Terzi. On the significance of rain droplet slow-down and deformation for leading-edge rain erosion. Wind Energy Science Discussions, wes-2023-169:1-42, 2023.

1. **N Barfknecht**, M Kreuseler, D de Tavernier, and D von Terzi. Performance analysis of wind turbines with leading-edge erosion and erosion-safe mode operation. Journal of Physics: Conference Series, 2265(3): 032009, May 2022.

Conference and poster presentations

5. **N. Barfknecht**, D. von Terzi, *Mitigating blade erosion damage through nowcast-driven erosion-safe mode control*, Poster presentation at Torque 2024, 2024.

4. **N. Barfknecht**, D. von Terzi, *Drop-size-dependent effects in leading-edge rain erosion and their impact for erosion-safe mode operation*, Oral presentation at the 5th International Symposium on Leading Edge Erosion of Wind Turbines, February 2024.

3. **N. Barfknecht**, D. von Terzi, *The impact of droplet slowdown and deformation on blade life*, Oral presentation at the 4th International Symposium on Leading Edge Erosion of Wind Turbines, February 2023.

2. **N. Barfknecht**, D. von Terzi, *Performance analysis of wind turbines with leading-edge erosion and erosion-safe mode operation*, Oral presentation at Torque 2022, 2022.

1. **N. Barfknecht**, D. von Terzi, *Is the best kind of erosion mitigation strategy turbine design dependent?*, Oral presentation at the 3rd International Symposium on Leading Edge Erosion of Wind Turbines, February 2023.

Acknowledgements

Curriculum Vitæ

Nils Barfknecht

2020-2024	PhD Aerospace Engineering
	Wind Energy Group
	Delft University of Technology, the Netherlands
	Thesis: Toward erosion-free wind turbine operation: Physical insights into leading-edge erosion and their application to the erosion-safe mode
	Promotor: Prof. Dr. D. von Terzi
	Promotor: Prof. Dr.-Ing. habil. S. Hickel
2016-2017	Industrial placement in aerodynamics
	Mercedes-AMG Petronas Formula One Team, United Kingdom
2015-2020	Master of Science Aerospace Engineering
	Delft University of Technology, the Netherlands
	Thesis: Error-estimate based adaptive mesh refinement: A user-independent approach for LES
2014-2015	Board year as chief engineer at TU Delft Dream Team
	Forze Hydrogen Racing Team Delft, the Netherlands
2012-2013	TU Delft minor abroad exchange program
	Iowa State University, United Sates of America
2011-2014	Bachelor of Science Aerospace Engineering (cum laude)
	Delft University of Technology, the Netherlands